DYNAMICS OF BINARY COMPACT OBJECTS: FROM NOVEL NUMERICAL APPROACHES TO THE CREATION OF HEAVY ELEMENTS

Dissertation
zur Erlangung des Doktorgrades
der Naturwissenschaften

vorgelegt beim Fachbereich Physik
der Johann Wolfgang Goethe -Universität
in Frankfurt am Main

von **Federico Maria Guercilena**
aus Milano (Italien)

Frankfurt am Main, Januar 2018
(D 30)

Erstbetreuer: Prof. Dr. Luciano Rezzolla
Zweitbetreuer: Prof. Dr. Erik Schnetter

vom Fachbereich Physik der
Johann Wolfgang Goethe-Universität als Dissertation angenommen.

Dekan: Prof. Dr. Owe Philipsen

Gutachter: Prof. Dr. Luciano Rezzolla
Prof. Dr. Erik Schnetter

Datum der Disputation:

Contents

Part I

Background

Chapter 1

Introduction

Compact objects - black holes and neutron stars - are fascinating objects, not only for the astrophysicists, but for a wide range of researchers, including astronomers, theoretical physicists, particle and nuclear physicists, condensed matter physicists and arguably for the layman as well.

First theorized in the first part of the twentieth century (Schwarzschild, 1916; Baade and Zwicky, 1934), for a long time these objects have been considered just exotic ideas or mathematical curiosities. Pulsar were however detected in the late 1960s (Hewish et al., 1968) and readily identified as rotating, radiating neutron stars, while the first candidate black hole, Cygnus X-1, was observed in 1972 (Shipman, 1975). Since then the interest in these objects has steadily grown.

The reasons behind this interest are easily understood considering that compact object dwell at the intersection of many different areas of physics, and are ideal laboratories to explore the interplay between these areas.

Black holes, which are purely gravitational objects, are perfectly suited to study the nature of gravity, its manifestations such as gravitational waves, and the differences between various theories of gravity in the regime where they are expected to be most relevant, *i.e.* the strong field regime. However, just like any massive astrophysical object, black holes are interested by accretion phenomena, which are thought to be the power source of some very bright astrophysical emitters of electromagnetic signals, such as active galactic nuclei or X-ray binaries.

At the same time, black holes exist in a variety of different mass scales, from stellar mass to supermassive black holes billions of times heavier. The latter play a very important and yet not fully understood role in the formation and evolution of galaxies, as well as in shaping the large scale structure of the universe, making them relevant to cosmology as well.

Neutron stars share with black holes the characteristic of being gravitationally dominated systems; but because they are composed of baryon matter, they display a much richer behaviour. It has been realized early on that the matter in neutron star cores reaches extreme densities, exceeding the one in atomic nuclei. This means that neutron stars could provide invaluable information on the behaviour of matter in such extreme conditions (which are impossible to achieve in laboratory experiments), such as details of the nucleonic interaction, the properties of hyperons or of quark-gluon plasmas.

The recent detections of gravitational waves from binary neutron stars (The LIGO Scientific Collaboration and The Virgo Collaboration, 2017) and binary black hole mergers (The LIGO Scientific Collaboration and the Virgo Collaboration, 2016; Abbott et al., 2016a; The LIGO Scientific Collaboration et al., 2017b) has heralded the beginning of the era of gravitational-wave astronomy and multi-messenger astronomy. The simultaneous detection of gravitational and electromagnetic signals (The LIGO Scientific Collaboration et al., 2017a; LIGO Scientific Collaboration et al., 2017) from a binary neutron star merger has provided convincings evidence that establishes such events as the origin of short gamma-ray bursts (SGRBs). Binary neutron stars are also now confirmed as the single most likely site of production of heavy elements, through the r-process nucleosynthesis taking place in the matter ejected from their merger; furthermore, this nucleosynthesis process (or rather the radioactive decay of its products) is expected to power another transient signal of great interest, the so called kilonova (also known as macronova in the literature) (Metzger, 2017a; Rosswog, 2013a).

While a lot of questions remain open, in the decades since their identification significant progress has been made in developing our understanding of these objects. This progress has been made possible thanks to an interplay of theoretical and observational/experimental advances. A few highlights of the observational discoveries have been *e.g.* the detection of very relativistic binary pulsars and the measurement of their orbital parameters with impressive precision from radioastronomy observations (Kramer and Wex, 2009); the tracking of stellar orbits near the Galactic center, allowing a direct measurement of the mass of the supermassive black hole in the center of our own Milky Way galaxy (Gillessen et al., 2009); the increasingly accurate imaging of astrophysical jet structures employing very long baseline interferometry (VLBI). The most striking, as well as one of the most recent, of these developments has arguably been the above mentioned detection of gravitational waves from merging binary black holes and neutron stars at LIGO (Laser Interferometer Gravitational-Wave Observatory), which opened the upcoming era of gravitational wave astronomy.

On the other hand, theoretical modelling has also greatly advanced our understanding of compact objects. Significant progress has been made in understanding the mathematical structure of general relativity, and in developing relativistic analogues of the theories of hydrodynamics, viscosity, electromagnetism and neutrino interactions; approximation schemes for the Einstein equations such as the post Newtonian (PN) formalism (Blanchet, 2006), gravitational self-force (GSF) formalism (Barack and Ori, 2003) or the effective one body (EOB) model (Buonanno and Damour, 1999) have been developed, allowing *e.g.* to compute the gravitational radiation waveforms from binary systems; advances have been made in characterizing the nuclear forces and translating this knowledge in equations of state (EOS) suitable to describe neutron stars; or in estimating the opacity of BNS ejecta, a key ingredient to compute kilonova light curves (Barnes et al., 2016). Many other examples would of course be possible.

However in the last decade a new approach to the study of system of compact objects has emerged. This goes under the name of numerical relativity, and consists in employing computational techniques to perform large scale simulations of these systems from which important information on their behaviour

can be extracted. This is a relatively young field (the first successful evolution of inspiralling and merging black holes able to extract the gravitational signal was performed by Pretorius (2005)), but has quickly reached maturity and has firmly established itself as a powerful research tool complementing the more traditional ones. It is in this context that the present work has been developed and carried out.

The biggest advantage of numerical relativity is that it can provide solutions for highly non-trivial, non-idealized system configurations, where an analytic solution cannot be obtained. The data generated by such simulations can by analyzed as if resulting from an observation or an experimental measure, enabling the researcher to infer the properties of the system. This has allowed numerical studies to provide important information about *e.g.* the post-merger gravitational wave signal of BNS system (Takami et al., 2015); the thermo- and hydrodynamical properties of the matter ejected by such events; or the topology and intensity of their the magnetic fields (Baiotti and Rezzolla, 2017).

Performing numerical simulations is however a very non-trivial endeavour in itself, and requires particular care in order to be successful. The equations encoding the physical theories describing the systems of interest have to be cast in a suitable form to guarantee numerical stability; stable, accurate and efficient numerical methods have to be devised to solve them in order both to generate the initial data and computing its evolution; care must be taken in coding these algorithm, to ensure their correctness and efficiency; and additional methods have to be designed and implemented to analyze the resulting data. Finally large scale numerical simulations have a non-negligible computational cost which must be managed and reduced as much as possible.

In tackling one of the first issues that are encountered in the field of numerical relativity, *i.e.* the development of a form of the equations suitable for numerical implementation, I have contributed to develop a new first-order formulation of the Einstein equations named FO-CCZ4, as published in Dumbser, Guercilena, Koeppel, Rezzolla, and Zanotti (2017). So that they can stably integrated numerically, systems of equations must be cast in hyperbolic form. This mathematical requirement physically means that information must propagate with finite speeds in the system under consideration (a natural requirement for modern, relativistic theories) (Sarbach and Tiglio, 2012). In turn, it can be shown that this implies the well-posedness of the system. Einstein equations as expressed in the usual four-dimensional, covariant form, are not manifestly hyperbolic, and thus must be manipulated to produce a well-posed system.

The FO-CCZ4 formulation described in this work has been proven to be strongly hyperbolic and therefore able to sustain long term, stable simulations. Like the CCZ4 formulation (Alic et al., 2012, 2013) on which it is based, it also include a damping mechanism to reduce violations of the constraints, enhancing its accuracy. Furthermore the system of equations is manifestly linearly degenerate in all its characteristics fields, which ensures that no shocks can be generated by it, which removes the thorny issue of dealing with discontinuous solutions ins the numerical evolution. While this is expected on physical grounds for Einstein equations, it is not a property automatically satisfied by all formulations. Finally, the FO-CCZ4 system is first order in both space and time, which makes it suitable to be solved by use of the highly accurate, efficient and scalable discontinuous Galerkin (DG) (Hesthaven and Warburton, 2007) methods. We therefore developed an implementation of this formulation

which relies on a state-of-the-art ADER-DG numerical scheme with WENO-subcell limiter. We have shown the code to easily pass all standard testbeds with remarkable accuracy and we successfully applied it to the simulation of isolated as well as colliding black holes. It has to be remarked that these are the first three-dimensional simulations of black hole spacetimes employing a DG scheme.

In order to treat non-vacuum spacetimes Einstein equations have to be couple with the equation of motion for the matter fields. The matter in these cases is commonly described as a single perfect fluid (Font, 2008), and so the relativistic Euler equations are to be solved along with Einstein equations. Euler equations are however genuinely non-linear (Leveque, 1992), which means they can develop shocks even starting from smooth initial data. In this context the challenge is to develop numerical methods that are not only accurate, but able to sharply resolve such discontinuities without developing spurious oscillations or other pathologies. The standard choice in numerical relativity is to rely on high-resolution shock-capturing (HRSC) techniques (Rezzolla and Zanotti, 2013). I have developed a novel numerical method, alternative to HRSC ones, named "entropy limited hydrodynamics" (ELH) (Guercilena, Radice, and Rezzolla, 2017) for the solutions of the equations of relativistic hydrodynamics that is simpler than these techniques, making it suitable for efficient implementation without sacrificing accuracy. This scheme is of flux-limiter type, combining a high-order, accurate flux formula with a low-order, stable one with a variable, solution dependent ratio. The ratio is obtained by computing a "viscosity function" proportional to the local production of entropy in the fluid. This has the immediate advantage that, since entropy can only be produced by shocks in a perfect fluid, the low-order contribution is only activated at the location of shocks, while accuracy is recovered automatically on smooth parts of the solution. I have implemented the ELH scheme in a finite-differences (FD) code and successfully tested in a number of special-relativistic test cases, as well as general-relativistic simulations of isolated neutron stars. In special-relativistic, one-dimensional tests such as shock tubes, the code can sharply resolve discontinuities while in the case of smooth solutions it recovers its nominal order of convergence (which can be easily adjusted to fit the peculiarities of the problem under study). In three-dimensional general-relativistic evolutions of neutron stars, I have shown the method to be stable and accurate in a systematic comparison with the MP5 scheme (a typical HRSC method), and to be able to handle highly relativistic and non-trivial scenarios, such as the gravitational collapse of a neutron star to a black hole. Furthermore, despite a non-optimized implementation, the scheme is able to deliver significant performance improvements, up to $\sim 50\%$ in some cases.

Once all such issues pertaining to accuracy, stability and efficiency have been properly addressed, numerical simulation reveal their power as scientific tools to investigate the physics of compact objects. One particular physical puzzle that numerical simulations have been successfully begun investigating recently is related to the origin of heavy elements in our universe. Elements heavier than iron are known to be produced primarily by neutron-capture processes on lighter seed nuclei, and for elements with mass number A higher then approximately 120 the main such process is the rapid neutron-capture process, or r-process. This process can take place in environments in which the neutron-to-seed ratio is so high that the beta decay timescale becomes much longer

than the neutron-capture one. Initially the matter ejected in core-collapse supernovae (CCSN) was thought to be the main astrophysical site of r-process nucleosinthesys, but recently the ejecta in BNS mergers has become a much more promising candidate, also supported by spectroscopic observations (Ji et al., 2016). The abundance patterns of heavy elements computed from BNS mergers have been shown to match quite well the ones measured in our Galaxy and our solar system in particular (Radice et al., 2016).

In this context I have participated in efforts to shed light on the dependence of the elements abundance on the neutron star EOS (Bovard, Martin, Guercilena, Arcones, Rezzolla, and Korobkin, 2017). By performing long term, accurate simulations of BNS mergers, in which the masses of the stars under considerations were systematically varied and employing several finite temperature EOSs spanning a large range in stiffness, we where able to measure the total amount of ejected mass (another very relevant but still poorly constrained variable, (Dietrich and Ujevic, 2017; Dietrich et al., 2017b)) and the hydro- and thermodynamical properties of this matter, including its morphology and angular dependency. Employing then a nuclear reaction network (Winteler, 2012) we recovered the heavy elements abundances for each BNS model. We found that while the properties of the ejecta show some correlation with the stiffness of the EOS, the r-process yields are remarkably robust against variations of astrophysical conditions, and consistently match the solar abundances within the present uncertainties on the properties of neutron-rich nuclei. We were also able to estimate the light curves of the electromagnetic signal powered by the radioactive decay of these elements, *i.e.* the so-called kilonovae (also known as macronovae); and performed one of the most comprehensive investigations to date regarding the angular distribution of the ejected material, revealing that the dependence of ejecta properties such as the electron fraction Y_e on the viewing angle might have significant repercussions on the light curves and spectra of kilonovae and their detectability.

The research on better formulations of equations is being constantly carried forward, spurred also by the increasing realism of simulations. The same holds true for numerical methods, since more realistic and accurate simulations require increasing computational resources. While computational facilities available for scientific research are being funded and upgraded, changes in computational architectures are part of this process. This means that suitable numerical methods must be devised to exploit their power. In this sense it would be very beneficial a optimized, vectorized implementation of the ELH method, coupled to highly scalable DG or compact FD (Lele, 1992) schemes. At the same time it is hoped that such advances in the numerical framework can increase the realism of the simulations to the point of providing a fully consistent and complete description of the inspiral, merger and post merger of binary neutron stars, including relativistic effects, neutrino interactions, viscosity, heat transfer, magnetic fields and possibly multifluids (Andersson et al., 2017). Such simulations could provide much tighter constraints on many of the issues left open by our study (as well as others), such as the precise dependency of the amount of ejected mass on the binary initial conditions and its microphysics, the kilonova signature and its detectability, or the dynamical feedback of the r-process nucleosynthesis on the ejecta morphology.

This thesis is organized as follows. Chapters 2 and 3 provide a review of the relevant physical theories, *i.e.* general relativity and relativistic hydrody-

namics and their formulation in a numerical context; followed by a description of the mathematical theory of partial differential equations (PDE) and of the numerical methods used in this work; part II presents the novel FO-CCZ4 formulation in the context of the 3+1 decomposition of general relativity; part III is devoted to the description of the ELH method and the results obtained from it; the study of the r-process nucleosynthesis and kilonova light curves in BNS merger ejecta is presented in part IV; finally I conclude in part V.

In the following I use the spacetime signature $(-,+,+,+)$, with Greek indices running from 0 to 3 and Latin indices from 1 to 3. I employ the Einstein convention for the summation over repeated indices. Unless otherwise stated, all quantities are expressed in a geometrized system of units in which $c = G = M_\odot = 1$.

Disclaimer note

The research and results presented in this thesis have been published in different form in the following research articles:

- *Dumbser et al. (2017);*
- *Guercilena et al. (2017);*
- *Bovard et al. (2017);*

in which I appear as co-author and hold joint copyright. Chapters 3, 4, 5 and 6 are partly based from these sources, adapted to fit into this thesis.

My specific contributions to these research articles have been:

- *discuss, suggest and develop the form of the relevant equations;*
- *cross-check analytical derivations;*
- *implement numerical methods;*
- *discuss and suggest numerical tests of the models/methods;*
- *perform numerical tests*
- *interpret the test results;*
- *discuss and suggest testing scenarios for both the method and the code;*
- *perform the numerical tests;*
- *analyze, visualize and interpret the generated data;*
- *assess the significance of the results;*
- *write the content of the research carried out in the form of an article;*
- *revise, correct and improve the articles during the peer reviewing process.*

Chapter 2

Mathematical framework

The following sections are intended as a very brief summary and introduction to the theory of general relativity, of relativistic hydrodynamics, and to the particular formulations of these theories that are employed in numerical computations. By necessity, the discussion is very succinct, therefore we list here a few references to the literature which cover in greater detail these very broad fields.

The standard reference to the theory of relativity is the classic textbook by Misner et al. (1973), which also covers aspects of hydrodynamics and cosmology. More formally rigorous are the monographs by Straumann (1984) and Wald (1984), including details of the Lagrangian and Hamiltonian formulations of general relativity.

The section on relativistic hydrodynamics is based mostly on the book by Rezzolla and Zanotti (2013), which also includes an introduction to the derivation of the hydrodynamics equations from the principles of kinetic theory. A different approach, based on a field theoretical point of view is explored in the Living Reviews article by Andersson and Comer (2007).

Details on the 3+1 decomposition of the field equations can be found in Baumgarte and Shapiro (2010); Bona et al. (2009); Gourgoulhon (2012) and again in Rezzolla and Zanotti (2013). The latter also serves as the main reference for the flux-conservative form of the hydrodynamics equations and their properties.

Finally, the section on gravitational waves is mostly modelled on the corresponding one of Baumgarte and Shapiro (2010). A similar presentation can be found in any book on relativity theory, including the ones referenced above. A much more detailed discussion can be found *e.g.* in the monograph by Maggiore (2007).

This chapter is structured as follows: section 2.1 gives a very brief introduction to general relativity; section 2.2 introduces the theory of relativistic hydrodynamics; in section 2.3 the 3+1 approach to reformulate relativistic theories in an initial value problem is reviewed, and then applied in sections 2.4 and 2.5 to obtain the corresponding formulations of Einstein and Euler equations, respectively; finally section 2.6 summarizes the description and properties of gravitational waves.

2.1 General relativity and the Einstein field equations

In general relativity the Newtonian concepts of absolute time and absolute space are superseded by the introduction of a dynamical *spacetime*. The spacetime is not simply, as in classical theories, the background on which physical phenomena take place, but it is a dynamical entity, which acts on the matter and energy present in the spacetime itself, and which is acted upon by matter and energy. This interaction and the resulting dynamics of matter are what we call gravitation.

Mathematically, the spacetime is represented as a four-dimensional manifold (three spatial dimensions plus one time dimension) equipped with a metric structure. This is usually indicated by the notation $(\mathcal{M}, g)$, where $\mathcal{M}$ is the manifold itself and g the metric tensor, a rank 2 symmetric tensor field which encodes the metric structure of the spacetime.

Through the metric one defines a diffeomorphism between covariant and contravariant vectors, so that tensor indices can be raised and lowered by contraction with the metric:

$$v^\mu := g^{\mu\nu} v_\nu \,. \tag{2.1}$$

From the metric a norm is also defined as:

$$||\boldsymbol{v}||^2 := \boldsymbol{v}^2 := v_\mu v^\mu = g_{\mu\nu} v^\mu v^\nu \,. \tag{2.2}$$

A vector $\boldsymbol{v}$ is said to be *timelike* if $\boldsymbol{v}^2 < 0$, *spacelike* if $\boldsymbol{v}^2 > 0$ and *null* or *lightlike* if $\boldsymbol{v}^2 = 0$.

One also needs to define a notion of *parallel transport* or equivalently of a *covariant derivative* operator for vectors in the spacetime, denoted by the symbol ∇. Out of the infinitely many possible definitions of such an operator, one is singled out by requiring it to be torsion-free, and compatible with the metric:

$$\nabla_\lambda g_{\mu\nu} = 0 \,, \tag{2.3}$$

i.e. the covariant derivative of the metric is required to be identically zero.

The resulting operator allows to take the covariant derivative of any tensor field in the spacetime, *e.g.* for a contravariant vector v^μ:

$$\nabla_\nu v^\mu := \partial_\nu v^\mu + \Gamma^\mu{}_{\nu\lambda} v^\lambda \,. \tag{2.4}$$

The quantities $\Gamma^\mu{}_{\nu\lambda}$ (which despite the notation do not form a tensor) are called Christoffel symbols and can be written in a coordinate basis, thanks to the requirement (2.3), as:

$$\Gamma^\sigma{}_{\mu\nu} = \frac{1}{2} g^{\sigma\lambda} (\partial_\nu g_{\lambda\mu} + \partial_\mu g_{\nu\lambda} - \partial_\lambda g_{\mu\nu}) \,. \tag{2.5}$$

The Christoffel symbols are symmetric in their last pair of indices, which corresponds to the absence of torsion.

It is also important to define a second derivative operator, the *Lie derivative*. While the covariant derivatives compares tensors along infinitesimal displacements in coordinate directions, the Lie derivative compares tensor at the end points of an infinitesimal displacement along a given curve in the spacetime.

Because of this the Lie derivative can be defined without the additional structure of the connection (represented by the Christoffel symbols) derived from the metric structure of the manifold, which is instead necessary to define the covariant derivative. The Lie derivative of a contravariant vector v^μ along the curve tangent to a second vector u^μ is defined as:

$$(\mathcal{L}_{\boldsymbol{u}}\boldsymbol{v})^\mu := u^\nu \partial_\nu v^\mu - v^\nu \partial_\nu u^\mu \,. \tag{2.6}$$

With these definitions in place it is possible to define the *Riemann tensor* $R^\mu{}_{\nu\alpha\beta}$ from the relation

$$2\nabla_{[\mu}\nabla_{\nu]} v_\alpha := R^\beta{}_{\alpha\nu\mu} v_\beta \tag{2.7}$$

for a generic vector $\boldsymbol{v}$. The Riemann tensor quantifies the failure of second covariant derivatives to commute for a given vector, and therefore offers a measure of the curvature of the spacetime. It is an object constructed from derivatives of the metric of order up to second, as its explicit expression in a coordinate basis makes clear:

$$R^\mu{}_{\nu\alpha\beta} := \partial_\alpha \Gamma^\mu{}_{\nu\beta} - \partial_\beta \Gamma^\mu{}_{\nu\alpha} + \Gamma^\nu{}_{\lambda\alpha}\Gamma^\lambda{}_{\nu\beta} - \Gamma^\mu{}_{\lambda\beta}\Gamma^\lambda{}_{\nu\alpha} \,. \tag{2.8}$$

Contracting the Riemann tensor one can construct the *Ricci tensor* $R_{\mu\nu}$,

$$R_{\mu\nu} := R^\lambda{}_{\mu\lambda\nu} \,, \tag{2.9}$$

which is the simplest symmetric rank 2 tensor constructed from second order derivatives of the metric. Finally it is useful to define the *Ricci scalar* $R = R^\lambda{}_\lambda$, *i.e.* the trace of the Ricci tensor.

The language briefly introduced in the above paragraphs allows us to finally write the *Einstein field equations*. They take the form:

$$R_{\mu\nu} - \frac{1}{2} R g_{\mu\nu} = 8\pi T_{\mu\nu} \,, \tag{2.10}$$

and relate the curvature of the spacetime to the distribution of matter/energy contained in it.

A few comments are in order to clarify the nature of these equations. First of all, the symmetric tensor $T_{\mu\nu}$ on the right hand side of the equations is referred to as *stress-energy tensor* or *energy-momentum tensor*. It represents the distribution of matter and energy in the spacetime, and it depends on the fields describing the particular type of matter under consideration, such as *e.g.* baryon density, temperature, electric and magnetic fields, scalar fields, *et cetera*. It will also depend in general on the metric tensor $g_{\mu\nu}$.

Secondly, the presence of the Ricci tensor and Ricci scalar on the left hand side makes the equations of second order with respect to the metric tensor. The equations are to be seen as a coupled set of differential equations for the metric: given a certain distribution of matter/energy $T_{\mu\nu}$, it is in principle possible to solve for the metric $g_{\mu\nu}$. The non-linearity of the equations makes however the search for a solution very difficult.

Note finally that the tensor $G_{\mu\nu} = R_{\mu\nu} - \frac{1}{2} R g_{\mu\nu}$, known as the *Einstein tensor*, on the left hand side of the equations is divergence-free:

$$\nabla_\mu G^{\mu\nu} = 0 \,. \tag{2.11}$$

On the other hand, one expects on physical grounds the stress-energy tensor to be divergence-free, *i.e.*

$$\nabla_\nu T^{\mu\nu} = 0\,, \tag{2.12}$$

since equation (2.12) expresses the local conservation of energy and momentum of the matter. Einstein equations equate this tensor on the right hand side with the Einstein tensor on the left hand side, which for consistency has to be divergence-free as well.

2.2 Relativistic hydrodynamics

Relativistic hydrodynamics is in essence the theory of the motions of fluids in a relativistic setting, *i.e.* in a generic, curved spacetime. Just like it's Newtonian counterpart, it essentially consist in rewriting Newton's equations of motion for a point particle in such a way that they can be applied to the time evolution of a set of fields (the mass density, energy density, momenta, *et cetera*) describing the state of the fluid.

At the microscopic level any fluid is made of discrete particles interacting with each other. While in principle it would be possible to prescribe initial conditions for each one of this particles, then integrate the equation of motion to get a complete description of the system, such an approach is not practical nor desirable: on one hand the sheer number of particles to be dealt with is humongous (generally at least on the order of Avogadro's number, $N_A \sim 10^{24}$), which makes a direct integration of the equation of motion impractical if not impossible; on the other hand, a microscopic description of the dynamics is not needed, since one is typically more interested in an averaged description of the behaviour of the fluid. In practice, we define a *fluid element* as a local "portion" of the fluid, whose size is infinitesimal with respect to the global size of the system, but still contains a very large number of particles. To each fluid element we associate physical quantities that are averages of the corresponding ones for each particle in the fluid element. Considering the collection of all fluid elements that compose the fluid, such quantities are naturally written as fields as a function of space and time. Note that a field theory perspective is also necessary to couple general relativity with a theory of matter, since the former is a field theory.

The central object in relativistic hydrodynamics is the stress-energy tensor (or energy-momentum tensor). If we consider *perfect fluids*, in which viscosity and heat fluxes can be neglected, and where stresses are isotropic, this takes the form:

$$T_{\mu\nu} = \rho h u_\mu u_\nu + p g_{\mu\nu}\,, \tag{2.13}$$

where ρ is the rest-mass density of the fluid (or baryon density), u_μ its 4-velocity and p its pressure. $h = 1 + \epsilon + p/\rho$ is the specific enthalpy of the fluid, and ϵ its specific internal energy. Note that the perfect fluid hypothesis is generally speaking justified in the study of neutron star binaries, since the dynamical timescales involved are much shorter than the viscous or heat transfer timescale, and there are no preferred direction effects, so that the stresses can be taken as isotropic.

The equations of motion of a fluid are equations (2.12) mentioned above, which generalize Euler equations to a generic curved spacetime. When applied

to the perfect fluid stress-energy tensor (2.13), they take the explicit form

$$u^\mu \nabla_\mu u_\nu + \frac{1}{\rho h} P^\mu{}_\nu \nabla_\mu p = 0 \tag{2.14}$$

$$u^\mu \nabla_\mu e + \rho h \nabla_\mu u^\mu = 0\,, \tag{2.15}$$

where $e = \rho(1+\epsilon)$ is the energy density and $P_{\mu\nu} = g_{\mu\nu} + u_\mu u_\nu$ a projector onto the hypersurface orthogonal to the fluid 4-velocity. When written in this form they manifestly are equations for the evolution of the fluid velocity (or momentum) and energy.

To these the continuity equation, which expresses the conservation of mass, has to be added:

$$\nabla_\mu(\rho u^\mu) = 0\,. \tag{2.16}$$

Note that the baryon density ρ is given by the product of a constant reference baryon mass m_b and the baryon number density n_b, *i.e.* the number of baryons in a unit volume, since baryons are the dominant particle species in terms of mass, even though other particles (*e.g.* electrons and photons) are clearly present.

Equations (2.16), (2.14) and (2.15) are closed by a so-called equation of state (EOS), *i.e.* a relation of the form $p = p(\rho, \epsilon)$ which gives the pressure as a function of density and energy. The equation of state is an intrinsic property of the fluid under study, and encodes information about its microphysics. Simple EOSs considered in this work are the *ideal gas* EOS

$$p = \rho\epsilon(\Gamma - 1)\,, \tag{2.17}$$

where the adiabatic index Γ is a constant (typically $\Gamma = 2$); as well as the polytropic EOS

$$p = K\rho^\Gamma\,, \tag{2.18}$$

where K is another constant (the polytropic constant).

We also consider realistic, nuclear physics motivated EOSs, in which the pressure is also a function of the composition of the fluid, in particular of the electron fraction $Y_\mathrm{e} = n_\mathrm{e}/n_\mathrm{b}$, *i.e.* $p = p(\rho, \epsilon, Y_\mathrm{e})$. In this case the densities of baryons and electrons (as well as protons, since by the assumption of charge neutrality the number of electrons and protons coincide) are separately conserved, so the continuity equation generalizes to the two following equations:

$$\begin{aligned} \nabla_\mu(\rho_\mathrm{b} u^\mu) &= 0 \\ \nabla_\mu(\rho_\mathrm{e} u^\mu) &= 0\,. \end{aligned} \tag{2.19}$$

Note that the equations of hydrodynamics as presented here can be derived in a number of different ways. From a kinetic theory point of view they can be seen as the equations resulting from applying a moment scheme to the Boltzmann equation for the distribution function of the fluid (see *e.g.* Rezzolla and Zanotti (2013) for an introduction to the subject). From the point of view of (classical) field theories, the equations are the Euler-Lagrange equations minimizing the action describing the fluid (Andersson and Comer, 2007). Such perspectives are in fact not only much more rigorous and justified than the simplified treatment presented here, but also more general. They are for instance the starting point to go beyond the single component, perfect fluid model and

investigate the properties of multifluids (*i.e.* fluids composed by more than one species of particles), and/or fluids in which viscous effects or heat transfer play a significant role.

2.3 Foliation of spacetime

In order to write the Einstein equations (2.10) in a way suitable for numerical integration, they have to be expressed as an initial value boundary problem (IVBP). To achieve this, the first step is to introduce a *foliation* of spacetime into a succession of spatial hypersurfaces (see figure 2.1). If the spacetime is globally hyperbolic (a condition that we assume to be fulfilled from now on), this is always possible.

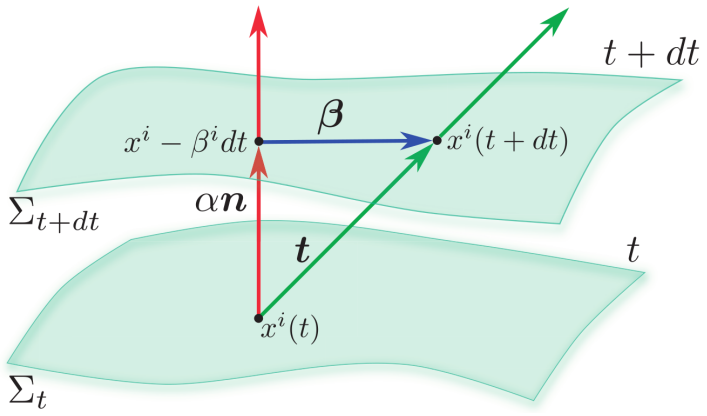

Figure 2.1: Representation of the 3+1 foliation of spacetime with hypersurfaces of constant time coordinate Σ_t and Σ_{t+dt}. *Figure courtesy of Rezzolla and Zanotti (2013).*

To begin, we define a scalar function t of spacetime, the *coordinate time*, and consider the hypersurfaces of $t = \text{constant}$. We denote any such hypersurface by the symbol Σ. The time vector t^μ can be defined as

$$t^\mu = \alpha n^\mu + \beta^\mu \,. \tag{2.20}$$

The lapse function α is related to the norm of of $\nabla_\mu t$ by $g^{\mu\nu}\nabla_\mu t \nabla_\nu t = -1/\alpha^2$, *i.e.* α is the local ratio between proper time and coordinate time. The vector n^μ is the timelike normal to Σ, *i.e.* $n^\mu = -\alpha g^{\mu\nu}\nabla_\nu t$. With this choice n^μ is normalized, timelike (which makes Σ a spacelike hypersurface), as well as future-directed (*i.e.* it points in the direction of increasing t). Finally the shift vector β^μ is a purely spatial (*i.e.* $\beta^\mu n_\mu = 0$) vector which indicates a change in the spatial coordinates from one time slice to the next.

It is now possible to construct the 3-metric induced onto the spatial hypersurfaces by the spacetime 4-metric as

$$\gamma_{\mu\nu} = g_{\mu\nu} + n_\mu n_\nu \,. \tag{2.21}$$

With these definitions in place and having chosen a coordinate basis adapted to the foliation (*i.e.* where $t^\mu = (1, 0, 0, 0)$), we can rewrite the spacetime line

element ds^2 as

$$ds^2 = \alpha^2 dt^2 + \gamma_{ij}(dx^i + \beta^i dt)(dx^j + \beta^j dt)\,, \tag{2.22}$$

where we now write the shift and 3-metric with Latin indices as they are purely spatial objects with vanishing time components. equationivalently, the covariant 4-metric can be written as

$$g_{\mu\nu} = \begin{bmatrix} -\alpha^2 + \beta_l\beta^l & \beta_i \\ \beta_j & \gamma_{ij} \end{bmatrix}\,, \tag{2.23}$$

while the normal to the slices takes the form $n^\mu = (1/\alpha, -\beta^i/\alpha)$.

The 3-metric as defined in the preceding equations is an object intrinsic to each spatial slice, and completely defines the geometry of that slice. To describe the extrinsic geometry of the slice, *i.e.* how each three dimensional slice is embedded in the surrounding four dimensional spacetime, it is necessary to define the *extrinsic curvature* as well, which takes the form

$$K_{\mu\nu} = -\frac{1}{2}\mathcal{L}_{\boldsymbol{n}}\gamma_{\mu\nu}\,, \tag{2.24}$$

i.e. is the Lie derivative of the 3-metric with respect to the timelike vector normal to the spatial slices.

For completeness, it should be mentioned that the 3+1 formalism presented in this section and in the following ones is not the only way to develop formulations of general relativity (and more in general relativistic theories) suitable for numerical implementation: alternatives are the generalized harmonics formalism (*e.g.* Lindblom et al. (2006)); the characteristic evolution formalism (Winicour, 2005); and the conformal approach (Friedrich, 2002; Husa, 2002). In this work we focus however exclusively on the 3+1 approach.

2.4 3+1 split of Einstein equations

Having defined a foliation of spacetime as outlined in the previous section, it is now possible to derive the splitting of the Einstein equations (2.10) into space and time parts as an IVBP. The procedure consists of projecting Einstein equations along the time direction (by contracting with the timelike normal n^μ) and onto the spatial hypersurfaces (by contracting with the 3-metric $\gamma^{\mu\nu}$). Since the tensors in the Einstein equations have rank two, three such projections are possible: a full projection along the timelike normal; a mixed projection, projecting one index along the timelike normal and another onto the spatial slices; a full projection along the timelike normal.

For later convenience, it's useful to consider first these projections applied to the stress-energy tensor and define the following symbols:

$$E := n^\mu n^\nu T_{\mu\nu}\,, \tag{2.25}$$

$$S_i := -\gamma^\mu{}_i n^\nu T_{\mu\nu}\,, \tag{2.26}$$

$$S_{ij} := \gamma^\mu{}_i \gamma^\nu{}_j T_{\mu\nu}\,; \tag{2.27}$$

as well as the trace S of S_{ij}, $S = \gamma^{ij}S_{ij}$.

Projecting first two times onto the spatial hypersurfaces, *i.e.*

$$\gamma^{\mu\alpha}\gamma^{\nu\beta}(R_{\mu\nu} - \frac{1}{2}g_{\mu\nu} - 8\pi T_{\mu\nu}) = 0\,, \tag{2.28}$$

yields the equation

$$R + K^2 - K_{ij}K^{ij} = 16\pi E\,, \tag{2.29}$$

where $K = \gamma^{ij}K_{ij}$ is the trace of the extrinsic curvature. equation (2.29) is called the *Hamiltonian constraint*. It is an elliptic equation, in which no time derivatives appear.

We consider then the mixed projection first along the time direction and then onto the spatial slices,

$$n^{\mu}\gamma^{\nu\alpha}(R_{\mu\nu} - \frac{1}{2}g_{\mu\nu} - 8\pi T_{\mu\nu}) = 0\,, \tag{2.30}$$

which yields the equation

$$\nabla_i K^i{}_j - \nabla_j K = 8\pi S_j\,. \tag{2.31}$$

This equation, also an elliptic one, is the so-called *momentum constraint*. Note that we have introduced here covariant derivatives constructed from the 3-metric γ_{ij}, which are denoted by ∇_i with a Latin index.

Finally we compute the double projection along n^{μ}, *i.e.*

$$n^{\mu}n^{\nu}(R_{\mu\nu} - \frac{1}{2}g_{\mu\nu} - 8\pi T_{\mu\nu}) = 0\,. \tag{2.32}$$

This yields the equation

$$\begin{aligned}\partial_{\perp}K_{ij} =& -\nabla_i\nabla_j\alpha + \alpha(R_{ij} - 2K_{ik}K^k{}_j + KK_{ij}) \\ &- 8\pi\alpha\left[S_{ij} - \frac{1}{2}\gamma_{ij}(S - E)\right]\,,\end{aligned} \tag{2.33}$$

where the notation $\partial_{\perp}$ is a shorthand for $\partial_t - \mathcal{L}_{\boldsymbol{\beta}}$, *i.e.* the partial time derivative minus the Lie derivative along the shift. This equation involves a time derivative and it's an actual evolution equation for the extrinsic curvature.

In order to close the system we need to consider the definition of the extrinsic curvature, equation (2.24), which can be rewritten to yield an evolution equation for the 3-metric:

$$\partial_{\perp}\gamma_{ij} = -2\alpha K_{ij}\,. \tag{2.34}$$

The constraints equations (2.29),(2.31) are conditions allowing a spatial hypersurface Σ with data (γ_{ij}, K_{ij}) to be embedded in the surrounding spacetime with 4-metric $g_{\mu\nu}$. They are elliptic equations, and must be solved to generate suitable initial data for the general relativistic IVBP. Once they are satisfied on a given slice, they are preserved on all other slices by the evolution equations.

The evolution equations are (2.34) and (2.33), which give the time derivatives of the fields γ_{ij}, K_{ij}. These are known as the ADM equations (from Arnowitt et al. (1962)). While along with the constraint equations they allow to formulate GR as a IVBP, they are not hyperbolic, and therefore unsuitable for numerical implementation. The notion of hyperbolicity of a system of equations, including why it is a desirable property, is properly defined in chapter 4.

2.4.1 Choice of a gauge

Note that neither the constraint equations (2.29),(2.31) nor the evolution equations (2.34),(2.33) provide any information on the value of the lapse α and shift β^i. The freedom in choosing these four functions is a restatement of the gauge freedom of general relativity, *i.e.* the invariance of the equations and their solutions under different choices of the frame of reference in which they are written. A prescription for the gauge has to be chosen, and can be used to try to enforce desirable properties in the resulting system of equations.

Typically such properties are the so called singularity avoidance, in which the lapse is made to tend to zero in the vicinity of a black hole singularity, therefore slowing proper time with respect to coordinate time and making it possible to evolve the interior of black holes (this technique is referred to as punctures evolution, as opposed to excision, where the inner part of black holes is simply removed from the computational domain to avoid these complications); and the freezing of horizons, *i.e.* avoiding that black horizons grow without bounds, encompassing the whole computational domain and crashing the simulation.

Many prescriptions have been developed to achieve these goals, but a few of them can be considered standard. The usual choice for the lapse evolution are the so called harmonic slicing and the 1+log slicing conditions. Harmonic slicing (so called because the time coordinate is imposed to be an harmonic function) takes the form

$$(\partial_t - \beta^i \partial_i)\alpha = -\alpha^2 K\,; \tag{2.35}$$

while 1+log slicing is

$$(\partial_t - \beta^i \partial_i)\alpha = -2\alpha K\,, \tag{2.36}$$

and takes its name from the fact that for zero shift it can be easily integrated to yield $\alpha = 1 + \ln\gamma$. Both conditions provide evolution equations for the lapse, and have been used in long-term simulations. The singularity avoiding capabilities of the 1+log conditions however are stronger than for harmonic slicing, and so the former is the choice in most simulations.

For the shift evolution, one prescription has emerged has the best choice, the so called Gamma driver condition. This condition can be seen as a simplification of the minimal distortion condition (*i.e.* minimizing the rate of change of the spatial metric), and takes the form

$$\begin{aligned} \partial_t \beta^i &= \frac{3}{4} b^i + \beta^k \partial_k \beta^i \\ \partial_t b^i &= \partial_t \tilde{\Gamma}^i - \eta b^i + \beta^k \partial_k b^i\,, \end{aligned} \tag{2.37}$$

where b^i is an auxiliary field and η is a damping constant usually set to a value close to the total mass of the spacetime to be evolved. $\tilde{\Gamma}^i = \tilde{\gamma}^{jk}\tilde{\Gamma}^i{}_{jk}$ is a contraction of the conformal 3-metric, which will be defined later in section 4.2 in relation to the BSSNOK formulation of Einstein equations. Together with the 1+log slicing, the Gamma driver condition has been extremely successful in dynamical moving punctures simulations, where black holes (and their singularities) are left free to move onto the computational domain.

2.5 Equations of relativistic hydrodynamics

Equations (2.16), (2.14) and (2.15) are not in a form suitable for numerical implementation. They have to be cast in *conservative form*, that is to say in the form

$$\partial_t \boldsymbol{U} + \partial_i \boldsymbol{F}^i(\boldsymbol{U}) = \boldsymbol{S}(\boldsymbol{U})\,, \tag{2.38}$$

where the fluxes $\boldsymbol{F}^i$ and the sources $\boldsymbol{S}$ may depend on the vector of unknowns $\boldsymbol{U}$, but not on its derivatives. Equations of the form (2.38) manifestly show that the integral of the quantity $\boldsymbol{U}$ over a fixed volume can only change due to a non zero flux of this quantity across the surface boundary of the volume. If the flux is zero (*e.g.* if the volume under consideration is the whole volume of an isolated system), the quantity is exactly conserved. This conservation property is strictly speaking only valid if the sources $\boldsymbol{S}$ are vanishing. If they are not, equations of the form (2.38) are sometimes referred to as flux-conservative equations or flux-balance equations.

The equations of relativistic hydrodynamics (2.16), (2.14) and (2.15) can be cast in conservation form by defining the conserved variables as

$$\begin{aligned} \boldsymbol{U} &:= \sqrt{\gamma} \begin{pmatrix} D \\ S_j \\ \tau \end{pmatrix} \\ &:= \sqrt{\gamma} \begin{pmatrix} \rho W \\ \rho h W^2 v_j \\ \rho h W^2 - p - \rho W \end{pmatrix} . \end{aligned} \tag{2.39}$$

The fluxes and sources, containing metric-dependent terms, are given by

$$\boldsymbol{F}^i = \sqrt{\gamma} \begin{pmatrix} (\alpha v^i - \beta^i) D \\ \alpha S^i{}_j - \beta^i S_j \\ \alpha (S^i - D v^i) - \beta^i \tau \end{pmatrix} , \tag{2.40}$$

and

$$\boldsymbol{S} = \sqrt{\gamma} \begin{pmatrix} 0 \\ \frac{1}{2} \alpha S^{lm} \partial_j \gamma_{lm} + S_k \partial_j \beta^k - E \partial_j \alpha \\ \alpha S^{ij} K_{ij} - S^k \partial_k \alpha \end{pmatrix} . \tag{2.41}$$

This formulation is known as the "Valencia formulation" and was first proposed by Banyuls et al. (1997). Note that the sources terms for the momentum and energy equations are non-vanishing, which corresponds to the fact that the momentum and energy of the fluid are not independently conserved, but the coupling of the fluid to the spacetime and vice versa has to be taken into account (see *e.g.* Rezzolla and Zanotti (2013); Shibata (2016); Baumgarte and Shapiro (2010) for details). In these equations the fluid three-velocity measured by the normal observers is defined as

$$v^i := \frac{1}{\alpha} \left(\frac{u^i}{u^t} + \beta^i \right) \tag{2.42}$$

which also contains metric-dependent terms, and the Lorentz factor is $W := (1 - v^i v_i)^{-\frac{1}{2}} = \alpha u^t$. We also have used the fact that $\sqrt{-g} = \alpha \sqrt{\gamma}$.

The eigenstructure of this system of equations is analyzed in chapter 4, where they are shown to be hyperbolic. The necessity of casting the equations in conservation form arises from the need to employ a conservative method (*i.e.* loosely speaking, a method based on the conservation form of the equations) to integrate them, because this guarantees that the approximate solution found will be a physical solution, *i.e.* in technical terms, an *entropy satisfying* solution. These concepts are introduced and elaborated in chapter 3.

2.6 Gravitational waves

Binary systems of compact objects that this work is mostly concerned with are strong emitters of gravitational waves (GW). Gravitational waves are, quite literally, ripples in the spacetime continuum, *i.e.* wave like perturbations of the metric components.

Gravitational waves are most easily described in vacuum and in the framework of linearized gravity. Consider a spacetime metric that is only a small deviation from a background solution, and where the background is chosen to be Minkowski spacetime:

$$g_{\mu\nu} = \eta_{\mu\nu} + h_{\mu\nu} \quad |h_{\mu\nu}| \ll 1 \,. \tag{2.43}$$

Introducing the trace reversed perturbation $\bar{h}_{\mu\nu} = h_{\mu\nu} - \frac{1}{2}\eta_{\mu\nu}h_\tau{}^\tau$ and imposing the gauge condition $\nabla_\mu \bar{h}^{\mu\nu} = 0$, the vacuum Einstein equations assume the form

$$\nabla_\tau \nabla^\tau \bar{h}_{\mu\nu} = 0 \,, \tag{2.44}$$

i.e. an homogeneous wave equation.

Using the remaining gauge freedom, one can impose the "transverse traceless" gauge (indicated by a ^{TT} superscript) on the metric perturbation, in which $\bar{h}^{TT}_{\mu 0} = 0$ and $\bar{h}^{TT\mu}_{\mu} = 0$. Note that the second condition implies that $\bar{h}_{\mu\nu} = h_{\mu\nu}$, so we can remove bars from the notation from now on. Fixing now a Cartesian coordinate system in which the gravitational waves are travelling along the z axis, the metric perturbation can be explicitly written as

$$h_{\mu\nu} = \begin{bmatrix} 0 & 0 & 0 & 0 \\ 0 & h_+ & h_\times & 0 \\ 0 & h_\times & -h_+ & 0 \\ 0 & 0 & 0 & 0 \end{bmatrix} \,. \tag{2.45}$$

h_+ and $h_\times$ are the two polarization states of gravitational waves, so called because the passage of a gravitational wave through a circle of test masses lying in the xy plane would deform it along the x and y axes in the case of the h_+ polarization, and on the diagonal axes in the case of $h_\times$. Note that the separation vector ξ between two free falling test masses subject to the passage of the wave satisfies the equation

$$\xi_i = \frac{1}{2}\partial_t^2 h_{ij}\xi^j \,. \tag{2.46}$$

Therefore the relative displacement $\delta\xi/\xi$ is proportional to h, which for this reason is called the gravitational wave *strain*.

Equation (2.44), being a wave equation, admits plane wave solutions of the form $\mathrm{Re}(A_{\mu\nu}e^{ik_\mu x^\mu})$, where the wave vector k_μ has components (ω, k^i). Now the linearized Einstein equations imply that k_μ is a null vector, *i.e.* $\omega = |k^i|$, which means GWs propagate at the speed of light. The previously described gauge choices imply $k^\mu A_{\mu\nu} = 0$, *i.e.* gravitational waves are transverse.

In the context of linearized gravity it is also possible to give simple expressions for the generation of GWs by a source. Consider again the equation

$$\nabla_\tau \nabla^\tau \bar{h}_{\mu\nu} = -16\pi T^{\mu\nu}\,, \tag{2.47}$$

i.e. equation (2.44) in which the stress-energy tensor, representing the wave emitting matter source, has been reinstated. In the transverse-traceless gauge, imposing outgoing boundary conditions, using a Green function approach and expanding the solution in the wave zone in negative powers of r (the distance from the source), the strain generated by the source can be written as

$$h^{TT}{}_{ij} = \frac{2}{r}\partial_t^2 \mathcal{I}_{ij}^{TT}(t-r)\,. \tag{2.48}$$

$\mathcal{I}_{ij}$ is the trace-free quadrupole moment of the mass distribution of the source, *i.e.* $\mathcal{I}_{ij} = I_{ij} - \frac{1}{3}\eta_{ij}I^k{}_k$ where $I^{ij} = \int \rho x^i x^j \mathrm{d}^3x$ and ρ is the energy density of the source. This enters the equation via the retarded time $t-r$, since due to the finite speed of propagation of GWs, the strain h at (t, r) depends on the source on the event's past light cone. Equation (2.48) is only valid for slow-moving sources in a weak-field regime.

From equation (2.48) explicit expressions for the energy, linear momentum and angular momentum carried away by GWs can be derived. For the energy E one finds that the GW luminosity can be written as

$$L_{\mathrm{GW}} = -\frac{\mathrm{d}E}{\mathrm{d}t} = \lim_{r\to+\infty}\frac{r^2}{16\pi}\int \langle(\partial_t h_+)^2 + (\partial_t h_\times)^2\rangle \mathrm{d}\Omega\,, \tag{2.49}$$

where the integral is on all angular directions and the integrand is averaged over several wavelengths. Equaiton (2.49) is widely known as the *quadrupole formula*.

In numerical applications the extraction of gravitational waves from the simulation results generally employs somewhat different techniques, since in this case there appear issues that are not of concern in a purely analytic treatment. These typically are the error associated with finite resolution; the finite size of the computational domain; as well as various numerical artifacts that can arise in particular applications (*e.g.* non-linear drifts appearing in the time integration of waveforms (Reisswig and Pollney, 2011)).

There are different theoretical frameworks to perform gravitational wave extraction. One possibility is characteristic extraction, where the sources are evolved on a succession of spacelike hypersurfaces (*i.e.* the 3+1 formalism described above), while the wave zone is evolved on null hypersurfaces in a compactified domain, so that the GW signal can be immediately read off at null infinity (Winicour, 2005). For simulations in which the grid does not extend to infinity (the most common case), there exists the Zerilli-Moncrief formalism (Moncrief, 1974; Nagar and Rezzolla, 2005), based on identifying perturbations of the metric over a Schwarzschild background at large distances from the GW sources.

Nowadays the most commonly employed framework, which we also use, is based on the Newman-Penrose formalism (Newman and Penrose, 1962). The starting point is the computation of the Weyl tensor,

$$C_{\mu\nu\alpha\beta} = R_{\mu\nu\alpha\beta} - \frac{1}{2}(g_{\mu\alpha}R_{\nu\beta} - g_{\mu\beta}R_{\nu\alpha} - g_{\nu\alpha}R_{\mu\beta} + g_{\nu\beta}R_{\mu\alpha}) + \frac{1}{6}(g_{\mu\alpha}g_{\nu\beta} - g_{\mu\beta}g_{\nu\alpha})R\,. \tag{2.50}$$

The ten independent components of the Weyl tensor can be expressed in five complex scalars, the Newman-Penrose scalars, by contracting it with the vectors of a suitable null tetrad $(l^\mu, k^\mu, m^\mu, \bar{m}^\mu)$, where l^μ and k^μ are radially outgoing and ingoing respectively, and $\bar{m}^\mu$ is the complex conjugate of m^μ. The fourth Weyl scalar Ψ_4 is the defined as

$$\Psi_4 = -C_{\mu\nu\alpha\beta}k^\mu\bar{m}^\nu k^\alpha\bar{m}^\beta\,, \tag{2.51}$$

and it can be shown that at infinity in the TT gauge the following relation holds between Ψ_4 and the metric perturbations $h_+, h_\times$ intrduced above:

$$\Psi_4 = \ddot{h}_+ - i\ddot{h}_\times\,, \tag{2.52}$$

where an overdot indicates a time derivative.

The procedure to extract gravitational waves is then to compute the Ψ_4 scalar on spherical surfaces at various radii; decompose it in spherical harmonics at each radius; use equation (2.52) to recover the waveform; and finally extrapolate the signal at different radii to null infinity.

Chapter 3

Numerical framework

This chapter serves as an introduction and review of the numerical methods used to integrate the systems of PDEs that describe the physical system of interest for this work, as described in the previous chapter. These schemes form the backbone of the techniques employed to arrive at physical results. As for chapter 2 we are limited by necessity to a rather brief and self-contained discussion, and we list here several references to the literature, which provide more detailed treatments and on which parts of this chapter are based.

An excellent introduction to the subject at hand is the monograph by Leveque (1992), which both reviews the underlying theory and surveys a number of numerical schemes, particularly finite-volumes (FV) ones.

The literature on finite-volumes schemes, employed to get the results discussed in chapter 6, is very vast, but useful publications on their applications to numerical relativity (in particular to relativistic hydrodynamics) are the Living Reviews articles by Font (2008) and Martí and Müller (2003), and the book by Rezzolla and Zanotti (2013), which also contains an extensive discussion of the Riemann problem. A comprehensive monograph on this particular subject is the one by Toro (2009).

Basic finite-differences (FD) methods are touched upon on every textbook on numerical methods. Useful ones for numerical relativity are the already mentioned ones by Baumgarte and Shapiro (2010); Bona et al. (2009). The standard reference on compact finite-differences is Lele (1992).

Finite-differences methods for non-linear conservation laws, which are used in the simulations of chapter 5, are best introduced in the papers by Zhang and MacFadyen (2006); Mignone et al. (2010); Radice and Rezzolla (2012); Radice et al. (2014b).

A comprehensive and detailed introduction on discontinuous Galerkin (DG) methods is found in the monograph by Hesthaven and Warburton (2007), while a briefer, more accessible one in Cockburn (2003). Finally, the particular flavour of DG methods described in section 3.5.1 and used for the results of chapter 4, the path-conservative ADER-DG schemes, is best approached from the work of Dumbser et al. (2009, 2010).

The chapter starts with reviewing the concepts of consistency and convergence of a method, as well as some properties of conservation laws, in section 3.1; sections 3.2, 3.3 and 3.4 are then devoted to defining the finite-volumes, finite-differences and discontinuous Galerkin methods.

3.1 Basic concepts

3.1.1 Conservation laws

In this section we consider equations in the form

$$\partial_t \boldsymbol{u} + \partial_i \boldsymbol{f}^i(\boldsymbol{u}) = 0\,, \tag{3.1}$$

on some domain Ω with initial data $\boldsymbol{u}(0,x) = \boldsymbol{u}_0$, where $\boldsymbol{u}$ is a vector of m unknowns, $\boldsymbol{f}$ is a d-dimensional (typically three-dimensional) flux. This is the same form of the Euler equations introduced in section 2.5, cf. equation 2.38, with a slightly different notation. We neglect here possible source terms on the right-hand side of 3.1 since they are purely algebraic and do not pose numerical issues. Note that the flux $\boldsymbol{f}$ can be a function of the solution $\boldsymbol{u}$ but not of its derivatives.

In general, the numerical methods discussed in this chapter can be applied to equations that are not written in the form 3.1 (this is the case of Einstein equations and its various formulations presented in chapter 4). However many methods and techniques have been developed thinking of conservative equations of this form. The reason is twofold: on one hand many physical laws can be cast in the form 3.1, which transparently expresses the conservation of a quantity; on the other, when conservation laws are non-linear, numerical methods based on the form 3.1 of the equations avoid problems known to arise in the case of discontinuous solutions. This is clearly very relevant here for the solution of the Euler equations.

A flux-conservative system of equation is said to be non-linear when the flux $\boldsymbol{f}$ is a non-linear function of $\boldsymbol{u}$. The solution of such systems can develop shocks in finite time, even if the initial data is analytic. For this reason 3.1 has to be interpreted in the sense of distributions. A function $\boldsymbol{u}$ is a *weak solution* of 3.1 if, for all continously differentiable test functions $v(t,\boldsymbol{x})$ with compact support

$$\int_0^\infty \int_\Omega (\boldsymbol{u}\partial_t v + \boldsymbol{f}^i \partial_i v)\mathrm{d}x\mathrm{d}t = \int_\Omega \boldsymbol{u}_0 \mathrm{d}x\,. \tag{3.2}$$

It can be shown however that in general even scalar conservation laws admit multiple weak solutions. To identify the "physically relevant" solution we introduce the concept of entropic solutions. A convex function $\eta(\boldsymbol{u})$ is said to be an entropy function if its Hessian $\partial^2_{\boldsymbol{u}}\eta$ symmetrizes the Jacobian of the flux $\partial_{\boldsymbol{u}}\boldsymbol{f}$:

$$\partial^2_{\boldsymbol{u}}\eta \cdot \partial_{\boldsymbol{u}}\boldsymbol{f} = [\partial_{\boldsymbol{u}}\boldsymbol{f}]^{\mathrm{T}} \cdot \partial^2_{\boldsymbol{u}}\eta\,. \tag{3.3}$$

If so an entropy flux $\boldsymbol{\Phi}$ exists, determined by the relation

$$[\partial_{\boldsymbol{u}}\eta]^{\mathrm{T}} \cdot \partial_{\boldsymbol{u}}\boldsymbol{f} = [\partial_{\boldsymbol{u}}\boldsymbol{\Phi}]^{\mathrm{T}}\,. \tag{3.4}$$

The tuple $(\eta, \boldsymbol{\Phi})$ is called an *entropy pair*.

An *entropic solution* is weak solution that satisfies the following *entropy inequality* for any entropy pair

$$\partial_t \eta + \partial_i \boldsymbol{\Phi}^i(\boldsymbol{u}) \leq 0\,, \tag{3.5}$$

in the sense of distributions.

Kružkov (1970) proved for scalar conservation laws the existence and uniqueness of the entropic solution under very general conditions. This has been extended to measure-valued solutions by DiPerna (1985), and to of conservation laws on manifolds by Ben-Artzi and LeFloch (2006).

Unfortunately very little is known concerning existence, uniqueness and stability of entropic solutions in the case of systems of conservation laws, in particular for the multi-dimensional case. Not even the existence of entropy pairs is guaranteed for general systems of equations. A promising approach is the one based on divergence-measure vector fields by Chen et al. (2009). In this framework Chen and Frid (2003) proved existence, uniqueness and stability of the entropic solution of the Euler equations for a classical ideal-gas of one-dimensional Riemann problems (see the following subsection). On the other hand, for general equation of state the existence of a weak solution to the Riemann problem is not even guaranteed Menikoff and Plohr (1989); Chen (2006). In the relativistic case, the existence of solutions to the Riemann problem was shown for ultrarelativistic equation of state by Smoller and Temple (1993).

The Riemann problem

The *Riemann problem* for a non-linear, hyperbolic system of conservation laws in the form (3.1) (plus possibly algebraic source terms) refers to the solution with discontinuous initial data of the form

$$\boldsymbol{u}(0,x) = \begin{cases} \boldsymbol{u}_L & \text{if } x < 0\,, \\ \boldsymbol{u}_R & \text{if } x > 0\,. \end{cases} \tag{3.6}$$

The subscripts L and R refer to a "left" and "right" state of the system, respectively, and we have restricted the discussion to the one-dimensional case in space, since this is the most common and useful situation. This type of problem has become the standard model to study the behaviour of non-linear equations with discontinuous initial data (see Rezzolla and Zanotti (2013) for a comprehensive introduction).

The Riemann problem also has a straightforward physical interpretation, at least when the equations under study are the hydrodynamics ones. It models a tube, filled with a fluid and divided in two halves by a membrane. The fluid in the left and right parts of the tube is in a different state of density, pressure, energy or velocity. At the initial time, the membrane is removed and the two fluids are free to interact. The evolution of the system is then given by the interaction of three types of non-linear hydrodynamical waves propagating from the position of the initial discontinuity: rarefaction waves, contact discontinuities and shocks.

The solution of the Riemann problem (which is self similar, *i.e.* $\boldsymbol{u}(t,x) = \boldsymbol{u}(x/t)$) cannot in general be expressed in a closed analytic form. However it can be computed to any degree of accuracy, and so it is in this sense known exactly. The solution is based on identifying the particular wave pattern for a given initial state. See figure 3.1 for a grphical representation of the Riemann problem solution.

The Riemann problem is relevant for the more general solution of non-linear conservation laws not only because of the theoretical insights it offers, but because many numerical schemes incorporate the solution of Riemann

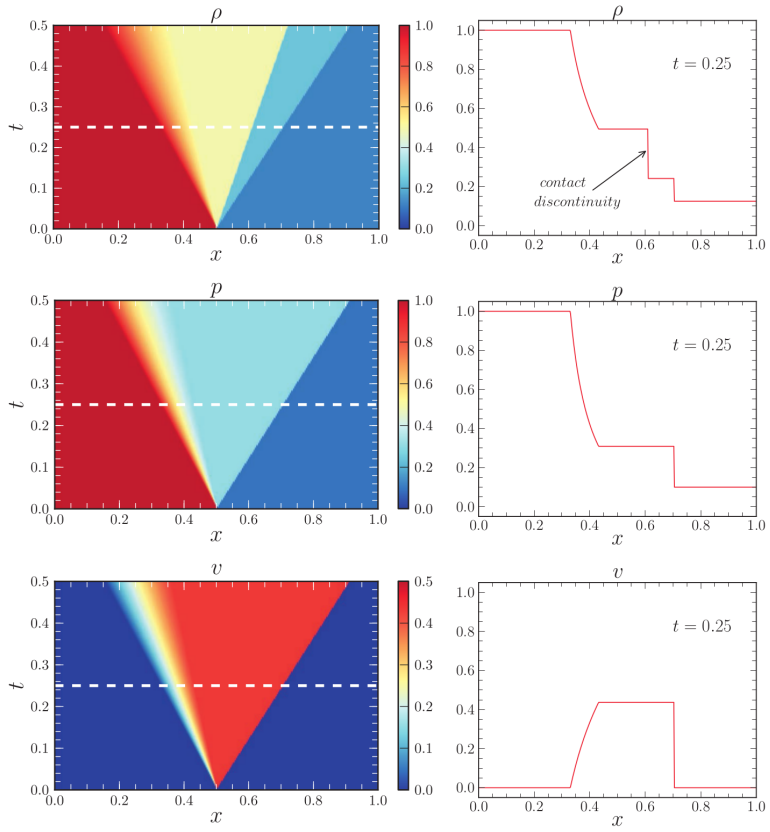

Figure 3.1: Spacetime diagrams for the development of nonlinear waves in the numerical solution of a Riemann problem (the Sod problem, Sod (1978)) . Shown from the top are the rest-mass density, the pressure and the velocity. Right panels: The corresponding profiles at $t = 0.25$ of the evolution. *Figure courtesy of Rezzolla and Zanotti (2013).*

problems in the solution algorithm (albeit generally employing an approximate Riemann solver rather than an exact one), starting with the classic Godunov's method of Godunov (1959).

There exist a number of generalizations of the Riemann problem. As a first step it is possible to consider multi-dimensional Riemann problems. The term *generalized Riemann problem* refers however to discontinuous initial data in which the left and right states are not constant, but polynomials of higher order. Such generalizations make solving the Riemann problem considerably more difficult however.

3.1.2 Consistency, stability and convergence for linear problems

In this section we consider more generally an initial boundary value problem (IBVP) defined on a domain Ω by an equation of the form

$$\partial_t u(t,x) = \mathcal{L}[u(x,t)]\,, \tag{3.7}$$

with initial data $u(0,x) = u_0(x)$ and appropriate conditions on the boundary $\partial\Omega$ of the domain. The unknown solution $u(t,x)$ is a function of time t and of the space coordinate x. For simplicity we carry on the discussion in the one-dimensional case, but most of it can be extended to higher (typically three) dimensions. In the same spirit, the unknown u is treated as a scalar function, but the discussion can be extended to systems of equations, where u is actually a vector field (in which case it is written as $\boldsymbol{u}$). $\mathcal{L}$ is a differential operator acting on u, and we consider in general operators that depend at most on the second derivative in space of u.

We define a computational mesh in space, composed by the set of points $\{x_i\}$ (often taken to be equally spaced), as well as succession of time steps $\{t^n\}$. Let u and $\tilde{u}$ be the true, analytic solution to (3.7) and an approximate solution obtained via some numerical method, respectively. u_i^n and $\tilde{u}_i^n$ are the values of these functions at $t = t^n$ and $x = x_i$ (the precise sense in which these values represent the values of the corresponding function at a given point depends on the choice of the numerical method and will made explicit in discussing each of them).

The numerical method used to discretize the operator $\mathcal{L}$ is denoted by $\tilde{\mathcal{L}}^{\Delta}$. It depends on some discretization parameter Δ, typically related to the grid spacing, *i.e.* the distance between two adjacent points x_i and x_{i+1} of the mesh.

We consider initially the case in which the operator $\mathcal{L}$ is linear, which greatly reduces the complexity of the problem at hand. We define the *pointwise error* of a numerical scheme as

$$E_i^n = \tilde{u}_i^n - u_i^n\,, \tag{3.8}$$

i.e. the difference of the numerical solution to the true one at a given point in time and space. The *global error* is the norm $||E(t)||$ of the pointwise error over the computational domain. The usual choice for the norm is the L^1-norm, or sometimes the L^2-norm. The use of the ∞-norm, while in principle desirable, leads to unrealistically stringent conditions for discontinuous solutions.

A numerical method is said to be **convergent** if

$$\lim_{\Delta\to 0} ||E(t)|| = 0 \quad \forall t\,, \tag{3.9}$$

i.e. if at all times the global error vanishes as the discretization parameter (grid spacing) tends to zero.

The *local truncation error* of the numerical scheme is defined as

$$H_i^n = \tilde{\mathcal{L}}^{\Delta}[u] - \mathcal{L}[u]\,. \tag{3.10}$$

The local truncation error is the difference between the original operator $\mathcal{L}$ and its discrete version $\tilde{\mathcal{L}}^{\Delta}$, both applied to the true solution u, and thus measures

how well the discrete version of the equation (3.7) approximates the original one locally. We say that a numerical scheme is **consistent** if

$$\lim_{\Delta \to 0} ||H(t)|| = 0 \quad \forall t \,, \tag{3.11}$$

i.e. if the local truncation error converges to zero in the continuum limit, for all possible initial data u_0. In particular a scheme is of order p if $||H(t)|| = \mathcal{O}(\Delta^p)$.

Finally, a scheme is said to be **stable** if the norm of the local truncation error is limited:

$$\sup_{u \neq 0} \frac{||H(t)||}{||u||} \leq C \quad \forall t \,, \tag{3.12}$$

where the constant C does not depend on u.

For linear equations, the Lax-Richtmeyer equivalence theorem guarantees that if a scheme is stable and consistent, then it is convergent (Lax and Richtmyer, 1956; Richtmyer and Morton, 1994). Furthermore, if the scheme is of order p, then $E(t) = \mathcal{O}(\Delta^p)$, *i.e.* the global error converges to zero with the p-th power of the discretization parameter.

3.1.3 Non-linear stability

To study the stability and convergence of non-linear equations it turns out to be important to consider the properties of both the spatial discretization and the time discretization. In the previous section we worked with semi-discrete schemes, where time was continuous. This is generally a valid approximation because the error term associated with the time discretization is often negligible compared to the one arising from the space discretization. In this section we will consider instead fully discrete schemes, *i.e.* where both the time and space dependence of the solution are discretized.

We introduce therefore a family of evolution operators $\{\mathcal{T}_s\}$, depending on the positive real parameter s (*i.e.* the time). They form a semi-group, *i.e.* $\mathcal{T}_s \circ \mathcal{T}_t = \mathcal{T}_{t+s}$, and are such that

$$u(t) = \mathcal{T}_t(u_0) \,, \tag{3.13}$$

i.e. the initial data u_0 is evolved to the time t by the operator $\mathcal{T}_t$ (see Kružkov (1970) for details). The discrete version of the operators is denoted by $\tilde{\mathcal{T}}_s^{\Delta}$, which depends yet again on the single parameter Δ since the time discretization is usually linked to the space one by a stability condition, *i.e.* the Courant-Friedrichs-Lewy condition (see the next section 3.1.4).

With these definitions, the fully discrete analogue of equation (3.7) can be written as

$$u(t + \Delta t) = \mathcal{T}^{\Delta}_{\Delta t}[u(t)] \,, \tag{3.14}$$

and we can translate the definitions of the previous section in the fully discrete case: the truncation error is

$$H(t) = \tilde{\mathcal{T}}^{\Delta}_{\Delta t}[u(t)] - \mathcal{T}_{\Delta t}[u(t)] \,; \tag{3.15}$$

a scheme is consistent if H tends to zero as Δ tends to zero for some choice of a norm; and in particular if $||H(t)|| = \mathcal{O}(\Delta^r)$ the scheme is said to be of order

r; finally, the scheme is linearly stable if

$$\sup_{u\neq 0}\frac{||H(t)||}{||u||}\leq C \quad \forall t\,, \tag{3.16}$$

for some C constant.

The Lax-Wendroff theorem (Lax and Wendroff, 1960) guarantees that if the solution to a non-linear conservation law obtained with a consistent and conservative scheme, *i.e.* such that

$$\int_\Omega \tilde{\mathcal{T}}_s^\Delta[v]\mathrm{d}\boldsymbol{x}=\int_\Omega v\mathrm{d}\boldsymbol{x} \tag{3.17}$$

for any $v\in L^1(\Omega)$, converges in the L^1-norm, then the solution u it converges to is a weak solution of the equation. Therefore if a convergence condition can be found, the Lax-Wendroff theorem will guarantee that the solution found is a weak solution (but not necessarily an entropic one, this has to be proven by different means).

We introduce now the concept of total variation of a function $v(x)$, $\mathrm{TV}(v)$, as

$$\mathrm{TV}(v)=\sup_{\epsilon\to 0}\frac{1}{\epsilon}\int_\Omega |v(x)-v(x-\epsilon)|\mathrm{d}x\,. \tag{3.18}$$

If v is differentiable this is equivalent to

$$\mathrm{TV}(v)=\int_\Omega |v'(x)|\mathrm{d}x\,, \tag{3.19}$$

and this last expression can also be used more generally for distributions if the derivative is interpreted as a distribution derivative.

A scheme is said to be TV-stable if for all initial data u_0 with finite total variation, there exist two positive constants C and Δ_0 such that

$$\mathrm{TV}(\tilde{\mathcal{T}}_s^\Delta[u_0])\leq 0 \quad \forall\Delta<\Delta_0\,. \tag{3.20}$$

A TV-stable scheme, if consistent and conservative, is convergent and the Lax-Wendroff theorem applies.

Most TV-stable schemes are actually so-called *total variation diminishing* (TVD) schemes, *i.e.* such that

$$\mathrm{TV}(\tilde{\mathcal{T}}_{\Delta t}^\Delta[u])\leq \mathrm{TV}(u)\,. \tag{3.21}$$

A way to ensure a scheme to be TVD is to require it to be *monotone*:

$$\text{if } u\geq v \text{almost everywhere, then } \tilde{\mathcal{T}}_t^\Delta[u]\geq\tilde{\mathcal{T}}_t^\Delta[v]\,. \tag{3.22}$$

Crandall and Tartar (1980) and Crandall and Majda (1980) proved that monotone schemes are TVD and converge to weak (and entropic solutions). However Harten et al. (1976) showed that monotone schemes are at most first order accurate.

To achieve high order accuracy without sacrificing non-linear stability, non-monotone TVD methods in one dimension have been formulated; but Goodman and LeVeque (1985) proved that while such schemes exist in the one-dimensional case, in higher dimensions they are again limited to first order

accuracy. Therefore even weaker stability conditions have been considered, such as schemes satisfying as maximum principle or *monotonicity preserving* schemes, *i.e.* schemes that (at least in one-dimension) cannot generate spurious extrema. In practice, many schemes commonly employed, including the ones presented here, have not been proven TV-stable or TVD, although numerical evidence seem to confirm that they converge to the correct entropic solutions. Furthermore for systems of equations no scheme has been proven stable or convergent for generic initial data, even in the one-dimensional case (Leveque, 2002).

3.1.4 The method of lines

A few of the methods discussed in the following sections (namely the original Godunov's method presented at the beginning of section 3.2 and the ADER-DG scheme of section 3.5.1) are fully discrete schemes, *i.e.* schemes which define a space and time discretization of the equations to be solved. The most common choice is however to only discretize the spatial part of the equations, retaining the exact time dependence. This means that a system of PDEs is transformed by such an approach in a (coupled) system of ODEs: one ODE for every evolved field and grid point in the computational mesh. When actually implementing the scheme this resulting system of ODEs can be then solved by using one of the many ODE time integrators available in the literature (see *e.g.* Hairer et al. (1993); Hairer and Wanner (1996)), which effectively takes care of the time discretization. This approach is known as the *method of lines* (Rezzolla and Zanotti, 2013; Baumgarte and Shapiro, 2010).

Of the many possible time integrators, the most popular class is that of Runge-Kutta (RK) methods. These are single-step methods (*i.e.* not depending on the past timelevels of the solution) which achieve high order by taking a suitable linear combination of different estimates of the time derivative of the solution. They are generally easy to implement and do not require any special startup procedure. Alternative methods, which are however not so common in the solutions of PDEs, are *e.g.* multi-step methods, such as Adams-Bashforth methods, Adams-Moulton methods or backward differentiation formulas.

All of these classes of methods contain *explicit* methods, in which the solution at time t^{n+1} can be obtained explicitly from the one at previous time, as well as *implicit* methods, where the solution at time t^{n+1} is to be found by solving an implicit algebraic equation, *e.g.* by means of a Newton-Raphson method. For non-stiff equations (such as the Euler equations), explicit methods, which are much simpler to implement and computationally cheaper, are adequate; however equations containing stiff terms (see again Hairer and Wanner (1996) for a definition) such as the equations of resistive magnetohydrodynamics would require prohibitively small timestep to be accurately solved with an explicit method. In this case implicit methods, which generally have a much larger region of stability and therefore allow for larger timesteps, are better suited.

Another limitation on the choice of the timestep, which is common to all systems of hyperbolic equations, is the Courant-Friedrichs-Lewy (CFL) condition (Courant et al., 1928). For a numerical scheme to be stable the timestep must be small enough that, at any point, the domain of dependence of the scheme should include the domain of dependence of the PDE. The former is

defined as the union of all the points in the grid that contribute to compute the solution at a given point at the next timestep; the latter is the union of all points that on which the exact solution at the point in question depends. Physically, this means that the propagation speed of a physical perturbation in the solution should always be smaller than the numerical speed $\Delta x/\Delta t$. This leads to the necessary condition

$$\Delta t \leq \frac{\Delta x}{\lambda}\,, \tag{3.23}$$

where Δt is the timestep, Δx the grid spacing and λ the maximum propagation speed of the PDE. This is just a necessary condition, and in practical implementations the timestep is set to

$$\Delta t = C_{CFL}\frac{\Delta x}{\lambda}\,. \tag{3.24}$$

The constant $C_{CFL} \leq 1$ is generally known as the CFL or Courant factor.

In section 3.1.3 it has been stressed how in the case of non-linear equations the time discretization also plays an important role to determine the stability and convergence of a numerical scheme. In practice, many of the stability proofs assume that the time discretization is carried out with the simple explicit first order Euler method. In practical applications however is desirable to achieve high order in the time discretization, which as outlined above can be easily done by replacing the Euler method with *e.g.* a high order RK method. In this case however there is no guarantee that the stability properties of the original scheme carry over to the modified one. For this reason is of particular interest a class of time integrators that go under the name of *strong stability preserving* (SSP) methods (Shu and Osher, 1988; Shu, 1988; Gottlieb et al., 2001; Gottlieb et al., 2009). Such methods can be written as a linear convex combinations of single Euler steps, which guarantees that whatever stability property characterizes the original discretization (*e.g.* monotonicity, TVD, ...), the high order time discretization will preserve as well. For this reason SSP methods are the time stepping procedure of choice for the integration of non-linear conservation laws with discontinuous solutions such as *e.g.* Euler equations.

3.2 Finite-volumes schemes

Finite-volumes schemes date back to a very influential work by Godunov (1959). Godunov realized that by assuming the solution to a conservation law to be *piecewise constant* over some subdivision of the computational domain into cells, the solution at the next time step can be computed exactly by solving the Riemann problem at each cell interface.

Restricting momentarily the discussion to the scalar, one-dimensional equation $\partial_t u + \partial_x f = 0$, Godunov's method can be illustrated as follows. Let's define a uniformly spaced spatial and temporal grid,

$$x_i = i\Delta x, \quad i \in \mathbb{Z} \qquad t^n = n\Delta t, \quad n \in \mathbb{N}\,, \tag{3.25}$$

where the constants Δx and Δt are the spatial and temporal grid spacing, respectively. We also define $x_{i\pm 1/2} = (i \pm \frac{1}{2})\Delta x$, *i.e.* the mid point between two grid points. A cell is a space-time volume with extents $[x_{i-1/2}, x_{i+1/2}] \times$

$[t^n, t^{n+1}]$. Furthermore we define the *cell average* of the solution over one cell at a given time t^n as:

$$u_i^n = \frac{1}{\Delta x} \int_{x_{i-1/2}}^{x_{i+1/2}} u(t^n, x) \mathrm{d}x \,. \tag{3.26}$$

Note that $u_i^n = u(x_i) + \mathcal{O}((\Delta x)^2)$, *i.e.* the cell average is a second order approximation of the point value of the solution at the cell center in the grid spacing. By averaging the conservation law over a space-time cell, we can rewrite it as

$$u_i^{n+1} = u_i^n - \frac{\Delta t}{\Delta x}(F_{i+1/2} - F_{i-1/2}) \,, \tag{3.27}$$

where we have defined $F_{i\pm1/2} = \frac{1}{\Delta t} \int_{t^n}^{t^{n+1}} f(u(t, x_{i\pm1/2}))\mathrm{d}t$. It has to be stressed that equation (3.27) is *exact*: no approximation has been introduced yet.

To solve equation (3.27) for u_i^{n+1} it is necessary to compute $F_{i\pm1/2}$. If one assumes u to be piecewise constant and equal to its cell average within each cell, *i.e.* $u(t^n, x) = u_i^n$ for $x \in [x_{i-1/2}, x_{i+1/2}]$, then a Riemann problem can be computed at each cell interface, obtaining the values $u(t, x_{i\pm1/2})$ for every i and all times $t \in [t^n, t^{n+1}]$. In particular at the interface between the i-th and $(i+1)$-th cells the Riemann problem for the following initial data is solved

$$u(t^n, x) = \begin{cases} u^- = u_i^n & \text{if } x < x_{i+1/2} \,, \\ u^+ = u_{i+1}^n & \text{if } x > x_{i+1/2} \,, \end{cases} \tag{3.28}$$

and similarly for every other cell pair. Figure 3.2 shows a schematic grpahical representation of how the Riemann problem solution at each cell interface generates the solution at the next time step.

This procedure is possible as long as the timestep is small enough so that the non-linear waves belonging to each Riemann fan do not intersect each other, or that their interaction is entirely contained within one cell (see also Leveque (1992) for further details). In particular the following condition has to be met:

$$\Delta t \leq \frac{\Delta x}{c} \,, \tag{3.29}$$

where c it the maximum propagation speed of the system. Furthermore the time integrals in the definition of $F_{i\pm1/2}$ are trivial, since the value of the solution at the cell interface is constant in $t \in [t^n, t^{n+1}]$.

Godunov's method, as we have expressed it in equation (3.27), is fully discrete, *i.e.* discrete both in time and space. As anticipated in section 3.1.4, we work in general with semi-discrete methods, since these are easier to generalize to higher order, and easier to couple with numerical methods for the solution of other types of equation, which may not be in fully-discrete form. In discrete form, Godunov's method reads

$$\partial_t u_i(t) = -\frac{F_{i+1/2} - F_{i-1/2}}{\Delta x} \,, \tag{3.30}$$

although the use of a high order time integrator is pointless in this case, since the time update is already exact.

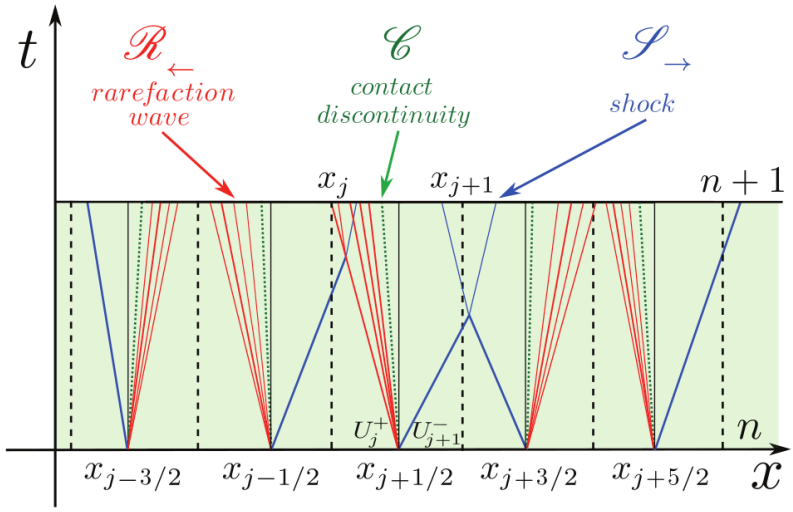

Figure 3.2: Representation of the characteristic waves originating from each cell interface as a result of the evolution from t^n to t^{n+1} of the sequence of Riemann problems in Godunov scheme. At each cell interface a Riemann fan will be opened comprising shock waves (blue solid lines), rarefaction waves (red solid lines) and contact discontinuities (green dotted lines). *Figure courtesy of Rezzolla and Zanotti (2013).*

A general FV method basically consist of the semi-discrete Godunov's method, where the numerical fluxes $F_{i\pm1/2}$ are not generally computed by exactly solving a Riemann problem. In the three-dimensional case, for a system of conservation laws, such a FV method can be expressed as

$$\frac{\mathrm{d}u_{ijk}}{\mathrm{d}t} = -\frac{1}{|\Omega_{ijk}|}\int_{\partial\Omega_{ijk}} \boldsymbol{f}^i \boldsymbol{n}_i \mathrm{d}\Sigma\,, \tag{3.31}$$

where, having defined Ω_{ijk} as the cell with barycentre $\boldsymbol{x}_{ijk}$, $|\Omega_{ijk}|$ is its volume, $\partial\Omega_{ijk}$ its boundary, $\boldsymbol{n}_i$ the outgoing normal to $\partial\Omega_{ijk}$ and Σ the surface element on $\partial\Omega_{ijk}$. For an equally spaced Cartesian grid $\boldsymbol{x}_{ijk} = (i\Delta x, j\Delta y, k\Delta z)^{\mathrm{T}}$, $i, j, k \in \mathbb{Z}$, this simplifies to

$$\begin{aligned}\frac{\mathrm{d}u_{ijk}}{\mathrm{d}t} = &-\frac{1}{\Delta x}[F^x_{i+1/2,j,k} - F^x_{i-1/2,j,k}] \\ &-\frac{1}{\Delta y}[F^y_{i,j+1/2,k} - F^y_{i,j-1/2,k}] \\ &-\frac{1}{\Delta z}[F^z_{i,j,k+1/2} - F^z_{i,j,k-1/2}]\,,\end{aligned} \tag{3.32}$$

where F^i are the components of the numerical fluxes in the three Cartesian directions.

In a FV scheme such as (3.32), a lot of information is discarded in imposing the solution to be piecewise constant. For this reason it is possible to construct stable FV schemes with simplified or approximate Riemann solvers, with the

benefit of a simpler implementation and increased performance. Examples of such Riemann solvers are the Roe solver (Roe, 1981), the Marquina solver (Donat and Marquina, 1996), the HLLE solver (Einfeldt, 1988). Note that although these are called "Riemann solvers", not all of them provide a numerical flux function as $F(u_L, u_R) = f(u(u_L, u_R))$, *i.e.* by solving the original Riemann problem and then evaluating the flux: some of them provide a numerical flux directly. As shown by Harten et al. (1983) (see also Leveque (1992) again), if a flux formula satisfies $F(u, u) = f(u)$ (*i.e.* it is **consistent**), the resulting scheme will be consistent and conservative.

3.2.1 Reconstruction operators and high order finite-volumes schemes

FV schemes as described in the previous section are first order accurate in the cell averages (but recall that the cell averages are themselves a second order accurate approximation of the solution point values). It is possible to obtaining a high order scheme by reconstructing the behaviour of the solution in every cell interior from the information in the neighbouring cells. The concept is to arrive at a better approximation of the values $\boldsymbol{u}^{\pm}$ of the solution at each cell interface, to be then fed to the Riemann solver, obtained from a higher order approximation of the solution in the two adjacent cells. If the reconstruction is non-linear, it is possible to obtain stable (*e.g.* TVD) schemes of order higher than one.

A first possibility is to upgrade the solution from being piecewise constant to piecewise linear, *i.e.*

$$u_i(x) = u_i + \sigma_i(x - x_i) \qquad x \in [x_{i-1/2}, x_{i+1/2}]\,. \tag{3.33}$$

Setting Riemann problem initial data to the values of this reconstructed solution evaluated at the cell interfaces, *i.e.* for the cell interface located at $x_{i+1/2}$, $u^- = u_i(x_{i+1/2})$ and $u^+ = u_{i+1}(x_{i+1/2})$, results in a scheme with overall second order accuracy in the cell averages.

The slopes σ_i are determined from the values u_i of the cell averages of the solution in the neighbouring cells. Conditions that ensure the resulting scheme to be TVD are known (Leveque, 1992), leading to non-linear *slope limiters*, such as *e.g.* the minmod limiter:

$$\sigma_i = \frac{1}{\Delta x}\mathrm{minmod}(u_{i+1} - u_i, u_i - u_{i-1})\,, \tag{3.34}$$

where

$$\mathrm{minmod}(a_1, \cdots, a_n) = \begin{cases} \min a_i & \text{if } a_i > 0\,\forall i\,, \\ \max a_i & \text{if } a_i < 0\,\forall i\,, \\ 0 & \text{otherwise}\,. \end{cases} \tag{3.35}$$

In greater generality, higher order FV schemes can be constructed by considering input values for the Riemann problem at cell interfaces resulting from a high order polynomial reconstruction of the solution in each cell, as illustrated in figure 3.3. This leads to the concept of a *reconstruction operator*. A reconstruction operator $\mathcal{R}$ is an operator acting on the volume (cell) averages

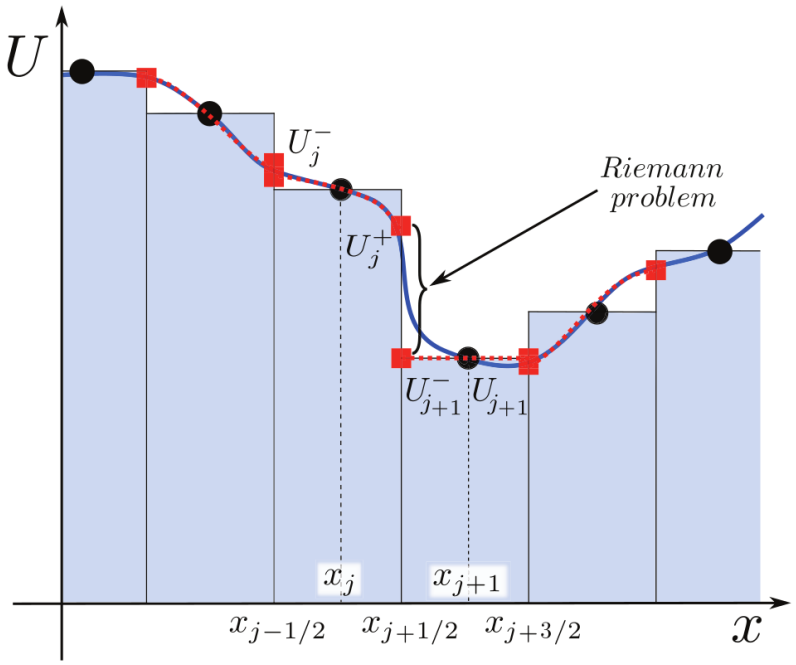

Figure 3.3: Representation of the boundary-extrapolated values (red solid boxes) providing the left and right states of the Riemann problem at each cell interface for a high order FV scheme. The reconstruction is made using the PPM method. *Figure courtesy of Rezzolla and Zanotti (2013).*

$\bar{v}_i$ of a function $v(x)$, and giving a high order approximation of the function point value at a given point x_0. We actually distinguish two operators, the left-biased one and the right-biased one, defined such that

$$\begin{aligned} [\mathcal{R}^-(\{\bar{v}_i\})] &= \lim_{y\to x^-} v(y) + \mathcal{O}(\Delta x^r) \\ [\mathcal{R}^+(\{\bar{v}_i\})] &= \lim_{y\to x^+} v(y) + \mathcal{O}(\Delta x^r)\,, \end{aligned} \tag{3.36}$$

to accommodate the fact that $v(x)$ might be discontinuous.

Many different such operators are available in the literature and many variations of them, such as the piecewise parabolic method (PPM) (Colella and Woodward, 1984; Colella and Sekora, 2008), the piecewise hyperbolic method (PHM) (Marquina, 1994), the essentially non-oscillatory (ENO) (Harten et al., 1987; Shu and Osher, 1988; Shu and Osher, 1989) and weighted essentially non-oscillatory (WENO) (Liu et al., 1994; Jiang and Shu, 1996) methods and the monotonicity-preserving (MP) (Suresh and Huynh, 1997) algorithm. The resulting methods, either formulated in a FV framework as described here, or in a FD framework as detailed in section 3.3.3, all go under the label of high-resolution shock-capturing (HRSC) techniques. While there is no formal definition of a HRSC scheme, they should generally satisfy three requirements: reach at least second order accuracy; sharp resolution of discontinuities; absence of spurious oscillations.

The PPM reconstruction extends the slope-limiter procedure to a piecewise parabolic interpolation, employing several limiters to avoid introducing of spurious oscillations.

The ENO scheme relies on standard Lagrange interpolation on multiple overlapping stencils and uses a recursive procedure to determine the stencil on which the solution is smoothest in order to avoid oscillations.

The WENO scheme modifies the original ENO approach. Instead of considering only the stencil on which the solution is smoothest and discarding the others, the WENO reconstruction takes a weighted average of the reconstructed polynomial on each stencil. The weights are chosen to be very small for non-smooth stencils, while the order of accuracy is maximized in smooth regions. WENO algorithms achieve a formal order of accuracy of $2r-1$, where r is the order of the ENO algorithm. Several modifications of the algorithms exist, *e.g.* the mapped-WENO schemes (Henrick et al., 2005) or the WENOZ scheme (Borges et al., 2008). Gerolymos et al. (2009) provide a comparative study of different WENO schemes, reporting tabulated coefficients and implementation details for methods of order up to 17.

The MP scheme is essentially a higher order extension of the PPM scheme. In the original scheme by Suresh and Huynh (1997) it uses a fifth order reconstruction stencil (MP5), but MP methods of order three, seven and nine (MP3, MP7, MP9) have been implemented as well (Obergaulinger, 2008). This is combined with a flattening procedure designed to avoid the creation of artificial extrema.

High order FV schemes can be extended to multiple dimensions, *e.g.* in a direction-by-direction fashion for Cartesian grids.

Below we give the explicit formulas of the unlimited fifth order and seventh order reconstruction stencils since they will play an important role in defining the novel numerical scheme of chapter 5. We refer to these stencils as U5 and U7; they are unlimited in the sense that they are simple interpolation formulas, not attempting to regularize the solution or introduce additional dissipation in any way. Note that the MP5 reconstruction operator is built on top of the U5 stencil. The expression for these stencils are:

$$v_{i+1/2} = {}^{5}\mathcal{R}^{-} := \frac{1}{60}(2\bar{v}_{i-2} - 13\bar{v}_{i-1} + 47\bar{v}_i + 27\bar{v}_{i+1} - 3\bar{v}_{i+2})\,; \tag{3.37}$$

and

$$\begin{aligned} v_{i+1/2} = {}^{7}\mathcal{R}^{-} := &-\frac{1}{140}\bar{v}_{i-3} + \frac{5}{84}\bar{v}_{i-2} - \frac{101}{420}\bar{v}_{i-1} + \frac{319}{420}\bar{v}_i \\ &+\frac{107}{210}\bar{v}_{i+1} - \frac{19}{210}\bar{v}_{i+2} + \frac{1}{105}\bar{v}_{i+3}\,. \end{aligned} \tag{3.38}$$

These are the left biased reconstruction operators, giving the point value of the function $v(x)$ at $x_{i+1/2}$. The right biased ones, reconstructing $v_{i-1/2}$, are obtained by simply reversing the order of the coefficients.

Note that in a FV framework the use of high order reconstruction generally results in a degradation of the scalability of the code. Reconstruction operators are essentially interpolation formulas, achieving high order by interpolating on an increasingly high number of data points. When decomposing the computational domain in components, each one typically evolved by a different CPU, ghost points have to be exchanged between components to provide boundary

conditions at every timestep. The number of ghost points generally increases with the order of the method, hindering the parallel performance of the algorithm. The same issue arises in the context of FD methods, described in the following section. The DG methods described in section 3.4 are instead explicitly designed so that the number of ghost points is constant (one for every coordinate direction) at every order.

3.3 Finite-differences schemes

Many different numerical schemes go under the general moniker of finite-difference schemes, sometimes having very little in common. Arguably, the single property of these schemes that is constantly present in all of them is the fact that they operate on point values rather than on volume averages, and this sets them apart from FV schemes. For this reason in this section the notation v_i refers to the value of a function $v(x)$ at the point x_i, *i.e.* $v_i = v(x_i)$, rather than to its cell average as in the previous section.

The basic FD schemes are introduced in section 3.3.1. They are the schemes to which the FD name is most commonly refers to. Because they are based on the discretization of derivative operators rather then relying on a particular form of the equations, they can (and generally are) applied to systems of equations not in flux-conservative form. On the other hand their simplicity makes them unsuitable to deal with discontinuous solutions, commonly leading to instabilities.

Compact FD (section 3.3.2) schemes are an interesting alternative to obtain high order FD schemes avoiding large ghost zones. Due to the larger number of degrees of freedom available in a compact FD stencil, they can be modified to increase dissipation and deal with discontinuities.

Finally, FD schemes as generally applied to non-linear conservation laws, presented in section 3.3.3, are on the surface very similar to FV schemes. They however act on point values of the solution and avoid the use of Riemann solvers, and are therefore considered separately.

3.3.1 Standard finite-differences

The simplest FD schemes are based on the idea of finding a discrete representation of the derivative operators themselves. The definition of the first derivative $\partial_x v(x_0)$ of a function $v(x)$ itself, *i.e.*

$$\partial_x v(x_0) = \lim_{x \to x_0} \frac{v(x) - v(x_0)}{x - x_0}\,, \tag{3.39}$$

suggests, given an equally spaced grid $x_i = i\Delta x$, to approximate the derivative at a grid point x_i as *e.g.*

$$\partial_x v(x_i) \simeq \frac{v_{i+1} - v_i}{x_{i+1} - x_i} = \frac{v_{i+1} - v_i}{\Delta x}\,. \tag{3.40}$$

This is a first order approximation of the derivative, *i.e.* the error term goes like $\mathcal{O}(\Delta x)$. Higher order approximations can be obtained by interpolating the values v_i in the vicinity of a given point with a high order polynomial and

evaluating its derivatives at the desired point. This algorithm, which is readily extended to unequally spaced grids (Fornberg, 1988) can generate FD approximations of essentially any derivative order (including the 0-th derivative, *i.e.* function interpolation) at any order of accuracy. This results in the well-known standard centered finite-difference stencils, *e.g.*

$$\partial_x v(x_i) = \frac{\frac{1}{4}v_{i-2} - 2v_{i-1} + 2v_{i+1} - \frac{1}{4}v_{i+2}}{3\Delta x} + \mathcal{O}(\Delta x^4) \tag{3.41}$$

(a centered fourth order approximation of the first derivative); or

$$\partial_x^2 v(x_i) = \frac{-\frac{1}{12}v_{i-2} + \frac{4}{3}v_{i-1} - \frac{5}{2}v_i + \frac{4}{3}v_{i+1} - \frac{1}{12}v_{i+2}}{\Delta x^2} + \mathcal{O}(\Delta x^4) \tag{3.42}$$

(a centered fourth order approximation of the second derivative).

Having defined a computational grid (commonly equally spaced), these stencils can be used to approximate all the derivative operators in the equations to be evolved, thus defining a discretization of the equations. Since the discretization is performed at the level of the derivative operators, this technique allows for the discretization of any system of equations, in any form (in particular systems in non-conservative form).

Note however that employing these simple FD stencils generally results in a non-conservative method, making this technique unsuitable for non-linear conservation laws. Also, the algorithm described in Fornberg (1988) simply returns the coefficients that result in the highest order of accuracy given the number of points used by the stencil. This means that in the case of discontinuous solutions spurious oscillations are almost guaranteed to be generated, another reason the makes these methods unsuitable for non-linear conservation laws.

On the other hand, FD methods are often a good choice for linear or linearly degenerate system of equations, where unless the initial data is itself discontinuous, no shocks can be produced in finite time, *i.e.* the solution is always smooth. In this case, the above FD stencils achieve their full accuracy without oscillations being problematic, and a modest amount of artificial dissipation (*e.g.* Kreiss-Oliger dissipation (Kreiss and Oliger, 1973)) is sufficient to stabilise the method. This is approach is particularly suited to very large and complicated systems of equations, where FD methods are much easier to implement than more sophisticated schemes. A prime example of this application are the 3+1 Einstein equations (such as the BSSN or CCZ4 formulations described in chapter 4)(see *e.g.* Brown et al. (2009a), as well as almost any publication involving general-relativistic simulations of dynamical spacetimes performed with the `Einstein Toolkit` (Löffler et al., 2012; Zilhão and Löffler, 2013; Einstein Toolkit Website) and the `McLachlan` code).

Note that the stencils (3.41) and (3.42) are symmetric with respect to the evaluation point, and so were called *centered*. The stencil (3.40) is instead asymmetric (right-biased in this case), using only points on one side of the evaluation point. Such stencils are said to be *one-sided*. One-sided stencils, as well as stencils that are biased in one direction without being completely one-sided, can be constructed for higher order derivatives as well (see again Fornberg (1988)). Such stencils are named *upwind* stencils, because they can be used to take advantage of the direction of propagation of information in the system

(when this is known *a priori*), thus resulting in an upwind scheme. This is often necessary in order to obtain a well-behaved scheme. One example are again the 3+1 Einstein equations, where upwind stencils are known to be necessary to discretize shift-advected terms (Pollney et al., 2011). This might not be necessary in the FV schemes described above, because the Riemann solver should take take care of this aspect. High order FD stencils are generally extended to multiple dimensions in a direction-by-direction fashion on Cartesian grids.

Finally, note that FD stencils also achieve high accuracy by high order interpolation on increasingly large stencils, *i.e.* high order FD methods suffer from the same scalability problems described for high order FV methods. As anticipated DG methods are able to circumvent this issue.

3.3.2 Compact finite-differences

Compact finite-differences (Lele, 1992) are an interesting extension of FD schemes with very desirable properties. As their name implies, they are compact, *i.e.* able to achieve high order on smaller stencils compared to standard FD schemes, which can greatly help to improve the scalability of a compact FD implementation. They improve on standard FD stencils in many other respects however, especially concerning the resolution of high frequency waves. On the other hand they are more involved to implement than standard FD schemes, especially when boundary conditions other than simple periodic ones are required.

The starting point of compact FD schemes is to consider an approximation for the derivative of a function $v(x)$ at the point x_i of the form

$$\begin{aligned}\beta v'_{i-2} + \alpha v'_{i-1} + v'_i + \alpha v'_{i+1} + \beta v'_{i+2} = \\ c\frac{v_{i-3} - v_{i+3}}{6\Delta x} + b\frac{v_{i-2} - v_{i+2}}{4\Delta x} + a\frac{v_{i-1} - v_{i+1}}{2\Delta x}\,,\end{aligned} \tag{3.43}$$

where the notation v'_i represents the first derivative of $v(x)$ at point x_i, and α,β,a,b and c are constants to be determined. Equation (3.43) represents a generalization of the standard central FD stencils introduced in the previous section, in the sense that the derivative is approximated not only as a linear combination of the function values, but of the derivative values themselves. Clearly the relation cannot be inverted locally to find the value of v'_i but when applied to the whole computational domain it results in a linear system (typically a tridiagonal or pentadiagonal one, depending on how the boundary conditions are implemented) that can be solved with standard methods.

The most noticeable advantage of formula (3.43) is that, by suitably choosing the coefficients, it results in an approximation of v'_i accurate up to tenth order, despite only using points three grid spacings or closer to x_i. This can help tremendously in enhancing the scalability of a code.

Lele (1992) has further shown that formulas of the form (3.43) are able to much better approximate the frequency content of oscillating functions. The difference is particularly striking in multi-dimensional applications, in which the wave resolution properties of standard FD stencils are very poor along the coordinate axes, while compact FD stencils behave much better along any direction.

Since formulas of type (3.43) have many more degrees of freedom than standard FD stencils using the same points, it is possible to choose the coefficients

not to achieve the highest order of accuracy, but to further improve the wave resolution properties, or introduce dissipation into the stencil. These possibilities make compact FD stencils attractive for application to non-linear conservation laws such as Euler equations (Kim and Sandberg, 2012). Similar stencils can be constructed for higher order derivatives, as well as upwind and one-sided ones. To the present date there have been however no applications of compact FD stencils in the context of numerical relativity.

3.3.3 Finite-differences schemes for non-linear conservation laws

In the case of conservation laws, finite-differences schemes can be written, in the case of Cartesian equally spaced grids, in the form

$$\begin{aligned}\frac{\mathrm{d}u_{ijk}}{\mathrm{d}t} = &-\frac{1}{\Delta x}[F^x_{i+1/2,j,k} - F^x_{i-1/2,j,k}] \\ &-\frac{1}{\Delta y}[F^y_{i,j+1/2,k} - F^y_{i,j-1/2,k}] \\ &-\frac{1}{\Delta z}[F^z_{i,j,k+1/2} - F^z_{i,j,k-1/2}]\,,\end{aligned} \tag{3.44}$$

which appears completely equivalent to equation (3.32) for FV schemes. The important difference (linked to the fact that u_{ijk} represents the point value of u rather than its volume average) however is that terms like $F^x_{i+1/2,j,k}$ are not defined via integrals on the corresponding cell, but $[F^x_{i+1/2,j,k} - F^x_{i-1/2,j,k}]/\Delta x$ is itself a high-order approximation of $\partial_x f^x$ at x_{ijk}.

This can be achieved by the following construction. As in Shu and Osher (1988) and Mignone et al. (2010), and restricting the discussion to the x-axis for ease of notation, we define F^x as

$$f^x_i = \frac{1}{\Delta x}\int_{x_{i-1/2}}^{x_{i+1/2}} F^x(\xi)\mathrm{d}\xi\,, \tag{3.45}$$

i.e. the point values of the flux are the cell averages of the numerical flux F^x. We furthermore introduce the function H^x as the primitive of F^x, *i.e.*

$$H^x = \int_{-\infty}^{x} F^x(\xi)\mathrm{d}\xi\,. \tag{3.46}$$

With this definition equation (3.45) becomes

$$f^x_i = \frac{1}{\Delta x}\int_{x_{i-1/2}}^{x_{i+1/2}} F^x(\xi)\mathrm{d}\xi = \frac{1}{\Delta x}[H^x(x_{i-1/2}) - H^x(x_{i+1/2})]\,. \tag{3.47}$$

Straightforward differentiation of this relation results in the expression

$$\partial_x f^x_i = \frac{1}{\Delta x}[F^x(x_{i-1/2}) - F^x(x_{i+1/2})]\,, \tag{3.48}$$

for the derivative of the flux, as in the first line of (3.44).

Since the flux values f^x_i are by definition the cell averages of the numerical flux, we can use the reconstruction operators defined in section 3.2.1 to obtain non-oscillatory, high order approximation of the latter. Stated differently,

FD schemes can also be included in the category of high-resolution shock-capturing (HRSC) methods introduced in section 3.2.1.

Note that the operators are in this case applied to the flux, which highlights another difference between FV and FD schemes for conservation laws: in the former, the solution at cell interfaces is reconstructed, from which the numerical flux is defined; in the latter, the numerical flux is directly reconstructed.

Since no Riemann solver is involved in the scheme, to ensure stability the reconstruction has to be upwinded. In the general case in which the sign of $f'(u)$ is undetermined, this is achieved by splitting it into a right-going part f^+ and a left-going one f^-, so that $f = f^+ + f^-$. The left(right)-biased reconstruction operator is applied to the right(left)-going part of the flux, and the two reconstructed values are then summed. Note that the use of a flux-splitting procedure is similar to the use of a Riemann solver in FV methods. In fact, many such methods can be associated with corresponding Riemann solvers. From the many possible way of splitting the flux for upwinding, we select here the Lax-Friedrichs (or Rusanov) formula (Shu, 1997), in which f^+ and f^- are defined as

$$f^{\pm} = f + au\,. \tag{3.49}$$

Here a is the maximum local propagation speed of the system: $a = \max|f'(u)|$ where the maximum is taken over the points acted upon by the stencil.

In the case of a system of equations, where the solution $\boldsymbol{u}$ and the flux $\boldsymbol{f}$ are vector valued, the procedure outlined above to compute the derivative $\partial_i \boldsymbol{f}^i$ can simply be carried out successively on every component of the system (which we refer to as a "component split" of the system). This simple approach can however result in spurious oscillations when a high order reconstruction is employed. To remedy this issue it is possible to perform the reconstruction on the *local characteristic variables*. Limiting the notation again to the x-axis for the sake of clarity, we introduce the local Jacobian matrix of the flux:

$$\boldsymbol{A}^x = \left.\frac{\partial \boldsymbol{f}^x}{\partial \boldsymbol{u}}\right|_{\bar{\boldsymbol{u}}}\,. \tag{3.50}$$

We need to reconstruct the numerical flux at the point $x_{i+1/2}$, so the derivative is evaluated at $\bar{\boldsymbol{u}} = (\boldsymbol{u}_{i+1} + \boldsymbol{u}_i)/2$, *i.e.* the average of the states of the fluid in the neighbouring cells. Assuming the system to be strongly hyperbolic, $\boldsymbol{A}^x$ is invertible with only real eigenvalues λ_n and a corresponding set of independent right- and left-eigenvectors, $\boldsymbol{r}_n$ and $\boldsymbol{l}_n$ (in these expressions the index n runs over the components of the system). Denoting $\boldsymbol{R}$ the matrix of right eigenvectors, *i.e.*

$$R^j{}_n = r^j_n\,, \tag{3.51}$$

and $\boldsymbol{L}$ its inverse (the matrix of left-eigenvectors), we can define the local characteristic variables as

$$\boldsymbol{w} = \boldsymbol{L}\boldsymbol{u} \qquad \boldsymbol{Q} = \boldsymbol{L}\boldsymbol{f}^x\,. \tag{3.52}$$

The reconstruction procedure can then be applied as follows: we locally compute $\boldsymbol{Q}$ and $\boldsymbol{w}$; let the reconstruction operator act on the components of $\boldsymbol{Q}$, where in the flux-splitting step $\boldsymbol{w}$ appears instead of $\boldsymbol{u}$ in equation (3.49); finally we "transform back" the reconstructed value by multiplying with the matrix of right-eigenvectors:

$$\boldsymbol{F}^x_{i+1/2} = \boldsymbol{R}\boldsymbol{Q}_{i+1/2}\,. \tag{3.53}$$

The procedure is similarly applied in the other directions. In the results presented in chapter 5, where a FD method using the MP5 reconstruction is employed as reference for comparison purposes with a novel approach, the "characteristic split" outlined above is always used in conjunction with the MP5 reconstruction.

Finite-differences flux-limiting schemes

A different different approach to finite-differences HRSC schemes is employed in the so-called *flux-limiting* schemes (see Leveque (1992) for an introduction and overview). A HRSC scheme is obtained by selecting a reconstruction operator with HRSC properties, in particular with an in-built mechanism to suppress spurious oscillations and deal with discontinuous solutions. In a flux-limiting scheme instead the numerical flux $F_{i+1/2}$ (we restrict hereafter the notation to one spatial dimension for simplicity) is split (or "hybridized") into two parts, *i.e.*

$$F_{i+1/2} = \theta F^{HO}_{i+1/2} + (1-\theta) F^{LF}_{i+1/2}\,. \tag{3.54}$$

In equation (3.54) $F^{HO}_{i+1/2}$ is a high order contribution to the flux, which is computed without the use of any limiting procedure, or inserting any artificial dissipation; $F^{LF}_{i+1/2}$ is instead a low order contribution, meant to introduce sufficient numerical dissipation for the method to be stable even in the case of discontinuous solutions; the parameter $\theta \in [0,1]$ controls the relative ratio of the two contributions.

The high order flux contribution can be obtained for example via the unlimited reconstruction stencils introduced in section 3.2.1, *i.e.* the U5 (3.37) or U7 (3.38) operators. This is in fact the choice used in the numerical results of chapter 5. The low order contribution is instead defined as the local Lax-Friedrichs flux (hence the LF superscript):

$$F^{LF}_{i+1/2} = \frac{1}{2}(f_i + f_{i+1}) - \frac{\kappa}{2}(u_i - u_{i+1})\,, \tag{3.55}$$

where κ is an estimate of the local maximum propagation speed of the system, *i.e.* $\kappa = \max|\frac{\mathrm{d}f}{\mathrm{d}u}|$ with the maximum taken over the stencil of the high order part.

Note that θ need not be a constant, but can be adjusted in space and time as necessary. Within this framework it is possible in fact to choose the value of θ such that the resulting scheme satisfies a maximum principle, *i.e.* if given two constants $m \leq M$ the initial data satisfies $m \leq u_0 \leq M$, the solution at time t will satisfy $m \leq u(t) \leq M$ as well. When applied to the Euler equations of (relativistic) hydrodynamics, this can be exploited to construct schemes in which the result of the evolution is always a physically admissible state (Wu, 2017) or more simply (as in the implementation tested in chapter 5) to ensure that the rest-mass density never becomes negative.

Schematically, this can be illustrated as follows: for a single Euler time integration step, the result of the evolution of u can be explicitly written as

$$u_i^{i+n} = \frac{1}{2}(u_i^n + 2\lambda F_{i-1/2}) + \frac{1}{2}(u_i^n - 2\lambda F_{i-1/2})\,, \tag{3.56}$$

where the fluxes are defined as in equation (3.54) and λ depends on the maximum propagation speed of the system as well as on the CFL factor. There

exist a value of θ that makes both terms in equation (3.56) positive, computed following the algorithm in section 2.2 of Hu et al. (2013), but replacing the rest-mass density ρ with its conserved relativistic counterpart $D = \rho W \sqrt{\gamma}$ (see Radice et al. (2014b) for details). Applied to the continuity equation (2.16) this guarantees that the density never becomes negative. We refer to this approach as the *positivity-preserving limiter*, an integral part of the ELH scheme of chapter 5.

3.4 Discontinuous Galerkin methods

Discontinuous Galerkin schemes belong to the class of finite-elements methods. In a DG approach the computational domain is subdivided in a number of non-overlapping elements, and in the interior of each element functions are represented by a spectral expansion over a set of basis functions. The expansion provides an accurate way to compute derivatives in the interior of each element, while the solution itself is discontinuous across element boundaries. A numerical flux is introduced to tie together the evolution of the elements.

DG methods posses a number of outstanding properties with respect to FV and FD methods. First of all, they can be proven to be non-linearly stable at all orders. They also satisfy an entropy inequality, meaning a solution to a non-linear conservation law obtained with a DG method is always the entropic one (Cockburn, 2003).

Secondly, they can exploit the so-called hp-adaptivity, referring to the possibility of both refining the size of the elements (h-adaptivity, h being a common shorthand for the grid spacing) and the accuracy of the spectral expansion within a single element (p-adaptivity, p being the order of the method). This means that (on smooth solutions), DG methods achieve polynomial accuracy in the grid spacing (as FV or FD schemes) but spectral accuracy in the number of basis functions employed.

Thanks to their very compact stencils, which in particular means they need only one ghost point at any order, they have nearly-optimal scalability, which makes them very attractive for large parallel applications. They also quite naturally accommodate unstructured meshes (see *e.g.* Boscheri and Dumbser (2017)).

Finally, they can be formulated in a covariant way, not needing a choice of coordinate system (Meier, 1999).

On the other hand, the drawbacks of DG methods are a greater complexity of the implementation; a larger memory footprint than other schemes; and most importantly, more severe limitations on the size of the timestep. The latter is a consequence of the fact that in the interior of each element, the spectral basis can be associated to a grid, and the limitation on the size of timestep is scales naturally with the spacing of this grid rather than with the element size.

In the context of hyperbolic equations, DG methods have been applied mostly to (first order) conservation laws of the form (3.1), and are generally formulated in this context. We will proceed in our exposition in this way as well for simplicity. Note however that DG methods can be applied to a larger class of equations, such as equation of second order in space (*e.g.* Hesthaven and Warburton (2007); Miller and Schnetter (2017)), or most importantly for the

present work, to conservation laws written in full or partial non-conservative form, as detailed in section 3.5.1.

3.5 Nodal semi-discrete DG methods

DG methods can be formulate as follows, where we refer for simplicity to a Cartesian coordinate system. The computational domain Ω is split in non-overlapping elements:

$$\begin{aligned}\Omega_i =&[x_i - \frac{1}{2}\Delta x_i, x_i + \frac{1}{2}\Delta x_i] \\ &\times [y_i - \frac{1}{2}\Delta y_i, y_i + \frac{1}{2}\Delta y_i] \\ &\times [z_i - \frac{1}{2}\Delta z_i, z_i + \frac{1}{2}\Delta z_i] \,,\end{aligned} \tag{3.57}$$

where

$$\boldsymbol{x}_i = (x_i, y_i, z_i) \qquad \Delta\boldsymbol{x}_i = (\Delta x_i, \Delta y_i, \Delta z_i) \tag{3.58}$$

are the barycentre and the size of the element Ω_i in each spatial coordinate direction, respectively. Clearly the union of all elements is the whole domain Ω, *i.e.* $\Omega = \bigcup \Omega_i$. Note that we employ an index i which runs over all elements, which implies some sort of ordering of the elements themselves has been chosen, *e.g.* by employing a space filling curve.

In the finite-element DG context, the solution to a system of equations, which we denote from now on by $\boldsymbol{u}$, belongs to the space of tensor products of piecewise polynomials of degree N in each spatial direction, itself indicated by the symbol $\mathcal{U}$. At a given time t^n, the solution is represented by some unknown degrees of freedom $\hat{\boldsymbol{u}}_{i,l}^n$ associated to some spatial basis functions $\Phi_l(\boldsymbol{x})$ in each element Ω_i as follows:

$$\boldsymbol{u}(\boldsymbol{x}, t^n) = \sum_l \hat{\boldsymbol{u}}_{i,l}^n \Phi_l(\boldsymbol{x}) := \hat{\boldsymbol{u}}_{i,l}^n \Phi_l(\boldsymbol{x}) \,, \tag{3.59}$$

where the spatial basis functions $\Phi_l(\boldsymbol{x}) = \varphi_{l_1}(\xi)\varphi_{l_2}(\eta)\varphi_{l_3}(\zeta)$ are the tensor products of one-dimensional basis functions $\varphi_k(\xi)$ on the one-dimensional reference element $[0, 1]$. $l := (l_1, l_2, l_3)$ is a multi-index, a shorthand for three indices which run over the degrees of freedom of each Cartesian direction in the interior of each element.

The mapping from physical coordinates $\boldsymbol{x} \in \Omega_i$ to reference coordinates $\boldsymbol{\xi} = (\xi, \eta, \zeta) \in [0, 1]^3$ is simply given by $\boldsymbol{x} = \boldsymbol{x}_i - \frac{1}{2}\Delta\boldsymbol{x}_i + (\xi\Delta x_i, \eta\Delta y_i, \zeta\Delta z_i)^T$. A common choice for the one-dimensional basis functions $\varphi_k(\xi)$ are the Lagrange interpolation polynomials passing through the Gauss-Legendre quadrature nodes ξ_j of an $N + 1$ point Gauss quadrature formula (see figure 3.4). With this choice the interpolation property $\varphi_k(\xi_j) = \delta_{kj}$ is satisfied. Due to this particular choice of a *nodal* basis, the entire scheme can be written in a dimension-by-dimension fashion, where all integral operators can be decomposed into a sequence of one-dimensional operators acting only on the $N + 1$ degrees of freedom in the respective dimension.

Note that these choices are by no means unique. Choosing the Lagrange polynomials as basis functions is very common, but other bases are sometimes

chosen. Using Lagrange polynomials results in a nodal basis where the interpolation property is valid; a different basis choice can result in *modal*, rather then nodal, DG schemes, in which the degrees of freedom $\hat{\boldsymbol{u}}_{i,l}^n$ are simply the coefficients of the basis functions in a spectral representation, but cannot be identified as point values of the solution at the chosen nodes, as in the nodal framework. Finally, while it is very common to choose Gauss-Lagrange nodes in a nodal framework, other choices are possible. The advantage of Gauss-Legendre nodes over *e.g.* equally spaced nodes is that it avoids matrices appearing later in the definition of the scheme to be severely ill-conditioned. Another popular choice with the same advantage is Gauss-Lobatto nodes, which puts nodes on the boundary of the element, meaning two adjacent element will each have a node in the same physical location, but the corresponding degrees of freedom (*i.e.* point values of the solution) might be different. These possibilities are reviewed in Hesthaven and Warburton (2007).

In deriving a DG scheme, one first multiplies the equations to be solved (3.1) (we refer in this section only to equations in flux conservative form, for simplicity) by a test function $\Phi_k \in \mathcal{U}$, identical to the spatial basis functions of equation (3.59) (this choice is distinctive of Galerkin schemes). After that, we integrate over an element Ω_i and obtain

$$\int_{\Omega_i} \Phi_k \frac{\partial \boldsymbol{u}}{\partial t} \mathrm{d}\boldsymbol{x} + \int_{\Omega_i} \Phi_k \partial_j \boldsymbol{f}^j(\boldsymbol{u}) \mathrm{d}\boldsymbol{x} = \int_{\Omega_i} \Phi_k \boldsymbol{s}(\boldsymbol{u}) \mathrm{d}\boldsymbol{x}\,, \tag{3.60}$$

where we have reintroduced the algebraic source terms $\boldsymbol{s}$ for generality. Here $\mathrm{d}\boldsymbol{x} = dx\,dy\,dz$, *i.e.* the integration is over a *coordinate volume*, not a physical one.

Using the ansatz (3.59) the expression (3.60) (the so called weak formulation of the DG scheme) can be rewritten as

$$\left(\int_{\Omega_i} \Phi_k \Phi_l \mathrm{d}\boldsymbol{x} \right) \frac{\mathrm{d}\hat{\boldsymbol{u}}_{i,l}}{\mathrm{d}t} + \int_{\Omega_i^\circ} \frac{\mathrm{d}\Phi_k}{\mathrm{d}x^j} \boldsymbol{f}^j(\boldsymbol{u}) \mathrm{d}\boldsymbol{x} + \int_{\partial\Omega_i} \Phi_k \mathcal{D}^- \left(\boldsymbol{u}^-, \boldsymbol{u}^+ \right) \cdot \boldsymbol{n} \mathrm{d}S = \int_{\Omega_i} \Phi_k \boldsymbol{s}(\boldsymbol{u}) \mathrm{d}\boldsymbol{x}\,. \tag{3.61}$$

In (3.61), upon explicitly inserting the expressions for the basis functions, the first integral expands into the mass matrix, which is diagonal for our choice of the basis and test functions; in the second integral the so-called stiffness matrix appears, and this term accounts for the smooth part of the discrete solution in the interior $\Omega_i^\circ = \Omega_i \backslash \partial\Omega_i$ of the element Ω_i; the third term takes the form of a boundary integral (where S is the surface element and $\boldsymbol{n}$ the outward normal vector to $\partial\Omega_i$) accounts for the jumps across the element interfaces (since the solution can be discontinuous at these locations); the last term on the right-hand side is simply due to the presence of the purely algebraic source terms $\boldsymbol{s}$.

In the boundary integral, the flux $\boldsymbol{f}$ has been replaced with the function $\mathcal{D}^-$, which depends on the states $\boldsymbol{u}^+$ and $\boldsymbol{u}^-$ at the edge of the two adjacent elements. This function takes the role of a numerical flux. It needs to be specified explicitly since the solution is discontinuous at element boundaries (*i.e.* $\boldsymbol{u}^+ \neq \boldsymbol{u}^-$), and as such the various elements would evolve completely independently in its absence. One of the most common choices of numerical flux (many are possible), giving satisfactory results in many cases, is the simple

Lax-Friedrichs flux:

$$\mathcal{D}^- = \frac{1}{2}(\boldsymbol{f}(\boldsymbol{u}^+) + \boldsymbol{f}(\boldsymbol{u}^-)) + \frac{a}{2}\boldsymbol{n}\cdot(\boldsymbol{u}^+ + \boldsymbol{u}^-)\,. \tag{3.62}$$

Here a is again (an estimate of) the maximum propagation speed of the system of equations, $a = \max|\partial_{\boldsymbol{u}}\boldsymbol{f}|$, where the maximum could be global or local. Other choices of numerical flux are available, in fact all the flux formulas discussed in section 3.2 are viable (*e.g.* Radice and Rezzolla (2011) employed the HLLE flux formula to discretize the general relativistic Euler equations in spherical symmetry).

Note that as the flux is general a non-linear function an aliasing error is introduced in approximating it with the ansatz (3.59). This is in general unavoidable, and can lead to problems concerning the non-linear stability of the scheme. It is however easily suppressed with the use of weak filtering (Hesthaven and Warburton, 2007).

Finally, DG methods can be combined with adaptive mesh refinement (AMR), as *e.g.* implemented in a cell-by-cell framework based on a tree structure (Khokhlov, 1998), together with local time stepping (Dumbser et al., 2013; Dumbser et al., 2014; Zanotti and Dumbser, 2015; Zanotti et al., 2015b,a).

3.5.1 Path-conservative ADER-DG schemes

DG methods as introduced in the previous section are applied to equations in flux-conservative form. It is however possible to apply the DG discretization framework even when the system of equation to solve is not in such form, but contains non-conservative products, or is in fully non-conservative (quasi-linear form),*i.e.*

$$\partial_t\boldsymbol{u} + \boldsymbol{A}^i\partial_j\boldsymbol{u} = \boldsymbol{s}(\boldsymbol{u})\,. \tag{3.63}$$

In this case, the main risk is that, if the equations are genuinely non-linear (as opposed to linearly degenerate) and the solution develops a discontinuity, the numerical method will converge to a non-entropy (and thus unphysical) solution. The path-conservative formulation guarantees that this won't happen.

In this section we review the path-conservative ADER-DG schemes, that are be used to obtain the results of chapter 4. The ADER scheme is a framework to obtain a high order time discretization of the system through the use of a predictor-corrector approach, resulting in a fully discrete scheme.

Basic ADER-DG scheme

The derivation of the path conservative ADER-DG method proceeds similarly as the one of the previous section. The equations (3.63) are multiplied by a test function $\Phi_k \in \mathcal{U}$, also in this case identical to the spatial basis functions of equation (3.59). We integrate over the spacetime element $\Omega_i \times [t^n; t^{n+1}]$ (integrating in both space and time rather than simply in space) and obtain

$$\int_{t^n}^{t^{n+1}}\int_{\Omega_i}\Phi_k\frac{\partial\boldsymbol{u}}{\partial t}\mathrm{d}\boldsymbol{x}\mathrm{d}t + \int_{t^n}^{t^{n+1}}\int_{\Omega_i}\Phi_k\left(\boldsymbol{A}(\boldsymbol{u})\cdot\nabla\boldsymbol{u}\right)\mathrm{d}\boldsymbol{x}\mathrm{d}t = \int_{t^n}^{t^{n+1}}\int_{\Omega_i}\Phi_k\boldsymbol{s}(\boldsymbol{u})\mathrm{d}\boldsymbol{x}\mathrm{d}t\,, \tag{3.64}$$

where for brevity $\boldsymbol{A} := \boldsymbol{A} \cdot \boldsymbol{n}$. Again the resulting jump terms have to be taken properly into account, since the solution is discontinuous across element interfaces.

This is achieved with the aid of the path-conservative approach, initially developed by Castro et al. (2006); Pares (2006) in the FV framework and subsequently extended to the DG framework in Rhebergen et al. (2008); Dumbser et al. (2009, 2010). In the ADER-DG framework, higher order in time is achieved with the use of an element-local space-time predictor, denoted by $\boldsymbol{q}(\boldsymbol{x},t)$, and which will be discussed later (as opposed to using a standard time-stepping algorithm, such as *e.g.* a Runge-Kutta scheme, resulting in a RKDG method). Starting from (3.59), one integrates the first term in time by parts and makes use of the local predictor solution $\boldsymbol{q}$ instead of $\boldsymbol{u}$. This leads to the weak formulation (3.64) to be rewritten as

$$\left(\int_{\Omega_i} \Phi_k \Phi_l \mathrm{d}\boldsymbol{x} \right) \left(\hat{\boldsymbol{u}}_{i,l}^{n+1} - \hat{\boldsymbol{u}}_{i,l}^{n} \right) + \int_{t^n}^{t^{n+1}} \int_{\Omega_i^\circ} \Phi_k \left(\boldsymbol{A}(\boldsymbol{q}) \cdot \nabla \boldsymbol{q} \right) \mathrm{d}\boldsymbol{x}\mathrm{d}t + \int_{t^n}^{t^{n+1}} \int_{\partial\Omega_i} \Phi_k \mathcal{D}^- \left(\boldsymbol{q}^-, \boldsymbol{q}^+ \right) \cdot \boldsymbol{n} \mathrm{d}S\mathrm{d}t = \int_{t^n}^{t^{n+1}} \int_{\Omega_i} \Phi_k \boldsymbol{s}(\boldsymbol{q}) \mathrm{d}\boldsymbol{x}\mathrm{d}t \,. \tag{3.65}$$

The jump terms are defined via a path-integral in phase space between the boundary states at the left $\boldsymbol{q}^-$ and at the right $\boldsymbol{q}^+$ of the interface as follows (see also (Dumbser and Toro, 2011)):

$$\mathcal{D}^- \left(\boldsymbol{q}^-, \boldsymbol{q}^+ \right) \cdot \boldsymbol{n} = \frac{1}{2} \left(\int_0^1 \boldsymbol{A}(\boldsymbol{\psi}) \cdot \boldsymbol{n} \mathrm{d}s \right) \left(\boldsymbol{q}^+ - \boldsymbol{q}^- \right) - \frac{1}{2} \boldsymbol{\Theta} \left(\boldsymbol{q}^+ - \boldsymbol{q}^- \right) , \tag{3.66}$$

with $\boldsymbol{A} \cdot \boldsymbol{n} = \boldsymbol{A_1} n_1 + \boldsymbol{A_2} n_2 + \boldsymbol{A_3} n_3$ the system matrix in normal direction and where we have used the simple segment path

$$\boldsymbol{\psi} = \boldsymbol{\psi}(\boldsymbol{q}^-, \boldsymbol{q}^+, s) = \boldsymbol{q}^- + s \left(\boldsymbol{q}^+ - \boldsymbol{q}^- \right) , \qquad 0 \leq s \leq 1 \,. \tag{3.67}$$

Note that in principle the integration path should belong to the family of paths connecting the two states $\boldsymbol{q}^-$ and $\boldsymbol{q}^+$ in phase space that define a weak solution of the non-conservative system of equations (3.63). In practice constructing such a path can be extremely difficult and expensive. Therefore the choice of a simple segment path is preferred, since it turns out to be adequate in most cases.

The last building block of the scheme, appearing in equation (3.66), is an appropriate numerical viscosity matrix $\boldsymbol{\Theta}0$. Following Dumbser et al. (2009, 2010); Dumbser and Toro (2011), the path integral appearing in (3.66) can simply be computed via a Gauss-Legendre quadrature formula of sufficient order of accuracy. In the results of chapter 4 we used one to three Gaussian quadrature points. For a simple path-conservative Rusanov-type method (Dumbser et al., 2009; Castro et al., 2010), the viscosity matrix reads:

$$\boldsymbol{\Theta}_{\text{Rus}} = s_{\max} \boldsymbol{I}, \qquad \text{with} \qquad s_{\max} = \max \left(\left| \Lambda(\boldsymbol{q}_h^-) \right| , \left| \Lambda(\boldsymbol{q}_h^+) \right| \right) , \tag{3.68}$$

where $s_{\max}$ is the maximum propagation speed at the elements' interface and $\boldsymbol{I}$ is the identity matrix.

Space-time predictor

The element-local space-time predictor $\boldsymbol{q}(\boldsymbol{x},t)$ allows the solution to be evolved in time with a high order method. It is computed from the solution $\boldsymbol{u}(\boldsymbol{x},t^n)$ at time t^n using a solution of the equations obtained *"in the small"*, that is to say independently in each element, without considering the interaction with the neighbors. In the ENO scheme of Harten et al. (1987), and in the original ADER approach of Titarev and Toro (2002, 2005); Toro and Titarev (2006), to obtain high accuracy in the time evolution the so-called Cauchy-Kovalewski procedure was used. This is very cumbersome as it is based on analytically computing a local Taylor series expansions in space and time of the equations, where time derivatives are replaced by the (known) space derivatives at time t^n by successively differentiating the PDE system with respect to space and time. See an example of the Cauchy-Kovalewski procedure applied to the Euler equations of compressible gas dynamics in Dumbser et al. (2007). It is however obvious that a highly complex PDE system (*e.g.* the FO-CCZ4 formulation of section 4.4.2) is not amenable to such an approach, which heavily relies on analytical manipulations of the PDE system. Therefore an alternative procedure has been developed in the form of a local space-time DG predictor (Dumbser et al., 2008; Dumbser and Zanotti, 2009; Dumbser et al., 2009), which only requires the pointwise computation of source terms and non-conservative products. The predictor solution $\boldsymbol{q}$ is again expanded into a local space-time basis

$$\boldsymbol{q}(\boldsymbol{x},t) = \sum_l \theta_l(\boldsymbol{x},t)\hat{\boldsymbol{q}}_{i,l} := \theta_l(\boldsymbol{x},t)\hat{\boldsymbol{q}}_{i,l}\,, \tag{3.69}$$

with the multi-index $l = (l_0, l_1, l_2, l_3)$ (the additional index l_0 being the time index). The space-time basis functions $\theta_l(\boldsymbol{x},t) = \varphi_{l_0}(\tau)\varphi_{l_1}(\xi)\varphi_{l_2}(\eta)\varphi_{l_3}(\zeta)$ are again generated from the same one-dimensional nodal basis functions $\varphi_k(\xi)$ as before. The spatial mapping $\boldsymbol{x} = \boldsymbol{x}(\boldsymbol{\xi})$ is also the same as before and the coordinate time is mapped to the reference time $\tau \in [0,1]$ via $t = t^n + \tau\Delta t$. Multiplication of the PDE system (3.63) with a test function θ_k and integration over $\Omega_i \times [t^n, t^{n+1}]$ yields the following weak form in space and time, which is different from (3.64), since now the test and basis functions are also time-dependent:

$$\int_{t^n}^{t^{n+1}} \int_{\Omega_i} \theta_k(\boldsymbol{x},t)\frac{\partial \boldsymbol{q}}{\partial t}\mathrm{d}\boldsymbol{x}\mathrm{d}t + \int_{t^n}^{t^{n+1}} \int_{\Omega_i} \theta_k(\boldsymbol{x},t)\left(\boldsymbol{A}(\boldsymbol{q})\cdot\nabla\boldsymbol{q}\right)\mathrm{d}\boldsymbol{x}\mathrm{d}t = \int_{t^n}^{t^{n+1}} \int_{\Omega_i} \theta_k(\boldsymbol{x},t)\boldsymbol{s}(\boldsymbol{q})\mathrm{d}\boldsymbol{x}\mathrm{d}t\,. \tag{3.70}$$

Since we are now interested in a purely local predictor solution, we do not account for the jumps in the solution, simply discarding the corresponding terms. This will be taken care of later in the final corrector step of the ADER-DG scheme (3.65). We have however to introduce the known discrete solution $\boldsymbol{u}(\boldsymbol{x},t^n)$ at time t^n. To this end, the first term can be integrated by parts in time

leading to

$$\int_{\Omega_i} \theta_k(\boldsymbol{x}, t^{n+1}) \boldsymbol{q}(\boldsymbol{x}, t^{n+1}) \mathrm{d}\boldsymbol{x} - \int_{\Omega_i} \theta_k(\boldsymbol{x}, t^{n}) \boldsymbol{u}(\boldsymbol{x}, t^{n}) \mathrm{d}\boldsymbol{x}$$
$$- \int_{t^n}^{t^{n+1}} \int_{\Omega_i} \frac{\partial}{\partial t} \theta_k(\boldsymbol{x}, t) \boldsymbol{q}(\boldsymbol{x}, t) \mathrm{d}\boldsymbol{x}\mathrm{d}t = \int_{t^n}^{t^{n+1}} \int_{\Omega_i} \theta_k(\boldsymbol{x}, t) \boldsymbol{s}(\boldsymbol{q}) \mathrm{d}\boldsymbol{x}\mathrm{d}t$$
$$- \int_{t^n}^{t^{n+1}} \int_{\Omega_i} \theta_k(\boldsymbol{x}, t) \left(\boldsymbol{A}(\boldsymbol{q}) \cdot \nabla \boldsymbol{q} \right) \mathrm{d}\boldsymbol{x}\mathrm{d}t \,. \tag{3.71}$$

Upon inserting the ansatz (3.69), this equation becomes an element-local nonlinear system for the unknown degrees of freedom $\hat{\boldsymbol{q}}_{i,l}$ of the polynomials $\boldsymbol{q}_h$. The solution to equations (3.71) can be computed easily via a fixed-point iteration method, which is simple and fast converging (see *e.g.* in Dumbser et al. (2009); Toro et al. (2009); Dumbser et al. (2014)).

ADER-WENO finite-volume subcell limiter

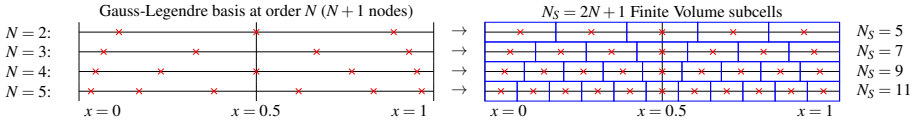

Figure 3.4: *Left*: Node locations in the reference 1D cell of the a DG scheme with Gauss-Lagrange dsegrees of freedom. The coordinate $x \in \{0, 1\}$ covers the computational cell holding N degrees of freedom, where $N+1$ is the order of the method. *Right*: The finite volume subcell structure for the ADER-WENO subcell limiter. Each cell is divided in a grid of $2N+1$ subcells. *Figure reproduced from Dumbser et al. (2017).*

The ADER-DG scheme as presented in the previous sections is unlimited, in the sense that no explicit mechanism is introduced to regularize the solution should a discontinuity occur. The use of this scheme is therefore justified for smooth solutions. If however discontinuities or singularities appear this can lead to numerical instabilities or even to a failure of the computation. Following the ideas outlined in Dumbser et al. (2014); Zanotti et al. (2015b,a), the scheme can be supplemented with a high-order ADER-WENO subcell finite-volume limiter. This is at the same much more robust than the pure, unlimited DG scheme, but still high-order accurate in both space and time.

The a posteriori limiting strategy is described in Dumbser et al. (2014); Zanotti et al. (2015b,a). Each element Ω_i that has been marked for limiting is split into $(2N+1)^3$ finite-volume subcells (denoted by $\Omega_{i,s}$) and satisfying $\Omega_i = \bigcup_s \Omega_{i,s}$ (see figure 3.4). Despite this very fine division of a DG element the time-step of the overall ADER-DG scheme is not reduced. This is because the CFL coefficient of the DG scheme scales as $1/(2N+1)$, while the CFL of the FV scheme is of order unity. The solution in the subcells $\Omega_{i,s}$ is represented at

time t^n by piecewise constant subcell averages $\bar{\boldsymbol{u}}_{i,s}^n$, *i.e.*

$$\bar{\boldsymbol{u}}_{i,s}^n := \frac{1}{|\Omega_{i,s}|} \int_{\Omega_{i,s}} \boldsymbol{u}(\boldsymbol{x}, t^n) \mathrm{d}\boldsymbol{x} \,. \tag{3.72}$$

These subcell averages are then evolved in time with a third-order ADER-WENO finite-volume scheme that looks very similar to the ADER-DG scheme (3.65), namely

$$\left(\bar{\boldsymbol{u}}_{i,s}^{n+1} - \bar{\boldsymbol{u}}_{i,s}^n\right) + \int_{t^n}^{t^{n+1}} \int_{\Omega_{i,s}^\circ} \left(\boldsymbol{A}(\boldsymbol{q}) \cdot \nabla \boldsymbol{q}\right) \mathrm{d}\boldsymbol{x}\mathrm{d}t + \int_{t^n}^{t^{n+1}} \int_{\partial\Omega_{i,s}} \mathcal{D}^- \left(\boldsymbol{q}^-, \boldsymbol{q}^+\right) \cdot \boldsymbol{n} \mathrm{d}S\mathrm{d}t$$
$$= \int_{t^n}^{t^{n+1}} \int_{\Omega_{i,s}} \boldsymbol{s}(\boldsymbol{q}_h) \mathrm{d}\boldsymbol{x}\mathrm{d}t \,. \tag{3.73}$$

In this equation again a predictor solution $\boldsymbol{q}$ is employed, computed from an initial condition given by a WENO (Jiang and Shu, 1996) reconstruction polynomial $\boldsymbol{w}(\boldsymbol{x}, t^n)$, itself computed from the cell averages $\bar{\boldsymbol{u}}_{i,s}^n$ via a multi-dimensional WENO reconstruction operator detailed in Dumbser and Kaeser (2007); Dumbser et al. (2013). The inner cell interface values $\hat{\boldsymbol{q}}_h^-$ are computed by taking the value of the neighbouring subcell, *i.e.* by 0-th order extrapolation.

So for each subcell $\Omega_{i,s}$ several reconstruction polynomials $\boldsymbol{w}^k(\boldsymbol{x}, t^n)$ are computed, by requiring integral conservation of $\boldsymbol{w}^k$ on a set of different stencils $\mathcal{S}_{i,s}^k$, *i.e.*

$$\frac{1}{|\Omega_{i,j}|} \int_{\Omega_{i,j}} \boldsymbol{w}_h^k(\boldsymbol{x}, t^n) \mathrm{d}\boldsymbol{x} = \bar{\boldsymbol{u}}_{i,j}^n \qquad \forall\, \Omega_{i,j} \in \mathcal{S}_{i,s}^k \,. \tag{3.74}$$

This system is solved via a constrained least-squares algorithm requiring at least exact conservation in the cell $\Omega_{i,s}$ itself (see Dumbser and Kaeser (2007) for details). The final WENO reconstruction polynomial $\boldsymbol{w}$ is then obtained by using a classical nonlinear weighted combination of the polynomials $\boldsymbol{w}^k$ (Jiang and Shu, 1996; Dumbser and Kaeser, 2007) as follows:

$$\boldsymbol{w}(\boldsymbol{x}, t^n) = \sum_k \omega_k \boldsymbol{w}^k(\boldsymbol{x}, t^n), \quad \text{with} \quad \omega_k = \frac{\tilde{\omega}_k}{\sum_l \tilde{\omega}_l} \quad \text{and} \quad \tilde{\omega}_k = \frac{\lambda_k}{(\sigma_k + \epsilon)^r} \,, \tag{3.75}$$

with

$$\omega_k := \frac{\tilde{\omega}_k}{\sum_l \tilde{\omega}_l} \quad \text{and} \quad \tilde{\omega}_k := \frac{\lambda_k}{(\sigma_k + \epsilon)^r} \,, \tag{3.76}$$

and where the oscillation indicators σ_k are computed as usual from

$$\sigma_k := \sum_{l \geq 1} \int_{\Omega_{i,s}} \Delta\boldsymbol{x}_{i,s}^{2l-1} \left(\frac{\partial^l}{\partial \boldsymbol{x}^l} \boldsymbol{w}^k(\boldsymbol{x}, t^n) \right)^2 \mathrm{d}\boldsymbol{x} \,. \tag{3.77}$$

The parameter ϵ in (3.76) is only needed to avoid division by zero. In the results of chapter 4 it is set to $\epsilon = 10^{-14}$ and the exponent in the denominator

is chosen as $r = 8$. The linear weights are chosen as $\lambda_1 = 10^5$ for the central stencil (*i.e.* $k = 1$), while all other stencils (*i.e.* $k > 1$) have linear weight $\lambda_k = 1$. This choice corresponds also to the one made in Dumbser and Kaeser (2007).

It is very convenient to write the WENO reconstruction polynomials in terms of a basis of functions $\psi_l(\boldsymbol{x})$ as $\boldsymbol{w}(\boldsymbol{x}, t^n) = \Psi_l(\boldsymbol{x})\hat{\boldsymbol{w}}_l^n$. In this work, following Dumbser et al. (2013), the basis functions Ψ_l are defined exactly as the Φ_l, *i.e.* as tensor products of Lagrange interpolation polynomials through the Gauss-Legendre quadrature nodes. For the WENO limiter, we only used a piecewise quadratic reconstruction, which leads to a nominally third-order accurate scheme. As already mentioned before, the predictor is computed according to (3.71), where the initial data $\boldsymbol{u}(\boldsymbol{x}, t^n)$ is replaced by $\boldsymbol{w}(\boldsymbol{x}, t^n)$ and the spatial control volumes Ω_i are replaced by the subcells $\Omega_{i,s}$.

Once all subcell averages $\bar{\boldsymbol{u}}_{i,s}^{n+1}$ inside an element Ω_i have been computed, the limited DG polynomial $\boldsymbol{u}'(\boldsymbol{x}, t^{n+1})$ at the next time level is obtained again via a classical constrained least squares reconstruction procedure requiring

$$\frac{1}{|\Omega_{i,s}|} \int_{\Omega_{i,s}} \boldsymbol{u}'(\boldsymbol{x}, t^{n+1}) \mathrm{d}\boldsymbol{x} = \bar{\boldsymbol{u}}_{i,s}^{n+1} \quad \forall \Omega_{i,s} \in \Omega_i \,, \tag{3.78}$$

$$\int_{\Omega_i} \boldsymbol{u}'(\boldsymbol{x}, t^{n+1}) \mathrm{d}\boldsymbol{x} = \sum_{\Omega_{i,s} \in \Omega_i} |\Omega_{i,s}| \bar{\boldsymbol{u}}_{i,s}^{n+1} \,, \tag{3.79}$$

and

$$\int_{\Omega_i} \boldsymbol{u}'(\boldsymbol{x}, t^{n+1}) \mathrm{d}\boldsymbol{x} = \sum_{\Omega_{i,s} \in \Omega_i} |\Omega_{i,s}| \bar{\boldsymbol{u}}_{i,s}^{n+1} \,, \tag{3.80}$$

where (3.80) is a constraint and imposes conservation at the level of the element Ω_i.

Part II

Hyperbolic formulations of Einstein equations

Chapter 4

The FO-CCZ4 formulation

This chapter is devoted to the presentation of a novel first order, strongly hyperbolic formulation of Einstein equations. General relativistic simulations require (among many other issues that have to be addressed) stable and accurate methods for evolving the spacetime, *i.e.* for solving the Einstein field equations. The development of hyperbolic formulations of the Einstein equations that allow for long term simulations of generic spacetimes, including the ones encompassing the physical singularities arising in the presence of BHs, has been therefore of great importance in the field of numerical relativity.

The first step in this direction has been the 3+1 (space + time) ADM formulation presented in section 2.4 (Arnowitt et al., 1962). While this formulation splits time and space and naturally presents general relativity as an initial boundary value problem (IBVP), suitable for numerical implementation, it is known to be not hyperbolic[1], and therefore unstable in numerical applications.

Subsequently, a lot of effort has been devoted to find hyperbolic formulations of the Einstein equations. A breakthrough has been the BSSNOK (Baumgarte-Shapiro-Shibata-Nakamura-Oohara-Kojima) formulation (Shibata and Nakamura, 1995; Baumgarte and Shapiro, 1999; Nakamura et al., 1987; Brown, 2009), which achieves hyperbolicity via a conformal transformation of the 3-metric and the promotion of some contractions of the Christoffel symbols to independently evolved variables and, most importantly, by inserting the momentum and Hamiltonian constraint expressions into the evolution system. A general-covariant alternative is the Z4 formulation of Bona et al. (2003, 2004); Alic et al. (2009), which has been presented both in first- and second-order form in the spatial derivatives. More successful have been formulations based on the Z4 one that include a conformal transformation of the metric and write the system in a form close to the BSSNOK one, namely Z4c (Bernuzzi and Hilditch, 2010) and CCZ4 (Alic et al., 2012, 2013) (see also Sanchis-Gual et al. (2014); Bezares et al. (2017)for some recent and slight variants). The Z4 family of formulations also admits mechanisms to damp constraint violations as they arise during the evolution Gundlach et al. (2005); Weyhausen et al. (2012); Alic et al. (2012, 2013).

The formulation presented here is a first order version of the CCZ4 one, and it was therefore named FO-CCZ4 and presented in Dumbser, Guercilena,

[1] at least when usual gauge choices are considered. See Sarbach and Tiglio (2012) for a discussion.

Koeppel, Rezzolla, and Zanotti (2017). It includes the constraint violation suppression mechanism of CCZ4, but it has been engineered in such a way that it was possible to prove, at least for a selected gauge choice, that it is strongly hyperbolic (and therefore well suited for numerical applications) and that all characteristics fields are linearly degenerate (which implies that no shocks can be produced by these equations). Finally, being first order in space and time makes it ideal for discretization with a DG scheme, which has been in fact the choice for all tests presented here.

This chapter is structured as follows: in section 4.1 the concept of a hyperbolic system of equations is reviewed; in section 4.2 the BSSNOK formulation, which introduced many of the ideas used in FO-CCZ4, is presented; section 4.3 describes the Z4 family of formulations, in particular CCZ4 on which FO-CCZ4 is based; finally section 4.4.2 presents the FO-CCZ4 system and the results of numerical tests performed with it.

4.1 The notion of hyperbolicity

A first order system of partial differential differential equations can be written the quasilinear form

$$\partial_t \boldsymbol{U} + \boldsymbol{A}^i(\boldsymbol{U})\partial_i \boldsymbol{U} = 0\,, \tag{4.1}$$

where possible source terms on the right hand side have been set to zero for simplicity, since they play no role in determining its hyperbolicity. The sum over the repeated index i runs over the number n of spatial dimensions of the problem. The matrices $\boldsymbol{A}^i$ (sometimes called the velocity matrices) are square matrices of dimensions $n \times n$, and can depend on the vector of unknowns $\boldsymbol{U}$, but not on its derivatives. If they are independent on $\boldsymbol{U}$ then the system is indeed linear.

Consider the contraction of $\boldsymbol{A}^i$ with the unit vector $\boldsymbol{n}_i$ associated with any direction in space:

$$\boldsymbol{A} = \boldsymbol{A}^i \boldsymbol{n}_i\,. \tag{4.2}$$

Then we have the following definitions:

- if $\boldsymbol{A}$ has real eigenvalues, the system (4.1) is *hyperbolic*;
- if $\boldsymbol{A}$ has real eigenvalues and a complete set of eigenvectors the system (4.1) is *strongly hyperbolic*;
- if $\boldsymbol{A}$ has real eigenvalues but not a complete set of eigenvectors, the system (4.1) is *weakly hyperbolic*;
- if the eigenvalues of $\boldsymbol{A}$ are real and distinct, the system (4.1) is *strictly hyperbolic* (which implies it is strongly hyperbolic);
- if $\boldsymbol{A}$ is symmetric or can be made so, the system (4.1) is *symmetric hyperbolic* (which again implies it is strongly hyperbolic).

A system being hyperbolic simply means that perturbation in the unknown fields propagate with finite speed. This is a requirement for modern physical theories, but it not enough to imply the system is well behaved: this requires

strong hyperbolicity. In particular in can be shown, *e.g.* Kreiss and Lorenz (1989), that if the system is strongly hyperbolic, then:

$$||\boldsymbol{U}(t,\boldsymbol{x})|| \leq ke^{at}||\boldsymbol{U}(0,\boldsymbol{x})|| \qquad \forall t>0\,, \tag{4.3}$$

for some constants k and a, and any initial data $\boldsymbol{U}(0,\boldsymbol{x})$. Equation (4.3) states that the norm of the solution at any time cannot grow faster than exponentially with respect the norm at the initial time. This is a requirement (along with existence of the solution and its unicity) for the system to be *well-posed*. Clearly this is a very desirable property in practical applications, because it guarantees that no variable in the computation grows without bounds, crashing the calculation.

Note that the Valencia formulation of the relativistic Euler equations presented in section 2.5 is strongly hyperbolic. Focusing for simplicity of the x direction, its eigenvalues are

$$\begin{aligned}\lambda_0 &= \alpha v^x - \beta^x \\ \lambda_\pm &= \frac{\alpha}{1-v^2c_s^2}\left\{v^x(1-c_s^2) \pm c_s\sqrt{(1-v^2[\gamma^{xx}(1-v^2c_s^2)-v^xv^x(1-c_s^2)])}\right\} - \beta^x\,,\end{aligned} \tag{4.4}$$

where c_s is the local speed of sound $c_s = \sqrt{\frac{\partial p}{\partial e}}$. The eigenvalues are not distinct, the first one is degenerate with triple multiplicity, so the system is not strictly hyperbolic. There is however a complete set of five eigenvectors (their explicit expressions can be found in *e.g.* Rezzolla and Zanotti (2013)), which proves the system is strongly hyperbolic.

In contrast the ADM system of section 2.4 is only weakly hyperbolic (see *e.g.* Kidder et al. (2001)), and this can result in the appearance of unbounded growing modes in the evolution of a given spacetime. This behaviour has indeed been observed in many applications and tests (*e.g.* Alcubierre et al. (2004a)), and renders the ADM formulation unsuitable for numerical implementation. In the following sections it will be detailed how these shortcomings can be overcome and a strongly hyperbolic formulation of Einstein equations defined.

4.2 The BSSNOK formulation

As anticipated in the previous section, the BSSNOK system is based on three building blocks: a conformal transformation of the metric; the promotion of the connection coefficients to independently evolved variables; and the addition of the constraints expressions to some of the evolution equations. The first two ideas give rise to the following definitions for the evolved fields

$$\phi := \frac{1}{12}\ln(\gamma) \tag{4.5a}$$

$$K := \gamma^{ij}K_{ij} \tag{4.5b}$$

$$\tilde{\gamma}_{ij} := e^{-4\phi}\gamma_{ij} \tag{4.5c}$$

$$\tilde{A}_{ij} := e^{-4\phi}\left(K_{ij} - \frac{1}{3}\gamma_{ij}K\right) \tag{4.5d}$$

$$\tilde{\Gamma}^i := \tilde{\gamma}^{jk}\tilde{\Gamma}^i{}_{jk}\,, \tag{4.5e}$$

where $\tilde{\Gamma}^i{}_{jk}$ are the Christoffel symbols computed from the conformal metric $\tilde{\gamma}_{ij}$ and γ is the determinant of the spatial metric γ_{ij}. As can be seen, the 3-metric (which is directly computed in the ADM system) has been replaced by the conformal factor ϕ and the conformal metric $\tilde{\gamma}_{ij}$. The same conformal transformation has been applied to the extrinsic curvature K_{ij}, which has also been split in its trace K and trace-free part $\tilde{A}_{ij}$. The new variable $\tilde{\Gamma}^i$ is a particular contraction of the conformal Christoffel symbols and, as anticipated, is independently evolved. The full BSSNOK equations take then the form (see Brown (2009) for a modern derivation):

$$\partial_\perp \phi = \frac{1}{6}\partial_k \beta^k - \frac{1}{6}\alpha K \tag{4.6a}$$

$$\partial_\perp \tilde{\gamma}_{ij} = -2\alpha \tilde{A}_{ij} - \frac{2}{3}\tilde{\gamma}_{ij}\partial_k \beta^k \tag{4.6b}$$

$$\partial_\perp K = \alpha\left(\tilde{A}_{ij}\tilde{A}^{ij} + \frac{1}{3}K^2\right) - \gamma^{ij}\nabla_i\nabla_j\alpha + 4\pi(S^k{}_k + E) \tag{4.6c}$$

$$\partial_\perp \tilde{A}_{ij} = e^{-4\phi}\left[\alpha(R_{ij} - 8\pi S_{ij}) - \nabla_i\nabla_j\alpha\right]^{\mathrm{TF}} - \frac{2}{3}\tilde{A}_{ij}\partial_k\beta^k + \alpha\left(K\tilde{A}_{ij} - 2\tilde{A}_{ik}\tilde{A}^k{}_j\right) \tag{4.6d}$$

$$\partial_\perp \tilde{\Gamma}^i = \tilde{\gamma}^{kl}\partial_k\partial_l\beta^i + \frac{2}{3}\tilde{\gamma}^{jk}\tilde{\Gamma}^i{}_{jk}\partial_l\beta^l + \frac{1}{3}\tilde{\nabla}^i(\partial_k\beta^k) - 2\tilde{A}^{ik}\partial_k\alpha + 2\alpha\tilde{A}^{kl}\tilde{\Gamma}^i{}_{kl} + 12\alpha\tilde{A}^{ik}\partial_k\phi - \frac{4}{3}\alpha\tilde{\nabla}^i K - 16\pi\alpha\tilde{\gamma}^{ij}S_j \tag{4.6e}$$

$$\partial_\perp \alpha = -2\alpha K \tag{4.6f}$$

$$\partial_t \beta^i = \frac{3}{4}b^i + \beta^k\partial_k\beta^i \tag{4.6g}$$

$$\partial_t b^i = \partial_t\tilde{\Gamma}^i - \eta b^i + \beta^k\partial_k b^i\,, \tag{4.6h}$$

where the operator $\partial_\perp$ stands for $\partial_t - \mathcal{L}_{\boldsymbol{\beta}}$, *i.e.* the derivative with respect to coordinate time minus the Lie derivative along the shift, and the notation $[\dots]^{\mathrm{TF}}$ indicates terms that are made trace free with respect to the conformal metric. The covariant derivatives ∇ and $\tilde{\nabla}$ are constructed from the physical and covariant three metric respectively. For completeness, the gauge evolution equations for the 1+log and Gamma driver conditions (see section 2.4.1) have been included as well, since they are employed in the results presented in chapters 5 and 6.

The three dimensional Ricci tensor R_{ij} is split in two parts, $R_{ij} = \tilde{R}^\phi_{ij} + \tilde{R}_{ij}$, the first involving the conformal factor ϕ and the second the derivatives of the

conformal metric $\tilde{\gamma}_{ij}$:

$$\tilde{R}^{\phi}_{ij} = \phi^{-2}\left[\phi\left(\tilde{\nabla}_i\tilde{\nabla}_j\phi + \tilde{\gamma}_{ij}\tilde{\nabla}^k\tilde{\nabla}_k\phi\right)\right. \tag{4.7a}$$
$$\left. -2\tilde{\gamma}_{ij}\tilde{\nabla}^k\phi\tilde{\nabla}_k\phi\right]$$
$$\tilde{R}_{ij} = -\frac{1}{2}\tilde{\gamma}^{lm}\partial_l\partial_m\tilde{\gamma}_{ij} + \tilde{\gamma}_{k(i}\partial_{j)}\tilde{\Gamma}^k \tag{4.7b}$$
$$+ \tilde{\Gamma}^k\tilde{\Gamma}_{(ij)k} + \tilde{\gamma}^{lm}\left[2\tilde{\Gamma}^k{}_{l(i}\tilde{\Gamma}_{j)km} + \tilde{\Gamma}^k{}_{im}\tilde{\Gamma}_{kjl}\right] .$$

Note that in equations (4.6c) and (4.6e) above the expressions of the Hamiltonian and momentum constraints respectively have been added to the right hand side (see again Brown (2009) for details). Such manipulations are always possible, since the constraints are identically zero for a solution of Einstein equations. Their addition however turned out to be vital to guarantee the hyperbolicity of the system.

In numerically integrating these equations a constrained approach is typically used, *i.e.* the additional constraints $\det(\tilde{\gamma}_{ij}) = 1$ and $\mathrm{tr}(\tilde{A}_{ij}) = 0$ are enforced at every time step in the computation.

The BSSNOK system is first order in time, but second order in space, and therefore it is a priori not clear how to define its hyperbolicity. One possibility is to define auxiliary fields starting from the spatial derivatives of the original evolved fields, and so bring the system in first order, quasilinear form. This has been accomplished by Beyer and Sarbach (2004), which managed to prove that for a large class of slicing conditions (including the standard harmonic and 1+log slicing) and for a prescribed (*i.e.* not evolved) shift the first order BSSNOK system is symmetric hyperbolic. A different definition of hyperbolicity, which applies to second order systems, has been exploited to prove that the original, second order BSSNOK system is indeed strongly hyperbolic also for generic shift conditions (see again Beyer and Sarbach (2004)). This explains the remarkable success of this formulation in practical applications, which not only behaves as desired in tests (*e.g.* Alcubierre et al. (2004a)), but is routinely employed in realistic simulations by a number of groups around the world.

4.3 The Z4 family of formulations

The Z4 has been introduced initially in Bona et al. (2003) to get a fully covariant formulation of Einstein equations which also provides a consistent way of treating terms proportional to the constraints in the evolution equations. The starting point is to introduce an additional auxiliary field, the 4-vector Z_μ, in the Einstein equations, so that they take the form:

$$R_{\mu\nu} + 2\nabla_{(\mu}Z_{\mu)} = 8\pi(T_{\mu\nu} - \frac{1}{2}Tg_{\mu\nu}) . \tag{4.8}$$

When the condition $Z_\mu = 0$ is satisfied, solutions to equations (4.8) are the same as solutions of the original equations (2.10). Note that these equations, as well as the Z4 system that results from them, can also be derived from an action principle (Bona et al., 2010).

Applying the 3+1 split to these equations as described in section 2.4, results in the following system of equations:

$$\begin{aligned}
\partial_\perp \gamma_{ij} &= -2\alpha K_{ij} && \text{(4.9a)}\\
\partial_\perp K_{ij} &= -\nabla_i\nabla_j\alpha + \alpha\left[R_{ij} - 2K_{ik}K^k{}_j + (K-2\Theta)K_{ij}\right] && \text{(4.9b)}\\
&\quad - 8\pi\alpha\left[S_{ij} - \frac{1}{2}\gamma_{ij}(S-E)\right]\\
\partial_\perp \Theta &= \frac{\alpha}{2}\Big[R + 2\nabla_k Z^k + (K-2\Theta)K - K_{ij}K^{ij}\\
&\quad - \frac{2}{\alpha}Z_k\nabla_k\alpha - 16\pi E\Big] && \text{(4.9c)}\\
\partial_\perp Z_i &= \alpha\Big[\nabla_j(K_i{}^j - \delta_i{}^j K) + \partial_i\Theta - 2K_i{}^j Z_j\\
&\quad - \frac{1}{\alpha}\Theta\nabla_i\alpha - 8\pi S_i\Big]\,, && \text{(4.9d)}
\end{aligned}$$

where $\Theta = n_\mu Z^\mu = \alpha Z^0$. The evolution equation for the extrinsic curvature almost identical to the original ADM one (2.33), while the evolution equations for the components of the Z_μ vector replace the Hamiltonian and momentum constraint equations. Note that they are indeed evolution equations, not elliptic ones. However by imposing the conditions $Z_\mu = \partial_t Z_\mu = 0$ on the initial slice, these two equations reduce to the usual constraint equations (Bona et al., 2003). This means that initial data for the Z4 system can be constructed as usual by solving the constraint equations on the initial slice, plus the initial value $Z_i = \Theta = 0$ for the auxiliary fields. Evolution with the system (4.9) will preserve these constraint.

Starting from the Z4 system, a number of other formulations of Einstein equations can be recovered, including the BSSNOK one and the KST one (Kidder et al., 2001). The hyperbolicity of the system has been studied in Bona et al. (2004) for a family of slicing conditions (including generalized versions of the harmonic and 1+log slicing) and zero shift, and was proven to be strongly hyperbolic. A first order version of the system, first considered in Bona et al. (2004) and then in more detail in Alic et al. (2009) where it was cast in flux-conservative form, was also found to be strongly hyperbolic.

Despite these encouraging results neither the second order version of the Z4 system nor the first order one have been applied to realistic simulations. The main drawback has been the inability to identify a suitable replacement of the Gamma driver shift conditions with the same horizon freezing properties: tests involving BH spacetimes and different shift prescription have resulted in a growth of the horizon radius (see Alic et al. (2009)).

To address this difficulty, conformal formulations of the Z4 system have been developed, in which the usual gauge conditions can be applied unmodified and used to obtain long-term stable evolutions as for the BSSNOK formulation. These systems, namely the Z4c one and the CCZ4 one, are the subject of the next two sections.

4.3.1 The Z4c formulation

The Z4c is a non-covariant, conformal formulation of the Einstein equations based on the second order Z4 one, written in such a way to be as close as possible to BSSNOK, initially developed by Bernuzzi and Hilditch (2010). Its derivation starts from the following form of the Einstein equations:

$$R_{\mu\nu} + 2\nabla_{(\mu} Z_{\mu)} = 8\pi(T_{\mu\nu} - \frac{1}{2} T g_{\mu\nu}) + \kappa_1 \left[2 n_{(\mu} Z_{\nu)} - (1+\kappa_2) g_{\mu\nu} n_\tau Z^\tau \right] . \quad (4.10)$$

In equation (4.10) the additional terms on the right hand side, absent in (4.8), are damping terms which drive to zero the growth of constraint violations (κ_1 and κ_2 being tunable damping constants). In applying the 3+1 approach to these equations, Bernuzzi and Hilditch (2010) chose to discard non-principal, non-damping terms, which breaks the covariance of the system, but allows to write the final form of the equations in a form which is very similar to the BSSNOK one (in the interest of brevity we do not report the full form of the equations here). The resulting system was proven to be strongly hyperbolic for the usual 1+log and Gamma driver gauge choices.

The Z4c formulation was extensively tested, in standard testbeds scenarios as well as in realistic BH and NS simulations, including compact binaries (Bernuzzi and Hilditch, 2010; Hilditch et al., 2013). In each case it was shown to be superior to BSSNOK, leading to very similar results, but with much lower levels of constraint violations. In the case of compact binaries, the system also allows for the extraction of more accurate waveforms, reducing both the dephasing and the amplitude variation in simulations performed at different resolutions. In a further development constraint-preserving outgoing boundary conditions have been found for the Z4c system (Ruiz et al., 2011), while they are not available for BSSNOK. Due to these desirable properties, Z4c has been employed in a host of different simulations of compact binaries, see *e.g.* Dietrich et al. (2015); Bernuzzi and Dietrich (2016); Dietrich et al. (2017a).

However successful, the Z4c system suffers from the drawback of being non-covariant. The CCZ4 system was initially developed precisely to address this issue.

4.3.2 The CCZ4 formulation

The CCZ4 (conformal and covariant Z4) system was developed by Alic et al. (2012), starting from the Z4 form of the Einstein equations with damping terms, *i.e.* equations (4.10). Casting the equations in the 3+1 form, one obtains the

system

$$\partial_\perp \gamma_{ij} = -2\alpha K_{ij} \tag{4.11a}$$

$$\partial_\perp K_{ij} = -\nabla_i \nabla_j \alpha + \alpha \left[R_{ij} - 2K_{ik}K^k{}_j + (K - 2\Theta)K_{ij} - \kappa_1(1+\kappa_2)\Theta\gamma_{ij} \right] - 8\pi\alpha \left[S_{ij} - \frac{1}{2}\gamma_{ij}(S-E) \right] \tag{4.11b}$$

$$\partial_\perp \Theta = \frac{\alpha}{2} \left[R + 2\nabla_k Z^k + (K - 2\Theta)K - K_{ij}K^{ij} - \frac{2}{\alpha} Z_k \nabla_k \alpha - 2\kappa_1(2+\kappa_2)\Theta - 16\pi E \right] \tag{4.11c}$$

$$\partial_\perp Z_i = \alpha \left[\nabla_j (K_i{}^j - \delta_i{}^j K) + \partial_i \Theta - 2K_i{}^j Z_j - \frac{1}{\alpha}\Theta\nabla_i\alpha - \kappa_1 Z_i - 8\pi S_i \right] , \tag{4.11d}$$

analogous to the (4.9) one, but including the constraint-damping terms. In contrast to Bernuzzi and Hilditch (2010), Alic et al. (2012) did not discard any terms in equations (4.11), obtaining a fully covariant formulation.

A conformal transformation is then applied to the evolution variables, in a fashion similar but slightly different from the BSSNOK case (4.5):

$$\phi := \gamma^{-\frac{1}{6}} \tag{4.12a}$$

$$K := \gamma^{ij} K_{ij} \tag{4.12b}$$

$$\tilde{\gamma}_{ij} := \phi^2 \gamma_{ij} \tag{4.12c}$$

$$\tilde{A}_{ij} := \phi^2 \left(K_{ij} - \frac{1}{3} K \gamma_{ij} \right) \tag{4.12d}$$

$$\tilde{\Gamma}^i := \tilde{\gamma}^{jk} \tilde{\Gamma}^i{}_{jk} \tag{4.12e}$$

$$\hat{\Gamma}^i := \tilde{\Gamma}^i + 2\tilde{\gamma}^{ij} Z_j \tag{4.12f}$$

$$\Theta := \alpha Z^0 . \tag{4.12g}$$

The differences from the BSSNOK variables are a different choice for the conformal factor ϕ; the definition of a new variable $\hat{\Gamma}^i$ which depends on the Z_i for vector and it is evolved instead of $\tilde{\Gamma}^i$; and naturally the inclusion of the Z4 variable Θ.

With this choice of variables, the CCZ4 system can finally be written as:

$$\partial_\perp \tilde{\gamma}_{ij} = -2\alpha \tilde{A}_{ij}^{\mathrm{TF}} - \frac{2}{3}\tilde{\gamma}_{ij}\partial_k \beta^k \tag{4.13a}$$

$$\begin{aligned}\partial_\perp \tilde{A}_{ij} = {} & \phi^2 \left[-\nabla_i \nabla_j \alpha + \alpha \left(R_{ij} + \nabla_i Z_j + \nabla_j Z_i - 8\pi S_{ij}\right)\right]^{\mathrm{TF}} \\ & + \alpha \tilde{A}_{ij}\left(K - 2\Theta\right) - 2\alpha \tilde{A}_{il}\tilde{A}^l_j - \frac{2}{3}\tilde{A}_{ij}\partial_k \beta^k\end{aligned} \tag{4.13b}$$

$$\partial_\perp \phi = \frac{1}{3}\alpha\phi K - \frac{1}{3}\phi \partial_k \beta^k \tag{4.13c}$$

$$\begin{aligned}\partial_\perp K = {} & -\nabla^i \nabla_i \alpha + \alpha\left(R + 2\nabla_i Z^i + K^2 - 2\Theta K\right) \\ & - 3\alpha\kappa_1\left(1+\kappa_2\right)\Theta + 4\pi\alpha\left(S - 3E\right)\end{aligned} \tag{4.13d}$$

$$\begin{aligned}\partial_\perp \Theta = {} & \frac{1}{2}\alpha\left(R + 2\nabla_i Z^i - \tilde{A}_{ij}\tilde{A}^{ij} + \frac{2}{3}K^2 - 2\Theta K\right) \\ & - Z^i \partial_i \alpha - \alpha\kappa_1\left(2+\kappa_2\right)\Theta - 8\pi\alpha E\end{aligned} \tag{4.13e}$$

$$\begin{aligned}\partial_\perp \hat{\Gamma}^i = {} & 2\alpha\left(\tilde{\Gamma}^i_{jk}\tilde{A}^{jk} - 3\tilde{A}^{ij}\frac{\partial_j \phi}{\phi} - \frac{2}{3}\tilde{\gamma}^{ij}\partial_j K\right) \\ & + 2\tilde{\gamma}^{ki}\left(\alpha\partial_k\Theta - \Theta\partial_k\alpha - \frac{2}{3}\alpha K Z_k\right) - 2\tilde{A}^{ij}\partial_j\alpha \\ & + \tilde{\gamma}^{kl}\partial_k\partial_l\beta^i + \frac{1}{3}\tilde{\gamma}^{ik}\partial_k\partial_l\beta^l + \frac{2}{3}\tilde{\Gamma}^i\partial_k\beta^k - \tilde{\Gamma}^k\partial_k\beta^i \\ & + 2\kappa_3\left(\frac{2}{3}\tilde{\gamma}^{ij}Z_j\partial_k\beta^k - \tilde{\gamma}^{jk}Z_j\partial_k\beta^i\right) \\ & - 2\alpha\kappa_1\tilde{\gamma}^{ij}Z_j - 16\pi\alpha\tilde{\gamma}^{ij}S_j\end{aligned} \tag{4.13f}$$

$$\partial_\perp \alpha = -2\alpha\left(K - K_0 - 2\Theta\right) \tag{4.13g}$$

$$\partial_t \beta^i = f b^i + \beta^k \partial_k \beta^i \tag{4.13h}$$

$$\partial_t b^i = \partial_\perp \hat{\Gamma}^i + \beta^k \partial_k b^i - \eta b^i\,, \tag{4.13i}$$

where again the 1+log and Gamma driver conditions have been included as well. In equations (4.13) the Ricci tensor R_{ij} is once again computed as $R_{ij} = \tilde{R}^\phi_{ij} + \tilde{R}_{ij}$, with the two terms defined as in equations (4.7), as for the BSSNOK system. Note that an arbitrary given function K_0 has been added to the slicing condition. This will be exploited in the following sections to enforce some particular behaviour of the lapse in a few test cases. Note also the κ_3 coefficient which has been added in equation (4.13f). This coefficient is not present in the original system (4.11), and has been added to allow for stable evolutions of BH spacetimes as described in the following.

The CCZ4 system has been thoroughly tested in standard testbeds and BH spacetimes (including BBHs) (Alic et al., 2012), as well as in BNS simulations (Alic et al., 2013). In all of the case considered the system allows for better results than the BSSNOK formulation, both concerning the constraint violations and the GW dephasing; and it compares favourably with the Z4c system. One unexpected caveat that has emerged in the use of the CCZ4 formulation in BH spacetimes is the presence of non-linear couplings between the various terms, such that in order to obtain stable evolutions with the value $\kappa_1 \neq 0$, the coefficient κ_3 needs to be set to the value 0.5, breaking the covariance of the system (see Alic et al. (2012)). However in (Alic et al., 2013) a different solution

was found, which enables stable evolutions of BH spacetimes while maintaining spatial covariance of the system (and full covariance of its non-damping terms).

The CCZ4 system has been extensively applied to realistic simulations of compact objects (see *e.g.* Radice et al. (2014b) and the review article by Baiotti and Rezzolla (2017)). To date however no proof of hyperbolicity of the system (in its second order form) is available in the literature.

4.4 The FO-CCZ4 formulation

4.4.1 Introduction

The FO-CCZ4 formulation of the Einstein equations presented here and published in Dumbser, Guercilena, Koeppel, Rezzolla, and Zanotti (2017) has been developed to pursue two main goals: firstly, to formulate a version of the CCZ4 system which is first order in both time and space, and therefore can be readily discretized with DG methods; secondly, to ensure the hyperbolicity of the formulation, a comprehensive analysis of which is still lacking for the CCZ4 formulation.

The need for the second requirement is clear: while in practical terms even a weakly hyperbolic system of equations could lead to a stable numerical integration, only a strongly hyperbolic formulation guarantees stability in every scenario. The CCZ4 system has been applied to realistic simulations in several cases, but the success of these applications does not rest yet on a very strong theoretical foundation.

On the other hand, the requirement of a first order formulation is natural when taking into account the goal of coupling it with a DG discretization. While DG methods can be formulated in such a way to accommodate second order system of equations (see Hesthaven and Warburton (2007) for an introduction; Field et al. (2010) and Miller and Schnetter (2017) for applications to numerical relativity), they are most naturally formulated for first order systems. In fact, DG methods are generally introduced in the context of flux-conservative equations, and as such we initially strove to cast CCZ4 in a first order fully conservative form. It clearly emerged however that a *fully non-conservative* formulation offers many advantages in simplifying the form of the equations and obtain an hyperbolicity proof; moreover, since the path-conservative ADER-DG method (described in section 3.5.1) we employed to discretize FO-CCZ4 can easily handle non-conservative terms in the equations, no workaround was necessary to numerically implement the system either.

The rest of this section is devoted to the description of the FO-CCZ4 system and its properties. Section presents a detailed derivation of the equations; in section 4.4.3 a proof of hyperbolicity is presented; in section 4.4.4 results pertaining to an extensive set of tests, obtained with the path-conservative ADER-DG method, are reported; finally section 4.4.5 summarizes our conclusions.

4.4.2 The FO-CCZ4 system of equations

Reduction to first order: auxiliary variables definition

In order to reduce any system of equations from second to first order form, derivatives of the original variables have to be promoted to new auxiliary variables, which will be then promoted to independently evolved variables. Starting from the original CCZ4 system we introduce the following 33 auxiliary variables, which correspond to first spatial derivatives of the metric terms:

$$A_i \;\; := \partial_i \ln\alpha = \frac{\partial_i \alpha}{\alpha} \tag{4.14a}$$

$$B_k{}^i \;\; := \partial_k \beta^i \tag{4.14b}$$

$$D_{kij} := \frac{1}{2}\partial_k \tilde{\gamma}_{ij} \tag{4.14c}$$

$$P_i \;\; := \partial_i \ln\phi = \frac{\partial_i \phi}{\phi}\,. \tag{4.14d}$$

The following second order ordering constraints (Gundlach and Martin-Garcia, 2006) are an immediate consequence of (4.14) and the symmetry of second-order derivatives (note that the spacetime functions are assumed to be twice continuously differentiable, since the spacetime is described as a differentiable manifold in general relativity):

$$\begin{aligned} \mathcal{A}_{ki} &:= \partial_k A_i - \partial_i A_k = 0\,, & \mathcal{B}^i{}_{kl} &:= \partial_k B_l{}^i - \partial_l B_k{}^i = 0\,, \\ \mathcal{D}_{klij} &:= \partial_k D_{lij} - \partial_l D_{kij} = 0\,, & \mathcal{P}_{ki} &:= \partial_k P_i - \partial_i P_k = 0\,. \end{aligned} \tag{4.15}$$

$\tilde{A}_{ij}$ is by construction trace-free, therefore the following additional constraint holds: $\tilde{\gamma}^{ij}\tilde{A}_{ij} = 0$; and thus

$$\mathcal{T}_k := \partial_k\left(\tilde{\gamma}^{ij}\tilde{A}_{ij}\right) = \partial_k\tilde{\gamma}^{ij}\tilde{A}_{ij} + \tilde{\gamma}^{ij}\partial_k\tilde{A}_{ij} = 0\,. \tag{4.16}$$

These relations will be employed later in order to enforce strong hyperbolicity of the system. The time evolution equations for the auxiliary quantities are obtained by the standard procedure of applying the time derivative operator ∂_t to equations (4.14), exchanging the order of the space and time derivatives on the right-hand side of the resulting equations and making use of the PDEs (4.13a), (4.13c) and the evolution equations for the lapse and shift to eliminate the time derivatives from the left hand side.

In principle many different first-order formulations of the CCZ4 system are possible, since any non purely algebraic term in the original second-order system can be written as a combination of conservative terms and non-conservative products (see (Gundlach and Martin-Garcia, 2006; Hilditch and Richter, 2015) for a parametric study of such families of systems). Two extreme cases are of particular interest: the first being a fully conservative form of the equations, in which all terms are cast in a flux-conservative form (see *e.g.* Alic et al. (2009) as an example for the first-order Z4 system); and a second formulation, fully non-conservative, similar to the ideas outlined in Alcubierre (2008), in which by making maximum use of the first-order ordering constraints the variables defining the 4-metric (α, β^i, ϕ and $\tilde{\gamma}_{ij}$) are evolved simply by a nonlinear

system of ordinary differential equations (ODEs) and the rest of the dynamics is encoded in non-conservative products. The coefficients of these non-conservative products are only functions of α, β^i, ϕ and $\tilde{\gamma}_{ij}$ and no terms involving derivatives of these variables appear. The dynamical variables of the FO-CCZ4 system (including the auxiliary variables involved in the formulation of the Gamma-driver shift condition) are then: $\tilde{A}_{ij}$, K, Θ, $\hat{\Gamma}^i$, b^i (b^i being the auxiliary field used to formulate the Gamma-driver condition) and the auxiliary variables A_k, B^i_k, P_k and D_{kij}. In this work we elected upon experimentation to follow the second approach, so that our final system of 58 evolution equations is in fully non conservative form and consist of 11 ODEs and 47 PDEs. The form of the system and the very special structure it assumes are presented in section 4.4.3.

The FO-CCZ4 equations

The final first-order form of the FO-CCZ4 system is non-conservative and appears in the following form

$$\frac{\partial \boldsymbol{Q}}{\partial t} + \boldsymbol{A_1}(\boldsymbol{Q})\frac{\partial \boldsymbol{Q}}{\partial x_1} + \boldsymbol{A_2}(\boldsymbol{Q})\frac{\partial \boldsymbol{Q}}{\partial x_2} + \boldsymbol{A_3}(\boldsymbol{Q})\frac{\partial \boldsymbol{Q}}{\partial x_3} = \boldsymbol{S}(\boldsymbol{Q}), \tag{4.17}$$

where the symbols shorthands for the state vector $\boldsymbol{Q}$, the system matrices $\boldsymbol{A}_i$ and the purely algebraic source terms $\boldsymbol{S}(\boldsymbol{Q})$ respectively.

From now on the discussion is restricted to the vacuum case for simplicity, *i.e.* assume the stress-energy tensor to be identically null in the following. The neglected matter terms can be trivially added to the equations as needed since they are purely algebraic terms; as such they do not enter the principal part of the system, and can be neglected in computing its eigenstructure and determining its hyperbolicity. For the same reason they also do not pose any issues to the numerical discretization. Therefore our final non-conservative

first-order FO-CCZ4 system reads as follows:

$$
\begin{aligned}
\partial_t \tilde{\gamma}_{ij} &= \beta^k 2D_{kij} + \tilde{\gamma}_{ki} B_j{}^k + \tilde{\gamma}_{kj} B_i{}^k - \frac{2}{3}\tilde{\gamma}_{ij} B_k{}^k \\
&\quad - 2\alpha \left(\tilde{A}_{ij} - \frac{1}{3}\tilde{\gamma}_{ij} \mathrm{tr}\tilde{A} \right) - \tau^{-1}(\tilde{\gamma} - 1)\tilde{\gamma}_{ij} && \text{(4.18a)} \\
\partial_t \ln \alpha &= \beta^k A_k - \alpha g(\alpha)(K - K_0 - 2\Theta c) && \text{(4.18b)} \\
\partial_t \beta^i &= s\beta^k B_k^i + s f b^i && \text{(4.18c)} \\
\partial_t \ln \phi &= \beta^k P_k + \frac{1}{3}\left(\alpha K - B_k^k\right) && \text{(4.18d)} \\
\partial_t \tilde{A}_{ij} &= \beta^k \partial_k \tilde{A}_{ij} + \phi^2 \Big[- \nabla_i \nabla_j \alpha + \alpha \left(R_{ij} + \nabla_i Z_j + \nabla_j Z_i \right) \Big] \\
&\quad - \phi^2 \frac{1}{3}\frac{\tilde{\gamma}_{ij}}{\phi^2} \Big[- \nabla^k \nabla_k \alpha + \alpha(R + 2\nabla_k Z^k) \Big] + \tilde{A}_{ki} B_j{}^k + \tilde{A}_{kj} B_i{}^k \\
&\quad - \frac{2}{3}\tilde{A}_{ij} B_k{}^k + \alpha \tilde{A}_{ij}(K - 2\Theta c) - 2\alpha \tilde{A}_{il}\tilde{\gamma}^{lm}\tilde{A}_{mj} - \tau^{-1}\tilde{\gamma}_{ij}\mathrm{tr}\tilde{A} && \text{(4.18e)} \\
\partial_t K &= \beta^k \partial_k K - \nabla^i \nabla_i \alpha + \alpha(R + 2\nabla_i Z^i) \\
&\quad + \alpha K(K - 2\Theta c) - 3\alpha\kappa_1(1 + \kappa_2)\Theta && \text{(4.18f)} \\
\partial_t \Theta &= \beta^k \partial_k \Theta + \frac{1}{2}\alpha e^2 (R + 2\nabla_i Z^i) + \frac{1}{2}\alpha e^2 \left(\frac{2}{3}K^2 - \tilde{A}_{ij}\tilde{A}^{ij} \right) \\
&\quad - \alpha\Theta K c - Z^i \alpha A_i - \alpha\kappa_1(2 + \kappa_2)\Theta && \text{(4.18g)} \\
\partial_t \hat{\Gamma}^i &= \beta^k \partial_k \hat{\Gamma}^i - \frac{4}{3}\alpha\tilde{\gamma}^{ij}\partial_j K + 2\alpha\tilde{\gamma}^{ki}\partial_k \Theta + \tilde{\gamma}^{kl}\partial_{(k} B_{l)}{}^i + \frac{1}{3}\tilde{\gamma}^{ik}\partial_{(k} B_{l)}{}^l \\
&\quad + s2\alpha\tilde{\gamma}^{ik}\tilde{\gamma}^{nm}\partial_k \tilde{A}_{nm} + \frac{2}{3}\tilde{\Gamma}^i B_k{}^k - \tilde{\Gamma}^k B_k{}^i + 2\alpha \left(\tilde{\Gamma}^i{}_{jk}\tilde{A}^{jk} - 3\tilde{A}^{ij} P_j \right) \\
&\quad - 2\alpha\tilde{\gamma}^{ki}\left(\Theta A_k + \frac{2}{3} K Z_k \right) - 2\alpha\tilde{A}^{ij} A_j + s2\alpha\tilde{\gamma}^{ik}\partial_k \tilde{\gamma}^{nm}\tilde{A}_{nm} \\
&\quad + 2\kappa_3 \left(\frac{2}{3}\tilde{\gamma}^{ij} Z_j B_k{}^k - \tilde{\gamma}^{jk} Z_j B_k{}^i \right) - 2\alpha\kappa_1 \tilde{\gamma}^{ij} Z_j && \text{(4.18h)} \\
\partial_t b^i &= s\beta^k \partial_k b^i + s\left(\partial_t \hat{\Gamma}^i - \beta^k \partial_k \hat{\Gamma}^i - \eta b^i \right), && \text{(4.18i)}
\end{aligned}
$$

with the PDEs for the auxiliary variables given by:

$$\begin{aligned}
\partial_t A_k &= \beta^l \partial_l A_k - \alpha g(\alpha) \left(\partial_k K - \partial_k K_0 - 2c\partial_k \Theta\right) - s\alpha g(\alpha)\tilde{\gamma}^{nm}\partial_k \tilde{A}_{nm} \\
&\quad - s\alpha g(\alpha)\partial_k \tilde{\gamma}^{nm}\tilde{A}_{nm} - \alpha A_k \left(K - K_0 - 2\Theta c\right)\left(g(\alpha) + \alpha g'(\alpha)\right) \\
&\quad + B_k{}^l A_l \qquad (4.19a) \\
\partial_t B_k{}^i &= -s\left(-\beta^l \partial_l B_k{}^i - f\partial_k b^i + \mu\tilde{\gamma}^{ij}\left(\partial_k P_j - \partial_j P_k\right)\right. \\
&\quad \left. -\mu\tilde{\gamma}^{ij}\tilde{\gamma}^{nl}\left(\partial_k D_{ljn} - \partial_l D_{kjn}\right)\right) + sB^l{}_k B^i{}_l \qquad (4.19b) \\
\partial_t D_{kij} &= \beta^l \partial_l D_{kij} - s\left(-\frac{1}{2}\tilde{\gamma}_{mi}\partial_{(k}B^m{}_{j)} - \frac{1}{2}\tilde{\gamma}_{mj}\partial_{(k}B^m{}_{i)} + \frac{1}{3}\tilde{\gamma}_{ij}\partial_{(k}B^m{}_{m)}\right) \\
&\quad - \alpha\partial_k \tilde{A}_{ij} + \frac{1}{3}\alpha\tilde{\gamma}_{ij}\tilde{\gamma}^{nm}\partial_k \tilde{A}_{nm} + B_k{}^l D_{lij} + B_j{}^l D_{kli} + B_i{}^l D_{klj} \\
&\quad - \frac{2}{3}B_l{}^l D_{kij} + \frac{1}{3}\alpha\tilde{\gamma}_{ij}\partial_k \tilde{\gamma}^{nm}\tilde{A}_{nm} - \alpha A_k\left(\tilde{A}_{ij} - \frac{1}{3}\tilde{\gamma}_{ij}\mathrm{tr}\tilde{A}\right) \qquad (4.19c) \\
\partial_t P_k &= \beta^l \partial_l P_k + \frac{1}{3}\alpha\partial_k K - \frac{1}{3}\partial_{(k}B^i{}_{i)} + s\frac{1}{3}\alpha\tilde{\gamma}^{nm}\partial_k \tilde{A}_{nm} + \frac{1}{3}\alpha A_k K \\
&\quad + B_k{}^l P_l + s\frac{1}{3}\alpha\partial_k \tilde{\gamma}^{nm}\tilde{A}_{nm}\,. \qquad (4.19d)
\end{aligned}$$

In the preceding equations those terms that have been added to the PDEs to obtain an approximate symmetrization of the sparsity pattern are indicated in red (see the discussion in section 4.4.3 and figure 4.1). Note that the function $g(\alpha)$ in equation (4.18b) controls the type of slicing gauge condition which is emplyed. In particular $g(\alpha) = 1$ leads to harmonic slicing and while $g(\alpha) = 2/\alpha$ to the so-called $1 + \log$ slicing condition Bona et al. (1995).

In order to obtain the shift advection terms in the evolution equations for the auxiliary variables, the identities (4.15) have been employed. In fact it results to be very important to use the second-order ordering constraints (4.15) in an appropriate way in order to guarantee strong hyperbolicity: a naive first-order formulation of the original CCZ4 system will general only result in a weakly, rather than strongly, hyperbolic system (see Gundlach and Martin-Garcia (2006) for a detailed discussion on the use of second-order ordering constraints in second order in space first order in time hyperbolic systems). More over we have found that the use of first and second-order ordering constraints alone is in fact not sufficient to get a strongly hyperbolic system, but that it is necessary to derive the PDE (4.19c) for the evolution of the D_{kij} field from (4.13a) by exploiting $\tilde{A}_{ij}$ being trace-free. This is done via the use of the constraint $\mathcal{T}_k$, by adding equation (4.16) to equation (4.19c). These additional terms in the FO-CCZ4 equations, related to the constraints (4.15) and (4.16) are the ones highlighted in red in equations (4.18a)-(4.19d), as mentioned above.

Note finally that a number of additional constants have been introduced in the FO-CCZ4 system, mostly for reasons of convenience. These are:

- τ is a relaxation time introduced to enforce the algebraic constraints on the determinant of $\tilde{\gamma}_{ij}$ and on the trace of $\tilde{A}_{ij}$ weakly (*i.e.* without the need to explicitly enforce these constraints after each evolution timestep in a numerical implementation; see the discussion in Alic et al. (2012)).

- e is a cleaning speed for the Hamiltonian constraint. This has been introduced following the ideas of the generalized Lagrangian multiplier

(GLM) approach of Dedner et al. (2002). In practice, this constant affects the speed at which violation of the Hamiltonian constraint are propagated away from their source. Note that the cleaning of the constraints is a non-physical process, and as such $e > 1$ (*i.e.* superluminal propagation speeds) is allowed; this choice would lead to faster constraint propagation, helping in reducing constraint violations; and is in fact also needed for strong hyperbolicity for certain gauge choices.

- $\mu > 0$ appears in equation (4.19b) and allows to adjust the relative contribution of second-order ordering constraints.

- s appears in the PDEs controlling the shift evolution. It simply allows to switch on or off the evolution of the shift vector, *i.e.* if $s = 0$ the gauge condition for the shift reduces to $\partial_t \beta^i = 0$, while for $s = 1$ the usual Gamma driver condition is recovered.

- c allows to turn off some of the algebraic source terms of the system.

Note that instead of evolving the lapse α and the conformal factor ϕ, their logarithms $\ln(\alpha)$ and $\ln(\phi)$ are evolved. While not a standard choice, this is a very simple way of preserving the positivity of the respective variables, even at the discrete level. Note also that at a black hole puncture location the lapse would vanish and its logarithm diverge. Therefore a positive lower limit on their values is imposed in our numerical implementation. Since the numerical method we selected to dicretize the FO-CCZ4 system is a DG scheme, in which the solution in every computational element is represented by an interpolating polynomial as described in the previous chapter, in an element surrounding the puncture the DG polynomial might if fact reach values lower than this lower limit due to the Runge phenomenon. However it would in any case not diverge.

The following explicit expressions and identities apply to various terms ap-

pearing in the evolution equations:

$$
\begin{aligned}
\mathrm{tr}\tilde{A} &= \tilde{\gamma}^{ij}\tilde{A}_{ij}, \qquad \text{and} \qquad \tilde{\gamma} = \det(\tilde{\gamma}_{ij}) && (4.20)\\
\partial_k \tilde{\gamma}^{ij} &= -2\tilde{\gamma}^{in}\tilde{\gamma}^{mj} D_{knm} := -2D_k{}^{ij} && (4.21)\\
\tilde{\Gamma}^k{}_{ij} &= \tilde{\gamma}^{kl}\left(D_{ijl} + D_{jil} - D_{lij}\right) && (4.22)\\
\partial_k \tilde{\Gamma}^m{}_{ij} &= -2D_k{}^{ml}\left(D_{ijl} + D_{jil} - D_{lij}\right) \\
&\quad + \tilde{\gamma}^{ml}\left(\partial_{(k}D_{i)jl} + \partial_{(k}D_{j)il} - \partial_{(k}D_{l)ij}\right) && (4.23)\\
\Gamma^k{}_{ij} &= \tilde{\gamma}^{kl}\left(D_{ijl} + D_{jil} - D_{lij}\right) - \tilde{\gamma}^{kl}\left(\tilde{\gamma}_{jl}P_i + \tilde{\gamma}_{il}P_j - \tilde{\gamma}_{ij}P_l\right) \\
&= \tilde{\Gamma}^k{}_{ij} - \tilde{\gamma}^{kl}\left(\tilde{\gamma}_{jl}P_i + \tilde{\gamma}_{il}P_j - \tilde{\gamma}_{ij}P_l\right) && (4.24)\\
\partial_k \Gamma^m{}_{ij} &= -2D_k{}^{ml}\left(D_{ijl} + D_{jil} - D_{lij}\right) + 2D_k{}^{ml}\left(\tilde{\gamma}_{jl}P_i + \tilde{\gamma}_{il}P_j - \tilde{\gamma}_{ij}P_l\right) \\
&\quad - 2\tilde{\gamma}^{ml}\left(D_{kjl}P_i + D_{kil}P_j - D_{kij}P_l\right) \\
&\quad + \tilde{\gamma}^{ml}\left(\partial_{(k}D_{i)jl} + \partial_{(k}D_{j)il} - \partial_{(k}D_{l)ij}\right) \\
&\quad - \tilde{\gamma}^{ml}\left(\tilde{\gamma}_{jl}\partial_{(k}P_{i)} + \tilde{\gamma}_{il}\partial_{(k}P_{j)} - \tilde{\gamma}_{ij}\partial_{(k}P_{l)}\right) && (4.25)\\
R^m{}_{ikj} &= \partial_k \Gamma^m{}_{ij} - \partial_j \Gamma^m{}_{ik} + \Gamma^l{}_{ij}\Gamma^m{}_{lk} - \Gamma^l{}_{ik}\Gamma^m{}_{lj} && (4.26)\\
R_{ij} &= R^m{}_{imj} && (4.27)\\
\nabla_i\nabla_j\alpha &= \alpha A_i A_j - \alpha\Gamma^k{}_{ij}A_k + \alpha\partial_{(i}A_{j)} && (4.28)\\
\nabla^i\nabla_i\alpha &= \phi^2\tilde{\gamma}^{ij}\left(\nabla_i\nabla_j\alpha\right) && (4.29)\\
\tilde{\Gamma}^i &= \tilde{\gamma}^{jl}\tilde{\Gamma}^i_{jl} && (4.30)\\
\partial_k\tilde{\Gamma}^i &= -2D_k{}^{jl}\tilde{\Gamma}^i{}_{jl} + \tilde{\gamma}^{jl}\partial_k\tilde{\Gamma}^i{}_{jl} && (4.31)\\
Z_i &= \frac{1}{2}\tilde{\gamma}_{ij}\left(\hat{\Gamma}^j - \tilde{\Gamma}^j\right) \qquad Z^i = \frac{1}{2}\phi^2(\hat{\Gamma}^i - \tilde{\Gamma}^i) && (4.32)\\
\nabla_i Z_j &= D_{ijl}\left(\hat{\Gamma}^l - \tilde{\Gamma}^l\right) + \frac{1}{2}\tilde{\gamma}_{jl}\left(\partial_i\hat{\Gamma}^l - \partial_i\tilde{\Gamma}^l\right) - \Gamma^l{}_{ij}Z_l && (4.33)\\
R + 2\nabla_k Z^k &= \phi^2\tilde{\gamma}^{ij}\left(R_{ij} + \nabla_i Z_j + \nabla_j Z_i\right). && (4.34)
\end{aligned}
$$

Here, we have again made use of the second-order ordering constraints (4.15) by *symmetrizing* the spatial derivatives of the auxiliary variables as follows:

$$
\begin{aligned}
\partial_{(k}A_{i)} &:= \frac{\partial_k A_i + \partial_i A_k}{2}, \qquad \partial_{(k}P_{i)} := \frac{\partial_k P_i + \partial_i P_k}{2} \\
\partial_{(k}B^i_{j)} &:= \frac{\partial_k B^i{}_j + \partial_j B^i{}_k}{2}, \quad \partial_{(k}D_{l)ij} := \frac{\partial_k D_{lij} + \partial_l D_{kij}}{2}\,. && (4.35)
\end{aligned}
$$

In general the above expressions contain terms contributing to the purely algebraic source term as well as to the non-conservative products, which need to be separate in the numerical implementation. Note also that the Ricci tensor R_{ij} is directly calculated from its definition in terms of the Riemann tensor $R^m{}_{ikj}$, the Christoffel symbols and their derivatives *ab definitionem*, *i.e.* we don't employ the typical split of the Ricci tensor as *e.g.* used in Alic et al. (2012). Since in general the identity $\tilde{\gamma}_{ij} = 1$ cannot be guaranteed to hold exactly at the discrete level (unless the algebraic constraints are rigorously enforced), the contracted Christoffel symbols $\tilde{\Gamma}^i$ are also directly computed from their definition.

The use of the second-order ordering constraints (4.15) and the constraint $\mathcal{T}_k$ to achieve strong hyperbolicity is motivated by examining the structure of the sparsity pattern of the system matrix $\boldsymbol{A}\cdot\boldsymbol{n} = \boldsymbol{A_1}n_1 + \boldsymbol{A_2}n_2 + \boldsymbol{A_3}n_3$. In figure 4.1 the sparsity pattern of the system matrix in the normal direction $\boldsymbol{n} = 1/\sqrt{3}(1,1,1)$ for the Gamma-driver shift condition and the $1+\log$ slicing condition for a randomly perturbed flat Minkowski spacetime is p[lotted, neglecting all matrix entries whose absolute value is below a threshold of 10^{-7}. The blue dots represent the original sparsity structure without the use of the second-order ordering constraints (4.15) and the constraint (4.16); while the combination of the blue and the red dots shows the sparsity pattern after those terms have been added to the PDE system. Our approach for finding a suitable form of the ordering constraints to be added is based on the approximate symmetrization of the sparsity pattern of the system matrix, in order to avoid Jordan blocks, which cannot be diagonalized. Such Jordan blocks are evidently present in the sparsity pattern indicated by the blue dots alone in figure 4.1, *i.e.* without the use of the ordering constraints.

It is clearly evident from figure 4.1 that the first 11 varibles of the FO-CCZ4 system, *i.e.* $\tilde{\gamma}_{ij}$, α, β^i and ϕ, are only evolved via ODEs and that the entire system does not include spatial derivatives of these variables: all entries in the first 11 rows and columns of the system matrix are zero. However this deos not imply that the FO-CCZ4 system is symmetric hyperbolic (in the sense of Friedrichs (1954)). Further work in this direction would be needed to achieve a symmetric hyperbolic form of FO-CCZ4. Note finally that in order to maintain the split of the system into 11 pure ODEs (4.37) for the metric variables α, β^i, $\tilde{\gamma}_{ij}$ and ϕ, and with no spatial derivatives of these quantities appearing in the remaining PDE system (4.38), and 47 PDEs, it is not possible to add damping terms proportional to the first-order ordering constraints (4.14) to the system. These terms would contain spatial derivatives of said variables and may eventually lead to Jordan blocks which cannot be diagonalized. We therefore refrain from adding these terms, in contrast to what has been done in Brown et al. (2012). For the same reason also writing the system in a flux-conservative form is not possible, since the fluxes would in general depend on the 4-metric and spatial derivatives of α, β^i, $\tilde{\gamma}_{ij}$ and ϕ would appear.

4.4.3 Proof of strong hyperbolicity

As mentioned above, by defining the state vector $\boldsymbol{Q}^T := \left(\tilde{\gamma}_{ij}, \ln\alpha, \beta^i, \ln\phi, \tilde{A}_{ij}, K, \Theta, \hat{\Gamma}^i, b^i, A_k, B^i_k, D_{kij}, P_k\right)$ containing a total of 58 variables, the FO-CCZ4 system (4.18a)-(4.19d) can be written in the compact form (4.17). The explicit ordering of the 58 variables for

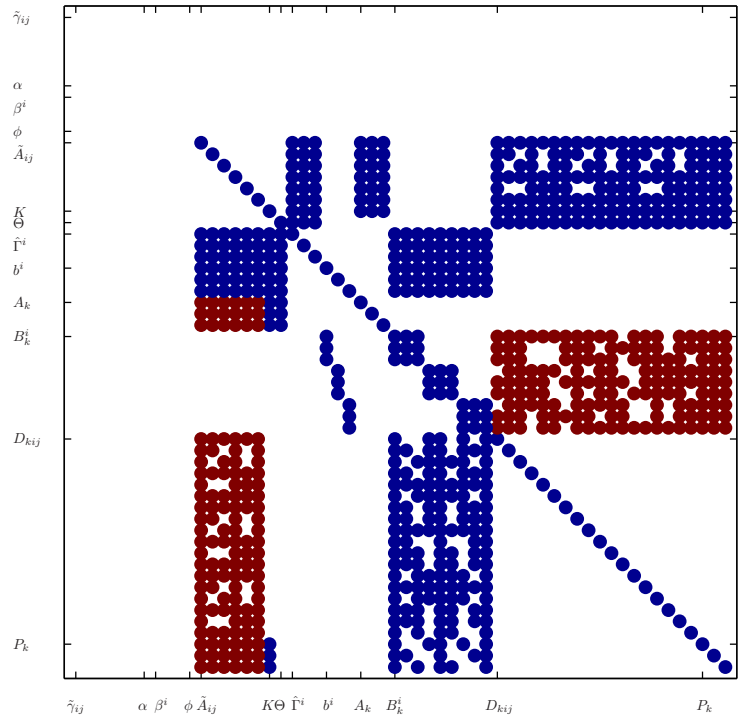

Figure 4.1: Sparsity pattern of the system matrix $\boldsymbol{A}\cdot\boldsymbol{n}$ with $\boldsymbol{n}=(1,1,1)/\sqrt{3}$ for a randomly perturbed flat Minkowski spacetime using the Gamma-driver shift condition ($s=1$) and $1+\log$ slicing ($g(\alpha)=2/\alpha$), without the use of the constraints (4.15) and (4.16) (blue dots) and with the use of these constraints (blue & red dots). The achieved approximate symmetrization of the sparsity pattern is evident. Note also the complete absence of non-zero entries in the first 11 lines and columns corresponding to the variables $\tilde{\gamma}_{ij}$,α, β^i and ϕ, which clearly highlights the special structure of our FO-CCZ4 system that can be split into a set of pure ODEs and a reduced PDE system, as discussed in Section 4.4.3. *Figure reproduced from Dumbser et al. (2017).*

the complete state vector $\boldsymbol{Q}$ we employ is explicitly given below as

$$
\begin{aligned}
\boldsymbol{Q}^T = \Big(& \tilde{\gamma}_{xx}, \tilde{\gamma}_{xy}, \tilde{\gamma}_{xz}, \tilde{\gamma}_{yy}, \tilde{\gamma}_{yz}, \tilde{\gamma}_{zz}, \\
& \ln\alpha, \beta^x, \beta^y, \beta^z, \ln\phi, \\
& \tilde{A}_{xx}, \tilde{A}_{xy}, \tilde{A}_{xz}, \tilde{A}_{yy}, \tilde{A}_{yz}, \tilde{A}_{zz}, \\
& K, \Theta, \hat{\Gamma}^x, \hat{\Gamma}^y, \hat{\Gamma}^z, \\
& b^x, b^y, b^z, \\
& A_x, A_y, A_x, \\
& B^x{}_x, B^x{}_y, B^x{}_z, B^y{}_x, B^y{}_y, B^y{}_z, B^z{}_x, B^z{}_y, B^z{}_z, \\
& D_{xxx}, D_{xxy}, D_{xxz}, D_{xyy}, D_{xyz}, D_{xzz}, D_{yxx}, D_{yxy}, D_{yxz}, \\
& D_{yyy}, D_{yyz}, D_{yzz}, D_{zxx}, D_{zxy}, D_{zxz}, D_{zyy}, D_{zyz}, D_{zzz}, \\
& P_x, P_y, P_z \Big) .
\end{aligned}
\tag{4.36}
$$

The vector $\boldsymbol{Q}$ can be split into two parts: $\boldsymbol{Q}^T = (\boldsymbol{V}^T, \boldsymbol{U}^T)$. The vector $\boldsymbol{V}$ contains the 11 quantities defining the 4-metric, $\boldsymbol{V}^T := (\tilde{\gamma}_{ij}, \ln\alpha, \beta^i, \ln\phi)$. The vector $\boldsymbol{U}$ encompasses the remaining 47 dynamic variables $\boldsymbol{U}^T := \left(\tilde{A}_{ij}, K, \Theta, \hat{\Gamma}^i, b^i, A_k, B^i_k, D_{kij}, P_k\right)$. As detailed above the vector $\boldsymbol{V}$ is evolved in time only via ODEs of the type

$$\frac{\partial \boldsymbol{V}}{\partial t} = \boldsymbol{S}'(\boldsymbol{Q})\,, \tag{4.37}$$

where $\boldsymbol{S}'(\boldsymbol{Q})$ contains the first 11 elements of the vector of source terms $\boldsymbol{S}(\boldsymbol{Q})$. Therefore the eigenvalues associated with this ODE subsystem, *i.e.* the propagation speeds for the variables of vector $\boldsymbol{V}$ are trivially zero. Since equations (4.18a)–(4.19d) do not contain any spatial derivative of the quantities in $\boldsymbol{V}$ due to our choices in employing the ordering constraints, the columns in the matrices of the related eigenvectors are trivially the unit vectors. The remaining reduced system to be analyzed is related to the vector $\boldsymbol{U}$ of the dynamic quantities and shows the very particular structure

$$\frac{\partial \boldsymbol{U}}{\partial t} + \boldsymbol{B_1}(\boldsymbol{V})\frac{\partial \boldsymbol{U}}{\partial x_1} + \boldsymbol{B_2}(\boldsymbol{V})\frac{\partial \boldsymbol{U}}{\partial x_2} + \boldsymbol{B_3}(\boldsymbol{V})\frac{\partial \boldsymbol{U}}{\partial x_3} = \boldsymbol{S}''(\boldsymbol{Q})\,, \tag{4.38}$$

where the source term $\boldsymbol{S}''(\boldsymbol{Q})$ contains the remaining elements of the source vector $\boldsymbol{S}(\boldsymbol{Q})$ and where the system matrices $\boldsymbol{B}_i$ depend only on the vector $\boldsymbol{V}$, but not on $\boldsymbol{U}$.

An immediate consequence of the very particular splitting of (4.17) into the ODEs (4.37) and the reduced PDEs (4.38) is that all fields appearing in the system (4.38) and thus in (4.17) are linearly degenerate (see Toro (2009) for a detailed discussion), since the eigenvalues λ_i depend only on $\boldsymbol{V}$ and not on $\boldsymbol{U}$ and hence $\partial\lambda_i/\partial\boldsymbol{Q}\cdot\boldsymbol{r}_i = 0, \forall\,\lambda_i$. This in turn means that smooth initial data evolved through the FO-CCZ4 system cannot generate shock waves and discontinuous solutions, since this would require the compression of characteristic lines and therefore the presence of genuinely nonlinear fields (Toro, 2009; Rezzolla and Zanotti, 2013).

To prove the strong hyperbolicity of the FO-CCZ4 system proposed above, we explicitly compute the entire eigenstructure of the system matrix $\boldsymbol{B}_1$ in the x_1 direction, restricting however our analysis to the simple shift condition $\beta^i = 0$ (hence $s = 0$) and for the case of harmonic slicing, *i.e.* $g(\alpha) = 1$. Since for this simplified shift condition there is no need for the auxiliary fields b^i and B^i_k, their corresponding PDEs can be neglected in the analysis (the associated eigenvalues are simply zero and the eigenvectors are the unit vectors). Note that in principle the system principal symbol eigenstructure should be computed in every direction in space. This is however not necessary in the case of formulations of Einstein equations, since they are isotropic (see Sarbach and Tiglio (2012) for details).

Eliminating the Gamma driver auxiliary variables, $\boldsymbol{U}$ is reduced to 35 components, namely $\boldsymbol{U}^T = (\tilde{A}_{ij}, K, \Theta, \hat{\Gamma}^i, A_k, D_{kij}, P_k)$. The 35 eigenvalues of matrix $\boldsymbol{B}_1$ in x_1 direction are

$$\begin{aligned} \lambda_{1,2,\cdots,21} &= 0\,, & \lambda_{22,23} &= \pm\sqrt{\tilde{\gamma}^{11}}\phi\,\alpha\,e\,, \\ \lambda_{24,25,\cdots,29} &= +\sqrt{\tilde{\gamma}^{11}}\phi\,\alpha\,, & \lambda_{30,31,\cdots,35} &= -\sqrt{\tilde{\gamma}^{11}}\phi\,\alpha\,. \end{aligned} \tag{4.39}$$

The associated complete set of 35 right eigenvectors defining the right eigenvector matrix $\boldsymbol{R}$ are given explicitly below.

$$
\begin{aligned}
\boldsymbol{r}_1^T &= \left(\frac{\tilde{\gamma}_{11}}{\tilde{\gamma}_{33}}, \frac{\tilde{\gamma}_{12}}{\tilde{\gamma}_{33}}, \frac{\tilde{\gamma}_{13}}{\tilde{\gamma}_{33}}, \frac{\tilde{\gamma}_{22}}{\tilde{\gamma}_{33}}, \frac{\tilde{\gamma}_{23}}{\tilde{\gamma}_{33}}, \frac{\tilde{\gamma}_{33}}{\tilde{\gamma}_{33}}, 0, \cdots, 0\right) \\
\boldsymbol{r}_2^T &= \left(0, \cdots, 0,\ \tilde{\gamma}^{11}\tilde{\gamma}^{11},\ \tilde{\gamma}^{11}\tilde{\gamma}^{12},\ \tilde{\gamma}^{11}\tilde{\gamma}^{13}, 0, 0, 0, 1, 0, \cdots, 0\right) \\
\boldsymbol{r}_3^T &= \left(0, 0, 0, 0, 0, 0, 0, 0, 2\tilde{\gamma}^{11}\tilde{\gamma}^{12}, 2\tilde{\gamma}^{11}\tilde{\gamma}^{22}, 2\tilde{\gamma}^{11}\tilde{\gamma}^{23}, 0, 0, 0, 0, 1, \cdots, 0\right) \\
\boldsymbol{r}_4^T &= \left(0, 0, 0, 0, 0, 0, 0, 0, 2\tilde{\gamma}^{11}\tilde{\gamma}^{13}, 2\tilde{\gamma}^{11}\tilde{\gamma}^{23}, 2\tilde{\gamma}^{11}\tilde{\gamma}^{33}, 0, 0, 0, 0, 0, 1, \cdots, 0\right) \\
\boldsymbol{r}_5^T &= \Bigg(0, 0, 0, 0, 0, 0, 0, 0, 0, \frac{\tilde{\gamma}_{33}}{(\tilde{\gamma}_{22}\,\tilde{\gamma}_{33} - \tilde{\gamma}_{23}^2)}, -\frac{\tilde{\gamma}_{23}}{(\tilde{\gamma}_{22}\,\tilde{\gamma}_{33} - \tilde{\gamma}_{23}^2)}, -\frac{\tilde{\gamma}^{12}}{\tilde{\gamma}^{11}}, \\
&\quad 1, 0, 0, 0, 0, \cdots, 0\Bigg) \\
\boldsymbol{r}_6^T &= \Bigg(0, 0, 0, 0, 0, 0, 0, 0, 0, -\frac{\tilde{\gamma}_{23}}{(\tilde{\gamma}_{22}\,\tilde{\gamma}_{33} - \tilde{\gamma}_{23}^2)}, \frac{\tilde{\gamma}_{22}}{(\tilde{\gamma}_{22}\,\tilde{\gamma}_{33} - \tilde{\gamma}_{23}^2)}, -\frac{\tilde{\gamma}^{13}}{\tilde{\gamma}^{11}}, \\
&\quad 0, 1, 0, 0, 0, \cdots, 0\Bigg) \\
\boldsymbol{r}_7^T &= \Big(0, 0, 0, 0, 0, 0, 0, 0, 0,\ \tilde{\gamma}^{12}\tilde{\gamma}^{11},\ \tilde{\gamma}^{12}\tilde{\gamma}^{12},\ \tilde{\gamma}^{12}\tilde{\gamma}^{13}, \\
&\quad 0, 0, 0, 0, 0, 0, 0, 0, 0, 1, 0, \cdots, 0\Big) \\
\boldsymbol{r}_8^T &= \Big(0, 0, 0, 0, 0, 0, 0, 0, 2\tilde{\gamma}^{12}\tilde{\gamma}^{12}, 2\tilde{\gamma}^{12}\tilde{\gamma}^{22}, 2\tilde{\gamma}^{12}\tilde{\gamma}^{23}, \\
&\quad 0, 0, 0, 0, 0, 0, 0, 0, 0, 0, 1, 0, \cdots, 0\Big) \\
\boldsymbol{r}_9^T &= \Big(0, 0, 0, 0, 0, 0, 0, 0, 2\tilde{\gamma}^{12}\tilde{\gamma}^{13}, 2\tilde{\gamma}^{12}\tilde{\gamma}^{23}, 2\tilde{\gamma}^{12}\tilde{\gamma}^{33}, \\
&\quad 0, 0, 0, 0, 0, 0, 0, 0, 0, 0, 0, 1, 0, \cdots, 0\Big) \\
\boldsymbol{r}_{10}^T &= \left(0, 0, 0, 0, 0, 0, 0, 0, 0, 0, 0, 0, 0, 0, 0, 0, 0, -\frac{\tilde{\gamma}^{12}}{\tilde{\gamma}^{11}}, 0, 0, 0, 0, 0, 1, 0, \cdots, 0\right) \\
\boldsymbol{r}_{11}^T &= \left(0, 0, 0, 0, 0, 0, 0, 0, 0, 0, 0, 0, 0, 0, 0, 0, 0, 0, -\frac{\tilde{\gamma}^{12}}{\tilde{\gamma}^{11}}, 0, 0, 0, 0, 0, 1, 0, \cdots, 0\right) \\
\boldsymbol{r}_{12}^T &= \left(0, 0, 0, 0, 0, 0, 0, 0, 0, 0, 0, 0, 0, 0, 0, 0, 0, 0, 0, -\frac{\tilde{\gamma}^{12}}{\tilde{\gamma}^{11}}, 0, 0, 0, 0, 0, 1, 0, \cdots, 0\right) \\
\boldsymbol{r}_{13}^T &= \left(0, 0, 0, 0, 0, 0, 0, 0, 0,\ \tilde{\gamma}^{13}\tilde{\gamma}^{11},\ \tilde{\gamma}^{13}\tilde{\gamma}^{12},\ \tilde{\gamma}^{13}\tilde{\gamma}^{13}, 0, \cdots, 0, 1, 0, 0, 0, 0, 0, 0, 0, 0\right) \\
\boldsymbol{r}_{14}^T &= \left(0, 0, 0, 0, 0, 0, 0, 0, 2\tilde{\gamma}^{13}\tilde{\gamma}^{12}, 2\tilde{\gamma}^{13}\tilde{\gamma}^{22}, 2\tilde{\gamma}^{13}\tilde{\gamma}^{23}, 0, \cdots, 0, 1, 0, 0, 0, 0, 0, 0, 0\right) \\
\boldsymbol{r}_{15}^T &= \left(0, 0, 0, 0, 0, 0, 0, 0, 2\tilde{\gamma}^{13}\tilde{\gamma}^{13}, 2\tilde{\gamma}^{13}\tilde{\gamma}^{23}, 2\tilde{\gamma}^{13}\tilde{\gamma}^{33}, 0, \cdots, 0, 1, 0, 0, 0, 0, 0, 0\right) \\
\boldsymbol{r}_{16}^T &= \left(0, 0, 0, 0, 0, 0, 0, 0, 0, 0, 0, 0, 0, 0, 0, 0, 0, -\frac{\tilde{\gamma}^{13}}{\tilde{\gamma}^{11}}, 0, \cdots, 0, 1, 0, 0, 0, 0, 0\right) \\
\boldsymbol{r}_{17}^T &= \left(0, 0, 0, 0, 0, 0, 0, 0, 0, 0, 0, 0, 0, 0, 0, 0, 0, 0, -\frac{\tilde{\gamma}^{13}}{\tilde{\gamma}^{11}}, 0, \cdots, 0, 1, 0, 0, 0, 0\right) \\
\boldsymbol{r}_{18}^T &= \left(0, 0, 0, 0, 0, 0, 0, 0, 0, 0, 0, 0, 0, 0, 0, 0, 0, 0, 0, -\frac{\tilde{\gamma}^{13}}{\tilde{\gamma}^{11}}, 0, \cdots, 0, 1, 0, 0, 0\right) \\
\boldsymbol{r}_{19}^T &= \Big(0, 0, 0, 0, 0, 0, 0, 0, -\tilde{\gamma}^{11}(2\tilde{\gamma}_{11}\tilde{\gamma}^{11} + 3\tilde{\gamma}_{12}\tilde{\gamma}^{12} + 3\tilde{\gamma}_{13}\tilde{\gamma}^{13}), \\
&\quad -\tilde{\gamma}^{12}(\tilde{\gamma}_{12}\tilde{\gamma}^{12} + \tilde{\gamma}_{22}\tilde{\gamma}^{22} + \tilde{\gamma}_{23}\tilde{\gamma}^{23}) + \tilde{\gamma}_{11}\tilde{\gamma}^{12}\tilde{\gamma}^{11}, \\
&\quad -\tilde{\gamma}^{13}(\tilde{\gamma}_{13}\tilde{\gamma}^{13} + \tilde{\gamma}_{23}\tilde{\gamma}^{23} + \tilde{\gamma}_{33}\tilde{\gamma}^{33}) + \tilde{\gamma}_{11}\tilde{\gamma}^{13}\tilde{\gamma}^{11}, \\
&\quad 0, 0, 0, 0, 0, 0, \tilde{\gamma}_{22}, \tilde{\gamma}_{23}, \tilde{\gamma}_{33}, 0, \cdots, 0, 1, 0, 0\Big)
\end{aligned}
$$

$$
\begin{aligned}
\boldsymbol{r}^T_{20} &= \big(0,0,0,0,0,0,0,0,-\tilde{\gamma}^{12}(2\tilde{\gamma}_{11}\tilde{\gamma}^{11}+3\tilde{\gamma}_{12}\tilde{\gamma}^{12}+3\tilde{\gamma}_{13}\tilde{\gamma}^{13}),\\
&\quad -\tilde{\gamma}^{22}(\tilde{\gamma}_{12}\tilde{\gamma}^{12}+\tilde{\gamma}_{22}\tilde{\gamma}^{22}+\tilde{\gamma}_{23}\tilde{\gamma}^{23})+\tilde{\gamma}_{11}\tilde{\gamma}^{12}\tilde{\gamma}^{12},\\
&\quad -\tilde{\gamma}^{23}(\tilde{\gamma}_{13}\tilde{\gamma}^{13}+\tilde{\gamma}_{23}\tilde{\gamma}^{23}+\tilde{\gamma}_{33}\tilde{\gamma}^{33})+\tilde{\gamma}_{11}\tilde{\gamma}^{13}\tilde{\gamma}^{12},\\
&\quad 0,0,0,0,0,0,\tilde{\gamma}_{22}\frac{\tilde{\gamma}^{12}}{\tilde{\gamma}^{11}},\tilde{\gamma}_{23}\frac{\tilde{\gamma}^{12}}{\tilde{\gamma}^{11}},\tilde{\gamma}_{33}\frac{\tilde{\gamma}^{12}}{\tilde{\gamma}^{11}},0,\cdots,0,1,0\Big)\\
\boldsymbol{r}^T_{21} &= \big(0,0,0,0,0,0,0,0,-\tilde{\gamma}^{13}(2\tilde{\gamma}_{11}\tilde{\gamma}^{11}+3\tilde{\gamma}_{12}\tilde{\gamma}^{12}+3\tilde{\gamma}_{13}\tilde{\gamma}^{13}),\\
&\quad -\tilde{\gamma}^{23}(\tilde{\gamma}_{12}\tilde{\gamma}^{12}+\tilde{\gamma}_{22}\tilde{\gamma}^{22}+\tilde{\gamma}_{23}\tilde{\gamma}^{23})+\tilde{\gamma}_{11}\tilde{\gamma}^{12}\tilde{\gamma}^{13},\\
&\quad -\tilde{\gamma}^{33}(\tilde{\gamma}_{13}\tilde{\gamma}^{13}+\tilde{\gamma}_{23}\tilde{\gamma}^{23}+\tilde{\gamma}_{33}\tilde{\gamma}^{33})+\tilde{\gamma}_{11}\tilde{\gamma}^{13}\tilde{\gamma}^{13},\\
&\quad 0,0,0,0,0,0,\tilde{\gamma}_{22}\frac{\tilde{\gamma}^{13}}{\tilde{\gamma}^{11}},\tilde{\gamma}_{23}\frac{\tilde{\gamma}^{13}}{\tilde{\gamma}^{11}},\tilde{\gamma}_{33}\frac{\tilde{\gamma}^{13}}{\tilde{\gamma}^{11}},0,\cdots,0,1\Big)\\
\boldsymbol{r}^T_{22,23} &= \Bigg(\mp\frac{1}{\sqrt{\tilde{\gamma}^{11}}}\left(2\tilde{\gamma}_{11}\tilde{\gamma}^{11}+3\tilde{\gamma}_{12}\tilde{\gamma}^{12}+3\tilde{\gamma}_{13}\tilde{\gamma}^{13}\right)e\phi,\pm\sqrt{\tilde{\gamma}^{11}}\tilde{\gamma}_{12}e\phi,\pm\sqrt{\tilde{\gamma}^{11}}\tilde{\gamma}_{13}e\phi,\\
&\quad \pm\sqrt{\tilde{\gamma}^{11}}\tilde{\gamma}_{22}e\phi,\pm\sqrt{\tilde{\gamma}^{11}}\tilde{\gamma}_{23}e\phi,\pm\sqrt{\tilde{\gamma}^{11}}\tilde{\gamma}_{33}e\phi,\mp3\sqrt{\tilde{\gamma}^{11}}e\phi,\\
&\quad \mp\frac{3}{2}\sqrt{\tilde{\gamma}^{11}}(e^2-1)e\phi,(3e^2-7)\tilde{\gamma}^{11},(3e^2-7)\tilde{\gamma}^{12},(3e^2-7)\tilde{\gamma}^{13},-3,0,0,\\
&\quad -1/\tilde{\gamma}^{11}\left(2\tilde{\gamma}_{11}\tilde{\gamma}^{11}+3\tilde{\gamma}_{12}\tilde{\gamma}^{12}+3\tilde{\gamma}_{13}\tilde{\gamma}^{13}\right),\tilde{\gamma}_{12},\tilde{\gamma}_{13},\tilde{\gamma}_{22},\tilde{\gamma}_{23},\tilde{\gamma}_{33},\\
&\quad 0,\cdots,0,1,0,0\Bigg)\\
\boldsymbol{r}^T_{24,30} &= \Big(0,0,0,0,0,0,\mp3\phi\sqrt{\tilde{\gamma}^{11}},0,-4\tilde{\gamma}^{11},-4\tilde{\gamma}^{12},-4\tilde{\gamma}^{13},-3,0,\cdots,0,1,0,0\Big)\\
\boldsymbol{r}^T_{25,31} &= \Bigg(\mp2\phi\tilde{\gamma}^{12}/\sqrt{\tilde{\gamma}^{11}},\pm\phi\sqrt{\tilde{\gamma}^{11}},0,0,0,0,0,0,0,0,0,0,0,0,-2\frac{\tilde{\gamma}^{12}}{\tilde{\gamma}^{11}},\\
&\quad 1,0,\cdots,0)\\
\boldsymbol{r}^T_{26,32} &= \Bigg(\mp2\phi\tilde{\gamma}^{13}/\sqrt{\tilde{\gamma}^{11}},0,\pm\phi\sqrt{\tilde{\gamma}^{11}},0,0,0,0,0,0,0,0,0,0,-2\frac{\tilde{\gamma}^{13}}{\tilde{\gamma}^{11}},\\
&\quad 0,1,0,\cdots,0)\\
\boldsymbol{r}^T_{27,33} &= \Bigg(\quad\mp\phi\tilde{\gamma}^{22}/\sqrt{\tilde{\gamma}^{11}},0,0,\pm\phi\sqrt{\tilde{\gamma}^{11}},0,0,0,0,0,0,0,0,0,-\frac{\tilde{\gamma}^{22}}{\tilde{\gamma}^{11}},\\
&\quad 0,0,1,0,\cdots,0)\\
\boldsymbol{r}^T_{28,34} &= \Bigg(\mp2\phi\tilde{\gamma}^{23}/\sqrt{\tilde{\gamma}^{11}},0,0,0,\pm\phi\sqrt{\tilde{\gamma}^{11}},0,0,0,0,0,0,0,0,-2\frac{\tilde{\gamma}^{23}}{\tilde{\gamma}^{11}},\\
&\quad 0,0,0,1,0,\cdots,0)\\
\boldsymbol{r}^T_{29,35} &= \Bigg(\quad\mp\phi\tilde{\gamma}^{33}/\sqrt{\tilde{\gamma}^{11}},0,0,0,0,\pm\phi\sqrt{\tilde{\gamma}^{11}},0,0,0,0,0,0,0,-\frac{\tilde{\gamma}^{33}}{\tilde{\gamma}^{11}},\\
&\quad 0,0,0,0,1,0,\cdots,0)\ .
\end{aligned}
$$

The associated 35 left eigenvectors, which define the inverse of the right

eigenvector matrix ($\boldsymbol{L} = \boldsymbol{R}^{-1}$), read

$$
\begin{aligned}
\boldsymbol{l}_1 &= \left(\frac{1}{3}\tilde{\gamma}_{33}\tilde{\gamma}^{11}, \frac{2}{3}\tilde{\gamma}_{33}\tilde{\gamma}^{12}, \frac{2}{3}\tilde{\gamma}_{33}\tilde{\gamma}^{13}, \frac{1}{3}\tilde{\gamma}_{33}\tilde{\gamma}^{22}, \frac{2}{3}\tilde{\gamma}_{33}\tilde{\gamma}^{23}, \frac{1}{3}\tilde{\gamma}_{33}\tilde{\gamma}^{33}, 0, \cdots, 0\right) \\
\boldsymbol{l}_2 &= \Bigg(0, \cdots, 0, -\frac{\tilde{\gamma}_{12}\tilde{\gamma}^{12} + \tilde{\gamma}_{13}\tilde{\gamma}^{13}}{\tilde{\gamma}^{11}\tilde{\gamma}^{11}}, \frac{\tilde{\gamma}_{12}}{\tilde{\gamma}^{11}}, \frac{\tilde{\gamma}_{13}}{\tilde{\gamma}^{11}}, -\frac{1}{\tilde{\gamma}^{11}} + \frac{1}{3}\tilde{\gamma}_{11}, \frac{1}{3}\tilde{\gamma}_{11}\frac{\tilde{\gamma}^{12}}{\tilde{\gamma}^{11}}, \frac{1}{3}\tilde{\gamma}_{11}\frac{\tilde{\gamma}^{13}}{\tilde{\gamma}^{11}}, \\
&\quad 1, 2\frac{\tilde{\gamma}^{12}}{\tilde{\gamma}^{11}}, 2\frac{\tilde{\gamma}^{13}}{\tilde{\gamma}^{11}}, \frac{\tilde{\gamma}^{22}}{\tilde{\gamma}^{11}}, 2\frac{\tilde{\gamma}^{23}}{\tilde{\gamma}^{11}}, \frac{\tilde{\gamma}^{33}}{\tilde{\gamma}^{11}}, 0, 2\frac{\tilde{\gamma}^{12}\tilde{\gamma}^{12}}{\tilde{\gamma}^{11}\tilde{\gamma}^{11}}, 2\frac{\tilde{\gamma}^{12}\tilde{\gamma}^{13}}{\tilde{\gamma}^{11}\tilde{\gamma}^{11}}, \frac{\tilde{\gamma}^{12}\tilde{\gamma}^{22}}{\tilde{\gamma}^{11}\tilde{\gamma}^{11}}, 2\frac{\tilde{\gamma}^{12}\tilde{\gamma}^{23}}{\tilde{\gamma}^{11}\tilde{\gamma}^{11}}, \frac{\tilde{\gamma}^{12}\tilde{\gamma}^{33}}{\tilde{\gamma}^{11}\tilde{\gamma}^{11}}, \\
&\quad 0, 2\frac{\tilde{\gamma}^{13}\tilde{\gamma}^{12}}{\tilde{\gamma}^{11}\tilde{\gamma}^{11}}, 2\frac{\tilde{\gamma}^{13}\tilde{\gamma}^{13}}{\tilde{\gamma}^{11}\tilde{\gamma}^{11}}, \frac{\tilde{\gamma}^{13}\tilde{\gamma}^{22}}{\tilde{\gamma}^{11}\tilde{\gamma}^{11}}, 2\frac{\tilde{\gamma}^{13}\tilde{\gamma}^{23}}{\tilde{\gamma}^{11}\tilde{\gamma}^{11}}, \frac{\tilde{\gamma}^{13}\tilde{\gamma}^{33}}{\tilde{\gamma}^{11}\tilde{\gamma}^{11}}, \frac{-2 - \tilde{\gamma}_{12}\tilde{\gamma}^{12} - \tilde{\gamma}_{13}\tilde{\gamma}^{13}}{\tilde{\gamma}^{11}}, \\
&\quad -4\frac{\tilde{\gamma}^{12}}{\tilde{\gamma}^{11}\tilde{\gamma}^{11}} + \frac{\tilde{\gamma}_{11}\tilde{\gamma}^{12}}{\tilde{\gamma}^{11}}, -4\frac{\tilde{\gamma}^{13}}{\tilde{\gamma}^{11}\tilde{\gamma}^{11}} + \frac{\tilde{\gamma}_{11}\tilde{\gamma}^{13}}{\tilde{\gamma}^{11}}\Bigg) \\
\boldsymbol{l}_3 &= \Bigg(0, \cdots, 0, \frac{1}{2}\frac{\tilde{\gamma}_{12}}{\tilde{\gamma}^{11}}, \frac{1}{2}\frac{\tilde{\gamma}_{22}}{\tilde{\gamma}^{11}}, \frac{1}{2}\frac{\tilde{\gamma}_{23}}{\tilde{\gamma}^{11}}, \frac{1}{3}\tilde{\gamma}_{12}, -\frac{1}{2}\frac{1}{\tilde{\gamma}^{11}} + \frac{1}{3}\tilde{\gamma}_{12}\frac{\tilde{\gamma}^{12}}{\tilde{\gamma}^{11}}, \frac{1}{3}\tilde{\gamma}_{12}\frac{\tilde{\gamma}^{13}}{\tilde{\gamma}^{11}}, \\
&\quad 0, 0, 0, 0, 0, 0, 0, -\frac{\tilde{\gamma}^{12}}{\tilde{\gamma}^{11}}, 0, 0, 0, 0, 0, -\frac{\tilde{\gamma}^{13}}{\tilde{\gamma}^{11}}, 0, 0, 0, 0, \tilde{\gamma}_{12}, \\
&\quad \frac{1}{2}\frac{1}{\tilde{\gamma}^{11}} + \tilde{\gamma}_{12}\frac{\tilde{\gamma}^{12}}{\tilde{\gamma}^{11}}, \tilde{\gamma}_{12}\frac{\tilde{\gamma}^{13}}{\tilde{\gamma}^{11}}\Bigg) \\
\boldsymbol{l}_4 &= \Bigg(0, \cdots, 0, \frac{1}{2}\frac{\tilde{\gamma}_{13}}{\tilde{\gamma}^{11}}, \frac{1}{2}\frac{\tilde{\gamma}_{23}}{\tilde{\gamma}^{11}}, \frac{1}{2}\frac{\tilde{\gamma}_{33}}{\tilde{\gamma}^{11}}, \frac{1}{3}\tilde{\gamma}_{13}, \frac{1}{3}\tilde{\gamma}_{13}\frac{\tilde{\gamma}^{12}}{\tilde{\gamma}^{11}}, -\frac{1}{2}\frac{1}{\tilde{\gamma}^{11}} + \frac{1}{3}\tilde{\gamma}_{13}\frac{\tilde{\gamma}^{13}}{\tilde{\gamma}^{11}}, \\
&\quad 0, 0, 0, 0, 0, 0, 0, 0, -\frac{\tilde{\gamma}^{12}}{\tilde{\gamma}^{11}}, 0, 0, 0, 0, 0, -\frac{\tilde{\gamma}^{13}}{\tilde{\gamma}^{11}}, 0, 0, 0, \tilde{\gamma}_{13}, \\
&\quad \tilde{\gamma}_{13}\frac{\tilde{\gamma}^{12}}{\tilde{\gamma}^{11}}, \frac{1}{2}\frac{1}{\tilde{\gamma}^{11}} + \tilde{\gamma}_{13}\frac{\tilde{\gamma}^{13}}{\tilde{\gamma}^{11}}\Bigg) \\
\boldsymbol{l}_5 &= (0, 0, 0, 0, 0, 0, 0, 0, 0, 0, 0, 0, 0, 1, 0, \cdots, 0) \\
\boldsymbol{l}_6 &= (0, 0, 0, 0, 0, 0, 0, 0, 0, 0, 0, 0, 0, 0, 1, 0, \cdots, 0) \\
\boldsymbol{l}_7 &= (0, 0, 0, 0, 0, 0, 0, 0, 0, 0, 0, 0, 0, 0, 0, 0, 0, 0, 0, 0, 0, 1, 0, \cdots, 0) \\
\boldsymbol{l}_8 &= (0, \cdots, 0, 1, 0, 0, 0, 0, 0, 0, 0, 0, 0, 0, 0, 0, 0) \\
\boldsymbol{l}_9 &= (0, \cdots, 0, 1, 0, 0, 0, 0, 0, 0, 0, 0, 0, 0, 0, 0, 0) \\
\boldsymbol{l}_{10} &= (0, \cdots, 0, 1, 0, 0, 0, 0, 0, 0, 0, 0, 0, 0, 0, 0, 0) \\
\boldsymbol{l}_{11} &= (0, \cdots, 0, 1, 0, 0, 0, 0, 0, 0, 0, 0, 0, 0, 0, 0, 0) \\
\boldsymbol{l}_{12} &= (0, \cdots, 1, 0, 0, 0, 0, 0, 0, 0, 0, 0, 0) \\
\boldsymbol{l}_{13} &= (0, \cdots, 0, 1, 0, 0, 0, 0, 0, 0, 0, 0, 0) \\
\boldsymbol{l}_{14} &= (0, \cdots, 0, 1, 0, 0, 0, 0, 0, 0, 0, 0) \\
\boldsymbol{l}_{15} &= (0, \cdots, 0, 1, 0, 0, 0, 0, 0, 0, 0) \\
\boldsymbol{l}_{16} &= (0, \cdots, 0, 1, 0, 0, 0, 0, 0, 0) \\
\boldsymbol{l}_{17} &= (0, \cdots, 0, 1, 0, 0, 0, 0) \\
\boldsymbol{l}_{18} &= (0, \cdots, 0, 1, 0, 0, 0) \\
\boldsymbol{l}_{19} &= \left(0, 0, 0, 0, 0, 0, 0, 0, 0, 0, 0, \frac{1}{3}, \frac{1}{3}\frac{\tilde{\gamma}^{12}}{\tilde{\gamma}^{11}}, \frac{1}{3}\frac{\tilde{\gamma}^{13}}{\tilde{\gamma}^{11}}, 0, \cdots, 0, 1, 0, 0\right) \\
\boldsymbol{l}_{20} &= (0, \cdots, 0, 1, 0) \\
\boldsymbol{l}_{21} &= (0, \cdots, 0, 1)
\end{aligned}
$$

$$
\begin{aligned}
\boldsymbol{l}_{22,23} = \Bigg(& 0,0,0,0,0,0,0,0, \mp\frac{1}{3\sqrt{\tilde{\gamma}^{11}}(e^2-1)e\phi}, \frac{1}{6\tilde{\gamma}^{11}(e^2-1)}, 0,0,0,0,0, \\
& -\frac{\tilde{\gamma}^{11}}{6(e^2-1)}, -\frac{\tilde{\gamma}^{12}}{3(e^2-1)}, -\frac{\tilde{\gamma}^{13}}{3(e^2-1)}, -\frac{\tilde{\gamma}^{22}}{6(e^2-1)}, -\frac{\tilde{\gamma}^{23}}{3(e^2-1)}, \\
& -\frac{\tilde{\gamma}^{33}}{6(e^2-1)}, -\frac{1}{6}\frac{\tilde{\gamma}^{11}\tilde{\gamma}^{12}}{\tilde{\gamma}^{11}(e^2-1)}, -\frac{1}{3}\frac{\tilde{\gamma}^{12}\tilde{\gamma}^{12}}{\tilde{\gamma}^{11}(e^2-1)}, -\frac{1}{3}\frac{\tilde{\gamma}^{13}\tilde{\gamma}^{12}}{\tilde{\gamma}^{11}(e^2-1)}, \\
& -\frac{1}{6}\frac{\tilde{\gamma}^{22}\tilde{\gamma}^{12}}{\tilde{\gamma}^{11}(e^2-1)}, -\frac{1}{3}\frac{\tilde{\gamma}^{23}\tilde{\gamma}^{12}}{\tilde{\gamma}^{11}(e^2-1)}, -\frac{1}{6}\frac{\tilde{\gamma}^{33}\tilde{\gamma}^{12}}{\tilde{\gamma}^{11}(e^2-1)}, -\frac{1}{6}\frac{\tilde{\gamma}^{11}\tilde{\gamma}^{13}}{\tilde{\gamma}^{11}(e^2-1)}, \\
& -\frac{1}{3}\frac{\tilde{\gamma}^{12}\tilde{\gamma}^{13}}{\tilde{\gamma}^{11}(e^2-1)}, -\frac{1}{3}\frac{\tilde{\gamma}^{13}\tilde{\gamma}^{13}}{\tilde{\gamma}^{11}(e^2-1)}, -\frac{1}{6}\frac{\tilde{\gamma}^{22}\tilde{\gamma}^{13}}{\tilde{\gamma}^{11}(e^2-1)}, \frac{1}{3}\frac{\tilde{\gamma}^{23}\tilde{\gamma}^{13}}{\tilde{\gamma}^{11}(e^2-1)}, \\
& -\frac{1}{6}\frac{\tilde{\gamma}^{33}\tilde{\gamma}^{13}}{\tilde{\gamma}^{11}(e^2-1)}, \frac{2}{3}\frac{\tilde{\gamma}^{11}}{\tilde{\gamma}^{11}(e^2-1)}, \frac{2}{3}\frac{\tilde{\gamma}^{12}}{\tilde{\gamma}^{11}(e^2-1)}, \frac{2}{3}\frac{\tilde{\gamma}^{13}}{\tilde{\gamma}^{11}(e^2-1)} \Bigg) \\
\boldsymbol{l}_{24,30} = \Bigg(& 0,0,0,0,0,0, \mp\frac{1}{6\phi\sqrt{\tilde{\gamma}^{11}}}, \pm\frac{1}{3\phi(e^2-1)\sqrt{\tilde{\gamma}^{11}}}, -\frac{1}{6(e^2-1)\tilde{\gamma}^{11}}, 0,0, \\
& -\frac{\tilde{\gamma}^{11}}{6\tilde{\gamma}^{11}}, -\frac{\tilde{\gamma}^{12}}{6\tilde{\gamma}^{11}}, -\frac{\tilde{\gamma}^{13}}{6\tilde{\gamma}^{11}}, \frac{\tilde{\gamma}^{11}}{6(e^2-1)}, \frac{\tilde{\gamma}^{12}}{3(e^2-1)}, \frac{\tilde{\gamma}^{13}}{3(e^2-1)}, \frac{\tilde{\gamma}^{22}}{6(e^2-1)}, \\
& \frac{\tilde{\gamma}^{23}}{3(e^2-1)}, \frac{\tilde{\gamma}^{33}}{6(e^2-1)}, \frac{\tilde{\gamma}^{12}\tilde{\gamma}^{11}}{6(e^2-1)\tilde{\gamma}^{11}}, \frac{\tilde{\gamma}^{12}\tilde{\gamma}^{12}}{3(e^2-1)\tilde{\gamma}^{11}}, \frac{\tilde{\gamma}^{12}\tilde{\gamma}^{13}}{3(e^2-1)\tilde{\gamma}^{11}}, \\
& \frac{\tilde{\gamma}^{12}\tilde{\gamma}^{22}}{6(e^2-1)\tilde{\gamma}^{11}}, \frac{\tilde{\gamma}^{12}\tilde{\gamma}^{23}}{3(e^2-1)\tilde{\gamma}^{11}}, \frac{\tilde{\gamma}^{12}\tilde{\gamma}^{33}}{6(e^2-1)\tilde{\gamma}^{11}}, \frac{\tilde{\gamma}^{13}\tilde{\gamma}^{11}}{6(e^2-1)\tilde{\gamma}^{11}}, \\
& \frac{\tilde{\gamma}^{13}\tilde{\gamma}^{12}}{3(e^2-1)\tilde{\gamma}^{11}}, \frac{\tilde{\gamma}^{13}\tilde{\gamma}^{13}}{3(e^2-1)\tilde{\gamma}^{11}}, \frac{\tilde{\gamma}^{13}\tilde{\gamma}^{22}}{6(e^2-1)\tilde{\gamma}^{11}}, \frac{\tilde{\gamma}^{13}\tilde{\gamma}^{23}}{3(e^2-1)\tilde{\gamma}^{11}}, \frac{\tilde{\gamma}^{13}\tilde{\gamma}^{33}}{6(e^2-1)\tilde{\gamma}^{11}}, \\
& -\frac{2}{3}\frac{\tilde{\gamma}^{11}}{(e^2-1)\tilde{\gamma}^{11}}, -\frac{2}{3}\frac{\tilde{\gamma}^{12}}{(e^2-1)\tilde{\gamma}^{11}}, -\frac{2}{3}\frac{\tilde{\gamma}^{13}}{(e^2-1)\tilde{\gamma}^{11}} \Bigg) \\
\boldsymbol{l}_{25,31} = \Bigg(& \mp\frac{\tilde{\gamma}_{12}\tilde{\gamma}^{11}}{6\phi\sqrt{\tilde{\gamma}^{11}}}, \mp\frac{-3+2\tilde{\gamma}_{12}\tilde{\gamma}^{12}}{6\phi\sqrt{\tilde{\gamma}^{11}}}, \mp\frac{\tilde{\gamma}_{12}\tilde{\gamma}^{13}}{3\phi\sqrt{\tilde{\gamma}^{11}}}, \mp\frac{\tilde{\gamma}_{12}\tilde{\gamma}^{22}}{6\phi\sqrt{\tilde{\gamma}^{11}}}, \mp\frac{\tilde{\gamma}_{12}\tilde{\gamma}^{23}}{3\phi\sqrt{\tilde{\gamma}^{11}}}, \\
& \mp\frac{\tilde{\gamma}_{12}\tilde{\gamma}^{33}}{6\phi\sqrt{\tilde{\gamma}^{11}}}, 0, \pm\frac{\tilde{\gamma}_{12}}{3\phi(e^2-1)\sqrt{\tilde{\gamma}^{11}}}, -\frac{(3e^2-1)\tilde{\gamma}_{12}}{12(e^2-1)\tilde{\gamma}^{11}}, -\frac{\tilde{\gamma}_{22}}{4\tilde{\gamma}^{11}}, -\frac{\tilde{\gamma}_{23}}{4\tilde{\gamma}^{11}}, \\
& -\frac{\tilde{\gamma}_{12}\tilde{\gamma}^{11}}{6\tilde{\gamma}^{11}}, \frac{1}{4\tilde{\gamma}^{11}} - \frac{\tilde{\gamma}_{12}\tilde{\gamma}^{12}}{6\tilde{\gamma}^{11}}, -\frac{\tilde{\gamma}_{12}\tilde{\gamma}^{13}}{6\tilde{\gamma}^{11}}, \frac{\tilde{\gamma}_{12}\tilde{\gamma}^{11}}{6(e^2-1)}, \frac{1}{2} + \frac{\tilde{\gamma}_{12}\tilde{\gamma}^{12}}{3(e^2-1)}, \frac{\tilde{\gamma}_{12}\tilde{\gamma}^{13}}{3(e^2-1)}, \\
& \frac{\tilde{\gamma}_{12}\tilde{\gamma}^{22}}{6(e^2-1)}, \frac{\tilde{\gamma}_{12}\tilde{\gamma}^{23}}{3(e^2-1)}, \frac{\tilde{\gamma}_{12}\tilde{\gamma}^{33}}{6(e^2-1)}, \frac{\tilde{\gamma}_{12}\tilde{\gamma}^{12}\tilde{\gamma}^{11}}{6(e^2-1)\tilde{\gamma}^{11}}, \frac{1}{2}\frac{\tilde{\gamma}^{12}}{\tilde{\gamma}^{11}} + \frac{\tilde{\gamma}_{12}\tilde{\gamma}^{12}\tilde{\gamma}^{12}}{3(e^2-1)\tilde{\gamma}^{11}}, \\
& \frac{\tilde{\gamma}_{12}\tilde{\gamma}^{12}\tilde{\gamma}^{13}}{3(e^2-1)\tilde{\gamma}^{11}}, \frac{\tilde{\gamma}_{12}\tilde{\gamma}^{12}\tilde{\gamma}^{22}}{6(e^2-1)\tilde{\gamma}^{11}}, \frac{\tilde{\gamma}_{12}\tilde{\gamma}^{12}\tilde{\gamma}^{23}}{3(e^2-1)\tilde{\gamma}^{11}}, \frac{\tilde{\gamma}_{12}\tilde{\gamma}^{12}\tilde{\gamma}^{33}}{6(e^2-1)\tilde{\gamma}^{11}}, \frac{\tilde{\gamma}_{12}\tilde{\gamma}^{13}\tilde{\gamma}^{11}}{6(e^2-1)\tilde{\gamma}^{11}}, \\
& \frac{1}{2}\frac{\tilde{\gamma}^{13}}{\tilde{\gamma}^{11}} + \frac{\tilde{\gamma}_{12}\tilde{\gamma}^{13}\tilde{\gamma}^{12}}{3(e^2-1)\tilde{\gamma}^{11}}, \frac{\tilde{\gamma}_{12}\tilde{\gamma}^{13}\tilde{\gamma}^{13}}{3(e^2-1)\tilde{\gamma}^{11}}, \frac{\tilde{\gamma}_{12}\tilde{\gamma}^{13}\tilde{\gamma}^{22}}{6(e^2-1)\tilde{\gamma}^{11}}, \frac{\tilde{\gamma}_{12}\tilde{\gamma}^{13}\tilde{\gamma}^{23}}{3(e^2-1)\tilde{\gamma}^{11}}, \\
& \frac{\tilde{\gamma}_{12}\tilde{\gamma}^{13}\tilde{\gamma}^{33}}{6(e^2-1)\tilde{\gamma}^{11}}, -\frac{(1+3e^2)\tilde{\gamma}_{12}\tilde{\gamma}^{11}}{6(e^2-1)\tilde{\gamma}^{11}}, -\frac{(1+3e^2)\tilde{\gamma}_{12}\tilde{\gamma}^{12}}{6(e^2-1)\tilde{\gamma}^{11}} - \frac{1}{4\tilde{\gamma}^{11}}, \\
& -\frac{(1+3e^2)\tilde{\gamma}_{12}\tilde{\gamma}^{13}}{6(e^2-1)\tilde{\gamma}^{11}} \Bigg)
\end{aligned}
$$

$$
\begin{aligned}
\boldsymbol{l}_{26,32} = \Bigg(& \mp\frac{\tilde{\gamma}_{13}\tilde{\gamma}^{11}}{6\phi\sqrt{\tilde{\gamma}^{11}}}, \mp\frac{\tilde{\gamma}_{13}\tilde{\gamma}^{12}}{3\phi\sqrt{\tilde{\gamma}^{11}}}, \mp\frac{-3+2\tilde{\gamma}_{13}\tilde{\gamma}^{13}}{6\phi\sqrt{\tilde{\gamma}^{11}}}, \mp\frac{\tilde{\gamma}_{13}\tilde{\gamma}^{22}}{6\phi\sqrt{\tilde{\gamma}^{11}}}, \mp\frac{\tilde{\gamma}_{13}\tilde{\gamma}^{23}}{3\phi\sqrt{\tilde{\gamma}^{11}}}, \\
& \mp\frac{\tilde{\gamma}_{13}\tilde{\gamma}^{33}}{6\phi\sqrt{\tilde{\gamma}^{11}}}, 0, \pm\frac{\tilde{\gamma}_{13}}{3\phi(e^2-1)\sqrt{\tilde{\gamma}^{11}}}, -\frac{(3e^2-1)\tilde{\gamma}_{13}}{12(e^2-1)\tilde{\gamma}^{11}}, -\frac{\tilde{\gamma}_{23}}{4\tilde{\gamma}^{11}}, -\frac{\tilde{\gamma}_{33}}{4\tilde{\gamma}^{11}}, \\
& -\frac{\tilde{\gamma}_{13}\tilde{\gamma}^{11}}{6\tilde{\gamma}^{11}}, -\frac{\tilde{\gamma}_{13}\tilde{\gamma}^{12}}{6\tilde{\gamma}^{11}}, \frac{1}{4\tilde{\gamma}^{11}} - \frac{\tilde{\gamma}_{13}\tilde{\gamma}^{13}}{6\tilde{\gamma}^{11}}, \frac{\tilde{\gamma}_{13}\tilde{\gamma}^{11}}{6(e^2-1)}, \frac{\tilde{\gamma}_{13}\tilde{\gamma}^{12}}{3(e^2-1)}, \\
& \frac{1}{2} + \frac{\tilde{\gamma}_{13}\tilde{\gamma}^{13}}{3(e^2-1)}, \frac{\tilde{\gamma}_{13}\tilde{\gamma}^{22}}{6(e^2-1)}, \frac{\tilde{\gamma}_{13}\tilde{\gamma}^{23}}{3(e^2-1)}, \frac{\tilde{\gamma}_{13}\tilde{\gamma}^{33}}{6(e^2-1)}, \frac{\tilde{\gamma}_{13}\tilde{\gamma}^{12}\tilde{\gamma}^{11}}{6(e^2-1)\tilde{\gamma}^{11}}, \\
& \frac{\tilde{\gamma}_{13}\tilde{\gamma}^{12}\tilde{\gamma}^{12}}{3(e^2-1)\tilde{\gamma}^{11}}, \frac{1}{2}\frac{\tilde{\gamma}^{12}}{\tilde{\gamma}^{11}} + \frac{\tilde{\gamma}_{13}\tilde{\gamma}^{12}\tilde{\gamma}^{13}}{3(e^2-1)\tilde{\gamma}^{11}}, \frac{\tilde{\gamma}_{13}\tilde{\gamma}^{12}\tilde{\gamma}^{22}}{6(e^2-1)\tilde{\gamma}^{11}}, \frac{\tilde{\gamma}_{13}\tilde{\gamma}^{12}\tilde{\gamma}^{23}}{3(e^2-1)\tilde{\gamma}^{11}}, \\
& \frac{\tilde{\gamma}_{13}\tilde{\gamma}^{12}\tilde{\gamma}^{33}}{6(e^2-1)\tilde{\gamma}^{11}}, \frac{\tilde{\gamma}_{13}\tilde{\gamma}^{13}\tilde{\gamma}^{11}}{6(e^2-1)\tilde{\gamma}^{11}}, \frac{\tilde{\gamma}_{13}\tilde{\gamma}^{13}\tilde{\gamma}^{12}}{3(e^2-1)\tilde{\gamma}^{11}}, \frac{1}{2}\frac{\tilde{\gamma}^{13}}{\tilde{\gamma}^{11}} + \frac{\tilde{\gamma}_{13}\tilde{\gamma}^{13}\tilde{\gamma}^{13}}{3(e^2-1)\tilde{\gamma}^{11}}, \\
& \frac{\tilde{\gamma}_{13}\tilde{\gamma}^{13}\tilde{\gamma}^{22}}{6(e^2-1)\tilde{\gamma}^{11}}, \frac{\tilde{\gamma}_{13}\tilde{\gamma}^{13}\tilde{\gamma}^{23}}{3(e^2-1)\tilde{\gamma}^{11}}, \frac{\tilde{\gamma}_{13}\tilde{\gamma}^{13}\tilde{\gamma}^{33}}{6(e^2-1)\tilde{\gamma}^{11}}, -\frac{(1+3e^2)\tilde{\gamma}_{13}\tilde{\gamma}^{11}}{6(e^2-1)\tilde{\gamma}^{11}}, \\
& -\frac{(1+3e^2)\tilde{\gamma}_{13}\tilde{\gamma}^{12}}{6(e^2-1)\tilde{\gamma}^{11}}, -\frac{(1+3e^2)\tilde{\gamma}_{13}\tilde{\gamma}^{13}}{6(e^2-1)\tilde{\gamma}^{11}} - \frac{1}{4\tilde{\gamma}^{11}} \Bigg) \\
\boldsymbol{l}_{27,33} = \Bigg(& \mp\frac{\tilde{\gamma}_{22}\tilde{\gamma}^{11}}{6\phi\sqrt{\tilde{\gamma}^{11}}}, \mp\frac{\tilde{\gamma}_{22}\tilde{\gamma}^{12}}{3\phi\sqrt{\tilde{\gamma}^{11}}}, \mp\frac{\tilde{\gamma}_{22}\tilde{\gamma}^{13}}{3\phi\sqrt{\tilde{\gamma}^{11}}}, \mp\frac{-3+\tilde{\gamma}_{22}\tilde{\gamma}^{22}}{6\phi\sqrt{\tilde{\gamma}^{11}}}, \mp\frac{\tilde{\gamma}_{22}\tilde{\gamma}^{23}}{3\phi\sqrt{\tilde{\gamma}^{11}}}, \\
& \mp\frac{\tilde{\gamma}_{22}\tilde{\gamma}^{33}}{6\phi\sqrt{\tilde{\gamma}^{11}}}, 0, \pm\frac{\tilde{\gamma}_{22}}{3\phi(e^2-1)\sqrt{\tilde{\gamma}^{11}}}, \frac{-\tilde{\gamma}_{22}}{6(e^2-1)\tilde{\gamma}^{11}}, 0, 0, -\frac{\tilde{\gamma}_{22}\tilde{\gamma}^{11}}{6\tilde{\gamma}^{11}}, \\
& -\frac{\tilde{\gamma}_{22}\tilde{\gamma}^{12}}{6\tilde{\gamma}^{11}}, -\frac{\tilde{\gamma}_{22}\tilde{\gamma}^{13}}{6\tilde{\gamma}^{11}}, \frac{\tilde{\gamma}_{22}\tilde{\gamma}^{11}}{6(e^2-1)}, \frac{\tilde{\gamma}_{22}\tilde{\gamma}^{12}}{3(e^2-1)}, \frac{\tilde{\gamma}_{22}\tilde{\gamma}^{13}}{3(e^2-1)}, \frac{1}{2} + \frac{\tilde{\gamma}_{22}\tilde{\gamma}^{22}}{6(e^2-1)}, \\
& \frac{\tilde{\gamma}_{22}\tilde{\gamma}^{23}}{3(e^2-1)}, \frac{\tilde{\gamma}_{22}\tilde{\gamma}^{33}}{6(e^2-1)}, \frac{\tilde{\gamma}_{22}\tilde{\gamma}^{12}\tilde{\gamma}^{11}}{6(e^2-1)\tilde{\gamma}^{11}}, \frac{\tilde{\gamma}_{22}\tilde{\gamma}^{12}\tilde{\gamma}^{12}}{3(e^2-1)\tilde{\gamma}^{11}}, \frac{\tilde{\gamma}_{22}\tilde{\gamma}^{12}\tilde{\gamma}^{13}}{3(e^2-1)\tilde{\gamma}^{11}}, \\
& \frac{1}{2}\frac{\tilde{\gamma}^{12}}{\tilde{\gamma}^{11}} + \frac{\tilde{\gamma}_{22}\tilde{\gamma}^{12}\tilde{\gamma}^{22}}{6(e^2-1)\tilde{\gamma}^{11}}, \frac{\tilde{\gamma}_{22}\tilde{\gamma}^{12}\tilde{\gamma}^{23}}{3(e^2-1)\tilde{\gamma}^{11}}, \frac{\tilde{\gamma}_{22}\tilde{\gamma}^{12}\tilde{\gamma}^{33}}{6(e^2-1)\tilde{\gamma}^{11}}, \\
& \frac{\tilde{\gamma}_{22}\tilde{\gamma}^{13}\tilde{\gamma}^{11}}{6(e^2-1)\tilde{\gamma}^{11}}, \frac{\tilde{\gamma}_{22}\tilde{\gamma}^{13}\tilde{\gamma}^{12}}{3(e^2-1)\tilde{\gamma}^{11}}, \frac{\tilde{\gamma}_{22}\tilde{\gamma}^{13}\tilde{\gamma}^{13}}{3(e^2-1)\tilde{\gamma}^{11}}, \frac{1}{2}\frac{\tilde{\gamma}^{13}}{\tilde{\gamma}^{11}} + \frac{\tilde{\gamma}_{22}\tilde{\gamma}^{13}\tilde{\gamma}^{22}}{6(e^2-1)\tilde{\gamma}^{11}}, \\
& \frac{\tilde{\gamma}_{22}\tilde{\gamma}^{13}\tilde{\gamma}^{23}}{3(e^2-1)\tilde{\gamma}^{11}}, \frac{\tilde{\gamma}_{22}\tilde{\gamma}^{13}\tilde{\gamma}^{33}}{6(e^2-1)\tilde{\gamma}^{11}}, \\
& -\frac{(1+3e^2)\tilde{\gamma}_{22}\tilde{\gamma}^{11}}{6(e^2-1)\tilde{\gamma}^{11}}, -\frac{(1+3e^2)\tilde{\gamma}_{22}\tilde{\gamma}^{12}}{6(e^2-1)\tilde{\gamma}^{11}}, -\frac{(1+3e^2)\tilde{\gamma}_{22}\tilde{\gamma}^{13}}{6(e^2-1)\tilde{\gamma}^{11}} \Bigg)
\end{aligned}
$$

$$
\begin{aligned}
\boldsymbol{l}_{28,34} = \Bigg(& \mp\frac{\tilde{\gamma}_{23}\tilde{\gamma}^{11}}{6\phi\sqrt{\tilde{\gamma}^{11}}}, \mp\frac{\tilde{\gamma}_{23}\tilde{\gamma}^{12}}{3\phi\sqrt{\tilde{\gamma}^{11}}}, \mp\frac{\tilde{\gamma}_{23}\tilde{\gamma}^{13}}{3\phi\sqrt{\tilde{\gamma}^{11}}}, \mp\frac{\tilde{\gamma}_{23}\tilde{\gamma}^{22}}{6\phi\sqrt{\tilde{\gamma}^{11}}}, \mp\frac{-3+2\tilde{\gamma}_{23}\tilde{\gamma}^{23}}{6\phi\sqrt{\tilde{\gamma}^{11}}}, \\
& \mp\frac{\tilde{\gamma}_{23}\tilde{\gamma}^{33}}{6\phi\sqrt{\tilde{\gamma}^{11}}}, 0, \pm\frac{\tilde{\gamma}_{23}}{3\phi(e^2-1)\sqrt{\tilde{\gamma}^{11}}}, \frac{-\tilde{\gamma}_{23}}{6(e^2-1)\tilde{\gamma}^{11}}, 0, 0, -\frac{\tilde{\gamma}_{23}\tilde{\gamma}^{11}}{6\tilde{\gamma}^{11}}, \\
& -\frac{\tilde{\gamma}_{23}\tilde{\gamma}^{12}}{6\tilde{\gamma}^{11}}, -\frac{\tilde{\gamma}_{23}\tilde{\gamma}^{13}}{6\tilde{\gamma}^{11}}, \frac{\tilde{\gamma}_{23}\tilde{\gamma}^{11}}{6(e^2-1)}, \frac{\tilde{\gamma}_{23}\tilde{\gamma}^{12}}{3(e^2-1)}, \frac{\tilde{\gamma}_{23}\tilde{\gamma}^{13}}{3(e^2-1)}, \frac{\tilde{\gamma}_{23}\tilde{\gamma}^{22}}{6(e^2-1)}, \\
& \frac{1}{2}+\frac{\tilde{\gamma}_{23}\tilde{\gamma}^{23}}{3(e^2-1)}, \frac{\tilde{\gamma}_{23}\tilde{\gamma}^{33}}{6(e^2-1)}, \frac{\tilde{\gamma}_{23}\tilde{\gamma}^{12}\tilde{\gamma}^{11}}{6(e^2-1)\tilde{\gamma}^{11}}, \frac{\tilde{\gamma}_{23}\tilde{\gamma}^{12}\tilde{\gamma}^{12}}{3(e^2-1)\tilde{\gamma}^{11}}, \frac{\tilde{\gamma}_{23}\tilde{\gamma}^{12}\tilde{\gamma}^{13}}{3(e^2-1)\tilde{\gamma}^{11}}, \\
& \frac{\tilde{\gamma}_{23}\tilde{\gamma}^{12}\tilde{\gamma}^{22}}{6(e^2-1)\tilde{\gamma}^{11}}, \frac{1}{2}\frac{\tilde{\gamma}^{12}}{\tilde{\gamma}^{11}}+\frac{\tilde{\gamma}_{23}\tilde{\gamma}^{12}\tilde{\gamma}^{23}}{3(e^2-1)\tilde{\gamma}^{11}}, \frac{\tilde{\gamma}_{23}\tilde{\gamma}^{12}\tilde{\gamma}^{33}}{6(e^2-1)\tilde{\gamma}^{11}}, \\
& \frac{\tilde{\gamma}_{23}\tilde{\gamma}^{13}\tilde{\gamma}^{11}}{6(e^2-1)\tilde{\gamma}^{11}}, \frac{\tilde{\gamma}_{23}\tilde{\gamma}^{13}\tilde{\gamma}^{12}}{3(e^2-1)\tilde{\gamma}^{11}}, \frac{\tilde{\gamma}_{23}\tilde{\gamma}^{13}\tilde{\gamma}^{13}}{3(e^2-1)\tilde{\gamma}^{11}}, \frac{\tilde{\gamma}_{23}\tilde{\gamma}^{13}\tilde{\gamma}^{22}}{6(e^2-1)\tilde{\gamma}^{11}}, \\
& \frac{1}{2}\frac{\tilde{\gamma}^{13}}{\tilde{\gamma}^{11}}+\frac{\tilde{\gamma}_{23}\tilde{\gamma}^{13}\tilde{\gamma}^{23}}{3(e^2-1)\tilde{\gamma}^{11}}, \frac{\tilde{\gamma}_{23}\tilde{\gamma}^{13}\tilde{\gamma}^{33}}{6(e^2-1)\tilde{\gamma}^{11}}, \\
& -\frac{(1+3e^2)\tilde{\gamma}_{23}\tilde{\gamma}^{11}}{6(e^2-1)\tilde{\gamma}^{11}}, -\frac{(1+3e^2)\tilde{\gamma}_{23}\tilde{\gamma}^{12}}{6(e^2-1)\tilde{\gamma}^{11}}, -\frac{(1+3e^2)\tilde{\gamma}_{23}\tilde{\gamma}^{13}}{6(e^2-1)\tilde{\gamma}^{11}} \Bigg) \\
\boldsymbol{l}_{29,35} = \Bigg(& \mp\frac{\tilde{\gamma}_{33}\tilde{\gamma}^{11}}{6\phi\sqrt{\tilde{\gamma}^{11}}}, \mp\frac{\tilde{\gamma}_{33}\tilde{\gamma}^{12}}{3\phi\sqrt{\tilde{\gamma}^{11}}}, \mp\frac{\tilde{\gamma}_{33}\tilde{\gamma}^{13}}{3\phi\sqrt{\tilde{\gamma}^{11}}}, \mp\frac{\tilde{\gamma}_{33}\tilde{\gamma}^{22}}{6\phi\sqrt{\tilde{\gamma}^{11}}}, \mp\frac{\tilde{\gamma}_{33}\tilde{\gamma}^{23}}{3\phi\sqrt{\tilde{\gamma}^{11}}}, \\
& \mp\frac{-3+\tilde{\gamma}_{33}\tilde{\gamma}^{33}}{6\phi\sqrt{\tilde{\gamma}^{11}}}, 0, \pm\frac{\tilde{\gamma}_{33}}{3\phi(e^2-1)\sqrt{\tilde{\gamma}^{11}}}, -\frac{\tilde{\gamma}_{33}}{6(e^2-1)\tilde{\gamma}^{11}}, 0, 0, -\frac{\tilde{\gamma}_{33}\tilde{\gamma}^{11}}{6\tilde{\gamma}^{11}}, \\
& -\frac{\tilde{\gamma}_{33}\tilde{\gamma}^{12}}{6\tilde{\gamma}^{11}}, -\frac{\tilde{\gamma}_{33}\tilde{\gamma}^{13}}{6\tilde{\gamma}^{11}}, \frac{\tilde{\gamma}_{33}\tilde{\gamma}^{11}}{6(e^2-1)}, \frac{\tilde{\gamma}_{33}\tilde{\gamma}^{12}}{3(e^2-1)}, \frac{\tilde{\gamma}_{33}\tilde{\gamma}^{13}}{3(e^2-1)}, \frac{\tilde{\gamma}_{33}\tilde{\gamma}^{22}}{6(e^2-1)}, \\
& \frac{\tilde{\gamma}_{33}\tilde{\gamma}^{23}}{3(e^2-1)}, \frac{1}{2}+\frac{\tilde{\gamma}_{33}\tilde{\gamma}^{33}}{6(e^2-1)}, \frac{\tilde{\gamma}_{33}\tilde{\gamma}^{12}\tilde{\gamma}^{11}}{6(e^2-1)\tilde{\gamma}^{11}}, \frac{\tilde{\gamma}_{33}\tilde{\gamma}^{12}\tilde{\gamma}^{12}}{3(e^2-1)\tilde{\gamma}^{11}}, \frac{\tilde{\gamma}_{33}\tilde{\gamma}^{12}\tilde{\gamma}^{13}}{3(e^2-1)\tilde{\gamma}^{11}}, \\
& \frac{\tilde{\gamma}_{33}\tilde{\gamma}^{12}\tilde{\gamma}^{22}}{6(e^2-1)\tilde{\gamma}^{11}}, \frac{\tilde{\gamma}_{33}\tilde{\gamma}^{12}\tilde{\gamma}^{23}}{3(e^2-1)\tilde{\gamma}^{11}}, \frac{1}{2}\frac{\tilde{\gamma}^{12}}{\tilde{\gamma}^{11}}+\frac{\tilde{\gamma}_{33}\tilde{\gamma}^{12}\tilde{\gamma}^{33}}{6(e^2-1)\tilde{\gamma}^{11}}, \frac{\tilde{\gamma}_{33}\tilde{\gamma}^{13}\tilde{\gamma}^{11}}{6(e^2-1)\tilde{\gamma}^{11}}, \\
& \frac{\tilde{\gamma}_{33}\tilde{\gamma}^{13}\tilde{\gamma}^{12}}{3(e^2-1)\tilde{\gamma}^{11}}, \frac{\tilde{\gamma}_{33}\tilde{\gamma}^{13}\tilde{\gamma}^{13}}{3(e^2-1)\tilde{\gamma}^{11}}, \frac{\tilde{\gamma}_{33}\tilde{\gamma}^{13}\tilde{\gamma}^{22}}{6(e^2-1)\tilde{\gamma}^{11}}, \frac{\tilde{\gamma}_{33}\tilde{\gamma}^{13}\tilde{\gamma}^{23}}{3(e^2-1)\tilde{\gamma}^{11}}, \\
& \frac{1}{2}\frac{\tilde{\gamma}^{13}}{\tilde{\gamma}^{11}}+\frac{\tilde{\gamma}_{33}\tilde{\gamma}^{13}\tilde{\gamma}^{33}}{6(e^2-1)\tilde{\gamma}^{11}}, -\frac{(1+3e^2)\tilde{\gamma}_{33}\tilde{\gamma}^{11}}{6(e^2-1)\tilde{\gamma}^{11}}, -\frac{(1+3e^2)\tilde{\gamma}_{33}\tilde{\gamma}^{12}}{6(e^2-1)\tilde{\gamma}^{11}}, \\
& -\frac{(1+3e^2)\tilde{\gamma}_{33}\tilde{\gamma}^{13}}{6(e^2-1)\tilde{\gamma}^{11}} \Bigg)
\end{aligned}
$$

Similar results can be obtained for the x_2 and x_3 directions.

Since the FO-CCZ4 system has only real eigenvalues and a complete set of linearly independent eigenvectors (and the matrix of eigenvectors is uniformly bounded) proves the strong hyperbolicity of the system. Note that the eigenvectors $\boldsymbol{r}_{22,23}$ are only linearly independent of $\boldsymbol{r}_{24,\cdots 35}$ if $e \neq 1$.

The analysis presented above is limited to the case of the harmonic slicing and zero shift. In principle it would be desirable to prove hyperbolicity for the choice of Gamma driver and 1+log slicing, since these are the gauge conditions effectively employed in realistic simulations of *e.g.* binary black holes and binary neutron stars. At the moment however we have been able to prove strong hyperbolicity for general lapse and shift conditions and general spatial metrics

only as long as one of the three independent off-diagonal components of the three-metric is zero. When considering the Gamma driver shift condition in particular, we have checked numerically that the system matrix is diagonalizable for a wide set of spacetimes, including the perturbed Minkowski metric, the Schwarzschild metric and the Kerr metric. On the basis of these fuindings we conjecture that the system is strongly hyperbolic in general, but an analytical proof of this statement is unfortunately still missing.

4.4.4 Numerical implementation and tests

In the following subsections the results of a battery of standard tests is presented, exploring the ability of the FO-CCZ4 formulation to carry out long-term stable evolutions of a number of different spacetimes. For this purpose we employ the path-conservative ADER-DG method with WENO subcell limiting described in section 3.5.1 (recall that one of the goals in developing FO-CCZ4 is to derive a firsto order formulation suitable for discretization with DG methods). In every test case we set initially $\Theta = 0$, $\hat{\Gamma}^i = \tilde{\Gamma}^i$ and $b^i = 0$, and the algebraic constraints on the unit determinant of $\tilde{\gamma}_{ij}$ and the zero trace of $\tilde{A}_{ij}$ have been rigorously enforced in the discrete solution $\boldsymbol{u}_h$ at the beginning of each time-step. However hey have not been enforced during the computation of the intermediate time-steps of the space-time predictor $\boldsymbol{q}_h$. For comparison, in the very common case of a semidiscrete scheme evolved in time with a high-order Runge-Kutta (RK) time integrator, our choice corresponds to to enforcing the constraints after a full time-step, but not in the RK intermediate stages. We therefore set $\tau \to \infty$ and thus neglect the corresponding source terms. In tests involving black holes, the lower limit on the lapse is set to 10^{-20}. In the following the notation P_N to indicate an ADER-DG scheme using piecewise polynomials of degree N is employed.

If not specified otherwise the HLLEM method described below is used to define the numerical fluxes at element boundaries. This choice allows to reduce the numerical dissipation of the ADER-DG method for the quantities evolved via ODEs, *i.e.* for α, β^i, $\tilde{\gamma}_{ij}$ and ϕ. So in alternative to the Rusanov scheme of section 3.5.1 we also employ the recently-proposed path-conservative HLLEM method (Dumbser and Balsara, 2016) (a generalization of the original HLLEM method of Einfeldt et al. (1991)) and for which the jump terms on the element boundary read

$$\begin{aligned}\mathcal{D}^-\left(\boldsymbol{q}^-,\boldsymbol{q}^+\right)\cdot\boldsymbol{n} = &-\frac{s_L}{s_R-s_L}\left(\int_0^1 \boldsymbol{A}(\boldsymbol{\psi})\cdot\boldsymbol{n}\mathrm{d}s\right)\left(\boldsymbol{q}^+-\boldsymbol{q}^-\right)\\ &+\frac{s_L s_R}{s_R-s_L}\left(\boldsymbol{q}^+-\boldsymbol{q}^-\right)-\frac{s_L s_R}{s_R-s_L}\boldsymbol{R}_*\boldsymbol{\delta}_*\boldsymbol{L}_*\left(\boldsymbol{q}^+-\boldsymbol{q}^-\right),\end{aligned} \tag{4.40}$$

with

$$\boldsymbol{\delta}_* = \boldsymbol{I}_{11\times 11} - \frac{\boldsymbol{\Lambda}_*^-}{s_L} - \frac{\boldsymbol{\Lambda}_*^+}{s_R}, \quad \text{and} \quad \boldsymbol{\Lambda}_*^{\pm} = \frac{1}{2}\left(\boldsymbol{\Lambda}_* \pm |\boldsymbol{\Lambda}_*|\right). \tag{4.41}$$

In the preceding equations $\boldsymbol{R}_*$ and $\boldsymbol{L}_*$ are the matrices containing only the right and left eigenvectors of the characteristic fields associated with the eigenvalues $\boldsymbol{\Lambda}_*$ that one wants to resolve exactly in the HLLEM Riemann solver.

These internal waves are none other than the 11 stationary contact waves associated with the 11 ODEs for α, β^i, ϕ and $\tilde{\gamma}_{ij}$: their wave speed is zero and thus $\boldsymbol{\Lambda}_* = 0$ and $\boldsymbol{\delta}_* = \boldsymbol{I}_{11\times 11}$. The associated 11 eigenvectors are the unit vectors, hence $\boldsymbol{R}_* = \boldsymbol{I}_{58\times 11}$ and $\boldsymbol{L}_* = \boldsymbol{I}_{11\times 58}$. With the left and right signal speeds simply chosen as $s_L = -s_{\max}$ and $s_R = +s_{\max}$ and computing $s_{\max}$ as in equation (3.68), the HLLEM scheme takes the same form of equation (3.66) but with a viscosity matrix given by

$$\boldsymbol{\Theta}_{\text{HLLEM}} = s_{\max}\left(\boldsymbol{I}_{58\times 58} - \boldsymbol{I}_{58\times 11}\boldsymbol{I}_{11\times 58}\right) . \tag{4.42}$$

Linearized gravitational-wave test

Firstly we test FO-CCZ4 in a simple one-dimensional wave-propagation test problem in the linearized gravity regime. The setup of this test follows the one described by Alcubierre et al. (2004b). We choose a computational domain $\Omega = [-0.5, 0.5]$ with periodic boundary conditions in the x direction. Two simulations are run until a final time of $t = 1000$, one using 4 P_5 elements (*i.e.* a total of 24 degrees of freedom) and one using 2 P_9 elements (*i.e.* 20 degrees of freedom). Since no discontinuities or singularities are present, we run this test with the unlimited version of the ADER-DG scheme, *i.e.* switching of the WENO subcell limiter. The exact solution for the metric is given in this case by

$$\mathrm{d}s^2 = -\mathrm{d}t^2 + \mathrm{d}x^2 + (1+h)\mathrm{d}y^2 + (1-h)\mathrm{d}z^2 ,$$

with $h := \epsilon \sin(2\pi(x-t))$. We choose the wave amplitude $\epsilon = 10^{-8}$, small enough so that terms $\mathcal{O}(\epsilon^2)$ can be neglected, *i.e.* the linear regime. Given that the shift is identically zero in the metric (4.4.4) ($\beta^i = 0$), we set $s = 0$ in the system and employ the harmonic slicing $g(\alpha) = 1$. Also $K_0 = 0$ and $c = 0$ are set and we switch off the damping terms of the system, setting $\kappa_1 = \kappa_2 = \kappa_3 = \eta = 0$.

Note that in the case of $s = 0$ and harmonic slicing, it is necessary to set $e > 1$ in order to get a strongly hyperbolic system. We select the value $e = 2$. From the metric (4.4.4), the the extrinsic curvature reduces to $K_{ij} = -\frac{1}{2}\partial_t \gamma_{ij}/\alpha$, resulting in $K_{xx} = K_{xy} = K_{xz} = K_{yz} = 0$, $K_{yy} = -\frac{1}{2}\partial_t h$ and $K_{zz} = +\frac{1}{2}\partial_t h$. From this information, the conformal factor ϕ, the conformal spatial metric $\tilde{\gamma}_{ij}$, the traceless conformal extrinsic curvature $\tilde{A}_{ij}$ and all auxiliary variables can be computed by a direct calculation according to their definitions, completing the setup of the initial data.

In figure 4.2 the temporal evolution of the Hamiltonian and momentum constraints is shown, as well as the errors of the algebraic constraints on the determinant of the conformal metric and on the trace of $\tilde{A}_{ij}$. A comparison of the extrinsic-curvature component $\tilde{A}_{22}$ with the exact solution is provided at the final time $t = 1000$, showing overall an excellent agreement between numerical and exact solution. The quality of the results obtained with the ADER-DG scheme and FO-CCZ4 formulation, is significantly superior to the results shown in Alcubierre et al. (2004b) for the same test problem using a finite difference scheme, despite the test setup in Alcubierre et al. (2004b) employing many more grid points (between 50 and 200) compared to the mesh used in these simulations. Note that a meaningful comparison between high order finite-difference schemes and DG schemes must be made taking into account

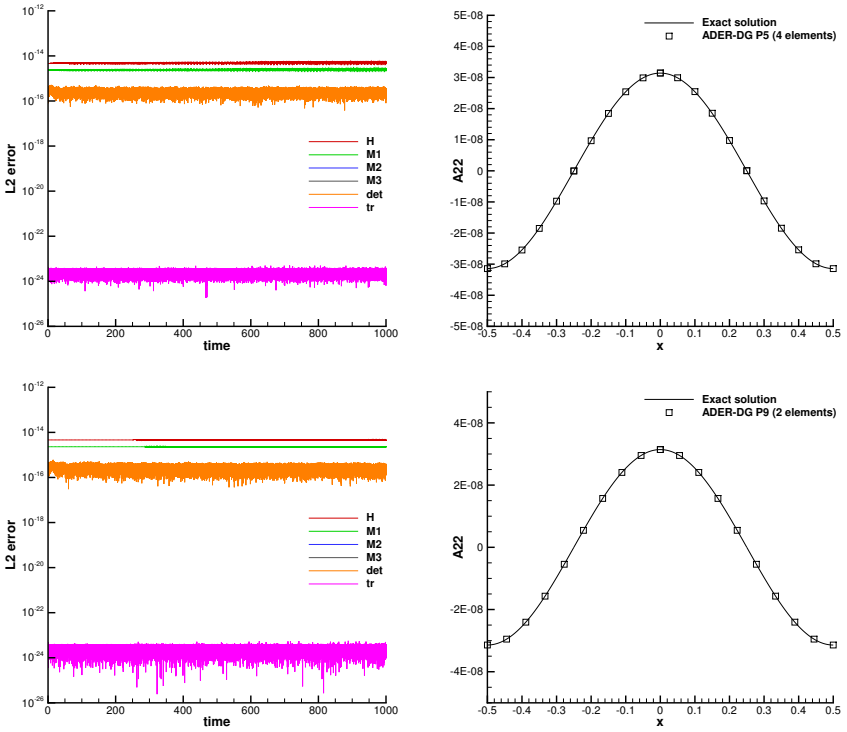

Figure 4.2: Linearized gravitational-wave test using an ADER-DG P_5 scheme with 4 elements (top row) and an ADER-DG P_9 scheme with only 2 elements (bottom row). The temporal evolution of the constraints (left column) is shown together with the waveform for the component $\tilde{A}_{22}$ of the traceless conformal extrinsic curvature after 1000 crossing times at time $t = 1000$ (right column). *Figure reproduced from Dumbser et al. (2017).*

the number of points per wavelength for finite-difference methods and degrees of freedom per wavelength for DG schemes, rather than *e.g.* the size of DG elements.

Gauge-wave test

The gauge-wave test problem has also been suggested by Alcubierre et al. (2004b). The metric in this case is

$$\mathrm{d}s^2 = -H(x,t)\mathrm{d}t^2 + H(x,t)\mathrm{d}x^2 + \mathrm{d}y^2 + \mathrm{d}z^2 \,,$$

with $H(x,t) := 1 - A\sin\left(2\pi(x-t)\right)$. Again zero shift is implied, therefore we use $s = 0$ together with harmonic slicing, *i.e.* $g(\alpha) = 1$. In this case too the undamped version of the FO-CCZ4 is used, in particular we set $\kappa_1 = \kappa_2 = \kappa_3 = \eta = 0$ and $e = 2$. The computational domain is two-dimensional, $\Omega = [-0.5, 0.5] \times [-0.05, 0.05]$ with periodic boundary conditions in all directions. Because the shift is identically zero, the extrinsic curvature is again given by

$K_{ij} = -\partial_t \gamma_{ij}/(2\alpha)$, *i.e.* $K_{yy} = K_{zz} = K_{xy} = K_{xz} = K_{yz} = 0$ and the remaining primary variables are

$$\phi^2 = H^{-1/3}, \qquad \alpha = \sqrt{H}, \qquad K_{xx} = -\pi A \frac{\cos\left(2\pi(x-t)\right)}{\sqrt{1 - A\sin\left(2\pi(x-t)\right)}}.$$

We set in this case too $K_0 = 0$ and $c = 0$. The auxiliary variables can be directly obtained from their definitions.

Initially the test was run with a perturbation amplitude of $A = 0.1$ until $t = 1000$, using the unlimited ADER-DG P_3 scheme and 100×10 elements covering the computational domain. Figure 4.3 shows the ADMD constraints violations as a function of time. Clearly only a very moderate growth of the constraints, sublinear in time, is present. It is worth emphasizing that despite using the undamped version of the FO-CCZ4 system, a stable evolution is nevertheless obtained. In contrast the original second-order CCZ4 formulation was reported to fail for this test problem in the undamped version, and only the damped CCZ4 system achieved a stable evolution (see Alic et al. (2012) for details). Both the first- and the second-order formulations of the BSSNOK system also fail this test (see Alic et al. (2012); Brown et al. (2012)). In figure 4.3 we also provide a direct comparison of the solution after 1000 crossing times for the conformal factor ϕ, the lapse α, as well as for the trace of the extrinsic curvature K. The overall very good agreement between the numerical solution and the exact one is apparent.

The gauge-wave test has a smooth, nontrivial analytical solution and is also tests the nonlinear regime of the equations, making it ideal to perform a convergence study. To this end, we reran this test with different choices of discretiziation order of the numerical scheme on a sequence of successively refined meshes. To enter the fully non-linear regime, we choose a very large perturbation amplitude of $A = 0.9$. The final simulation time is set to $t = 10$.

The L_2 norm of the error on the conformal factor ϕ, the lapse α and the trace of the extrinsic curvature K, together with the observed order of convergence of the different schemes are summarized in table 4.1. Essentially we observe the expected order of convergence of the scheme (*i.e.* its nominal order) for $N = 3$ and $N = 4$, while superconvergence is observed for $N = 5$ and $N = 7$. This is most likely due to the strong non-linearity of the PDE system, appearing due to the choice of $A = 0.9$, so that some leading errors may be dominated by quadratic terms in the metric and the conformal factor, which can lead to a faster error decay than $N + 1$ for coarse meshes. We expect that this superconvergence phenomenon would disappear on sufficiently refined meshes; but since the absolute errors are already getting close to machine accuracy on the meshes used here, it is not possible to refine the mesh much more with double-precision arithmetics. For the fifth-order scheme using 100×10 elements a comparison between the numerical and exact solution of the wave profiles for ϕ, α, K and D_{xxx} is displayed in figure 4.4 at the final time $t = 10$: again the agreement between exact and numerical solutions is excellent.

Robust stability test

A staple of spacetime codes test suites, the robust stability test is also taken from Alcubierre et al. (2004b). While in the previous test cases a simple frozen

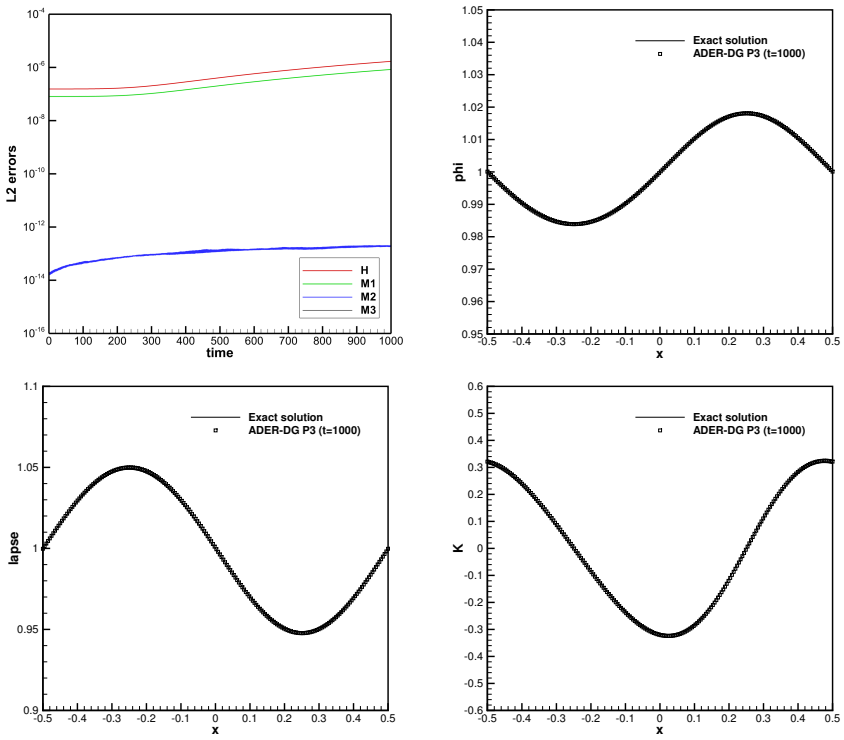

Figure 4.3: Gauge-wave test case with amplitude $A = 0.1$. Temporal evolution of the Hamiltonian and momentum constraints (top left). Comparison of the wave form of the conformal factor ϕ (top right), the lapse α (bottom left) and the trace of the extrinsic curvature K (bottom right) with the exact solution at time $t = 1000$. Since in this test the momentum constraint $M_3 = 0$, it is not plotted when using a logarithmic axis. *Figure reproduced from Dumbser et al. (2017).*

shift condition $\partial_t \beta^i = 0$ was enforced (by setting $s = 0$), here we employ the classical Gamma-driver shift condition, paired to the $1 + \log$ slicing condition, *i.e.* $g(\alpha) = 2/\alpha$. The parameter f of the Gamma driver is set to the typical value of $f = 0.75$ (Alic et al., 2012). We set $e = 2$, $\kappa_1 = \kappa_2 = \kappa_3 = 0$, $K_0 = 0$, $c = 1$ and $\eta = 0$.

As per the test specifications, we start from the flat Minkowski metric

$$\mathrm{d}s^2 = -\mathrm{d}t^2 + \mathrm{d}x^2 + \mathrm{d}y^2 + \mathrm{d}z^2 \,,$$

to which an uniformly distributed random perturbation is added. The perturbation affects all variables of the FO-CCZ4 system. The two-dimensional computational domain chosen is $\Omega = [-0.5, 0.5]^2$ and we run four simulations with the unlimited ADER-DG third-order scheme on four successively refined meshes, consisting of $10\rho \times 10\rho$ elements, corresponding to $40\rho \times 40\rho$ degrees of freedom, where $\rho \in \{1, 2, 4, 8\}$. The perturbation amplitude is $\epsilon = 10^{-7}/\rho^2$, *i.e.* three orders of magnitude larger that those suggested in Alcubierre et al. (2004b).

Table 4.1: Numerical convergence results for the large amplitude gauge-wave test problem with $A = 0.9$ at a final time of $t = 10$. The L_2 errors and corresponding observed convergence order are reported for the variables ϕ, α and K. *Table reproduced from Dumbser et al. (2017).*

$N_x \times N_y$	L_2 error ϕ	$\mathcal{O}(\phi)$	L_2 error α	$\mathcal{O}(\alpha)$	L_2 error K	$\mathcal{O}(K)$
			$N = 3$			
60×6	3.0492E-04		8.9295E-04		1.1176E-02	
80×8	8.5100E-05	4.4	2.4729E-04	4.5	3.1193E-03	4.4
100×10	3.2704E-05	4.3	9.4724E-05	4.3	1.1996E-03	4.3
120×12	1.5158E-05	4.2	4.3826E-05	4.2	5.5628E-04	4.2
			$N = 4$			
60×6	2.1446E-05		3.3190E-05		1.5793E-03	
80×8	3.3430E-06	4.6	6.4050E-06	4.1	1.8676E-04	5.3
100×10	9.8295E-07	4.3	2.1320E-06	3.8	4.8667E-05	4.7
120×12	3.7104E-07	4.4	8.5418E-07	4.1	1.7326E-05	4.6
			$N = 5$			
60×6	4.0478E-05		1.4412E-04		1.3372E-03	
80×8	1.2792E-06	8.5	4.0905E-06	8.8	4.5055E-05	8.4
100×10	1.4713E-07	7.5	4.4742E-07	7.7	5.2647E-06	7.5
120×12	3.0080E-08	7.1	8.8915E-08	7.2	1.0837E-06	7.1
			$N = 7$			
30×3	3.0806E-05		1.2306E-04		9.6081E-04	
40×4	4.7556E-07	14.5	1.8946E-06	14.5	1.2950E-05	15.0
60×6	2.4404E-09	13.0	8.6716E-09	13.3	8.0893E-08	12.5
80×8	1.0925E-10	10.8	3.5637E-10	11.1	3.8987E-09	10.5

The ADM constraint violation as function of time is plotted in figure 4.5 for all four simulations. It can be seen that after an initial decay the constraints remain essentially constant in time for all different grid resolutions, indicating that our FO-CCZ4 system indeed passes the robust stability test with the standard Gamma driver and $1 + \log$ gauge conditions.

Convergence tests on three-dimensional black-hole spacetimes

We then consider the evolution of isolated Schwarzschild and Kerr black holes of mass $M = 1$ in 3D Cartesian Kerr-Schild coordinates, order to perform a convergence study in a realistic, non-trivial scenario. The metric in these coordinates is known analytically and thus the primary variables of our evolution system are given by

$$\alpha = S^{-\frac{1}{2}}, \quad \beta^i = \frac{2H}{S} l_i, \quad \gamma_{ij} = \begin{pmatrix} 1+2Hl_x^2 & 2Hl_xl_y & 2Hl_xl_z \\ 2Hl_xl_y & 1+2Hl_y^2 & 2Hl_yl_z \\ 2Hl_xl_z & 2Hl_yl_z & 1+2Hl_z^2 \end{pmatrix},$$

with

$$H := M\frac{r^3}{r^4+a^2z^2}, \quad S := 1+2H, \quad l_x := \frac{rx+ay}{r^2+a^2}, \quad l_y := \frac{ry-ax}{r^2+a^2}, \quad l_z := \frac{z}{r},$$

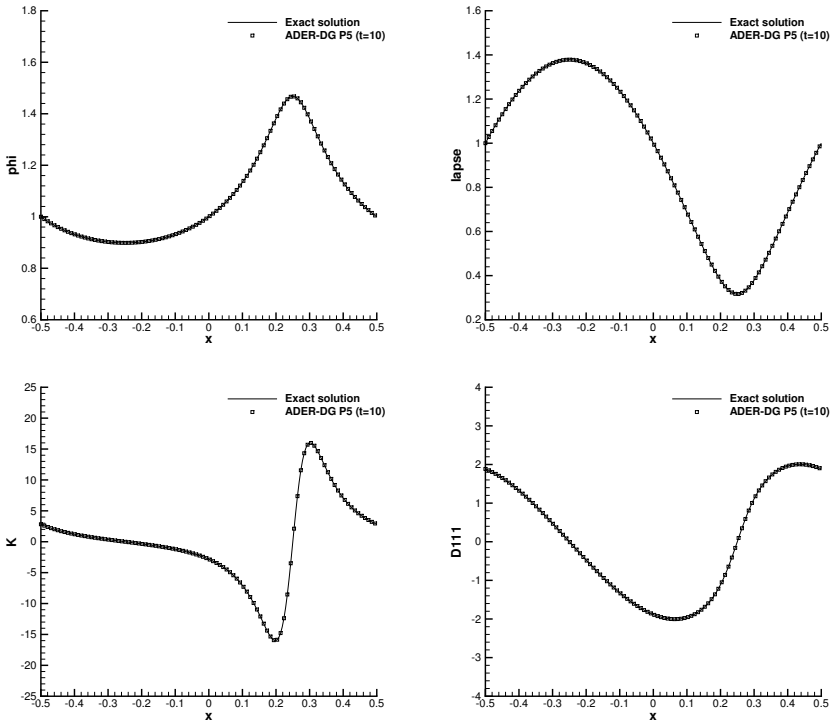

Figure 4.4: Highly nonlinear gauge-wave test case with very large amplitude $A = 0.9$. Comparison of the wave form with the exact solution at time $t = 10$ for an ADER-DG P_5 scheme and 100×10 elements. *Figure reproduced from Dumbser et al. (2017).*

and

$$r := \sqrt{(x^2 + y^2 + z^2 - a^2)/2 + \sqrt{((x^2 + y^2 + z^2 - a^2)/2)^2 + z^2 a^2}}\,.$$

Exploiting the fact that the solution is stationary, *i.e.* $\partial_t \gamma_{ij} = 0$, the extrinsic curvature K_{ij} is computed as follows (Rezzolla and Zanotti, 2013):

$$K_{ij} = \frac{1}{2\alpha} \left(\nabla_i \beta_j + \nabla_j \beta_i \right) .$$

K_0 is set as $K_0 = \left(K - \beta^k \partial_k \alpha\right) / \left(\alpha^2 g(\alpha)\right)$, so that $\partial_t \alpha = 0$ and the Gamma-driver shift condition is simplified to $\partial_t \beta^i = f b^i$, $\partial_t B^i_k = f \partial_k b^i$ and $\partial_t b^i = \partial_t \hat{\Gamma}^i$. This choice of gauge has the consequence that the above exact solution corresponds to a stationary solution of the FO-CCZ4 system. In other words, we remove the advection terms from the evolution equations of the shift β^i and the variable b^i (see also Alcubierre (2008)). The conformal factor ϕ and the auxiliary variables can be computed according to their definition. We choose the computational domain as $\Omega = [1, 5]^3\, M^3$, and as boundary conditions the exact solution, given by the initial condition, is imposed at all times. Note that the BH is in any case centered on the point $x = y = z = 0$, so that we evolve only

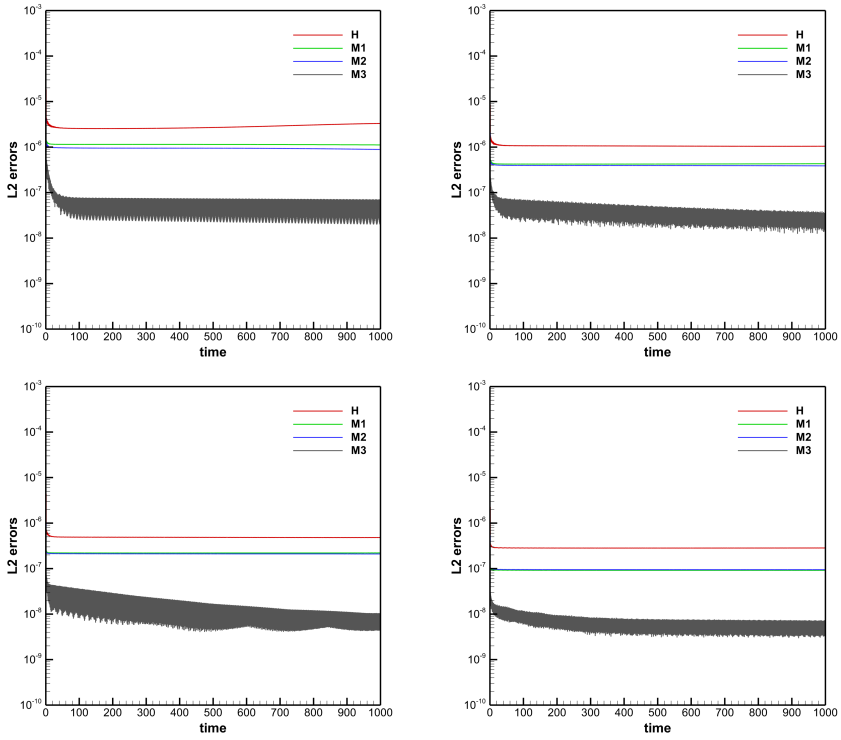

Figure 4.5: Robust stability test case with Gamma-driver shift condition and $1 + \log$ slicing with random initial perturbation of amplitude $10^{-7}/\rho^2$ in all quantities on a sequence of successively refined meshes on the unit square in 2D using an ADER-DG P_3 scheme. Top left: 10×10 elements, corresponding to 40×40 degrees of freedom ($\rho = 1$). Top right: 20×20 elements, corresponding to 80×80 degrees of freedom ($\rho = 2$). Bottom left: 40×40 elements, corresponding to 160×160 degrees of freedom ($\rho = 4$). Bottom right: 80×80 elements, corresponding to 320×320 degrees of freedom ($\rho = 8$). *Figure reproduced from Dumbser et al. (2017).*

a section of the domain offset from the singularity (but encompassing regions both inside and outside of the horizon), *i.e.* we effectively employ excision. We set $e = 2$, $c = 1$, $\eta = 0$, and again employ the undamped CCZ4 system with the $1 + \log$ slicing, *i.e.* we set $\kappa_1 = \kappa_2 = \kappa_3 = 0$, $f = 0.75$ and $g(\alpha) = 2/\alpha$.

Again we perform several simulations with different ADER-DG schemes on a sequence of successively refined meshes, until a final time of $t = 10\,M$. The Rusanov method is used as approximate Riemann solver at the element interfaces. In the case of the Schwarzschild black hole we of course set the dimensionless BH spin $a = 0$, while for the Kerr black hole we choose $a = 0.9$. The numerical convergence rates are reported for both cases in table 4.2, where we observe that the designed order of accuracy $N + 1$ of our high order fully-discrete one-step ADER-DG schemes has been properly reached.

Table 4.2: Numerical convergence results of FO-CCZ4 with simplified gamma-driver for the Schwarzschild black hole (left) and the Kerr black hole (right) in 3D Cartesian Kerr-Schild coordinates at a final time of $t = 10$. The L_2 errors and corresponding observed convergence order are reported for the variables ϕ. *Table reproduced from Dumbser et al. (2017).*

Schwarzschild black hole					
N_x	L_2 error ϕ	$\mathcal{O}(\phi)$	N_x	L_2 error ϕ	$\mathcal{O}(\phi)$
	$N = 3$			$N = 5$	
10	6.2008E-06		5	2.5618E-06	
15	1.2046E-06	4.0	10	3.8444E-08	6.1
20	3.8623E-07	4.0	15	3.1675E-09	6.2
25	1.5837E-07	4.0	20	5.0252E-10	6.4
Kerr black hole					
N_x	L_2 error ϕ	$\mathcal{O}(\phi)$	N_x	L_2 error ϕ	$\mathcal{O}(\phi)$
	$N = 3$			$N = 5$	
10	1.0038E-05		5	2.1336E-06	
15	1.9331E-06	4.1	10	4.7108E-08	5.5
20	5.8999E-07	4.1	15	3.9143E-09	6.1
25	2.3312E-07	4.2	20	7.0393E-10	6.0

Evolution of a single puncture black hole

We next have applied the FO-CCZ4 formulation to a single puncture (*i.e.* Bowen-York initial data) black hole (Brandt and Brügmann, 1997). Again we choose a BH mass of $M = 1$ and a dimensionless spin of $a = 0$ (*i.e.* we evolve a Schwarzschild BH, albeit in a different gauge then the usual one). The black hole is located at the origin of a three-dimensional computational domain $\Omega = [-150, 150]^3\, M^3$ with periodic boundary conditions in all directions. The domain is discretized employing a two-level mesh with grid spacing $\Delta x = \Delta y = \Delta z = 2.5\, M$ within the inner level $\Omega_b = [-15, 15]^3\, M^3$, while $\Delta x = \Delta y = \Delta z = 7.5\, M$ is used in the outer part of the domain. In the innermost region $\Omega_l = [-3, 3]^3\, M^3$, covering the puncture itself, the third-order subcell ADER-WENO finite-volume limiter is activated throughout the entire simulation. In is important to mention that this simulation could only be run by activating the finite-volume subcell limiter, since a scheme more robust than a pure DG one is needed in order to deal with the puncture singularity. Without such a limiter we observed the code crashing after just a few time-steps. In our simulation we use an ADER-DG P_3 scheme ($N = 3$), corresponding to $2N + 1 = 7$ finite-volume subcells per DG element, *i.e.* the effective mesh spacing in terms of points (cell averages) inside the domain Ω_l is $\Delta x = \Delta y = \Delta z = 0.357\, M$. Note that we set up the mesh so that the puncture is located at the boundary of DG elements, and given the location of the degrees of freedom in the subcell grid (see figure 3.4), no grid point coincides with the puncture. We set the FO-CCZ4 parameters to $\kappa_1 = 0.1$, $\kappa_2 = 0$, $\kappa_3 = 0.5$ and $\eta = 0$. The constant μ accounting for the second-order ordering constraints in the evolution of B^i_k is set to $\mu = 1/5$, while for this test we use $c = 1$ and $e = 1$ to be as close as

possible to a standard second-order CCZ4 formulation, where the cleaning of the Hamiltonian constraint is done at the speed of light[2]. For convenience and since the puncture is not moving, we neglect the algebraic source term on the right-hand side of the Gamma-driver equation (4.19b).

The initial data for the metric and the lapse function are computed via a stand alone version of the `TwoPunctures` code (Ansorg et al., 2004), itself a part of the Einstein Toolkit software (Löffler et al., 2012). Explicitly, the lapse is set initially to

$$\alpha = \frac{1}{2}\left(\frac{1-\frac{1}{2}\frac{M}{r^*}}{1+\frac{1}{2}\frac{M}{r^*}}+1\right), \tag{4.43}$$

where $r^* = (r^4 + 10^{-24})^{\frac{1}{4}}$ and r is the coordinate distance of a grid point from the puncture. The auxiliary quantities (which are spatial derivatives of the primary quantities) are obtained via a simple fourth order central finite difference applied to α and γ_{ij}. The shift and the extrinsic curvature are set initially to zero.

The evolution was carried out until a final time of $t = 1000\,M$. Figure 4.6 plots the behaviour in time of the average L_2 error of the ADM constraints, which we define as

$$\overline{L}_2 = \sqrt{\frac{\int_\Omega \epsilon^2 \mathrm{d}\boldsymbol{x}}{\int_\Omega \mathrm{d}\boldsymbol{x}}},$$

where ϵ denotes the local deviation from zero of either the Hamiltonian H constraint or one component of the momentum constraint M_i. Also shown in figure 4.6 are a view of the 3D grid setup and a zoom into the central region, where the lapse function and the shift vector are shown at a time of $t = 200\,M$. Towards the end of the simulation, we note a growth of the constraints, but this may simply be related to our inappropriate and simplistic choice of the boundary conditions. Further research on this topic will be carried out in the future.

These are the first results obtained for a puncture black-hole spacetime using a fully three-dimensional DG finite-element method with AMR and LTS. Previous results obtained with high order DG schemes for black-hole spacetimes were essentially limited to the one-dimensional case (see, *e.g.* Field et al. (2010); Brown et al. (2012); Miller and Schnetter (2017)).

Preliminary results for moving punctures

The last test we performed is an application, albeit only preliminary at this point, of the FO-CCZ4 system to the evolution of a binary system of two moving puncture black holes. We consider a head-on collision of two non-rotating black holes of equal mass $M = 1$ with zero initial linear momentum. The BHs are located at positions $\boldsymbol{x}^- = (-1, 0, 0)$ and $\boldsymbol{x}^+ = (+1, 0, 0)$ on the $x-$axis. The three-dimensional domain is chosen $\Omega = [-25, 25]^3\,M^3$ and flat Minkowski spacetime is used to supplement boundary conditions everywhere and at all times. The FO-CCZ4 parameters are set to $\kappa_1 = 0.1$, $\kappa_2 = 0$, $\kappa_3 = 0.5$, $\eta = 0$ and we choose $c = 1$, $e = 1$ and $\mu = 1/5$. Again the initial metric and the lapse

[2]For the Gamma driver the system is empirically found to be hyperbolic also for the choice $e = 1$.

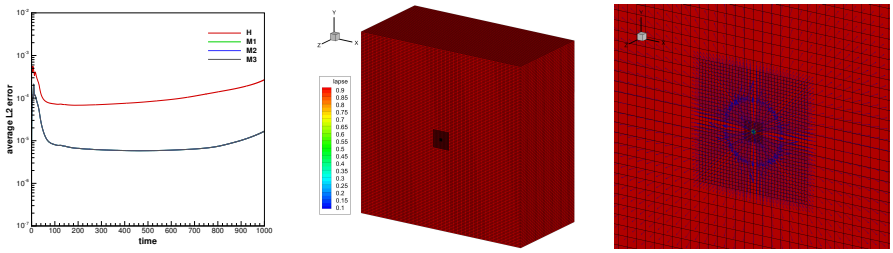

Figure 4.6: Time evolution of the ADM constraints for the single puncture black hole using an ADER-DG P_3 scheme with AMR and ADER-WENO subcell finite-volume limiter until $t = 1000$ (left). Color contours for the lapse at $t = 200$ and grid setup showing the domain Ω, the refined box Ω_b and the zone with active subcell finite-volume limiter Ω_l (center). Zoom into the center region at $t = 200$ with color contours for α and shift vector β^i (right). *Figure reproduced from Dumbser et al. (2017).*

are provided by the `TwoPunctures` code (Ansorg et al., 2004), with the lapse set initially to

$$\alpha = \frac{1}{2}\left(\frac{1 - \frac{1}{2}\frac{m_-}{r_-^*} - \frac{1}{2}\frac{m_+}{r_+^*}}{1 + \frac{1}{2}\frac{m_-}{r_-^*} + \frac{1}{2}\frac{m_+}{r_+^*}} + 1\right), \tag{4.44}$$

where r_-^* and r_+^* (the coordinate distances of a grid point from either puncture) are defined analogously to the previous section and m_- and m_+ are the so called bare masses of the two black holes (see Ansorg et al. (2004)) and in this case are equal. The auxiliary quantities are computed from the primary variables via a fourth-order central finite-difference method. Note that although the punctures are moving, we neglect the algebraic source term on the right-hand side of the Gamma-driver equation (4.19b), ad we use the simple and well-tested Rusanov method as an approximate Riemann solver on the element boundaries. The shift and extrinsic curvature are initially set to zero in this case as well.

The domain is discretized again with a two-level mesh of spacing $\Delta x = \Delta y = \Delta z = 5/12\, M$ within the inner level $\Omega_b = [-2.5, 2.5]^3\, M^3$, while $\Delta x = \Delta y = \Delta z = 1.25\, M$ is used in the outer part of the domain. In the innermost zone $\Omega_l = [-5/3, 5/3]^3\, M^3$ the third-order subcell ADER-WENO finite-volume limiter is activated throughout the entire simulation. As for a single puncture, we use an ADER-DG P_3 scheme ($N = 3$), whose $2N + 1 = 7$ finite-volume subcells lead to an effective mesh spacing inside the domain Ω_l of $\Delta x = \Delta y = \Delta z = 0.0595$. Once again we remark that the use of the finite-volume subcell limiter is essential in order to obtain a stable evolution. The simulation was run until a final time of $t = 40\, M$.

The evolution of the contour surfaces of the lapse and the shift vector are displayed in figure 4.7. The contour surfaces of the conformal factor at the final time as well as the evolution of the ADM constraints violations are depicted in figure 4.8. Clearly, no sign of growth in the violation of the constraints appears, even after the two punctures have merged at $t \simeq 10\, M$.

Although these results are meant as a proof-of-concept rather than as a

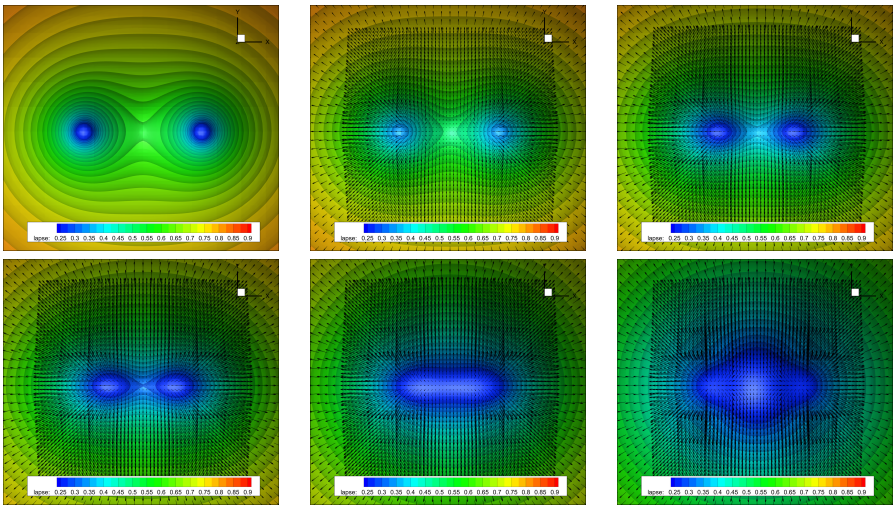

Figure 4.7: Time evolution of the contour surfaces of the lapse α and the shift vector β^i for the head-on collision of two puncture black holes of equal mass $M = 1$ at times $t = 0,\ 5,\ 7,\ 8,\ 10\,M$ and $t = 15\,M$, from top left to bottom right. *Figure reproduced from Dumbser et al. (2017).*

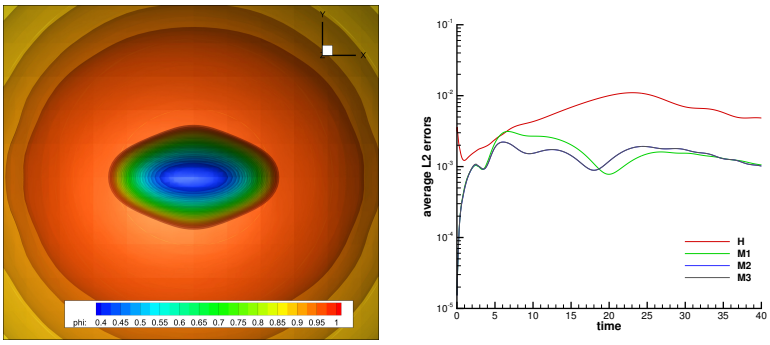

Figure 4.8: Head-on collision of two puncture black holes: contour surfaces of the conformal factor ϕ at time $t = 34\,M$ after the merger (left) and time evolution of the ADM constraints (right). The curves for the second and third momentum constraint almost coincide. *Figure reproduced from Dumbser et al. (2017).*

realistic modelling of the inspiral and merger on binary black-hole systems, they provide convincing evidence that the evolution of binary systems of black holes can be evolved stably with our path-conservative ADER-DG scheme with ADER-WENO subcell finite-volume limiter and the FO-CCZ4 formulation proposed here. A more detailed and systematic investigation, which should include the study of the emission of gravitational waves from the system, as well as a proper way of tracking the BH horizons, will be the subject of future work.

4.4.5 Conclusions

This chapter has presented the work related to FO-CCZ4, a new formulation of the Einstein equations based on the conformal and covariant Z4 (CCZ4) system of Alic et al. (2012), which is strongly hyperbolic and first order in both space and time. The system consists of 58 evolution equations for the vector of state variable given by

$$\boldsymbol{Q}^T := \left(\tilde{\gamma}_{ij}, \ln\alpha, \beta^i, \ln\phi, \tilde{A}_{ij}, K, \Theta, \hat{\Gamma}^i, b^i, A_k, B^i_k, D_{kij}, P_k\right) .$$

To the best of our knowledge, this is the first time that a first-order, strongly hyperbolic formulation of the CCZ4 system has been proposed. The chapter also summarizes the results of numerical tests conducted with the FO-CCZ4 formulation when discretized with a path-conservative ADER-DG numerical method.

The guiding principle in order to obtain a strong hyperbolic formulation of the equation has been the approximate symmetrization of the sparsity pattern of the system matrix, via the appropriate use of various typologies of constraints, with the goal of avoiding the appearance of Jordan blocks that cannot be diagonalized. A second technique employed to obtain the FO-CCZ4 formulation as presented in this chapter is the use of first-order ordering constraints in such a way to reduce the evolution equations for the lapse α, the shift β^i, the conformal metric $\tilde{\gamma}_{ij}$ and the conformal factor ϕ to a system of pure ordinary differential equations (as opposed to PDEs) (Alcubierre, 2008). In other words, whenever differential terms with respect to α, β^i, ϕ and $\tilde{\gamma}_{ij}$ appear, they are replaced by the corresponding auxiliary variables A_k, B^i_k, P_k and D_{kij}, thus becoming algebraic source terms. This choices greatly simplified the hyperbolicity analysis of the FO-CCZ4 system, since the eigenvalues and eigenvectors associated with α, β^i, ϕ and $\tilde{\gamma}_{ij}$ become trivial. A further advantage is that for the rest of the analysis a reduced system of partial differential equations relative to only 47 dynamic variables (namely $\boldsymbol{U} = (\tilde{A}_{ij}, K, \Theta, \hat{\Gamma}^i, b^i, A_k, B^i_k, D_{kij}, P_k)$) can be considered. What's more the system matrix of the reduced system is a function of α, β^i, ϕ and $\tilde{\gamma}_{ij}$ only, which not only substantially simplifies the hyperbolicity analysis but also leads to the important result that all fields of our FO-CCZ4 system are linearly degenerate. This in turn implies that no shock waves can be generated from smooth initial data by evolving it with the FO-CCZ4 system.

In contrast with the first-order Z4 system proposed in Bona et al. (1997); Alic et al. (2009), the FO-CCZ4 system is written in a fully non-conservative form, which is another key idea of the present approach. It's worth pointing out that the above mentioned simplifications are not possible if a conservative formulation of the system is sought, *e.g.* the ones proposed in Bona et al. (1997); Alic et al. (2009). This follows by the fact that the Jacobian $\partial\boldsymbol{F}/\partial\boldsymbol{Q}$ of the flux $\boldsymbol{F}(\boldsymbol{Q})$ would in general depend also on the dynamical variables and the quasi-linear form of the system would also contain differential terms in α, β^i, ϕ and $\tilde{\gamma}_{ij}$. This by construction not the case in the present non-conservative formulation.

Thanks to the choices outlined above we have been able to provide a proof of strong hyperbolicity for completely general lapse and spatial metric for the simple gauge choice $\beta^i = 0$, by a direct explicit calculation of all eigenvalues

and all left and right eigenvectors of the system. While it would be desirable to prove hyperbolicity also for more realistic choices of the shift condition, *e.g.* for the Gamma-driver gauge, at the moment we have only reached a proof for general lapse and shift conditions and general spatial metrics only as long as one of the three independent off-diagonal components of the three-metric is zero. We conjecture that the formulation is strongly hyperbolic in all cases, but a general analytical proof is at present missing and left to future work.

We have implemented numerically the FO-CCZ4 system via a discretization based on a family of high order fully-discrete one-step ADER discontinuous Galerkin (DG) schemes, coupled with an ADER-WENO finite-volume limiter (the latter being necessary in order to deal with the physical singularities arising in the case of black hole spacetimes). The non-conservative nature of the formulation is naturally treated within the DG framework by the use of path-conservative schemes, first proposed by Castro and Parés in the finite-volume context (Castro et al., 2006; Pares, 2006) and later extended also to ADER-DG schemes in Dumbser et al. (2009, 2010). In order to ensure the positivity of the numerical solution of α and ϕ, we have evolve the logarithms of these quantities.

Following a well established practice, we have applied the FO-CCZ4 formulation to a series of standard test cases, *i.e.* a subset of the Apples-with-Apples tests suggested in Alcubierre et al. (2004b), namely the gauge-wave test, the robust stability test and the linear-wave test bed. Besides providing evidence that the new system is able to reproduce accurately and with moderate costs the known analytic solutions, we have carried out numerical convergence studies of the method on the gauge-wave test in the highly nonlinear regime, as well as on further tests involving Schwarzschild and Kerr black holes using 3D Cartesian Kerr-Schild coordinates. We have also provided numerical evidence that the FO-CCZ4 formulation coupled with ADER-DG schemes (with the ADER-WENO finite-volume subcell limiter) is able to perform a long time integration of a single puncture black hole with the usual Gamma driver and $1 + \log$ gauge conditions. Finally we have also shown some first preliminary results for two moving puncture black holes. To the best of our knowledge, the numerical results shown here represent the first simulations of the 3+1 Einstein equations ever done with high order DG and WENO finite-volume schemes on three-dimensional grids.

Future research will concern the extension of the present algorithms to dynamic AMR (adaptive mesh refinement), as well as the extraction of the gravitational waveforms generated by binary black-hole mergers (see Centrella et al. (2010); Bishop and Rezzolla (2016) for reviews) and binary neutron-star mergers (see Baiotti and Rezzolla (2017) for a review), and also the characterization of black hole horizon properties.

Part III

High-order numerical schemes for relativistic hydrodynamics

Chapter 5

The Entropy Limited Hydrodynamics Scheme

5.1 Introduction

In order to study astrophysical systems involving compact objects, such as black holes and neutron stars, large-scale general-relativistic hydrodynamical numerical simulations have been shown to be a very powerful tool (Font, 2008; Shibata and Taniguchi, 2011; Rezzolla and Zanotti, 2013; Martí and Müller, 2015; Shibata, 2016; Baiotti and Rezzolla, 2017; Paschalidis, 2017). Performing such simulations however is a very non-trivial task, which requires dealing with a plethora of different physical, mathematical and computational issues. One of the most challenging of such issues, which can lead to significant differences on the outcome of said simulations, especially when the resolution employed is not very high, is the choice of the numerical method for which is employed in the solution of the relativistic hydrodynamics equations.

As already mentioned in chapter 3, in this context the most commonly used methods are generally known as high-resolution shock-capturing (HRSC) techniques. HRSC methods have been shown in general to be very effective in take care of shocks waves and suppressing spurious oscillations in the numerical solution of PDEs, and have been employed with varying degree of success in astrophysical simulations. Recently much effort has gone into improving these schemes (*e.g.* by employing innovative mesh refinement techniques such as in DeBuhr et al. (2015)) or moving beyond them; one promising and popular alternative is that of discontinuous Galerkin (DG) methods, which have been introduced in section 3.4 and used in obtaining the results of chapter 4. Both "standard" HRSC schemes and their improvements however potentially suffer from a few shortcomings. First they are in general complex to derive and implement, or to extend and modify (*e.g.* in order to increase the formal order of accuracy. This does not apply to DG methods however); they often depend on a large number of a priori unknown coefficients, requiring some degree of optimisation (*e.g.* a typical example being WENO methods); they may lead to load imbalance in parallel implementations as a result of their complexity.

In this chapter an alternative approach, different from the HRSC mindset, is proposed, able to address some of these shortcomings. These alternative

scheme is named "entropy-limited hydrodynamics" (ELH) and we formulate it in a finite-differences framework. This is a variant of the "flux-limiting" FD scheme described in chapter 3, where the underlying concept prescribing how the limiter should be activated and driven is relatively straightforward: to determine which gridpoints are in need of the low-order contribution, we employ a "shock detector", which not only marks regions of the computational domain in need of limiting, but also determines the relative ratio of the high and low-order fluxes.

Such a shock detector is offered by the entropy viscosity function described by Guermond et al. (we refer primarily to Guermond et al. (2011), but see also Guermond and Pasquetti (208); Zingan et al. (2013)), in which the local production of entropy is used to identify shocks. Since entropy is produced only in the presence of shocks, this choice results in a stable method, which is nonetheless able to recover high-order in regions of smooth flow. We have extended the definition of the entropy viscosity function from the classical to the relativistic regime, and rather than a prefactor to additional viscous terms in the hydrodynamical equations, we choose to employ it to drive the lower-order flux in the flux limiting scheme. Therefore in contrast to the approach of Guermond et al. (2011) the underlying equations of relativistic hydrodynamics are not modified in this approach by introducing additional entropy-related terms.

In the following the method itself and the details of our implementation are described, followed by a summary of the results of tests we conducted in order to gauge its behaviour against a standard HRSC method, namely the MP5 scheme (Suresh and Huynh, 1997). This chapter is structured as follows: in sections 5.2 and 5.3 the ELH method and its present implementation are described, while the results of the numerical tests are presented in section 5.4. Conclusions and an outlook are collected in section 5.5.

5.2 Description of the ELH scheme

As mentioned, the ELH scheme belongs to the category of flux-limiting schemes, described in section 3.3.3. Therefore it consists of mainly two building blocks: a function detecting shocks and limiter scheme of the high order fluxes. The lmiter has been described in section 3.3.3. In the following the shock detector is presented.

Since the hybridisation of the high order fluxes with the Lax-Friedrichs ones should be activated only in regions of the flow that are problematic, a criterion to flag such regions is needed. We introduce to this end a regularisation function that we refer to as the "viscosity" ν (see further below on the choice of this name). Hence we redefine the parameter $\theta \in [0, 1]$ in equation (3.54) as

$$\theta := \min \left[\tilde{\theta}, 1 - \frac{1}{2}(\nu_i + \nu_{i+1}) \right] , \tag{5.1}$$

so that the contribution of the Lax-Friedrichs flux depends linearly on the viscosity. The value of the coefficient $\tilde{\theta}$ is the one mentioned in section 3.3.3 to guarantee the positivity of the rest-mass density. It is clear that the choice (5.1) for the limiting coefficient θ results in additional dissipation being inserted

when ν attains large values, as well as in near-vacuum regions. Conversely in regions of smooth flow and away from near vacuum, θ is close to unity, ensuring that the high order flux is dominant over the low order one and preserving the high accuracy of the method.

Naturally the viscosity ν needs to be associated to some property of the flow. To this end we follow the ideas of Guermond et al. (2011) and associate ν to the local specific entropy s. Generally speaking the precise functional form of s on the other thermodynamical and hydrodynamica variables will depend on the EOS of the fluid. In this work we restrict ourselves to the simple case of a perfect fluid with an ideal-fluid EOS (*i.e.* equation (2.17)), implying the following form of the specific entropy (apart from constant multiplicative factors): (Rezzolla and Zanotti, 2013)

$$s = \ln\left(\frac{\epsilon}{\rho^{\Gamma-1}}\right) . \tag{5.2}$$

Clearly the specific entropy satisfies the second law of thermodynamics. We can introduce therefore the entropy residual, or entropy-production rate, $\mathcal{R}$ as

$$\mathcal{R} := \partial_\mu(\rho s u^\mu) \geq 0 . \tag{5.3}$$

The inequality satisfied by $\mathcal{R}$ is a restatement of the second principle of thermodynamics.

The expected behaviour of the entropy residual based on its thermodynamical interpretation is that it cannot decrease in time (for an isolated system) and that is non-null only in very small spatial regions, in the neighbourhood of shocks, in fact ideally expressed a delta function peaked at the location $\boldsymbol{x}_s$ of shocks, *i.e.* $\mathcal{R} \propto \delta(\boldsymbol{x} - \boldsymbol{x}_s)$. A physical justification for this latter expectation is rather simple to motivate. Euler equations generally apply to perfect fluids, and while they can capture non-ideal features (*i.e.* shocks), the description of the latter is only approximate. As long as the flow is smooth and the perfect-fluid approximation holds, all phenomena are reversible and there can be no production of entropy, therefore $\mathcal{R} = 0$. However in those regimes where the perfect-fluid approximation breaks down and non-ideal effects appear, *i.e.* at the location of shocks, the entropy production is nonzero and the entropy jumps locally to a higher value. Since shocks are regions of dimension $N-1$ in spatial manifolds with N spatial dimensions, the entropy residual $\mathcal{R}$ must be a Dirac delta peaked at shock locations for it to provide a finite contribution.

It is therefore a quite natural choice to set the entropy viscosity ν_e proportional to the entropy residual, defining it as

$$\nu_e := c_e \Delta |\mathcal{R}| . \tag{5.4}$$

The absolute value on $\mathcal{R}$ is introduced in the expression since the inequality (5.4) is not guaranteed to be satisfied strictly at the discrete level. In fact $\mathcal{R}$ should approximate a delta function, and is therefore expected to oscillate, reaching potentially negative values in practical numerical applications. In expression (5.4), Δ is the spacing of the mesh, c_e is a positive tunable constant with dimensions of $[\text{time}]^3 \times [\text{temperature}] \times [\text{mass}]^{-1}$, making ν_e dimensionless. Note that despite ν_e not having the dimensions of a physical viscosity, we refer to it nonetheless as the "entropy viscosity", mostly for convenience and in analogy with the very similar quantity defined in Guermond et al. (2011).

An further advantage of this definition of the viscosity is the ability of the resulting scheme to differentiate automatically between shocks and contact discontinuities. This property follows by the observation that at the location of contact discontinuities there is no entropy production and therefore the viscosity there would be zero as well (Rezzolla and Zanotti, 2013).

A potential problem of the definition (5.4) is that it can lead the viscosity reach unbounded high values, since the entropy residual $\mathcal{R}$ is itself not physically upper limited. However the value of θ should not exceed unity, and so the viscosity must not exceed this value as well. To satisfy this requirement and cut-off potentially problematic large values of the entropy viscosity, we set the viscosity to be actually used in the limiter (5.1) as

$$\nu := \min[\nu_e, c_{\max}] \,. \tag{5.5}$$

where ν_e is given by equation (5.4). $c_{\max}$ is a tunable dimensionless coefficient playing the role of an upper limit. In the following we have assumed both c_e and $c_{\max}$ to equal to one in all of the tests presented.

5.3 Implementation details

We employ a rather straightforward numerical implementation for the computation of the entropy residual (5.3). First its definition is rewritten in a way that involves only derivatives of the specific entropy s

$$\mathcal{R} = \partial_\mu(s\rho u^\mu) = s\partial_\mu(\rho u^\mu) + \rho u^\mu \partial_\mu s = \rho u^\mu \partial_\mu s \,, \tag{5.6}$$

where the continuity equation (2.16) was used to obtain the final expression in (5.6). By expressing the 4-velocity u^μ in terms of the fluid three-velocity v^i, we finally write the residual as

$$\mathcal{R} = \rho W \left(\partial_t s + v^i \partial_i s\right) \,. \tag{5.7}$$

In equation (5.7) the spatial derivatives of the specific entropy are approximated by standard centered finite-difference stencil of order $p+1$, where p is the order of the stencil used to approximate the physical fluxes. This restriction on the order of the derivative operators is a consequence of the need to ensure that the viscosity converges to zero fast enough so not to spoil the overall convergence of the scheme at the nominal order. The time derivative in (5.7) is also approximated by finite differences. At every iteration the current value of the specific entropy and the values at the two previous timesteps are combined to compute a second-order approximation of $\partial_t s$ via a one-sided stencil:

$$(\partial_t s)^n = \frac{1}{2\Delta t}\left(3s^n - 4s^{n-1} + s^{n-2}\right) + \mathcal{O}\left((\Delta t)^2\right) \,. \tag{5.8}$$

Note that the time derivative of the specific entropy in equation (5.7) is computed with a low-order method. In principle this could be a limiting factor for the convergence of the overall scheme. In practice we have found that the spatial discretization error dominates over the temporal one. As a consequence the scheme achieves high order convergence as expected. Note also that the high order flux $f^{\rm HO}$ is computed component by component (refer to section

3.3.3 for the description of components vs. characteristic reconstruction). The unlimited reconstruction operators that we employ (namely U5 and U7, (3.37) and (3.38) respectively) are linear in fact linear, and as such they commute with the matrices used to perform the characteristic decomposition. There is therefore no difference in this case between component-by-component and characteristic decomposition. Switching to the much simpler components reconstruction leads to a significant speed-up of the code (up to $\sim 50\%$, depending on the setup of the grid on the computing nodes) with respect to the MP5 scheme, since there is no need to compute the system eigenvectors and apply the resulting matrix (the performance difference is also due to other intrinsic differences in the formulation of the schemes, so that in fact the ELH scheme is somewhat faster than MP5 also when the components reconstruction is employed for the latter). The MP5 reconstruction, being nonlinear, does not commute with the characteristic decomposition. As a result, when using MP5 we always switch to characteristic variables, since this is known to reduce spurious numerical oscillations in high order methods (Suresh and Huynh, 1997).

We choose to further modify the viscosity before using it in equation (5.1). First, because the viscosity is found to be very close to zero in near-vacuum regions, we improve the behaviour of the scheme close to atmosphere values by simply setting the viscosity to some small and constant value ν_v. A grid point x_{ijk} gets assigned this value of the viscosity whenever the rest-mass density at the given point, and at all nearest neighbours, is below a certain threshold ρ_v, *i.e.* if

$$\rho_{i+l,j+m,k+n} < \rho_v \qquad \forall\, l,m,n = -1,0,1$$

then

$$\nu_{ijk} = \nu_v \,.$$

To clarify this point, is useful to rewrite (5.5) slightly:

$$\nu := \begin{cases} \nu_v & \text{if } \rho < \rho_v \\ \min[\nu_e, \nu_{\max}] & \text{elsewhere}\,. \end{cases} \tag{5.9}$$

In all of the numerical tests presented in the following section we have used $\nu_v = 10^{-12}$ and $\rho_v = 10^{-11}\, M_\odot^{-2}$ (*i.e.* the threshold is 5 orders of magnitude larger then the atmosphere floor, $\rho_{\rm atmo} = 10^{-16}\, M_\odot^{-2}$). Secondly (following the original implementation in Guermond et al. (2011)) we introduce a smoothing step which removes unwanted oscillations in the viscosity profile. This is accomplished by applying a five-point stencil of the form

$$\bar{\nu}_{ijk} := \sum_{l=-2}^{2} \sum_{m=-2}^{2} \sum_{n=-2}^{2} a_l\, a_m\, a_n\, \nu_{i+l,j+m,k+n}\,, \tag{5.10}$$

where the coefficients a_l have values $a_0 = 0.58$, $a_{\pm 1} = 0.06$ and $a_{\pm 2} = 0.15$ to the viscosity grid function. The stencil in equation (5.10) is constructed so that it approximates the convolution of a given function with a Gaussian kernel of characteristic cutoff length scale 4 times the grid spacing, in such a way that the residual of the transfer function of the target filter and of its approximation is

minimised over a broad range of wavelengths (see Sagaut and Grohens (1999) for details).

A further advantage follows from the application of this smoothing procedure, in addition to dampening oscillations in the viscosity. In our approach the viscosity is computed once at the beginning of every timestep before its value is used in (5.1), *i.e.* the viscosity is kept constant during the Runge-Kutta substages. Therefore it "lags behind" in time with respect to the solution of the hydrodynamical variables. The smoothing procedure partly addresses this issue, even though in practice we have found that this does not represent a problem in our tests. The smoothing (5.10) also prevents the viscosity to plunge to very small values where it should instead be non negligible. This can happen, *e.g.* close to stellar surfaces as a result of oscillations in the solution. The application of the smoothing operator removes this problem by joining seamlessly the values of the viscosity in the neighbouring points.

5.4 Numerical tests

In this section the results of the tests obtained with the ELH method are reported. In each case we compare the ELH results with those obtained using the monotonicity preserving, fifth-order scheme (MP5). Unless otherwise stated, we couple the ELH method to the fifth-order U5 stencil (3.37), in order to have a fair and meaningful comparison between methods of the same order. In some cases however we employ the seventh-order stencil U7 (3.38). The two variants of the ELH scheme resulting from the choice of a different stencil will be referred to as EL5 and EL7, respectively. It is important to remark that in all tests no attempt was made to tune the coefficients c_e and $c_{\max}$ introduced in section 5.2: they have both been set to unity. Despite this very simple choice, the ELH method is stable and accurate in all cases considered. It however possible, in fact likely, that the curent results could be further improved by careful exploration of the changes in the solution upon a change of c_e and $c_{\max}$; however we leave this exploration to future work.

5.4.1 Special-relativistic tests

This section is concerned mostly with one-dimensional tests, restricted to special-relativistic (as opposed to general-relativistic) hydrodynamics. The metric $g_{\mu\nu}$ is therefore fixed to the flat Minkowski metric $\eta_{\mu\nu}$ and no spacetime evolution is performed.

Smooth nonlinear wave

First, in order to show the accuracy of the scheme, we test it in the case of a smooth solution and measure rigorously its convergence order, so as to show that the entropy-driven limiter does not spoil the convergence properties of the high order method upon which it is built. The test setup has been discussed in Radice and Rezzolla (2012) (itself adapted from Zhang and MacFadyen (2006)). We consider a one-dimensional, large-amplitude, smooth, nonlinear wave with

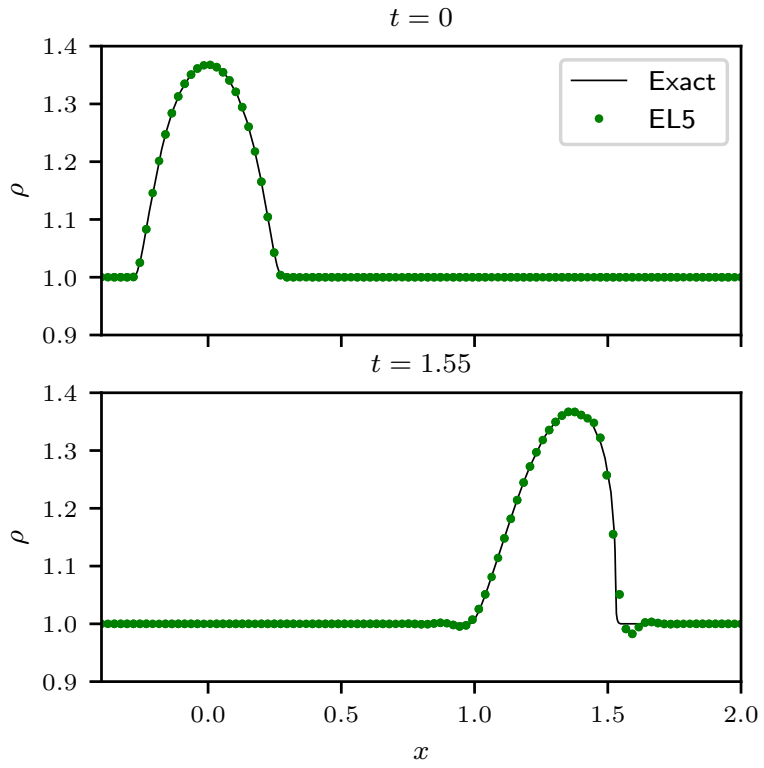

Figure 5.1: Rest-mass density profiles for the smooth nonlinear wave test. The EL5 data shown corresponds to the coarsest resolution of 100 gridpoints over the domain. *Figure reproduced from Guercilena et al. (2017).*

initial rest-mass density profile given by

$$\rho_0(x) = \begin{cases} 1 + \exp\left[-1/(1 - x^2/L^2)\right] & \text{if } |x| < 1 \\ 1 & \text{elsewhere}\,, \end{cases} \tag{5.11}$$

where $L = 0.3$. The initial data employs a polytropic EOS, $p = K\rho^{\tilde{\gamma}}$, with $K = 100$ and $\tilde{\gamma} = 5/3$, and we evolve it in time with the ideal-fluid EOS (2.17) with $\Gamma = 5/3$. Since in this test discontinuities are absent (so that $\tilde{\gamma} = \Gamma$) and there are no stability issues, we use as time integrator the standard fourth-order RK4 method (as opposed to the RK3 SSP method) with a timestep of ~ 0.13 times the grid spacing.

The test has an analytic solution (visible in figure 5.1 with a black solid line) which consists of a wave profile propagating towards the right and "steepening" in the direction of its motion. At time $t_c \simeq 1.6$ the wave turns into a shock. the analytic solution can be computed using the method of characteristics (Anile, 1990) up to the formation of the caustic, on a Lagrangian grid. A sufficiently accurate approximation is obtained by computing it on a very fine grid of 10^5 gridpoints and interpolating the solution using cubic splines on the

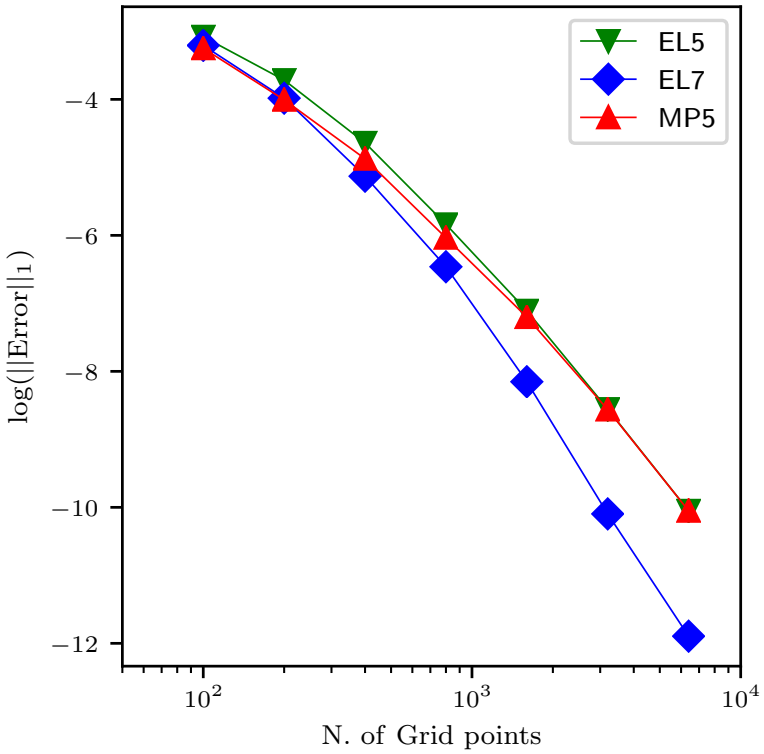

Figure 5.2: L_1-norm of the error on the rest-mass density for the smooth nonlinear-wave test at time $t = 0.8$. *Figure reproduced from Guercilena et al. (2017).*

Eulerian grid. This solution, which we refer to as the "exact" solution, is then the one used as reference against which the numerical solutions are compared.

The test has been performed twice, with both the EL5 and EL7 variants of the ELH method, showing that high order schemes can be employed with great ease in our approach, simply by swapping a lower-order stencil for a higher-order one; this operation is far more demanding in standard finite-volume or finite-differences HRSC schemes.

In figure 5.2 the L_1-norm of the error with respect to the analytic solution at time $t = 0.8$ is shown for the various schemes and at various resolutions. Different resolutions are parametrized by the number of gridpoints used on the x-axis. We have employed a total of seven resolutions, each twice as fine as the preceding one, going from 100 gridpoints up to 6400. At the lowest resolutions all schemes produce very similar deviations from the exact solution, MP5 being the most accurate by a small margin. As the resolution is increased, the gap in accuracy between EL5 and MP5 decreases and disappears at very high resolutions. The error curve for the EL7 scheme, being a higher-order scheme, decreases much more rapidly with resolution: at the highest resolution of 6400 gridpoints its error is two orders of magnitude lower than for the fifth-order

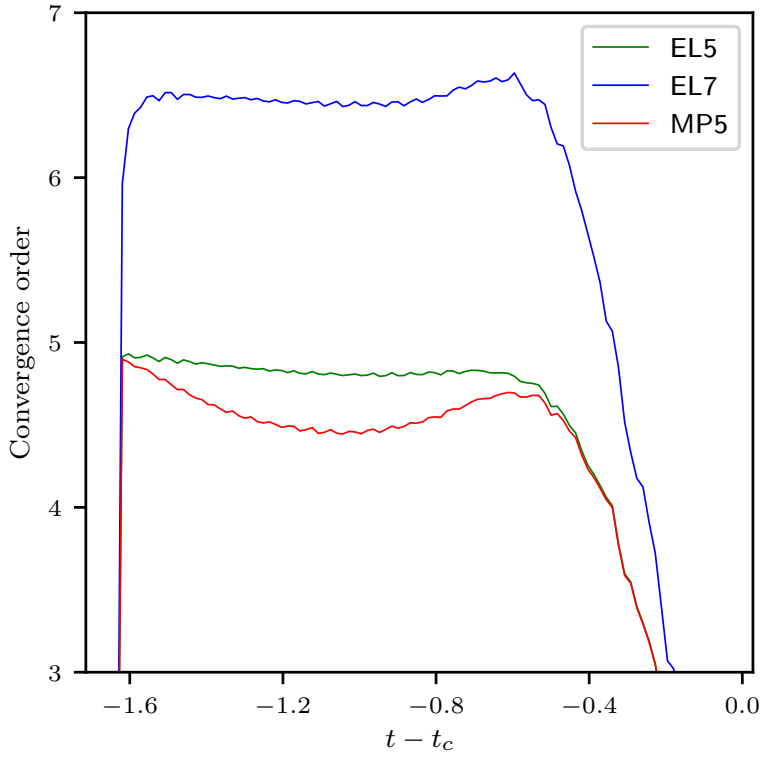

Figure 5.3: Convergence order computed on the smooth nonlinear-wave test as a function of time to caustic formation. *Figure reproduced from Guercilena et al. (2017).*

schemes.

The convergence order of the various schemes has also been explicitly computed using the data at resolutions of 1600 and 3200 gridpoints. The result is shown in figure 5.3 as a function of time, up to the time at which the shock is developed. The computed order should be equal to the nominal order of each scheme as long as the solution is smooth, gradually degrading to first order as the caustic is approached. It can be clearly seen that this description is matched by every scheme. The convergence order of EL5 in particular is almost exactly five. EL7 similarly appears to saturate just below its nominal convergence order of seven. Deviations from the nominal convergence order of each scheme are due to contaminations from other error sources, which become increasingly significant at high resolution. These additional sources of error are the truncation error due to the time-integrator, the accuracy of the inversion from conservative to primitive variables, and the low-order approximation for the evolution of the entropy. It is however clear that the ELH method does not interfere with the convergence properties of the underlying stencil, so that their accuracy can be exploited.

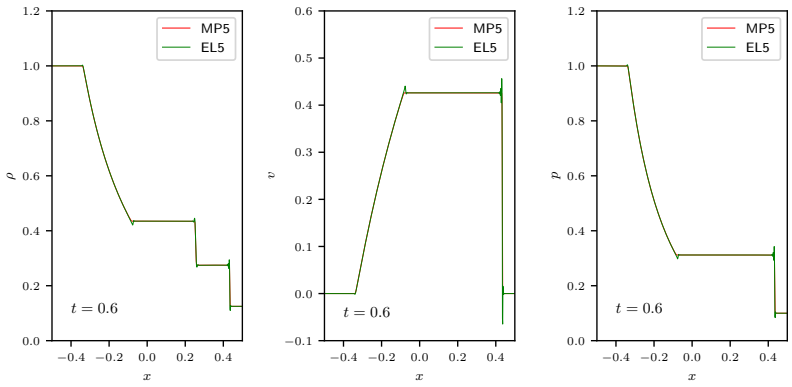

Figure 5.4: Profiles of the rest-mass density (left), velocity (center) and pressure (right) for the special-relativistic Sod test at $t = 0.6$. The solution is computed on a grid of 800 points. The EL5 scheme correctly captures the features of the solution despite oscillations at the discontinuities. *Figure reproduced from Guercilena et al. (2017).*

Shock-tube tests

Shock-tube tests are a standard way of gauging the performance of hydrodynamics codes and their ability to handle discontinuous solutions. As a first shock-tube test the special-relativistic version of the classical Sod test (Sod, 1978) was chosen. The adiabatic index for both the polytropic initial data EOS and the ideal-fluid evolution EOS is in this case $\Gamma = 1.4$ and the right (R) and left (L) initial states are

$$\begin{aligned}(\rho_R, v_R, p_R) &= (0.125, 0, 0.1)\,,\\ (\rho_L, v_L, p_L) &= (1, 0, 1)\,.\end{aligned} \tag{5.12}$$

The analytic solution consists in a left-going rarefaction wave and a right-going shock wave separated by a right-going contact discontinuity. We perform the test with a variety of spatial resolutions ranging from $\Delta x = 0.01$ to $\Delta x = 3.125 \times 10^{-4}$, and a timestep $\Delta t = 0.1\,\Delta x$.

The test results at time $t = 0.6$ are shown in figure 5.4 for the EL5 and MP5 schemes at resolution $\Delta x = 1.25 \times 10^{-3}$. Both schemes capture the main features of the solution as described above, with the shocks being resolved within ~ 3 gridpoints, as are the constant plateaus in the pressure and velocity. The EL5 scheme displays however some oscillations downstream of the shock, plus some over- and undershoots around the location of the discontinuities and in the transition between the rarefaction wave and the surrounding flat regions. The MP5 scheme on the other hand is able to avoid such artefacts. This is not surprising since MP5 is a monotonicity preserving scheme (the number of local maxima and minima cannot increase by effect of this method, therefore over- and undershoots cannot occur by construction) while EL5 is not. Note however that this property of the MP5 scheme is valid only for scalar equations in one spatial dimension. It important to stress that the EL5 scheme is nonetheless indeed stable and that the oscillations that are present in the solution converge

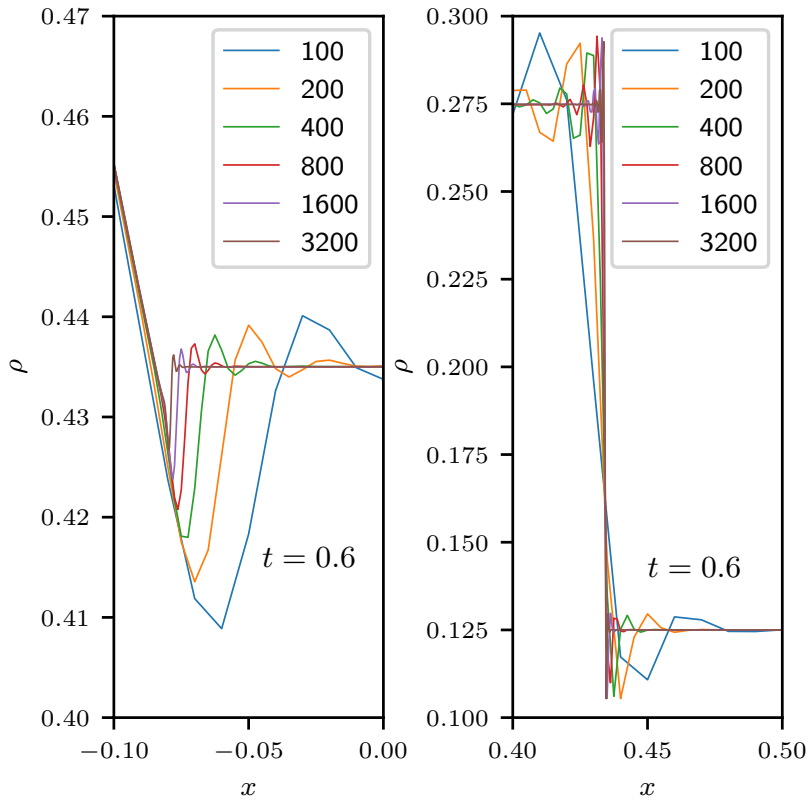

Figure 5.5: Rest-mass density profiles, zoomed on the right edge of the rarefaction wave (left) and on the shock (right) for the special-relativistic Sod test at $t = 0.6$, computed with EL5 at different resolutions (parametrized by the number of points on the x axis). The oscillations in the solution can be seen converging away with resolution. *Figure reproduced from Guercilena et al. (2017).*

away with resolution (see figure 5.5).

The behaviour of the viscosity in this test is displayed in figure 5.6. It develops four well distinct peaks, each corresponding to the four nonlinear waves generated by the Riemann problem, namely: the edges of the rarefaction wave, where the solution is continuous but non-smooth, the contact discontinuity and the shock. The viscosity is higher in correspondence with the shock with respect with the peaks present at the location of the other features. It can also be seen clearly how the peaks in the viscosity sharpen as the resolution is increased, mirroring the decreasing size of the aforementioned features (see figure 5.5), and tending as expected towards a delta function at infinite resolution.

The second shock-tube test selected is a more extreme "blast-wave" test (Martí and Müller, 2003). The adiabatic index used is $\Gamma = 5/3$ and the right and left initial states are

$$\begin{aligned}(\rho_R, v_R, p_R) &= (10^{-3}, 0, 1)\,,\\ (\rho_L, v_L, p_L) &= (10^{-3}, 0, 10^{-5})\,.\end{aligned} \tag{5.13}$$

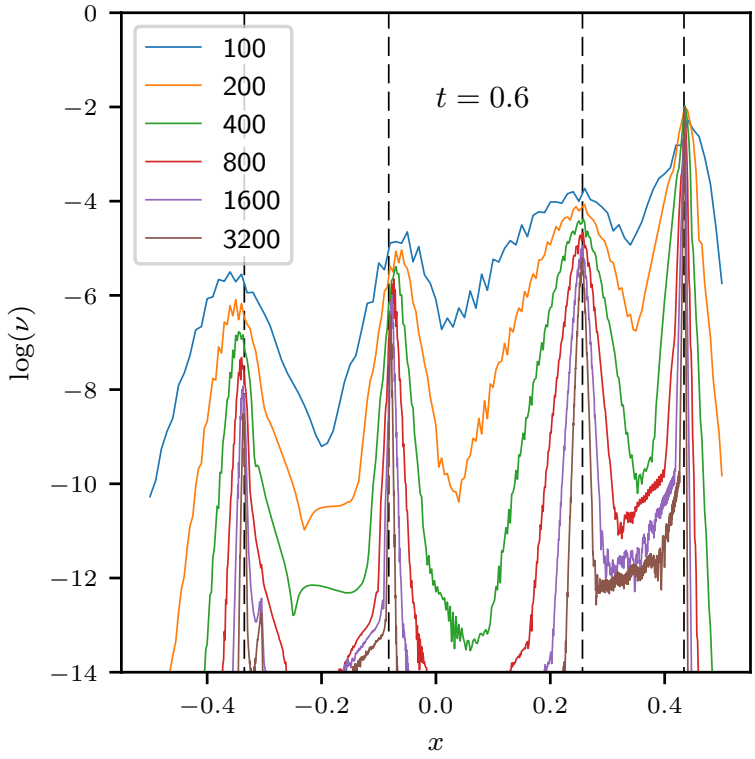

Figure 5.6: Profiles of the viscosity in logarithmic scale for the special-relativistic Sod test at $t = 0.6$, computed with EL5 at different resolutions (parametrized by the number of points on the x axis). The four peaks correspond to the four different features of the solution, *i.e.* from left to right, the edges of the rarefaction wave, the contact discontinuity and the shock (vertical dashed lines highlight their location). As the resolution increases, they tend to delta functions. *Figure reproduced from Guercilena et al. (2017).*

The exact solution consists in a right-going shock wave, followed by a contact discontinuity and a left-going rarefaction wave. The same resolutions and timestep choices as for the Sod test are employed.

Figure 5.7 displays the solution of the blast-wave test at time $t = 0.4$. Note that this is a very extreme test (the pressure has an initial jump of five orders of magnitude) in which the contact discontinuity and shock wave move at essentially the same speed, resulting in a very narrow constant rest-mass density state between the two. The oscillations in the EL5 scheme data are in this case more severe than in the Sod shock-tube test, especially around the shock location. Consequently the solution with the EL5 scheme tends to a decrease of the pressure between the rarefaction wave and the shock wave with respect to the analytical solution. The error is however of $\lesssim 7\,\%$ at most; the MP5 scheme performs better and has a relative error in pressure that is $\sim 1\%$. In both cases, the agreement with the exact solution improves with resolution.

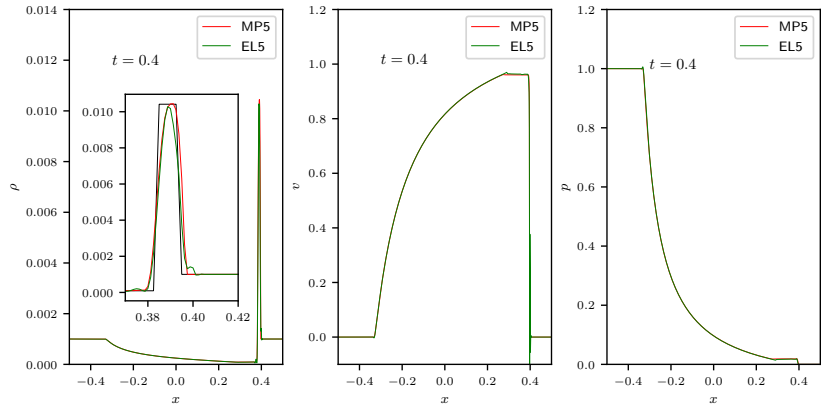

Figure 5.7: Profiles of the rest-mass density (left), velocity (center) and pressure (right) for the special-relativistic blast-wave test at $t = 0.4$. The solution is computed on a grid of 800 points. The inset in the density panel magnifies the blast wave, showing also the exact solution in black. Inversion failures due to oscillations when using the EL5 scheme spoil the quality of the solution. *Figure reproduced from Guercilena et al. (2017).*

Finally a three-dimensional shock-tube problem is performed, involving non-grid-aligned shocks, namely the relativistic-explosion test. The initial data in this case is given by

$$\begin{cases} (\rho, v_i, p) = (1, 0, 1) & \text{if } r \leq 0.4\,, \\ (\rho, v_i, p) = (0.125, 0, 0.1) & \text{otherwise}\,, \end{cases}$$

where r is the distance from the origin. The computational domain is a cube of side 1 centered on the origin, and we use a grid spacing of $\Delta x = 0.01$ and a timestep $\Delta t = 0.1\,\Delta x$. The adiabatic index for this test is again $\Gamma = 1.4$. The features of the solution are similar to those of the Sod test *i.e.* an ingoing rarefaction wave and an outgoing shock, separated by an outgoing contact discontinuity. Note however that because of the spherical symmetry of the test (compared to the planar symmetry in the Sod case), the regions at the two sides of the contact discontinuity are no longer constant states in rest-mass density, velocity and pressure, but posses a radial dependence, which is however smooth.

The rest-mass density for this test at time $t = 0.25$ is shown in figure 5.8, on the (x, y) plane as well as on the x axis. Both EL5 and MP5 perform very similarly, the differences being barely noticeable in the two-dimensional plot. The one-dimensional plot of the x axis profiles reveal that while both schemes capture the features of the solution, as in the Sod test, the EL5 scheme is slightly more oscillatory.

Overall, these shock-tube tests demonstrate how the entropy-driven hybridisation of the high order stencil is sufficient to stabilise the scheme even for discontinuous initial data and it is remarkable that such a simple scheme can achieve good accuracy.

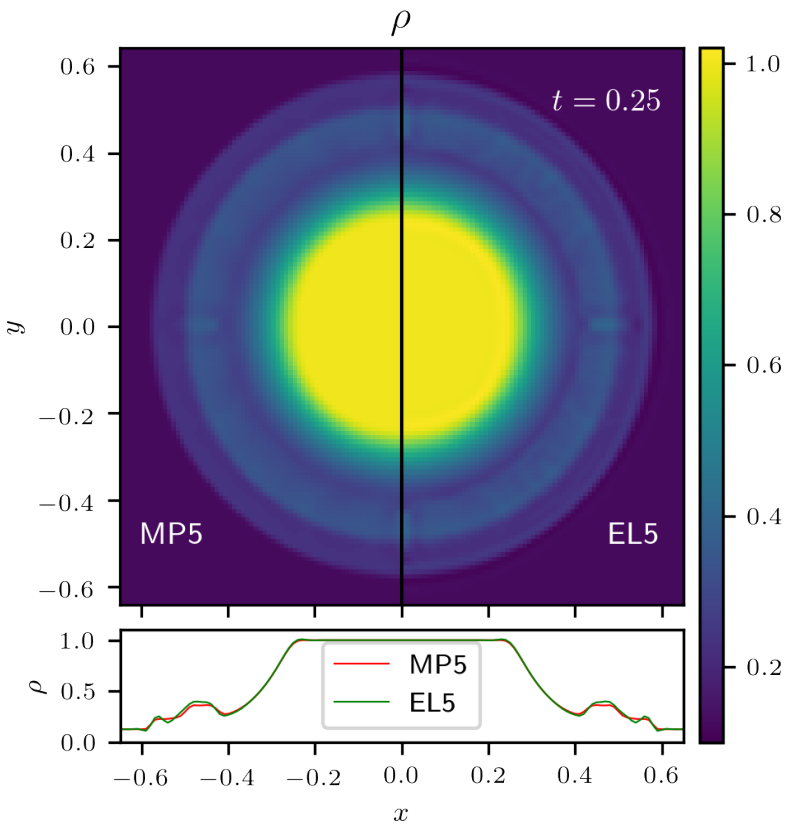

Figure 5.8: Rest-mass density for the relativistic-explosion test at time $t = 0.25$. In the top panel the distribution on the (x, y) plane is plotted, MP5 on the left side and EL5 on the right. In the bottom panel, the rest mass density is plotted on the x axis. Both schemes capture very well the solution. *Figure reproduced from Guercilena et al. (2017).*

5.4.2 Three-dimensional general-relativistic tests: neutron stars

Being interested in the practical applications of the ELH scheme to general-relativistic hydrodynamics and the modelling of compact stars, we then a series of three-dimensional tests mostly based on the evolution of single, isolated neutron stars in general relativity (with the exception of grazing-collision test of section 5.4.2), employing the EL5 variant of the scheme. In each test we employ for the evolution the ideal-fluid EOS (2.17) with $\Gamma = 2$. The neutron star initial data is constructed using a polytropic EOS $p = K\rho^{\tilde{\gamma}}$ also with $\tilde{\gamma} = 2$ and $K = 100\ M_{\odot}^{-2}$. For the spacetime evolution we employ the BSSNOK formulation of section 4.2 with standard 1+log and Gamma driver gauge conditions, discretized with a finite-differences algorithm (see section 3.3.1). This BSSNOK implementation is provided by the `McLachlan` code, part of the open-source `Einstein Toolkit` (Löffler et al., 2012; Zilhão and Löffler, 2013; Einstein Toolkit Website).

Isolated star in the Cowling approximation

At first we perform the evolution of a stable non-rotating (or TOV, from Tolmann-Oppenheimer-Volkoff) neutron star in a fixed spacetime (*i.e.* adopting the Cowling approximation). The goal of the test is to assess the properties of the EL5 scheme over long timescales. Despite its conceptual simplicity (a TOV is just a static solution of the Einstein-Euler equations) such test can be rather challenging. The reason lies in the stationary nature of the location of the stellar surface, which is the hardest feature to simulate due to the steep gradient in the hydrodynamics variables. Because this feature is essentially stationary errors can accumulate and grow in its vicinity, affecting the accuracy of the simulation locally as well as globally. This behaviour is to be contrasted with the typical situation encountered when evolving inspiralling binary neutron stars, where the stellar surfaces move very supersonically with respect to the floor and most of the errors at the surface are absorbed into the shocks.

We build and evolve a TOV model with central rest-mass density $1.28 \times 10^{-3}\, M_\odot^{-2}$, yielding a (baryon) rest mass of $1.5\, M_\odot$ and a radius of $\sim\ 10\, M_\odot$. We perform the test on a single refinement level with outer boundaries placed at $16\, M_\odot$ and a resolution of $\Delta^i = 0.2\, M_\odot \simeq 0.3$ km. The timestep is set to 0.15 times the grid spacing, and the time integrator is RK3.

Figure 5.9 shows the distribution of the viscosity on the equatorial (x, y) plane. A local annular peak around the location of the stellar surface is clearly visible, corresponding to the location where the hydrodynamical variables experience the most violent variations, leading to large values of the viscosity. In the external low-density fluid, the viscosity is set to a small constant value almost everywhere as detailed in section 5.3. The inner part of the neutron star is expected to be isentropic, as it consists of a shock-free perfect fluid. Indeed it can be clearly seen how in the stellar interior the viscosity is nonzero but also 10^2 to 10^3 times smaller than at the surface, *i.e.* a value which does not significantly affect the evolution. Such features of the viscosity profile are typical in all the tests we considered, in each case in which a sharp matter/vacuum interface is present.

The general behaviour of the EL5 scheme, when compared to the MP5 scheme, is well illustrated by figure 5.10, which shows the rest-mass density distribution on the equatorial (x, y) plane for the two schemes (the left part of the panel, *i.e.* for $x < 0$, refers to the MP5 scheme, while the right part, *i.e.* for $x > 0$, to the EL5 scheme). Both schemes accurately capture the solution in the stellar interior, but significant differences arise at the surface and in the exterior. The MP5 scheme shows a rather diffusive behaviour, with a smooth transition to the external near vacuum state (*i.e.* to a region close to the rest-mass density floor) and extended low-density tails. The EL5 scheme on the other hand produces a sharper edge. Oscillations in the solution can be seen just outside of the star, resulting in shell-like structures around the surface, which are particularly noticeable in the coordinate axes directions. The stellar exterior is much closer to the vacuum with the EL5 scheme and, in contrast to MP5, it also displays small-scale dynamics at very low densities. Note that the use of a higher-order stencil in the ELH approach, *e.g.* EL7, does not yield improvements in the solution; the treatment of the low-density regions is far more delicate and the mass conservation is degraded.

The nature of the oscillations visible in the solution computed with the EL5

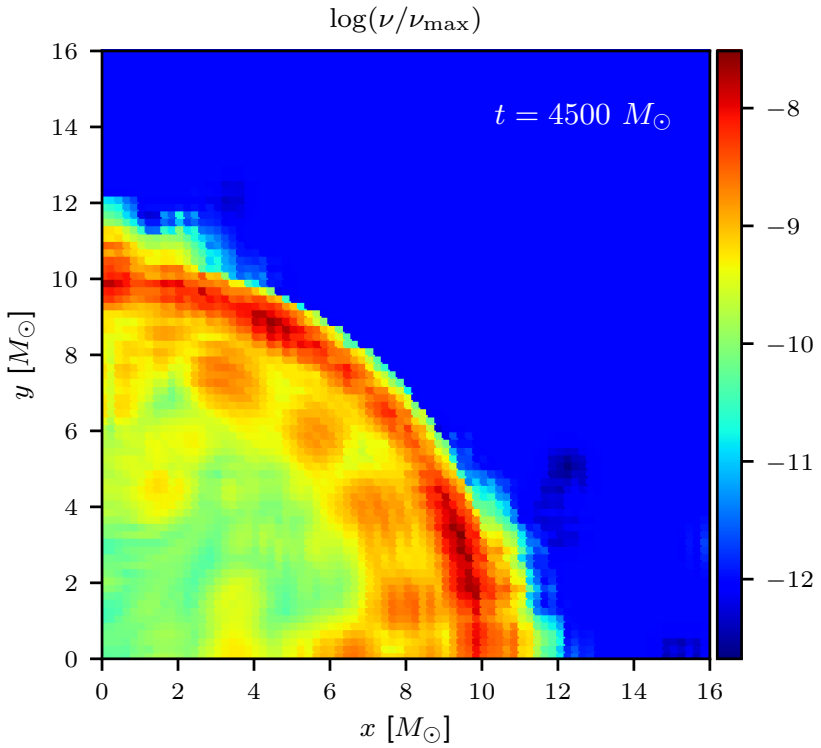

Figure 5.9: Two-dimensional viscosity distribution relative to its upper limit on the equatorial (x, y) plane at time $t = 4500\, M_\odot$ for the Cowling TOV test. The viscosity peaks at the stellar surface, identified as a shock by the scheme, and drops in the interior. *Figure reproduced from Guercilena et al. (2017).*

scheme are clarified in figure 5.11, which shows the rest-mass density profiles along different radial cuts. Along the x direction the oscillations in the EL5 data have a large amplitude (a similar behaviour is observed along the y and z axes). On the other hand, on the three-dimensional diagonal (*i.e.* along the $x = y = z$ line), the EL5 scheme manages to capture the sharp transition between the stellar interior and the outside vacuum almost perfectly, without significant oscillations or other artefacts. The use of the MP5 scheme leads instead to smooth profiles that are only slowly decaying in all directions. Note that in both cases the amount of rest-mass outside the star is minute, being only 10^{-7} of the initial rest-mass for the EL5 scheme and $\sim 10^{-5}$ for the MP5 scheme.

The direction-dependent behaviour shown in figure 5.11 for the EL5 scheme is due to the well-known anisotropy of the phase error common to finite-differencing stencils (Vichnevetsky and Bowles, 1982; Lele, 1992). The MP5 scheme is able to mask this behaviour, but at the price of sacrificing the ability to sharply resolve the stellar surface. We expect that the performance of the EL5 scheme could be improved through the use of multidimensional stencils (*i.e.* employing a multidimensional interpolation in the reconstruction step), as opposed to

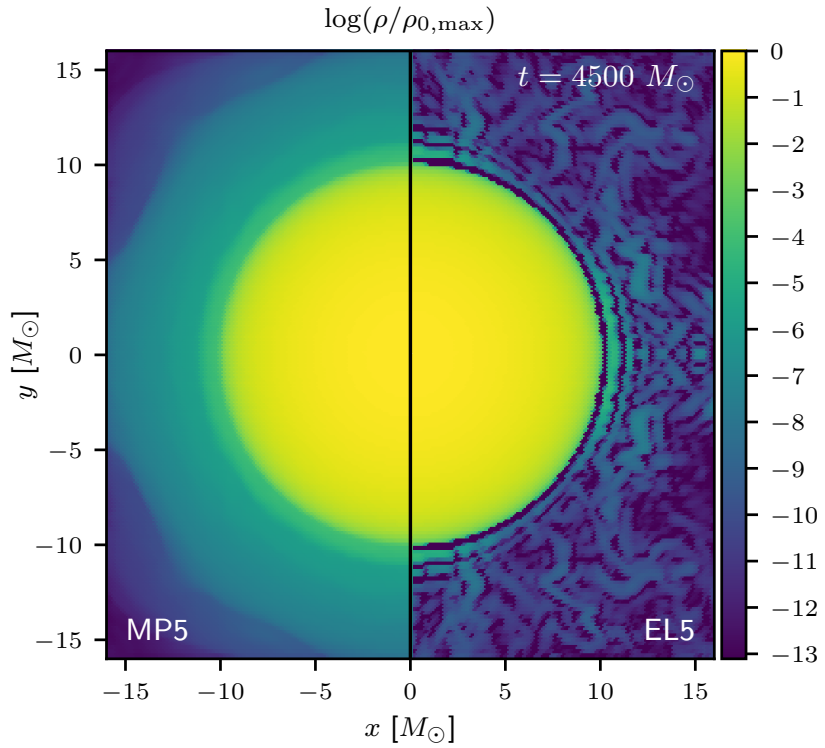

Figure 5.10: Two-dimensional rest-mass density distribution relative to the initial data maximum value on the equatorial (x, y) plane at time $t = 4500\, M_\odot$ for the Cowling TOV test; the left part of the panel (*i.e.* $x < 0$) refers to the MP5 scheme, while the right (*i.e.* $x > 0$) part to the EL5 scheme. Oscillations are visible with the EL5 scheme at the stellar surface, but the exterior fluid is visibly less dense than in the MP5 case. *Figure reproduced from Guercilena et al. (2017).*

the current approach in which the stencil is simply oriented in the direction of the flux to be reconstructed.

The quantitative differences between the two schemes are summarized in figure 5.12, where the evolution of the total rest mass and of the central rest-mass density are plotted. We recall that the total rest mass (or baryon mass), is defined as

$$M := \int \rho W \sqrt{\gamma}\, d^3x\,, \tag{5.14}$$

where the integral extends over the whole computational domain. From the continuity equation (2.16) it follows that M should be conserved in absence of a net total flow of matter in or out of the domain. The numerical schemes we employ are conservative (see *e.g.* Leveque (1992)), and therefore preserve the value of the rest mass to the one determined by the initial data. Nonetheless, violations of this conservation can take place in at least three different ways.

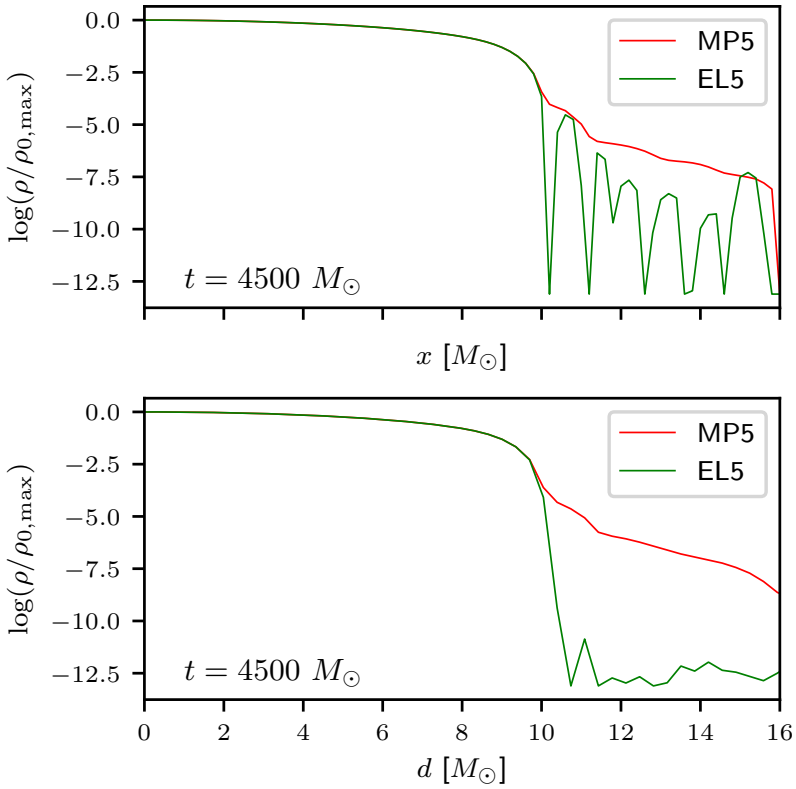

Figure 5.11: One-dimensional rest-mass density profiles in the x (top) and d direction (bottom) at time $t = 4500\,M_\odot$ relative to the initial data maximum value for the Cowling TOV test. The oscillations seen in the EL5 data are a direction dependent artefact, absent in the diagonal direction. *Figure reproduced from Guercilena et al. (2017).*

First, winds originating at the stellar surface (physically, as *e.g.* in binary neutron star merger, or spuriously as in a stationary case such as the present one) can yield a net loss of mass when they reach the outer boundary and leave the computational domain. Second, matter can be spuriously created or destroyed, in a way that is hard to control, because of floating-point or interpolation errors at the boundaries of refinement levels (this is not the case for this particular test clearly, since we employ a single grid, but it is important to point it out, since it is instead relevant for the following tests). Finally, when a value of the density is floored, *e.g.* as result of a failure of the conversion between conserved and primitive variables, mass is spuriously created or destroyed. It is therefore important to characterize the interplay between the numerical scheme and these grid related effects.

The left panel of figure 5.12 shows deviations of the rest mass from the initial value, in absolute value, for both schemes. The EL5 scheme is evidently much better at conserving mass in this test than MP5, and leads to a cumulative deviation of $\sim\ 10^{-7}\,M_\odot$, which is almost three orders of magnitude smaller

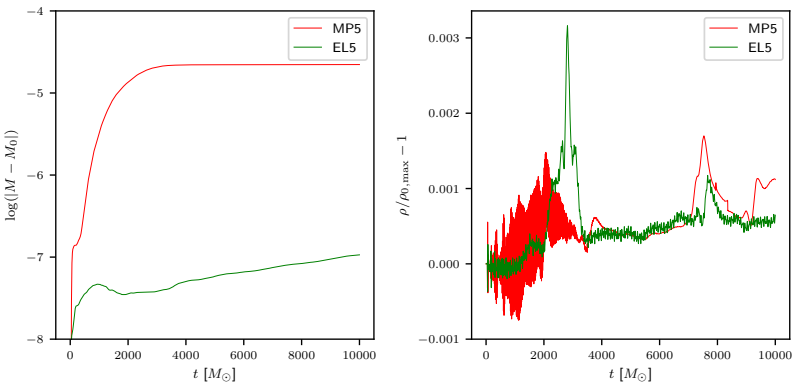

Figure 5.12: Deviation of the total rest mass (left panel) and central rest-mass density (right panel) from the initial values for the Cowling TOV test. *Figure reproduced from Guercilena et al. (2017).*

than the MP5 value.

The central rest-mass density also undergoes an evolution (right panel of figure 5.12), with oscillations triggered by the treatment of the stellar surface. Both schemes perform at a similar level of accuracy, with relative variations from the initial value no greater than about 0.3% (even though spurious peaks are present in both data series at various, different times). The frequency content in the two data series is noticeably different, with the MP5 scheme seeming to show more pronounced high-frequency modes. However, at later times both schemes appear to relax and oscillations decrease significantly in amplitude.

Isolated star in a dynamical spacetime

For the following test the Cowling approximation is relaxed and w test the ELH method coupled with a dynamically evolved spacetime. We evolve the same initial data for a isolated stable star as in the previous section (*i.e.* with central density $1.28 \times 10^{-3}\, M_\odot^{-2}$, baryon mass of $1.5\, M_\odot$ and radius $\sim\ 10\, M_\odot$). The test is preformed on a grid consisting of three refinement levels centered on the star with sides lengths 16, 32 and $60\ M_\odot$ from finest to coarsest, and with a constant refinement factor of 2. The spatial resolution of the innermost and finest level is set to $\Delta^i = 0.2\, M_\odot \simeq 0.3$ km, and the timestep to 0.15 times the grid spacing. This factor is largest possible to guarantee the positivity of the rest-mass density (see discussion in section 3.3.3 and in Radice et al. (2014b) for details). The atmosphere value of the density is set to $10^{-16}\ M_\odot^{-2}$, *i.e.* almost 13 orders of magnitude smaller than the maximum value. As a time integrator we select the third-order SSP Runge-Kutta RK3. Unless stated differently the same grid setup is employed for each of the following single star tests.

The distribution of rest-mass density on the equatorial (x, y) plane is shown in figure 5.13, again with the MP5 and EL5 schemes shown on the left and right parts of the panel, respectively. It can be appreciated how the MP5 scheme produces rest-mass tails which are even more dense and extended than in the Cowling case, making the near vacuum solution obtained by the EL5 scheme

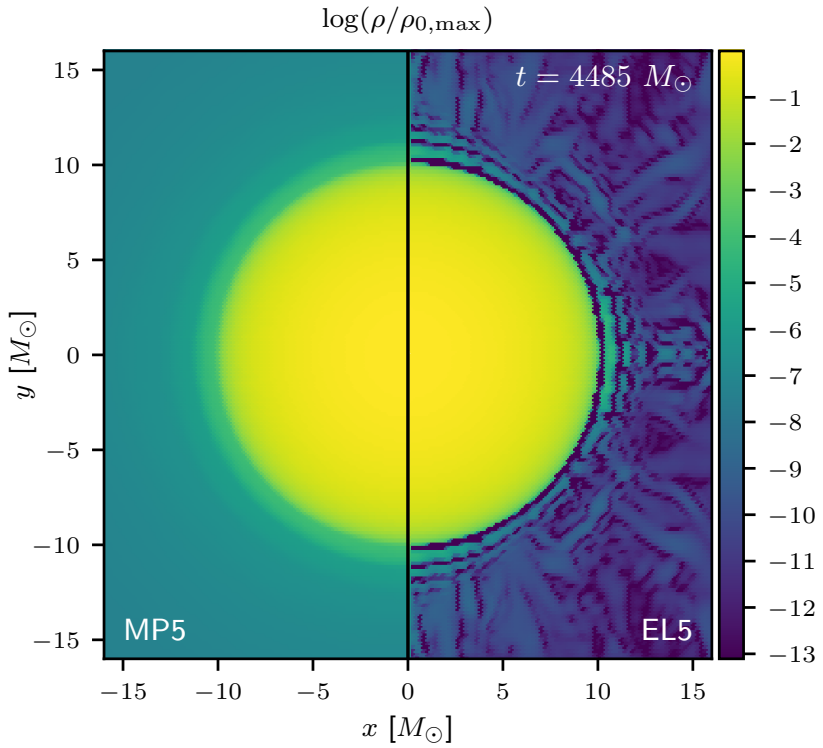

Figure 5.13: Two-dimensional rest-mass density distribution relative to the initial data maximum value on the equatorial (x, y) plane at time $t = 4485\, M_\odot$ for the dynamical TOV test. The matter tails are even more extended in MP5 case compared with the Cowling test, EL5 instead preserves its behaviour at the stellar surface and exterior. *Figure reproduced from Guercilena et al. (2017).*

all the more striking.

A further difference from the Cowling test is to be seen in the conservation of the rest mass (left panel of figure 5.14). Also in this case the EL5 scheme is able to conserve the initial value to an accuracy roughly two orders of magnitude better than the MP5 scheme. It is interesting to notice however how the behaviour of the EL5 scheme is much more smooth and predictable; MP5 by contrast leads to both spurious losses and gains of mass, resulting in the zero crossings clearly visible in the figure. This is due to interpolation errors arising during the restriction and prolongation operations between different refinement levels. These errors are more severe with MP5 due to the presence of long tails of low density matter in the stellar exterior, as we checked by varying the extent of the refinement levels. In contrast, the EL5 scheme is less affected since the exterior of the star (especially away from the coordinate axes) is nearly vacuum.

The evolution of the central rest-mass density, which is shown in the right panel of figure 5.14, is similar to the one shown in the previous section for

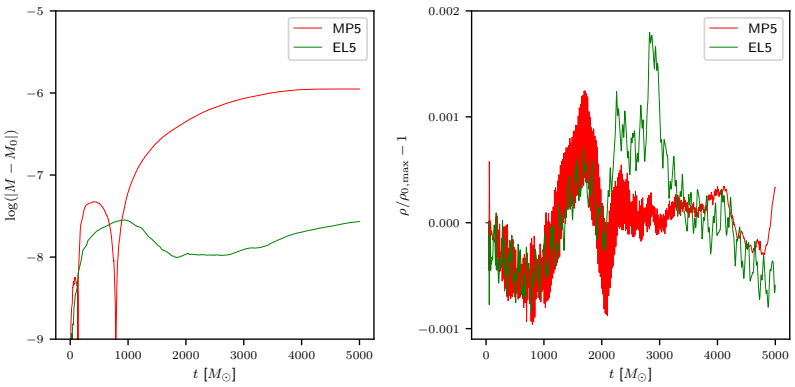

Figure 5.14: Deviation of the total rest mass (left panel) and central rest-mass density (right panel) from the initial values for the dynamical TOV test. *Figure reproduced from Guercilena et al. (2017).*

the Cowling approximation, with both schemes varying no more than 0.2% from the initial value, but with MP5 displaying oscillations at much higher frequency.

This point can be investigated further by computing the power spectral density (PSD) of the density time series, in order to quantitatively gauge the differences between the two schemes. The PSD is computed over the first $5000\,M_\odot$ of data and with the use of a Hann window function. Before computing the PSD, any linear trend in the signal is removed via a least-squares fit.

Figure 5.15 shows the PSDs for both schemes, along with the oscillation frequencies of this stellar model as computed in a perturbative fashion following the methods discussed in Yoshida and Eriguchi (2001); Takami et al. (2011), shown as vertical dashed lines. In both cases the PSD is dominated by a low-frequency component due the well-known secular changes in the central rest-mass density (Font et al., 2002) which disappear with resolution. Peaks are however clearly visible above the noise. The lowest-frequency peaks correspond to the fundamental oscillation mode of the star and its first overtone, while the following ones are higher overtones and are progressively more offset from the corresponding perturbative eigenfrequencies. The peaks in the EL5 data appear to be more clearly identifiable and less broad than in the MP5 case. Above $\sim$ 8000 Hz (not shown in figure 5.15) the MP5 scheme shows significant high-frequency noise, clearly visible in the first part of the corresponding curve in figure 5.14. These same frequencies are instead greatly suppressed in the EL5 scheme. This test also highlights that the EL5 scheme captures quite well the physical behaviour of the system as predicted from perturbative methods and is free from some of the artefacts which appear instead in the evolution with the MP5 scheme.

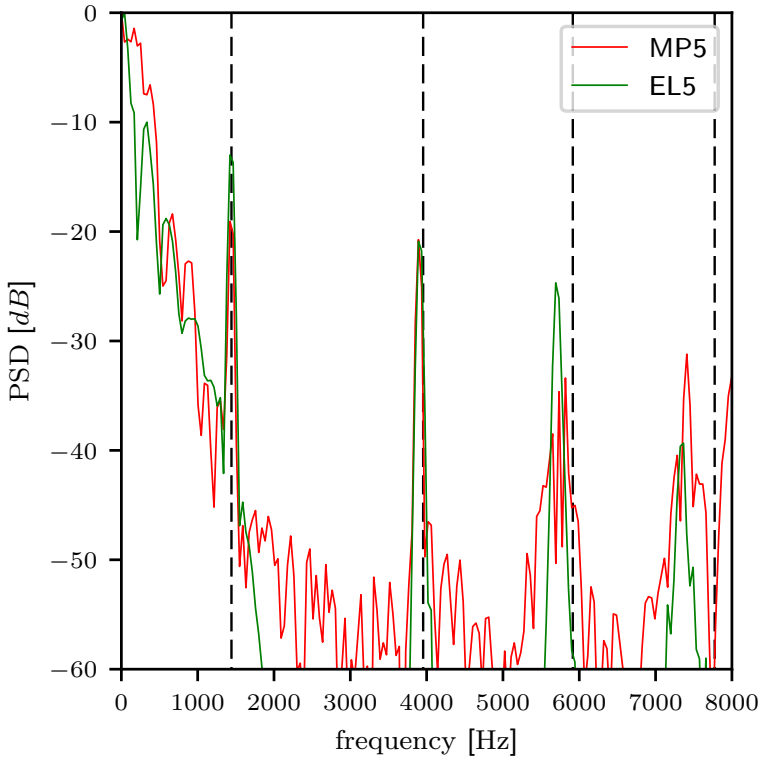

Figure 5.15: PSD of the central rest-mass density evolution and physical eigenfrequencies of the stellar model for the dynamical TOV test. Note the good agreement between the first eigenfrequencies and the peaks in the data. *Figure reproduced from Guercilena et al. (2017).*

Perturbed isolated star

The next test we perform is a slight modification of previous setup, *i.e.* we evolve the same isolated neutron star model, but applying a small velocity perturbation to the initial solution. The perturbation is radially outgoing and with a profile growing linearly in radius to a maximum value of 0.005.

This scenario, which is more realistic than the simple smooth-wave test of section 5.4.1, can be employed to measure the convergence order of the EL5 and MP5 methods. We performed three sets of simulations at resolutions 0.24, 0.12 and 0.06 $M_\odot$ on the finest level, extracting the evolution of the rest-mass density over time. The initial perturbation is added so that the density evolution is not dominated by the truncation error, but posses a cleaner behaviour. Otherwise as the resolution is increased the density evolution would show additional high-frequency modes, which would make the dependence on resolution discontinuous, making it difficult to compute the instantaneous convergence order.

The instantaneous convergence order has been computed using the values

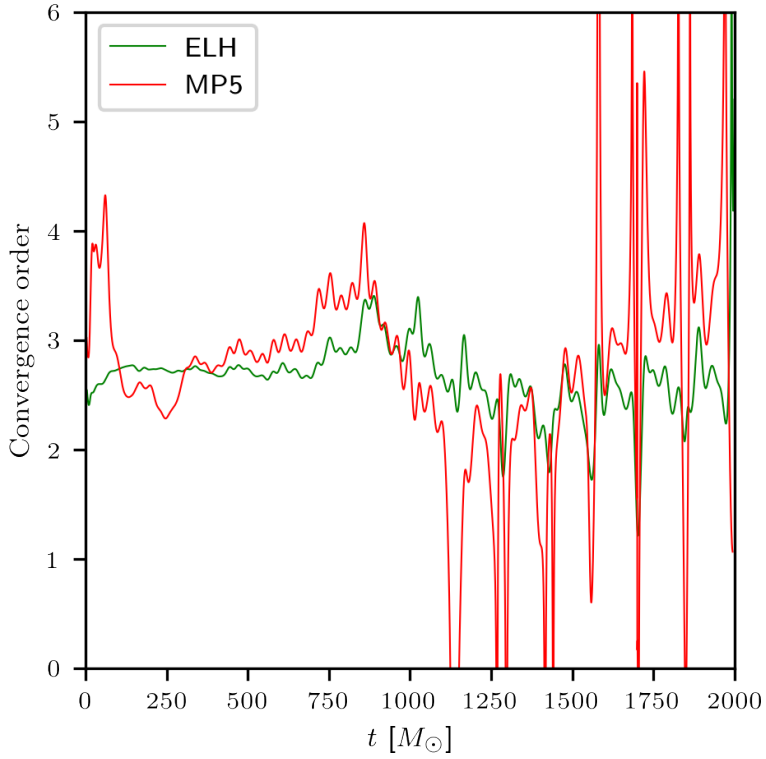

Figure 5.16: Instantaneous convergence order measured in a perturbed TOV simulation, computed from the L_1-norm of the rest-mass density. *Figure reproduced from Guercilena et al. (2017).*

of the L_1-norm of the rest-mass density over the domain at the three resolutions, and it is shown in figure 5.16. Because this is the instantaneous convergence order and because the underlying system is oscillating, the curves are somewhat noisy (especially for MP5); however, as clear when taking the running average, both schemes generally show a convergence order just below three, consistent with the results in Radice et al. (2014a,b). It is also however apparent how EL5 maintains a fairly constant order of convergence through time, while the behaviour of MP5 is more irregular, especially at later times.

While both hydrodynamics schemes are formally fifth-order accurate, other components of the algorithm and computing infrastructure operate at different degrees of accuracy. In particular, both the time integrator and the prolongation operator are third-order accurate, which most likely accounts for the convergence order being closer to three than to five. The result is also consistent with the ones found for the MP5 scheme in Radice et al. (2014a,b, 2015). Overall this test highlights how both the ELH and MP5 schemes perform fairly consistently over time, with no major loss of accuracy.

Migration test

A quite important test is the migration of a TOV star, moving from a solution on the unstable branch of equilibrium solutions to a stable one. Recall that for any given EOS, increasingly massive but stable TOV models can be constructed by using increasingly large values of the central rest-mass density. This process can continue until a maximum mass is reached, at which point an increase of the central rest-mass density corresponds to a decrease of the mass of the star. Models on this second branch of the mass/density curve are unstable, upon perturbation they will evolve to either a stable configuration or collapse to a black hole. This is precisely the physical scenario that the migration test simulates: a model on the unstable branch of the mass/density curve is constructed, then force its migration to a stable configuration by applying a suitable velocity perturbation.

This is a very common test for numerical relativity codes (see *e.g.* Font et al. (2002); Baiotti et al. (2005); Baiotti et al. (2003); Cordero-Carrión et al. (2009); Thierfelder et al. (2011)), and has been studied in detail in Radice et al. (2010). We build a non-rotating stellar model on the unstable branch of the equilibrium solutions with central rest-mass density of $7 \times 10^{-3}\, M_{\odot}^{-2}$ (yielding a total rest mass of $1.6\, M_{\odot}$ and a radius of $6\, M_{\odot}$). The migration is then triggered by injecting a radially outgoing velocity perturbation where the velocity grows linearly in radius, reaching a maximum value of 0.01 (note that an outgoing perturbation is employed to ensure that the system evolves towards a stable configuration; an ingoing perturbation would cause a compression of the star and might lead to a collapse to a black hole instead; see section 5.4.2 for this second scenario). The star then undergoes a series of violent expansions and contractions as it migrates to the stable branch and then settles on the new equilibrium. During each contraction and expansion strong shocks are formed, and the shocked matter is ejected at large velocities.

The rest-mass density distribution is shown in figure 5.17 on the equatorial (x, y) plane for both schemes during one of the contractions of the star, just before the central rest-mass density reaches a maximum (see also figure 5.18). The snapshot clearly shows that both the EL5 and MP5 schemes produce almost identical results for this test. This is not surprising and mainly due to the matter outflow driven by the stellar oscillations, which rapidly fills the domain and removes the sharp feature of the stellar surface, which is the most problematic structure to resolve and the main difference in the two schemes.

The behaviour over time of the maximum rest-mass density is shown in figure 5.18, where the values are normalized to their initial value. The agreement between the two schemes is extremely good during the entire evolution and the main difference between the two solutions is the presence of some high-frequency modes near the maxima of the density in the EL5 data. Such oscillations are the result of inward-propagating shock waves generated in the outer layers of the star during the contraction phase. Figure 5.19 shows a magnification of the behaviour of the maximum rest-mass density at the peak of the first contraction, comparing not only the two schemes but also the evolutions with two different resolutions. At high resolution, both the MP5 and the EL5 scheme show small-scale and high-frequency oscillations that are less pronounced in the low-resolution data. Interestingly, these oscillations are essentially smoothed out in the low-resolution run of the MP5 scheme, while

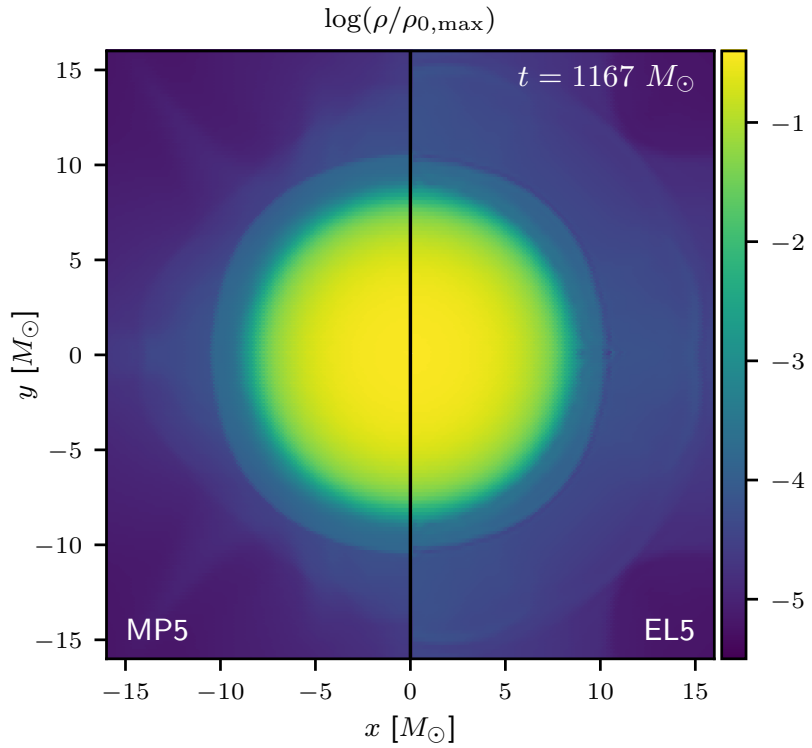

Figure 5.17: Two-dimensional rest-mass density distribution relative to the initial data maximum value on the equatorial (x, y) plane at time $t = 1167\,M_\odot$ for the migration test. Virtually no difference can be detected in the two schemes behaviour. *Figure reproduced from Guercilena et al. (2017).*

they are very visible in the low-resolution EL5 run. This seems to indicate that the two schemes tend, with increasing resolution, towards a solution where the small-scale oscillations are present and therefore physically correct and not a numerical artefact. Finally, as the evolution progresses, the contraction/expansion phases become less and less violent as part of the kinetic energy is converted into internal energy, thereby leading to milder and milder shocks, and the high-frequency oscillations in the central rest-mass density all but disappear.

Isolated rotating neutron star

We perform one last test involving a stable (or metastable) isolated relativistic star, namely the evolution of a rapidly and uniformly rotating star. We set up axisymmetric initial data relative to a uniformly rotating neutron star with polytropic EOS with $K = 100\,M_\odot^{-2}$ and $\Gamma = 2$, having a central rest-mass density of $1.28 \times 10^{-3}\,M_\odot^{-2}$ and a polar to equatorial axis ratio of 0.8. The initial data was computed using the `RNS` code (Stergioulas and Friedman, 1995).

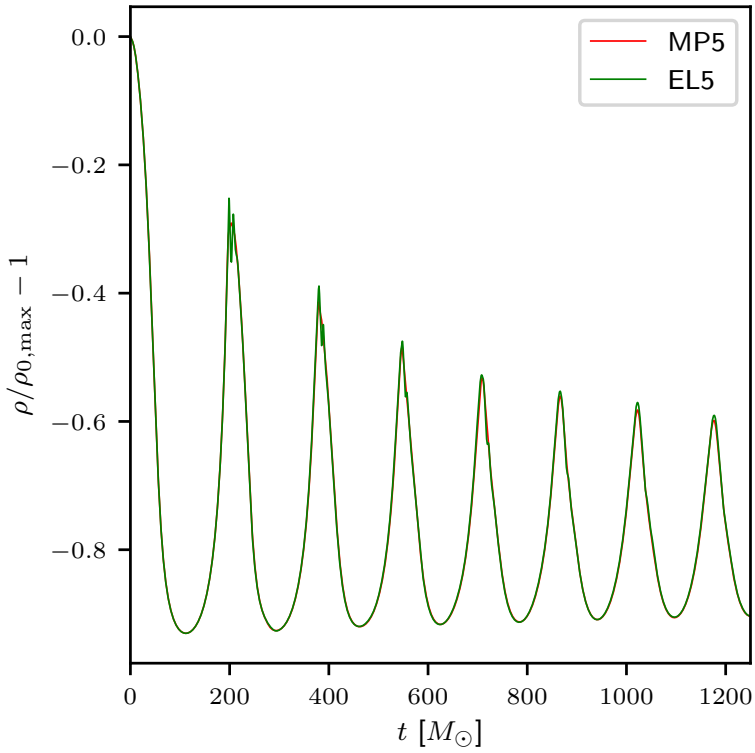

Figure 5.18: Central rest-mass density in the migration test. The agreement between the two schemes is apparent over the whole evolution, apart from high-frequency modes at the maxima in EL5 data. *Figure reproduced from Guercilena et al. (2017).*

This setup results in a star with total rest mass $1.6\,M_\odot$, radius $10\,M_\odot$, rotation frequency $f = 673.2$ Hz (about 60% of the mass shedding frequency) and dimensionless angular momentum $J/M^2 = 0.46$.

Again figure 5.20 reports the rest-mass density distribution on the equatorial (x, y) plane for both the EL5 and MP5 schemes at time $t = 4300\,M_\odot$, *i.e.* after about 14 rotation periods. Clearly both schemes evolve the rotating star with no noticeable problems and again the part of the domain exterior to the stellar surface rapidly fills with matter. In this case as well the behaviour of the two methods in the low-density regions is rather different, with the MP5 scheme filling the exterior volume by uniform but comparatively higher-density material, while the EL5 scheme produces a more rarefied stellar exterior but with small-scale condensations (cf. figures 5.10 and 5.13 for the equivalent behaviour in the absence of rotation).

Differently from the behaviour seen in the case of non-rotating stars, the dynamics of the low-density material in the stellar exterior results in a degradation of the conservation of mass for the EL5 scheme. This is shown in the left panel of figure 5.21 (cf. the left panels of figure 5.12 and 5.14 for the equiv-

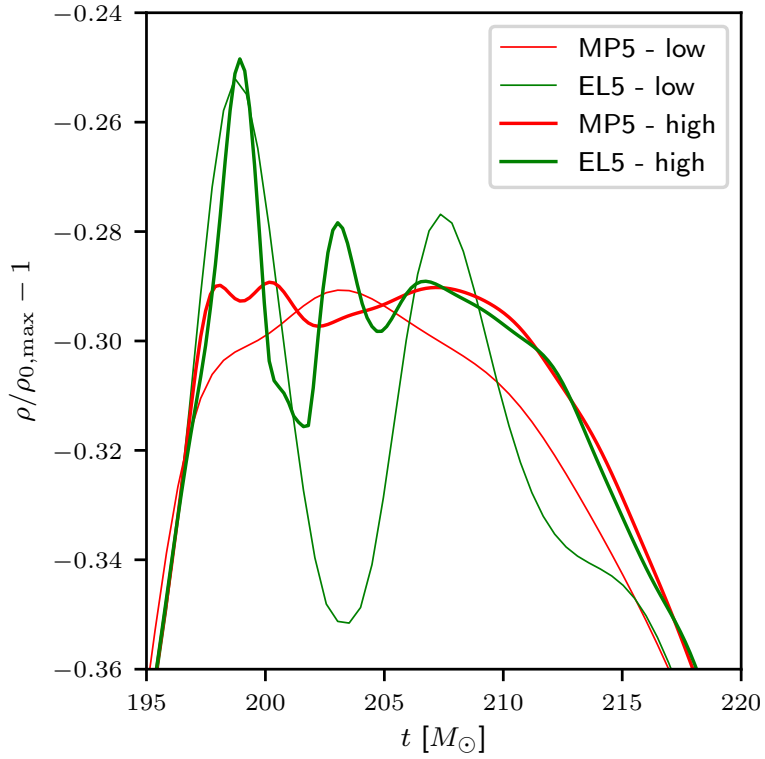

Figure 5.19: Magnification of the central rest-mass density evolution around the first contraction of the migrating star. The low-resolution data (thin curves) corresponds to figure 5.18 and to a grid spacing of $0.2\,M_\odot$. The high-resolution data (thick curves) corresponds to a grid spacing of $0.086\,M_\odot$. The high-frequency modes present in the EL5 data at low resolution persist at high resolution in both schemes. *Figure reproduced from Guercilena et al. (2017).*

alent behaviour in the absence of rotation). The deviation of the total rest-mass density from its initial value is more than one order of magnitude larger for the EL5 scheme than for MP5 and reaches values of $\sim 10^{-5}\,M_\odot$. This is the result of failures in the conversion from the conserved variables to the primitive ones, triggered by oscillations in the solution. The mechanism is as follows: the solution can be locally evolved to an unphysical state; in this case the rest-mass density could reach values below the atmosphere floor value; if so the conversion routine resets the affected cells to the (higher) atmosphere value; thus effectively creating spurious mass. We speculate that most of these failures result from the large tangential velocity that is acquired by the shell-like distribution of matter that builds up in the case of the EL5 scheme and that is present already in the non-rotating case. While rather innocuous in the absence of rotation, this shell of matter can fling material to large distances (but within the computational domain) and lead to a much more chaotic dynamics of the fluid in the low-density regions (see the discussion in sec. 3.2.3 of Radice et al.

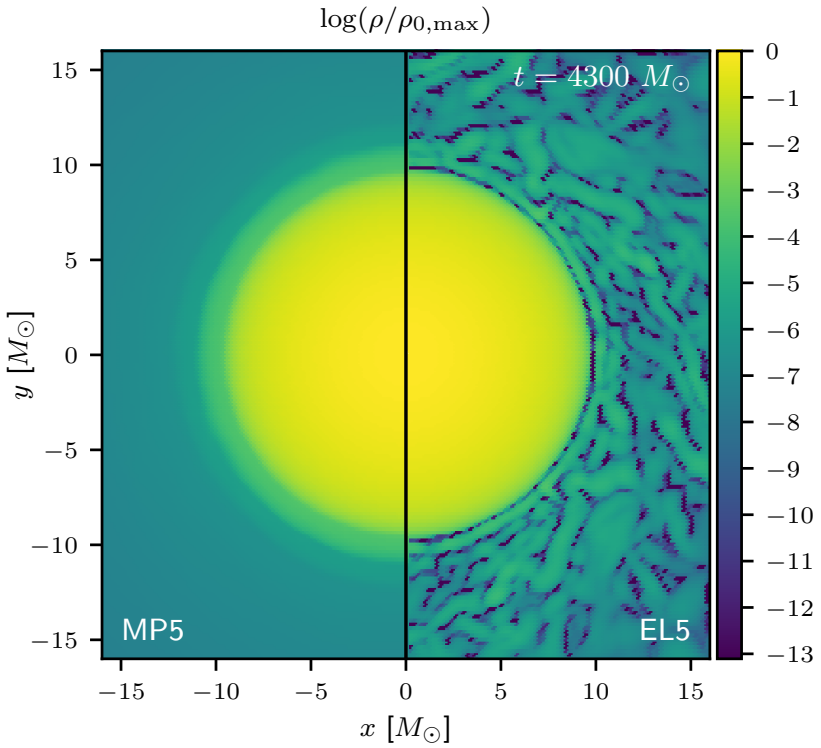

Figure 5.20: Two-dimensional rest-mass density distribution relative to the initial data maximum value on the equatorial (x, y) plane at time $t = 4300\, M_\odot$ for the rotating star test. The behaviour of the star exterior is dynamic and chaotic with EL5 as compared with MP5. *Figure reproduced from Guercilena et al. (2017).*

(2014b)).

To assess the impact, if any, of the fluid dynamics in the stellar exterior on the evolution of the star itself, *i.e.* to understand if the above described issues result in a degradation of the solution for the high density part, we plot the evolution of the central rest-mass density for the two schemes in the right panel of figure 5.21. It can be seen that the low-density fluctuations appearing in the stellar exterior with the EL5 scheme do not impact the solution in the stellar interior: the low-frequency central density oscillations essentially being in phase for the two schemes. It is also apparent that the EL5 scheme yields rather constant-amplitude oscillations and this should contrasted with the behaviour of the MP5 scheme, where the oscillations are comparatively larger in the first $\sim$ 2000 $M_\odot$ of the evolution. In both cases however the oscillations are extremely small and below 0.1% of the initial value.

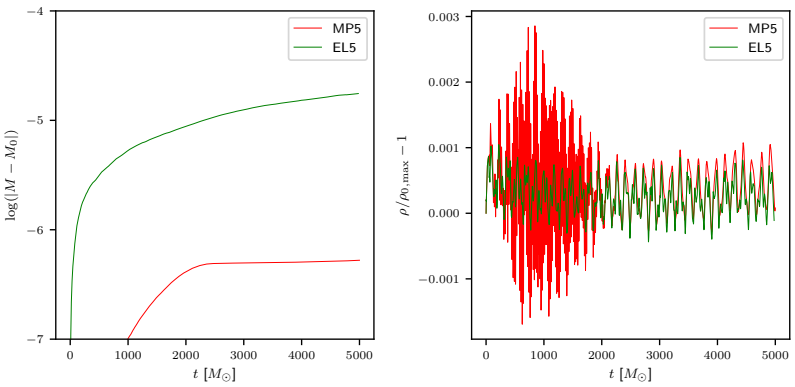

Figure 5.21: Deviation of the total rest mass (left panel) and central rest-mass density (right panel) from the initial values for the rotating-star test. *Figure reproduced from Guercilena et al. (2017).*

Grazing collision of neutron stars

Moving further from test of (meta-)stable, isolated stars, we perform a truly dynamical test: the motion across the numerical grid of two neutron stars in a grazing collision. The setup for this test is in fact very similar to that of a binary-neutron star system in quasi-circular orbit. The most obvious difference, in fact basically the only one, is that contrary to a BNS the initial momenta of the two stars do not result in quasi-circular orbits and that the initial fluid velocity can be taken to be arbitrary. The initial data in this case is set up by generating two identical TOV models (the same as considered in sections 5.4.2 and 5.4.2), superimposing the two data sets on the computational grid and imparting suitable initial momenta resulting in a small, but nonzero, impact parameter. Such initial data is only approximated, since the stars are not in the hydrostatic equilibrium and the intial metric and extrinsic curvature are not a solution of the Einstein constraints equations.

These violations of the ADM constraints and of hydrostatic equilibrium lead to rather large initial oscillations in the evolution (see Kastaun et al. (2013); Tsatsin and Marronetti (2013) for a more detailed discussion of a more sophisticated setup in which the stars are also subject to a spin up). The impact of these oscillations can however be reduced significantly simply by setting the initial distance of the two stars to a rather large value (which results in the approximate initial data to approach more closely constraint satisfying, physical initial data). However these oscillations simply do not interfere with the main goal of this test, *i.e.* validating the ability of the ELH scheme to preserve sharply the features of the stellar surface also when the star moves across the numerical grid.

We set the star centers at positions $(x_1, y_1, z_1) = (50, -50, 0)$ and $(x_2, y_2, z_2) = (-50, 50, 0)$ in units of $M_\odot$, *i.e.* symmetric with respect to the grid center on the (x, y) plane and at a distance of $\sim$ 141 $M_\odot$. The initial 3-velocities are $(v_1^x, v_1^y, v_1^z) = (0, -0.1, 0)$ and $(v_2^x, v_2^y, v_2^z) = (0, 0.1, 0)$ respectively. We evolve the system on a cubic grid of radius 512 $M_\odot$, but employ reflection symmetry

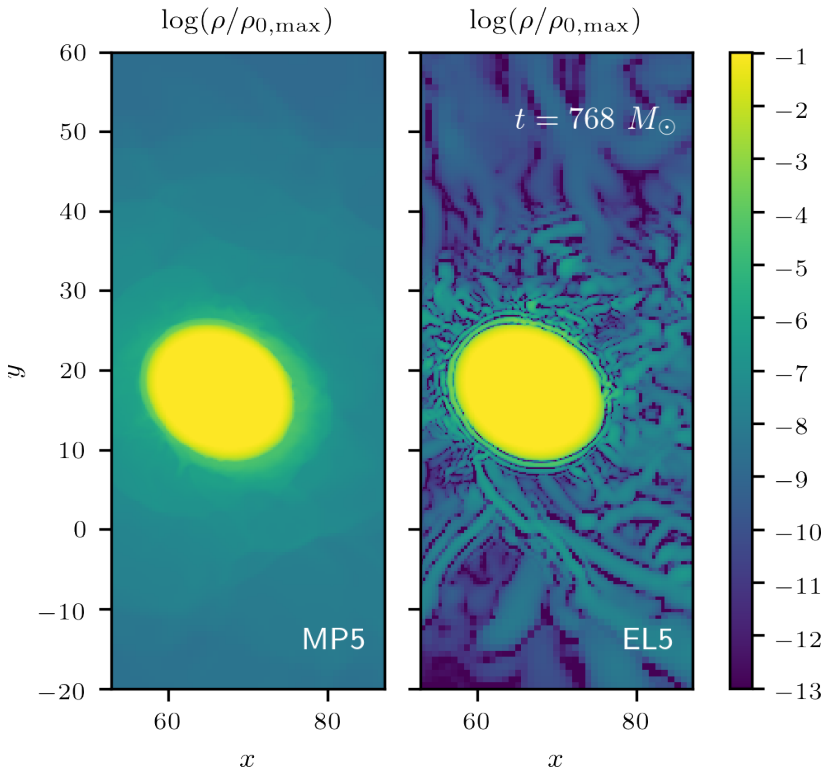

Figure 5.22: Two-dimensional rest-mass density distribution relative to the initial data maximum value on the equatorial (x, y) plane for the grazing-collision tests at time $t = 768\,M_\odot$, *i.e.* after the point of closest approach. *Figure reproduced from Guercilena et al. (2017).*

boundary conditions across the (x, y) plane and 180 degrees rotation symmetry boundary conditions across the (y, z) plane to reduce the computational cost. The grid structure consists of two identical box-in-box refinement levels hierarchies with refinement factor 2, each centered on a star and consisting of 5 cubic levels with radii $12, 25, 50, 100, 200\ M_\odot$, plus the coarse base level with radius $512\ M_\odot$, so that the grid spacing in the innermost refinement level is $\Delta^i = 0.2\,M_\odot \simeq 0.3$ km. The refinement levels moved to track the positions of the stars during the evolution (see also Radice et al. (2016) for further details on the initial data and grid structure). We set again $\Delta t = 0.15\,\Delta x$.

The two stars initially traverse the grid in the x direction and approach each other, then their trajectories bend in a gravitational scattering process; we do not follow the dynamics of the process after the first fly-by. Figure 5.22 shows the rest-mass density distribution on the (x, y) plane. The snapshots of one of the two stars (which are identical to each other due to the chosen boundary conditions) are taken at time $t = 768\ M_\odot$, *i.e.* when the two stars are past the point of closest approach and are flying apart. The deformation due to the velocity boost, the acquired spin angular momentum and the tidal

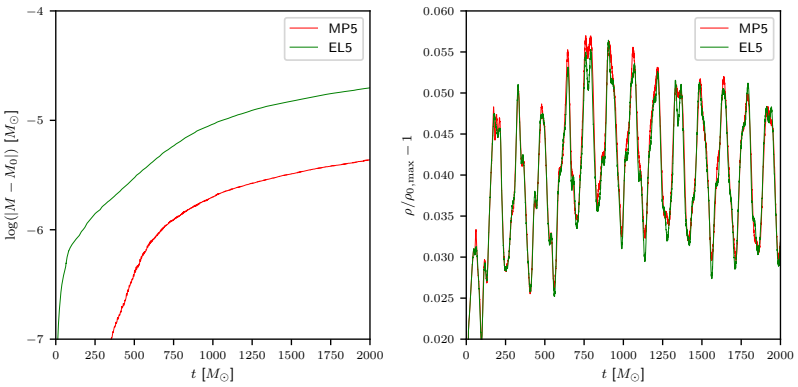

Figure 5.23: Deviation of the total rest mass (left panel) and central rest-mass density (right panel) from the initial values for the grazing-collision test. *Figure reproduced from Guercilena et al. (2017).*

gravitational interaction can be clearly seen. From the hydrodynamics point of view the behaviour of the MP5 and EL5 schemes is consistent with what found in the previous tests, in particular the TOV in a dynamical spacetime: EL5 shows a sharper star surface with respect to MP5, as well as a surrounding region closer to vacuum, while the bulk of the star itself is very well resolved by both schemes.

Once gain we judge quantitatively the performance of the two schemes by looking at the conservation of the total rest mass (left panel of figure 5.23). The evolution of this quantities is similar in this case to the what has been seen in the rotating-star case, *i.e.* a better performance by the MP5 scheme. Note however that the differences between the schemes are far smaller in the grazing collision test, less than one order of magnitude. Note also that in contrast with the preceding tests the grid structure in this case is much more complicated as well as dynamically updated to track the stars. Interpolation errors at the refinement level boundaries play therefore a greater role in the conservation of rest mass.

To the same end we show the evolution of the rest-mass density at the star centers in the right panel of figure 5.23, which is very similar for both schemes. There is an initial sudden increase in the density of about 4% with respect to the initial value, due to the evolution scheme bringing the star in hydrostatic equilibrium from the approximate initial state. The density then oscillates around this new value, due to perturbations that in this case are not only induced by the treatment of the stellar surface, but also by the violations of the ADM constraint but and by the gravitational interaction. Both schemes however reproduce well all of these effects and show a very good agreement.

Gravitational collapse to a black hole

The final test we consider the (violently dynamical) collapse of an unstable star to a black hole. This is also a common numerical-relativity benchmark (see *e.g.* Font et al. (2002); Baiotti et al. (2005); Baiotti and Rezzolla (2006); Thierfelder

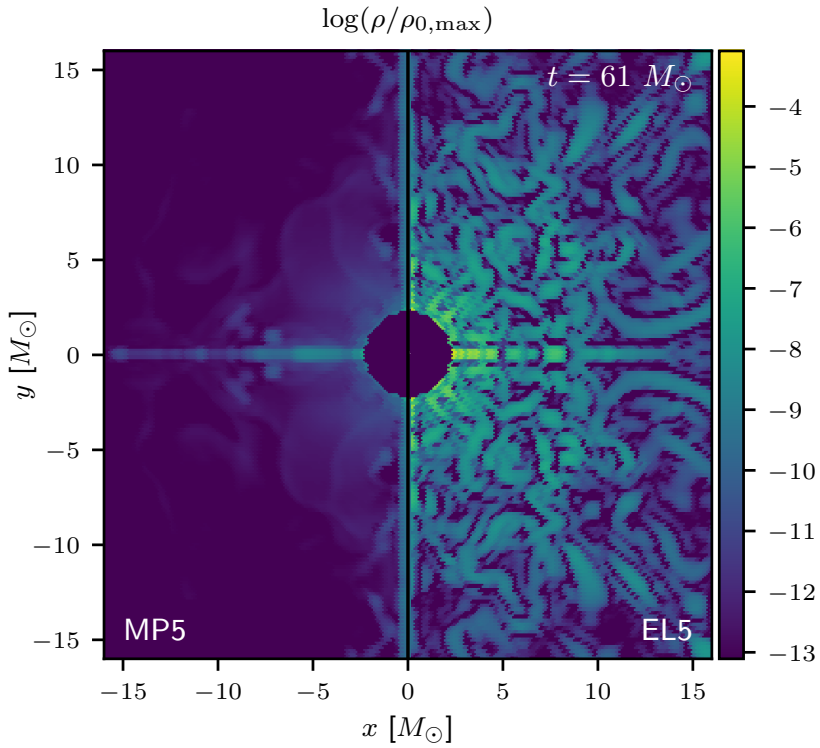

Figure 5.24: Two-dimensional rest-mass density distribution relative to the initial data maximum value on the equatorial (x, y) plane at time $t = 61\,M_\odot$ for the collapse test. Streams of matter ejected during collapse and accreting back onto the black hole are clearly visible and more prominent in EL5 data. *Figure reproduced from Guercilena et al. (2017).*

et al. (2010)), which allows us to validate ELH in the presence of a physical singularity and of an apparent horizon. The setup consists of a nonrotating star with central rest-mass density $8\times10^{-3}\,M_\odot^{-2}$, corresponding to a baryon mass of $1.5\,M_\odot$ and radius $6\,M_\odot$, and initiate the collapse with a velocity perturbation analogous to the one used in the migration test, but with the opposite sign, *i.e.* radially ingoing. This test is therefore in some sense the counterpart of the migration test of section 5.4.2.

The time of black-hole formation is defined, as customary in numerical relativity, as the time of first detection of an apparent horizon in the numerical domain. In the given chosen setup, this happens at $t \simeq 48\,M_\odot$. Because we use singularity avoiding slicing conditions, we do not need to excise the interior spacetime of the black hole (Baiotti and Rezzolla, 2006; Baiotti et al., 2007; Thierfelder et al., 2010). However we do set the hydrodynamical variables to their atmosphere values inside a surface with the same shape as the apparent horizon, but radius $r = 0.9\,r_{\rm AH}$ in every angular direction, $r_{\rm AH}$ being the radius of the apparent horizon. This hydrodynamic excision is not strictly nec-

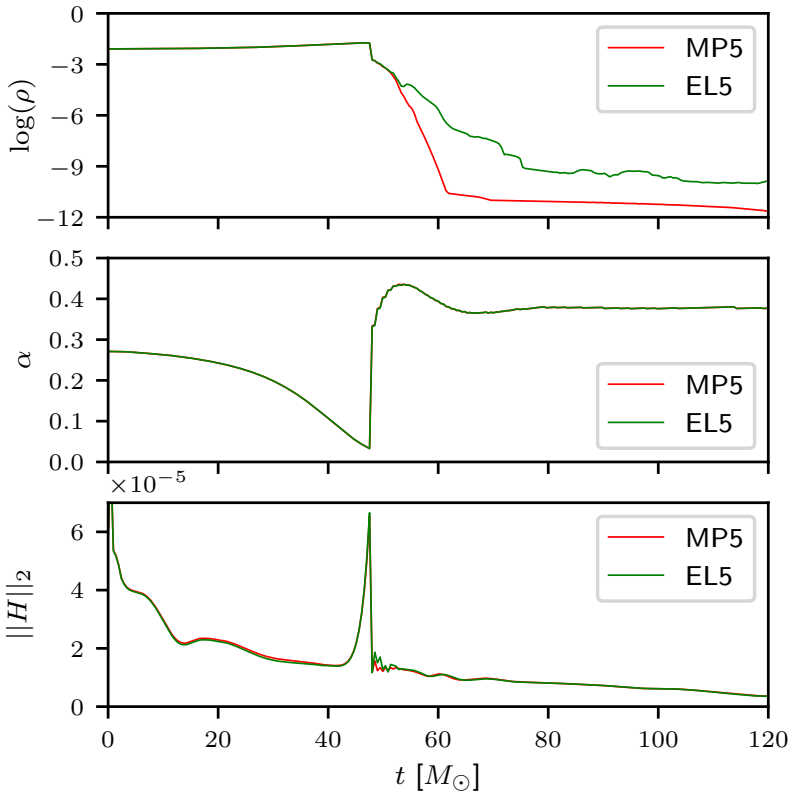

Figure 5.25: Maximum rest-mass density (top), minimum lapse (middle) and L_2-norm of the Hamiltonian constraint (top) for the stellar-collapse test. Note that the violation of the Hamiltonian constrain will grow on longer timescales as it is typical of BSSNOK evolutions (Alic et al., 2013). *Figure reproduced from Guercilena et al. (2017).*

essary (our code can handle the collapse without it, regardless of the scheme we employ). We have however observed that its use improves the accuracy of the subsequent evolution. Most notably it improves the behaviour of the rest-mass density and we therefore choose to employ it nonetheless.

In figure 5.24 we show a snapshot of the rest-mass density on the equatorial (x, y) plane just after the collapse has taken place according to the above definition. A central area of uniform, low density is clearly visible. This is where the hydrodynamical excision has been applied, in the interior of the BH apparent horizon. Note how in this plot this area appears of identical size and shape for the two codes. The region outside the horizon are instead filled with matter spuriously ejected from the outer layers of the star during the collapse. The rest-mass density is evidently higher in the case of the EL5 scheme, corresponding to a slightly higher amount of matter ejected during the collapse. This spurious ejection is in turn triggered by larger oscillations around the stellar surface when the EL5 scheme is employed. For both schemes however the total rest mass outside the horizon is tiny, $\sim 10^{-6}\, M_\odot$ for the EL5 scheme and

$\sim 10^{-9}\, M_\odot$ for MP5, and thus dynamically irrelevant on the properties of the solution. Note that most of this matter is gravitationally bound and hence accretes back onto the newly formed black hole, resulting in streams of infalling matter. This is particularly evident along the coordinate directions, where the numerical viscosity of the high order finite-differences stencil is smaller, independently of the scheme employed (cf. figure 5.11).

How the two schemes actually agree very closely between each other is summarised in figure 5.25. Here the evolution of the central rest-mass density, minimum lapse and L_2-norm of the Hamiltonian constraint violation are plotted. The peaks and discontinuities in the curves at about $50\, M_\odot$ correspond to the time of collapse and are present because we exclude points inside the horizon in the calculation of both extrema and norms. In each panel, before the time of formation of the apparent horizon, the curves corresponding to the EL5 and MP5 schemes are essentially on top of each other (the largest differences being of the order of 0.3%, 0.6%, and 4.7% for each plot, respectively), showing the very good agreement in the evolution between the two schemes. Note also that after the apparent horizon formation, due to our approach of hydrodynamic excision and to the way we compute norms and extrema, the upper panel of figure 5.25 shows the maximum of the density in the exterior of the horizon rather than the central density. The disagreement in the EL5 and MP5 curves relates therefore to the tiny amount of residual matter outside of the black hole, and as such it has no relevance on gauging the agreement of the black-hole solution.

A final confirmation of the equivalence between the two numerical solutions can be obtained by comparing directly quantities pertaining to the black hole itself, such as the BH masses as computed using the dynamical horizon formalism (Ashtekar and Krishnan, 2003). This quantity is shown in figure 5.26. As can be seen from the figure, we find again very close agreement between the two schemes.

5.5 Conclusions

This chapter has presented a new high order numerical method for the solution of the Euler equations of (general-relativistic) hydrodynamics, which has been named "entropy-limited hydrodynamics" (ELH). This is flux-limiting scheme (see section 3.3.3), *i.e.* it maintains stability by combining a high order numerical flux with a stable low-order method, namely the Lax-Friedrichs flux. The flux-limiting is activated and driven by a shock indicator based on a measure of the entropy generated by the solution. This approach has been inspired by the entropy-viscosity method proposed recently for the solution of the classical equations of hydrodynamics (Guermond et al., 2011), but extended to the relativistic case. It is also important to stress that differently from Guermond et al. (2011), our approach does not require any change in the equations of relativistic hydrodynamics.

To assess the robustness and accuracy of this new method, which has been implemented in the `WhiskyTHCEL` code (itself based on the `WhiskyTHC` code), it has been tested and validated with an extensive series of tests, comparing the results of ELH with those obtained with another well-tested and high order HRSC scheme: the fifth-order monotonicity-preserving MP5 method (Suresh

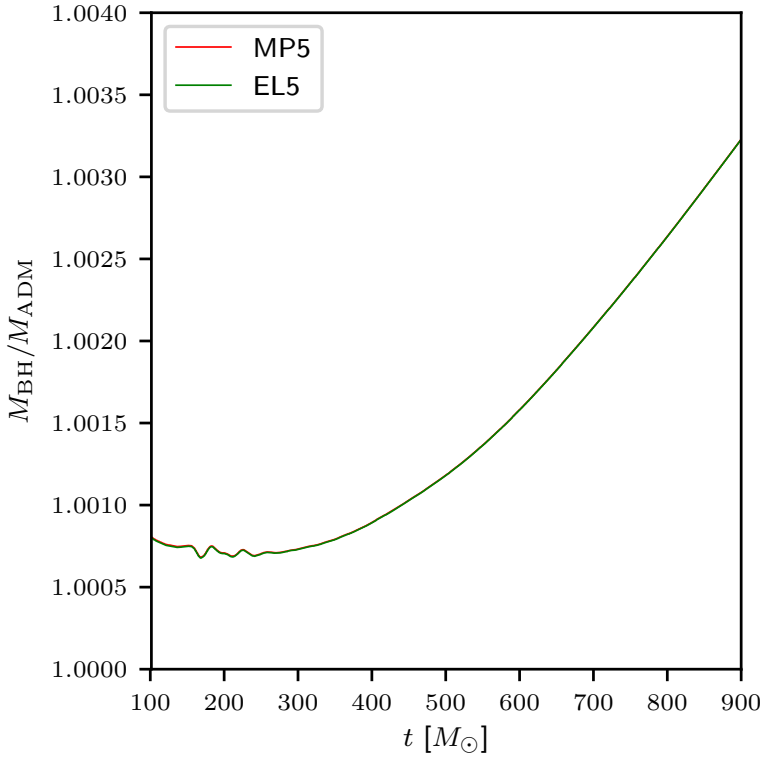

Figure 5.26: Ratio of the apparent-horizon mass to the ADM mass in the stellar-collapse test. Note that the growth is actually very small and is amplified here to show the difference between the two schemes. *Figure reproduced from Guercilena et al. (2017).*

and Huynh, 1997). We have found that the ELH scheme is stable and able to cope with shocks and discontinuities, both in classical test such as shock-tube tests, as well as in realistic astrophysical simulations.

Under all the whole extensive range of conditions in which it has been tested the scheme has been found to be stable and to yield accuracy that is comparable, if not better, of that of the MP5 method. In some tests involving nonrotating or nonmoving stars, it offers definite advantages, such as a sharper resolution of the surface/vacuum interface. At the same time however it shows a worse conservation of the baryon mass for stars that are rotating or moving across the computational domain (the opposite is true for stationary non-rotating stars, where the new method conserves rest mass more accurately). Remarkably, all of the results presented here were obtained without any fine tuning of the two arbitrary coefficients that enter the definition of the scheme. Thanks to its linearity and simplicity, the ELH method can also offer advantages in terms of performance. In our tests we have found EL5 to be $\sim 50\%$ faster than MP5, even though the current implementation is not particularly optimized. A definite advantage of ELH, which we did not yet exploit,

is that it lends itself easily to vectorization. Note however that the exact speed-up that can be achieved with ELH depends also on external factors, such as the grid setup and number of ghost zones, which generally vary for different applications. An interesting development in this sense would be the use of this scheme in a discontinuous Galerkin framework, whose superior scalability properties should decouple the performance of the ELH method from the grid setup.

The work presented here could be improved in at least two ways. The ability of the scheme to capture steep gradients such as stellar surfaces, already quite good, could be further enhanced and the full capabilities of the scheme further exploited by coupling it to truly multidimensional stencils. Secondly, the two free coefficients that appear in the method, and that we have here set to unity for simplicity, could potentially be tuned to optimise some of the features of the solution. Both of these aspects will be explored in future work.

In conclusion it has been shown that entropy-limited hydrodynamics is a robust, stable, and accurate alternative to commonly employed HRSC schemes. Its performance reaches the level of accuracy and stability necessary to apply it to realistic astrophysical simulations. Given these encouraging prospects, work is already in progress to apply this method to realistic simulations of binaries involving neutron stars and black holes.

Part IV

Ejected matter in binary neutron star mergers: r-processes, production of heavy elements and kilonovae

Chapter 6

Equation of state dependence of r-processes and kilonova signals

6.1 Introduction

Recently the era of gravitational-wave astronomy and multi-messenger astronomy has begun with the detection of gravitational waves from binary neutron stars (The LIGO Scientific Collaboration and The Virgo Collaboration, 2017) (BNS) and binary black hole mergers (The LIGO Scientific Collaboration and the Virgo Collaboration, 2016; Abbott et al., 2016a; The LIGO Scientific Collaboration et al., 2017b). In the case of the gravitational-wave event GW170817 a simultaneous electromagnetic counterpart was detected (The LIGO Scientific Collaboration et al., 2017a; LIGO Scientific Collaboration et al., 2017), providing convincing evidence that the puzzle of the origin of short gamma-ray bursts (SGRBs) is to be solved in terms of merging BNSs (Eichler et al., 1989; Narayan et al., 1992; Rezzolla et al., 2011; Berger, 2014; The LIGO Scientific Collaboration and The Virgo Collaboration, 2017; The LIGO Scientific Collaboration et al., 2017a). So far only one single neutron star merger has been detected in the gravitational-wave band, but more are expected to be observed in the coming years.

Among the various electromagnetic counterparts that a merger of neutron stars is expected to generate, one that has recently received significant attention is that of a kilonova (Li and Paczyński, 1998; Rosswog et al., 2013; Piran et al., 2013; Grossman et al., 2014; Perego et al., 2014; Wanajo et al., 2014; Just et al., 2015; Sekiguchi et al., 2015; Radice et al., 2016; Just et al., 2016; Sekiguchi et al., 2016; Metzger and Zivancev, 2016; Tanaka, 2016; Barnes et al., 2016; Rosswog et al., 2017; Wollaeger et al., 2017). This is a signal visible in the infrared/optical band which is powered by the decay of heavy elements produced in the neutron-rich matter ejected from the merger. The dominant contributions to the kilonova signal come from the elements near the second r-process peak (*i.e.* ^{133}I, ^{132}Te and ^{133}Xe), and subdominant ones from the third r-process peak and unstable transuranian elements. Throughout the history

of our universe this nucleosynthesis process has given rise to about half of the elements heavier than iron. They can be formed in the aftermath of a BNS merger due to the onset of rapid neutron-capture processes (r-processes, (Metzger, 2017a)). A kilonova has been indeed detected in coincidence with the gravitational-wave event GW170817, but kilonovae may have potentially been observed already in correspondence with a few GRBs: GRB 130603B (Berger et al., 2013; Tanvir et al., 2013), GRB 060614 (Yang et al., 2015; Jin et al., 2015) and GRB 050709 (Jin et al., 2016). However very large uncertainties in these measurement have prevented an unambiguous identification.

The fundamental concept of the r-process has been known for decades (Burbidge et al., 1957), but its astrophysical site of onset had not been unambiguously identified previously. For matter to undergo r-process nucleosynthesis, a very neutron-rich environment is required and this puts constraints on the potential astrophysical sites where the process should take place. The two most commonly suggested astrophysical sites are core-collapse supernovae (CCSNs) and BNS mergers. Recent simulations of CCSNs have shown however that the environment in the outer layers of the star undergoing the explosion is not neutron-rich enough and have been unable to reproduce the observed solar system abundances of heavy elements (Hüdepohl et al., 2010a,b; Fischer et al., 2010; Wanajo, 2013) (note however that rare forms of CCSN driven by magnetic fields are also a viable possibility (Winteler et al., 2012; Mösta et al., 2014; Nishimura et al., 2017)). Conversely neutron star mergers are increasingly considered the main source site of heavy elements. This conclusion has been strongly supported by recent observations of ultrafaint dwarf galaxies (Ji et al., 2016), whose heavy-element abundance favors BNS over CCSN as the events which have generated it.

From the numerical point of view, numerical-relativity simulations with neutrino transport have shown that not only significant amounts of material are ejected (due to a variety of physical processes) in BNS mergers, but the environment in the ejecta provides the necessary conditions to trigger and sustain robust r-process nucleosynthesis. Broadly speaking the four mechanisms responsible for matter ejection are: dynamical ejecta (Rosswog et al., 1999; Rezzolla et al., 2010; Roberts et al., 2011; Kyutoku et al., 2014; Rosswog, 2013b; Bauswein et al., 2013; Foucart et al., 2014; Hotokezaka et al., 2013; Wanajo et al., 2014; Sekiguchi et al., 2015, 2016; Radice et al., 2016; Lehner et al., 2016; Dietrich and Ujevic, 2017), neutrino-driven winds (Dessart et al., 2009; Perego et al., 2014; Just et al., 2015; Martin et al., 2015b,a; Just et al., 2016; Murguia-Berthier et al., 2014; Fujibayashi et al., 2017), magnetically driven winds (Shibata et al., 2011; Kiuchi et al., 2012; Siegel et al., 2014; Rezzolla and Kumar, 2015; Ciolfi and Siegel, 2015), and viscous evolution of the accretion disk (Beloborodov, 2008; Metzger et al., 2008; Goriely et al., 2011; Fernández and Metzger, 2013). Their typical time scales are approximately ~ 10 ms for dynamical ejecta, ~ 100 ms for magnetically driven or neutrino-driven winds, and ~ 1 s for viscous evolution. Note however that due to the high computational cost of performing long-term fully relativistic simulations, mostly dynamical ejecta have been studied in full relativity, while other mechanisms have been the subject of mostly Newtonian simulations.

In the work presented in this chapter we present the results and analysis of a number of high-resolution numerical-relativity simulations of BNS mergers, with the goal to investigate the effects of the neutron-star initial masses,

mass ratios and equation of state (EOS) on the resulting r-process nucleosynthesis as well as the corresponding kilonova signals. We consider three fully temperature-dependent EOSs spanning a wide range of stiffness. For each EOS, we consider three equal-mass initial setups covering a realistic range of initial BNS masses. Additionally, we consider for each EOS one unequal-mass case.

We have found that the amount of dynamically ejected mass is of the order of $10^{-3}\,M_\odot$, *i.e.* consistent with current constraints on the typical BNS merger rates and observed abundances of heavy elements in the Milky Way. Although some variation in the properties of the ejected mass (*i.e.* typical values of the electron fraction, entropy or velocity) are observed and appear to loosely correlate with the choice of EOS or neutron-star mass for a given BNS model, these differences have minimal influence on the final r-process nucleosynthesis yields. Given the kilonova light curves associated to our simulations, we find that the prospects for their direct observation are rather limited; however this may be not a conclusive statement, given the approximations made in our current analysis. Finally we have studied an interesting geometrical structure in the angular distribution of the ejecta which could have important implications on the properties of the kilonova signal.

This chapter is structured as follows: section 6.2 summarizes the main properties of the physical models and their numerical implementation that we employ to study the BNS evolution as well as to recover the heavy-element abundances. In section 6.3 the initial BNS configurations that we evolve are summarized.Sections 6.4–6.5.4 present our results and findings in terms of the mass ejected, the electron fraction, the specific entropy, and the ejecta velocity. Sections 6.7–6.8 report our estimates for the kilonova light curves and their detectability, together with the constraints on the merger rates of BNSs. Finally the coclusions are presented in section 6.9.

6.2 Overview of the physical models and of the computational infrastructure

In this section the salient features of the physical models we employ to study the evolution of the BNS systems are introduced. Details about the numerical methods used and their implementation are also given. Note that since the approach we have chosen does not significantly differ from well-known ones already described in the literature (as well as in previous chapters), the discussion is rather succinct.

6.2.1 Neutrino treatment in the framework of general-relativistic hydrodynamics

As explained in chapter 2, in particular sections 2.2 and 2.5, we model the neutron-star matter (as well as the matter ejected by the system) as a perfect fluid. As equation of state we use temperature-dependent EOSs (the choice of EOSs will be explained in more detail in section 6.3; note however that the use of a simple barotropic EOS would not be suitable for our purposes, since it would not capture the non-isentropic processes taking place in the fluid. Neu-

trino interactions depend instead sensitively on the temperature and composition of the fluid). The fluid evolution is described by the continuity equation, which expresses the conservation of baryon mass, and the relativistic Euler equations (taking the form of local conservation of the fluid stress-energy tensor components), as elaborated in section 2.5.

Since neutrino interactions can modify the composition of the material, and in particular the value of the electron fraction (which would be otherwise simply advected by the fluid velocity) we have to include their treatment to the otherwise purely hydrodynamic one. To this end we employ a "leakage" scheme (van Riper and Lattimer, 1981; Ruffert et al., 1996; Rosswog and Liebendörfer, 2003), taking into account cooling due to neutrino emission, not modelling neutrino absorption and the subsequent heating. So a source term must be added both to the continuity equation and Euler equations, which take the form (Galeazzi et al., 2013)

$$\nabla_\alpha(n_\mathrm{b}\, u^\alpha) = 0\,, \tag{6.1}$$

$$\nabla_\alpha(n_\mathrm{e}\, u^\alpha) = R\,, \tag{6.2}$$

$$\nabla_\beta T^{\alpha\beta} = Q u^\alpha\,, \tag{6.3}$$

where n_b and n_e are the baryon and electron number density, u^α is the fluid 4-velocity and $T^{\alpha\beta}$ is the fluid stress-energy tensor. We denote with R the net lepton-number emission rate, while Q is the net neutrino-cooling rate, and both are defined per unit volume and in the fluid rest-frame. A detailed discussion on the estimation of Q and R is contained in Galeazzi et al. (2013); Radice et al. (2016).

Contrary to the approach presented in chapter 5, we have chosen for the simulations presented here to solve the hydrodynamics equations with a finite-volumes method, as introduced in section 3.2 (applied of course to the flux-conservative formulation of equations (6.3), *i.e.* the formulation of section 2.5 plus the neutrino source terms presented here). We employ the fifth-order MP5 (Suresh and Huynh, 1997) reconstruction scheme and the HLLE Riemann solver (Harten et al., 1983), as well as the positivity-preserving limiter of Hu et al. (2013); Radice et al. (2014b) (introduced in section 3.3.3). We also make use of the refluxing technique (Berger and Colella, 1989) to minimize numerical spurious losses or gains of mass at the interface between refinement levels. This choice of setup, much more conservative than the somewhat innovative techniques presented in chapters 4 and 5, stems from a need of reliability of the numerical scheme. FV schemes and HRSC methods are a time-tested combination which leads to robust results, so they were selected in order to ensure that the final results would be physically meaningful. The scheme briefly discussed here is implemented in the `WhiskyTHC` code of Radice and Rezzolla (2012); Radice et al. (2014b).

A similar choice was made for the integration of Einstein equations for the spacetime evolution: we employed a fourth order finite-differences method applied to the BSSNOK formulation (Shibata and Nakamura, 1995; Baumgarte and Shapiro, 1999; Brown, 2009) of Einstein equations. The gauge conditions are the standard "1+log" and "Gamma driver" choices (see, *e.g.* Baumgarte and Shapiro (2010)). The spacetime evolution scheme was provided by the `Mclachlan` code (Brown et al., 2009b), and coupled to the hydrodynamics evolution through the evaluation of the fluid stress-energy tensor as customary.

An adaptive mesh refinement (AMR) approach, provided by the box-in-box, Berger-Oliger-type AMR capabilities provided by the `Carpet` driver (Schnetter et al., 2004), was used to increase resolution as well as extend the spatial domain, placing the outer boundary as close as possible to the wave zone. A Cartesian 3D grid with six levels of mesh refinement (promoted to seven after merger) was employed, so that the finest, innermost level during the inspiral has a resolution of $0.15\,M_\odot \simeq 215\,\mathrm{m}$. The outer boundary of the domain extends to $512\,M_\odot \simeq 760\ \mathrm{km}$. The timestep is fixed to a factor of 0.15 of the grid spacing (as necessary to allow the positivity preserving limiter to operate properly, see section 3.3.3) and as in chapter 5 the third-order strong stability preserving Runge-Kutta method (RK3) was used for the time integration.

6.2.2 Outflow analysis: Tracer particles and outflow detectors

Since we are interested primarily in the behaviour and properties of the matter after merger, specific techniques have to be employed to follow its the flow. We employed two different such techniques. The first one is the use of tracer particles (Wanajo et al., 2014; Kastaun et al., 2016; Mewes et al., 2016; Bovard and Rezzolla, 2017), *i.e.* massless particles which are placed in the computational domain at some point during the computation and then passively advected by the fluid. In the simulations presented here a total of $2 \cdot 10^5$ tracers are placed with a uniform distribution in the density interval $10^7\,\mathrm{g/cm^3} \lesssim \rho \lesssim 10^{15}\,\mathrm{g/cm^3}$ at the time of merger (see Bovard and Rezzolla (2017) for a discussion on why this distribution of tracers is the optimal one). Fluid properties, both hydro- and thermodynamical are interpolated at the tracers location at each timestep, providing a detailed description of the evolution of the associated fluid element. Since the history of the evolution of a tracer particle provides the initial input for the nuclear reaction network discussed in section 6.2.4, which finally allows to compute the abundances of heavy elements produced, a mass has to be associated to each tracer, in order to be able to combine the nucleosynthesis output of all tracers in a mass-averaged fashion (not however that this concept of "tracer mass" has no bearing on the inertia of the tracer, but it is only used in the nucleosynthesis computation: as said above, the tracers are passively advected by the fluid). A way of defining the tracer mass is provided for example in Bovard and Rezzolla (2017). More details are provided in section 6.6.

The second technique employed to follow the ejected material consists in the use of so-called outflow detectors, *i.e.* spherical surfaces placed at a fixed coordinate radius around the center of the computational domain. These detectors measure the flux of the fluid quantities through their surface; recording it as a function of time. In our simulations we define nine detectors set at radii between 100 and $500\,M_\odot$ from the center of the domain (which is also the location of the merger remnant) with a separation of $50\,M_\odot$. Each detector has a resolution of 55 points in the polar and 96 points in the azimuthal direction, and the detector located at a radius of $200 M_\odot \approx 300\,\mathrm{km}$ is selected as the fiducial one. As the fluid passes through a detector surface, hydrodynamical and thermodynamical variables are interpolated onto it at each timestep, allowing to record the entire evolution of the fluid properties in all angular directions. Note that when defining the total ejected mass we compute it by integrating the unbound mass flux over the surface of the fiducial detector. This choice is

in contrast to another common one, *e.g.* Hotokezaka et al. (2013), which consists in integrating the rest-mass density of all unbound fluid elements over the whole computational domain (see section 6.5.1 for further details and a comparison between the two methods).

6.2.3 Selection of unbound material

It is furthermore necessary to define a criterion to identify gravitationally unbound material, which will not accrete back onto the merger remnant and can be considered ejected from the system. Bound material will have very different properties from unbound matter, and it won't undergo r-process nucleosynthesis or contribute to the kilonova signal. It is therefore necessary to define a selection criterion to identify unbound matter. Note that such a selection is of course necessary regardless of whether tracer particles or outflow detectors are used to analyze the flow.

Identifying gravitationally unbound material is not a straightforward process mostly due to the finite size of the computational domain. Ejecta can only be followed to its the edge, which is still relatively close to the BNS merger product, sot they can still be influenced by its gravitational pull. This problem can be alleviated in principle by using a larger grid (or even a compactified domain, extending all the way to infinity), but this comes at greater computational cost and some numerical drawbacks (*e.g.* poor resolution, either in an AMR setup or a compactified domain). A related problem is that we are interested in tracking the evolution of the ejected material to study the kilonova signal. This is however expected to peak days after merger, and computing the evolution of the ejecta for such long timescales is currently computationally unfeasible in full numerical-relativity simulations, which are limited at most to timescales of the order of tens/hundreds of milliseconds after merger.

Consequently a criterion to define unbound material is therefore needed and we choose to define a fluid element as "unbound" if it satisfies the so-called *geodesic criterion* (*e.g.* Kastaun and Galeazzi (2015); Sekiguchi et al. (2015)), *i.e.* if $u_t \leq -1$, where u_t is the covariant time component of the fluid element 4-velocity. The justification of such a criterion is clear when considering its Newtonian limit. In this case $u_t \approx -1 - \phi - v^2/2$, where ϕ is the gravitational potential (Rezzolla and Zanotti, 2013). At large separations from the gravitational source, the gravitational potential can be neglected, $\phi \simeq 0$ and thus $u_t \approx -1 - v^2/2 \leq -1$. The criterion amounts therefore to imposing that the fluid element should have non-zero velocity at infinity.

Clearly this is not the only possible choice. An alternative one, that has been studied in Kastaun and Galeazzi (2015), is the so-called *Bernoulli criterion*, which defines a fluid element to be unbound if $hu_t \leq -1$, h being the fluid specific enthalpy. Unless otherwise stated, in the following we only consider the geodesic criterion, and the adjective "unbound" will refer exclusively to material satisfying it. We have however considered the impact that the choice of the criterion for material to be unbound can have on the properties of the dynamically ejected material in section 6.5.5, where we present a comparison of the results obtained with the geodesic and Bernoulli criteria. Note however that since $h \geq 1$ (Rezzolla and Zanotti, 2013), it is clear that the Bernoulli criterion will be in general less restrictive than the geodesic one, always yielding a larger amount of ejected material than the geodesic one.

6.2.4 Nucleosynthetic processes: the nuclear network

Once the evolution of the ejected matter has been recorded by the (unbound) tracers, we carry out the nucleosynthesis calculations with a complete nuclear reaction network, namely the `WinNet` one (Winteler et al., 2012; Korobkin et al., 2012).

A nuclear network is a system of coupled ordinary differential equations (ODE) governing the evolution of the abundances of a set of element and particle species. The abundances are evolved under the influence of the possible reactions responsible for creating, destroying and exchanging particles of the various species. Each of the equations can be written as

$$\begin{aligned}\frac{\mathrm{d}Y_i}{\mathrm{d}t} = &\sum_j N^i_j \lambda_j Y_j + \\ &\sum_{j,k} N^i_{j,k} \rho N_A \langle j,k \rangle Y_j Y_k + \\ &\sum_{j,k,l} N^i_{j,k,l} \rho^2 N_A^2 \langle j,k,l \rangle Y_j Y_k Y_l \,, \end{aligned} \tag{6.4}$$

where $Y_i := N_i/N_B$ is the abundance of the i-th species, *i.e.* the ratio of the number of particles of species i and the number of baryons; ρ is the rest-mass density; N_A is Avogadro's number; $N_{i,[j,[l]]}$ are numerical factor to account for the total number of particles destroyed or created in a given interaction and avoid double counting; and most importantly λ_i is the reaction rate of species i with species j, while $\langle j,k \rangle$ and $\langle j,k,l \rangle$ are two- and three-body integrated collision cross-sections (see Hix and Thielemann (1999); Lippuner and Roberts (2017) for a derivation and further details). Note that the three terms in equation (6.4) refer to reactions that destroy or create a particle of species i with one, two or three other reactant particles, respectively.

The abundances evolution depends on the rest-mass density of the material and its temperature as functions of time. While $\rho(t)$ is a function prescribed a priori (in this case from the trajectory of a tracer), the temperature has to be computed by taking into account the energy released by the nuclear reactions themselves. The total energy released for unit time and per baryon is

$$\dot{\epsilon} = -\dot{\epsilon}_\nu + \dot{\epsilon}_{\mathrm{ext}} - \frac{1}{\Delta t} \sum_i Y_i (m_i - A_i m_u) \,. \tag{6.5}$$

The first term is the energy lost due to neutrino cooling, the second a possible external energy source, while the third is the energy released by the nuclear reactions. In this equation Δt is the network timestep, m_i the mass of a particle of species i, A_i is species i mass number (*i.e.* the total number of baryon in a particle of that species), and m_u is the atomic mass unit. Knowing the energy production, the variation in entropy Δs from the previous iteration can be computed, and by inverting the EOS relation (which for the `WinNet` network is the Helmholtz EOS (Timmes and Arnett, 1999; Timmes and Swesty, 2000)) we recover the temperature.

The set of equations (6.4) can be very stiff, due to the very different timescales associated to different reactions. To ensure stability the ODE system is therefore integrated using the first-order, implicit backwards Euler method (see *e.g.* Hairer et al. (1993); Hairer and Wanner (1996)).

Generally speaking, in such computations the system is assumed to be in nuclear statistical equilibrium (NSE) when the temperature is high enough. This means that all strong reactions are in equilibrium with their inverse ones. This situation can also be thought of as an equilibrium between the reaction of forming a nucleus (Z, N) from Z free protons and N free neutrons, and its inverse reaction, namely completely dissociating a nucleus (Z, N) into Z protons and N neutrons. When nucleons are in chemical equilibrium with all other nuclear species, the energetic cost of turning Z_i protons and N_i neutrons into a single nucleus must be zero, *i.e.*

$$\mu_i = Z_i \mu_{\rm p} + N_i \mu_{\rm n} \,, \tag{6.6}$$

where $\mu_{[i,{\rm p},{\rm n}]}$ are the chemical potentials of the i-th species, of free protons and free neutrons, respectively. Therefore if the conditions for NSE are satisfied (in our computations, this means that $T \geq 10GK$), rather then computing the abundances from equations (6.4), they are set in such a way to satisfy equation (6.6).

The main final output of the network is a set of abundances, one for each nuclear species, taken at a late time when the system has settled to an equilibrium state. By considering such abundances for every representative tracer trajectory in a given simulation and summing them taking into account the mass associated with each tracer, the abundance plots of section 6.6 can be generated.

Over 5800 nuclei between the valley of stability and the neutron-drip line are taken into account by `WinNet`. The reaction rates are taken from the compilation of Rauscher and Thielemann (2000) for the Finite Range Droplet Model (FRDM, see Möller et al. (1995)) and we consider weak-interaction rates including neutrino absorption on nucleons (Möller et al., 2003; Fröhlich et al., 2006). Neutron-capture rates for nuclei with atomic number $Z \gtrsim 80$ and neutron-induced fission rates are taken from Panov et al. (2010). We furthermore include beta-delayed fission probabilities from Panov et al. (2005). `WinNet` has been used as a benchmark in a recent comparison with another general-purpose nuclear reaction network (Lippuner and Roberts, 2017), showing a very good overall agreement.

We post-process representative subsets of unbound tracers from the hydrodynamical simulations according to three different methods of selection (see section 6.6). As already mentioned above, from every tracer a time series of the rest-mass density, temperature, specific entropy, and electron fraction is extracted, on which the nuclear network acts. As most of the tracer trajectories were simulated only until ~ 20 ms after the merger, we extrapolate them to very large distances using the following prescriptions for the position, density and temperature evolution (Fujimoto et al., 2008; Korobkin et al., 2012)

$$r(t) = r_0 + v_0 t, \tag{6.7}$$

$$\rho(t) = \rho_0 \left(\frac{t}{t_0}\right)^{-3}, \tag{6.8}$$

$$T(t) = T\left[s, \rho(t), Y_{\rm e}(t)\right] \,. \tag{6.9}$$

where ρ is the total rest-mass density, r the coordinate radius, v the 3-velocity, s the specific entropy, and $Y_{\rm e} := n_{\rm e}/n_{\rm b}$ the electron fraction. The subscript

"0" indicates the last available values from the hydrodynamical simulations, and the temperature is computed from the Helmholtz EOS (Timmes and Arnett, 1999; Timmes and Swesty, 2000). This ansatz for the ejecta expansion is well justified, at least at late times, as shown in Bovard and Rezzolla (2017), where tracers were reported to move ballistically along radial directions and to expand adiabatically at large distances from the merger product.

Note that the network is "self-heating": it computes the energy released by the r-processes and includes its impact on the evolution of the fluid entropy (Freiburghaus et al., 1999), rather than simply using the values provided by the tracer evolution. The major contribution to the radioactive heating is expected to come from beta decays and we assume the energy to be about equally distributed between thermalising electrons and photons, and escaping neutrinos and photons (Metzger et al., 2010).

6.3 Physical setup and initial data

We consider both equal- and unequal-mass BNS systems on quasi-circular orbits, with initial configurations constructed from three different EOSs, spanning a wide range in stiffness. From the stiffest to the softest, these EOSs are: (i) DD2 (Typel et al., 2010); (ii) LS220 (Lattimer and Swesty, 1991) with compressibility parameter $K = 220\,\mathrm{MeV}$; SFHO (Steiner et al., 2013). Note that recent calculations in Tews et al. (2016) have shown that the LS220 EOS does not satisfy constraints stemming from a lower bound on the energy per nucleon provided by the unitary-gas approximation. This result disfavours the LS220 as a viable model for the microphysics of neutron stars, but since this EOS is also one of the most well-studied in numerical applications, we include it in our study since it provides a useful comparison with the literature. Additionally, the DD2 and SFHO EOSs include additional light nuclei that are not included in the LS220, which impacts the neutrino interactions (Stellarcollapse Website).

For each EOS, we consider three different equal-mass setups, with neutron-star gravitational masses of $1.25, 1.35$ and $1.45\,M_\odot$, respectively; and one unequal-mass system, with star masses of 1.2 and $1.35\,M_\odot$, resulting in a mass ratio $q = 0.9$ and a total ADM mass (see Gourgoulhon (2012) for a definition) of the system which is intermediate between the two lightest equal-mass configurations for the same EOS. The stars' initial separation is chosen to be $45\,\mathrm{km}$, resulting in an inspiral phase of approximately ~ 3 orbits. Table 6.1 summarizes the properties of each system. The stars initial states are computed at neutrinoless beta equilibrium, *i.e.* at zero neutrino chemical potential, thus setting the initial values of the electron fraction. The initial data for every binary was constructed using the `LORENE` pseudo-spectral elliptic solver (Gourgoulhon et al., 2001) and refers to irrotational binaries in quasi-circular orbit.

6.4 Overview of the general dynamics

This section discusses the outcome of the simulations, comparing the outflow properties of the dynamically ejected material such as the mass ejected $M_{\rm ej}$, the electron fraction $Y_{\rm e}$, the specific entropy s, and the ejecta velocity $v_{\rm ej}$, for

Model	EOS	q	M_1 $[M_\odot]$	M_2 $[M_\odot]$	R_1 [km]	R_2 [km]	$M_{\rm ADM}$ $[M_\odot]$
LS220-M1.25	LS220	1.0	1.25	1.25	12.80	12.80	2.48
LS220-M1.35	LS220	1.0	1.35	1.35	12.75	12.75	2.67
LS220-M1.45	LS220	1.0	1.45	1.45	12.67	12.67	2.87
LS220-q09	LS220	0.9	1.21	1.35	12.81	12.75	2.61
DD2-M1.25	DD2	1.0	1.25	1.25	13.20	13.20	2.48
DD2-M1.35	DD2	1.0	1.35	1.35	13.23	13.23	2.68
DD2-M1.45	DD2	1.0	1.45	1.45	13.25	13.25	2.87
DD2-q09	DD2	0.9	1.22	1.35	13.19	13.23	2.55
SFHO-M1.25	SFHO	1.0	1.25	1.25	11.97	11.97	2.48
SFHO-M1.35	SFHO	1.0	1.35	1.35	11.92	11.92	2.68
SFHO-M1.45	SFHO	1.0	1.45	1.45	11.87	11.87	2.87
SFHO-q09	SFHO	0.9	1.22	1.35	11.97	11.92	2.55

Model	$M_{\rm b,1}$ $[M_\odot]$	$M_{\rm b,2}$ $[M_\odot]$	$M_{\rm TOV}$ $[M_\odot]$	$R_{\rm TOV}$ [km]	$\mathcal{C}_1$ -	$\mathcal{C}_2$ -	J $[M_\odot^2]$
LS220-M1.25	1.36	1.36	2.04	10.65	0.144	0.144	6.42
LS220-M1.35	1.47	1.47	2.04	10.65	0.156	0.156	7.26
LS220-M1.45	1.60	1.60	2.04	10.65	0.169	0.169	8.20
LS220-q09	1.32	1.47	2.04	10.65	0.140	0.156	6.98
DD2-M1.25	1.35	1.35	2.42	11.90	0.140	0.140	6.40
DD2-M1.35	1.47	1.47	2.42	11.90	0.151	0.151	7.31
DD2-M1.45	1.59	1.59	2.42	11.90	0.161	0.161	8.19
DD2-q09	1.31	1.47	2.42	11.90	0.136	0.151	6.68
SFHO-M1.25	1.36	1.36	2.06	10.31	0.155	0.155	6.40
SFHO-M1.35	1.48	1.48	2.06	10.31	0.167	0.167	7.28
SFHO-M1.45	1.61	1.61	2.06	10.31	0.181	0.181	8.20
SFHO-q09	1.32	1.48	2.06	10.31	0.150	0.167	6.67

Table 6.1: Summary of the properties of the systems under consideration. The columns denote, respectively: the EOS; the gravitational mass ratio $q := M_1/M_2$ at infinite separation; the gravitational masses $M_{1,2}$ of the two stars at infinite separation; the stars' radii $R_{1,2}$ at infinite separation; the ADM mass $M_{\rm ADM}$ of the system; the baryon masses $M_{\rm b,1,2}$; the maximum mass of a non-rotating model of the given EOS $M_{\rm TOV}$; the radius of the maximum mass non-rotating model of the given EOS $R_{\rm TOV}$; the compactnesses $\mathcal{C}_{1,2} := M_{1,2}/R_{1,2}$; the total angular momentum J at the initial separation. *Table reproduced from Bovard et al. (2017).*

the different simulation parameters. Each simulation was run until at least 10 ms after merger, in order to ensure a sufficient time for the dynamical ejecta to reach $300\,\mathrm{km}$, which is where its properties are measured.

Given the initial separation of each BNS model, we simulate approximately ~ 3 orbits before merger. The time of merger is defined as the time at which the gravitational-wave amplitude reaches its first peak, as customary (Baiotti et al., 2010); in the following we define the time origin such that $t = 0$ corresponds to the time of merger. Given the maximum mass of non-rotating neutron star models $M_{\rm TOV}$ corresponding to our choices of masses and EOSs, and the initial mass of the merging binaries, all the mergers that do not yield a

prompt collapse to a black hole produce a hypermassive neutron star (HMNS), *i.e.* a neutron star whose mass exceeds the maximum mass supported by uniform rotation, $M_{\rm max} \simeq 1.20 M_{\rm TOV}$ (Breu and Rezzolla, 2016), and that is in a metastable equilibrium state supported by differential rotation, with a quasi-universal rotation profile (Hanauske et al., 2017).

The three binaries which instead collapse to a black hole are `SFHO-M1.35`, `SFHO-M1.45`, and `LS220-M1.45` with the latter two yielding a prompt collapse: for `SFHO-M1.45` the collapse is right at the time of merger and results in very little material being ejected (see the discussion in section 6.5.1), while for `LS220-M1.45` the collapse takes place about ~ 0.5 ms after merger, which is sufficient for material to be ejected. For `SFHO-M1.35` the collapse to a black hole takes place at $\sim$ 10 ms after merger instead, when the HMNS has lost sufficient angular momentum.

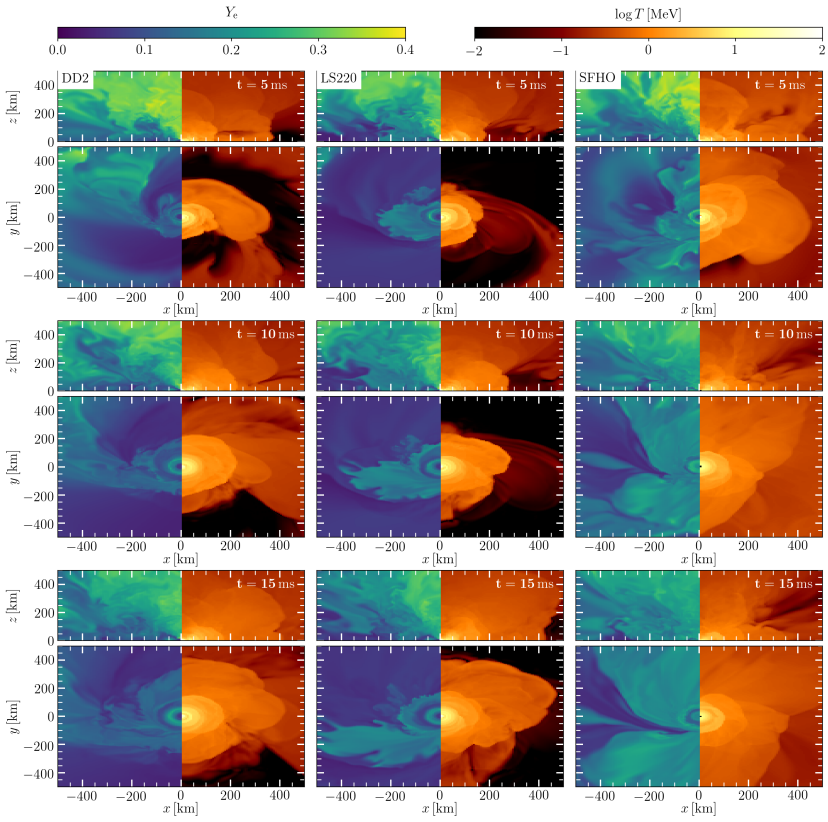

Figure 6.1: Evolution of the electron fraction (left parts of panels) and of the temperature (right parts of panels) on the (x, z) plane (top panels) and on the (x, y) plane (bottom panels), for the different EOSs, namely: DD2, LS220, SFHO, from left to right. All panels refer to binaries with masses of $2 \times 1.35 M_\odot$ and at the same representative times: 5 ms (top row), 10 ms (middle row), and 15 ms (bottom row) after the merger. *Figure reproduced from Bovard et al. (2017).*

To show the spatial distributions of various quantities pertaining to the

ejected matter in the simulations, figure 6.1 plots three different time slices ($5, 10, 15$ ms from top to bottom) of the electron fraction (left panels) and the temperature (right panels) in the (x, y)- (bottom panels) and (x, z)-planes (top panels) for the three $1.35 M_\odot$ equal-mass initial data with different EOSs.

Model	$M_{\rm ej}$ $[10^{-3}\,M_\odot]$	$\langle Y_{\rm e}\rangle$ -	$\langle s\rangle$ $[{\rm k_B}/{\rm baryon}]$	$\langle v_{\rm ej}\rangle$ $[10^{-1}{\rm c}]$	$\langle v_\infty\rangle$ $[10^{-1}{\rm c}]$
LS220-M1.25	0.61	0.08	10.3	2.2	1.6
LS220-M1.35	0.82	0.10	12.7	2.2	1.5
LS220-M1.45	1.09	0.11	10.5	2.6	2.1
LS220-q09	0.90	0.09	11.9	2.2	1.5
DD2-M1.25	0.96	0.13	13.9	2.3	1.7
DD2-M1.35	0.58	0.14	16.5	2.4	1.8
DD2-M1.45	0.50	0.17	19.2	2.7	2.1
DD2-q09	0.46	0.14	18.5	2.3	1.7
SFHO-M1.25	0.55	0.14	15.6	2.5	2.0
SFHO-M1.35	3.53	0.16	12.7	2.7	2.2
SFHO-M1.45	0.01	0.24	35.9	3.1	2.6
SFHO-q09	0.76	0.16	18.8	2.4	1.8

Model	$t_{H,\rm peak}$ [days]	$L_{\rm peak}$ $[10^{40}\,{\rm erg/s}]$	$m_{J,\rm peak}$ [AB]	$m_{H,\rm peak}$ [AB]	$m_{K,\rm peak}$ [AB]
LS220-M1.25	0.53	2.24	-12.6	-12.6	-12.4
LS220-M1.35	0.51	2.00	-12.5	-12.4	-12.2
LS220-M1.45	0.48	2.62	-12.8	-12.7	-12.5
LS220-q09	0.50	1.94	-12.4	-12.3	-12.1
DD2-M1.25	0.50	2.24	-12.6	-12.5	-12.4
DD2-M1.35	0.50	2.44	-12.7	-12.7	-12.5
DD2-M1.45	0.50	2.89	-12.9	-12.9	-12.5
DD2-q09	0.53	2.34	-12.7	-12.6	-12.4
SFHO-M1.25	0.47	2.54	-12.8	-12.7	-12.5
SFHO-M1.35	0.53	3.36	-13.2	-13.2	-13.0
SFHO-M1.45	0.16	0.86	-11.1	-10.9	-10.5
SFHO-q09	0.60	2.92	-12.0	-13.0	-12.9

Table 6.2: Summary of the mass-averaged quantities of section 6.5 and kilonova observational quantities of section 6.7 computed from the simulations. The columns are, respectively: $M_{\rm ej}$ the dynamical mass ejecta measured at $300\,{\rm km}$, $\langle Y_{\rm e}\rangle$ the mass-averaged electron fraction, $\langle s\rangle$ the mass-averaged entropy, $v_{\rm ej}$ the mass-averaged velocity of the ejecta, $\langle v_\infty\rangle$ the velocity of the ejecta at infinity using equation (6.12), $t_{H,\rm peak}$ the peak time in the H-band of the kilonova signal, $L_{\rm peak}$ the peak luminosity of the kilonova, $m_{X,\rm peak}$ the peak absolute magnitude in the $X = J, H, K$ bands respectively. *Table reproduced from Bovard et al. (2017).*

As anticipated in the introduction, when considering dynamical ejecta there are two main processes which can eject material, namely tidal forces and shock heating. The former are a straightforward process arising from tidal interactions during merging and eject material primarily along the orbital plane: they are a manifestation of the gravitational interaction of the two stars. Shock heating instead results in an approximately spherically symmetric ejection of mat-

ter (Sekiguchi et al., 2015) and depends on the thermal properties of the fluid rather than on the gravitational interaction. These two distinct mechanisms are illustrated in figure 6.1 where the orbital plane region shows lower $Y_{\rm e}$ and denser material, while the polar regions have higher $Y_{\rm e}$ and less dense material.

We first consider the tidal ejecta. This kind of ejecta tends to be very neutron-rich, since it becomes unbound immediately during and following merger, and originates from matter near the surfaces of the stars. These tidal tails can be observed in the (x, y)-plane at 5 ms (top row) panels of figure 6.1, where the they are visible in the outer regions beyond $300\,\mathrm{km}$. This ejected material also tends to present lower temperature, around 1 MeV. In contrast, in the (x, z)-plane, $Y_{\rm e}$ reaches much higher values of approximately 0.3 (*i.e.* the matter is much less neutron rich), that are not observed in the orbital plane. These higher values in the electron fraction are due to the material being shocked-heated. In the polar regions right above the HMNS, no material is ejected tidally and neutrinos become free streaming very close to the merger product. As a result of weak interactions by means of which the free neutrons are converted into protons, the material becomes less neutron-rich. However, as the angle from the pole decreases, the material becomes more optically thick and more neutron-rich as the neutrino interactions are not as strong. This angular dependence is also seen in the temperature profiles as there are higher temperatures near the polar axis when compared with the orbital plane.

Note that although neutrinos are only treated simplistically (Galeazzi et al., 2013) in these simulations, this broad-brush description is qualitatively similar to more sophisticated approaches, such as the use of an M1 neutrino transport scheme, which leads to an increase in the amount of ejected material in the polar regions (Foucart et al., 2016b,a,c; Sekiguchi et al., 2015, 2016) and higher $Y_{\rm e}$.

There is a clear overall trend to be deduced from figure 6.1 concerning the dependence of the simulation outcome from the EOSs employed. The "softer" an EOS is, the hotter the matter tends to be. This is due to the fact that a softer EOS allows for a deeper gravitational well, which in turn allows for the material to become hotter. This dependence is clearest when comparing the softer SFHO and the stiffer LS220 EOSs (left and right columns), where the temperature in the (x, y)-plane is much hotter for the SFHO than the LS220, as per the explanation sketched above. As a result, because neutrino interactions depend on the temperature, the electron fraction is also higher the softer an EOS is. Again this is most clear when examining the fluid properties on the (x, y)-plane of the SFHO and LS220 simulations, where the data referring to the LS220 EOS is much more neutron-rich when compared with the SFHO EOS.

6.5 Properties of the matter outflow

This section is dedicated to a comprehensive discussion of the properties of the matter that is dynamically ejected at and after the merger, focusing on the total amount of ejected matter as well as on the distribution of this matter in terms of the electron fraction, the specific entropy and the velocity of the fluid elements.

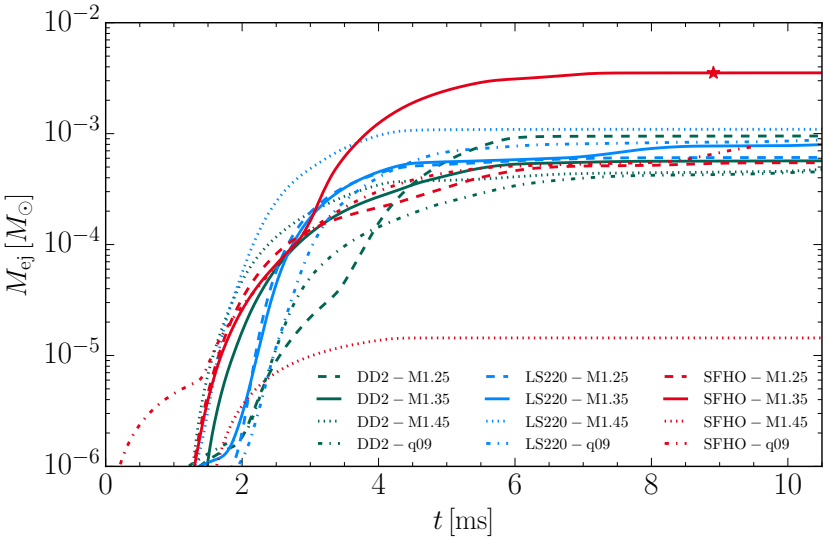

Figure 6.2: Evolution of the dynamically ejected unbound mass $M_{\rm ej}$ as measured through a detector at radius $300\,\mathrm{km}$ when using the geodesic criterion and for the various binaries considered. The star denotes the time of black-hole formation for model `SFHO-M1.35`. Binaries `LS220-M1.45` and `SFHO-M1.35` collapse shortly after merger and are not visible in the plot. *Figure reproduced from Bovard et al. (2017).*

6.5.1 Total ejected mass

It essential to accurately measure the total amount of ejected material from a binary merger in order to characterize the amount r-process elements produced and the potential observable properties of the kilonova signal (see section 6.7). In section 6.2.2 the definition of the total ejected mass was anticipated, which makes use of an outflow detectors to measure the flux of unbound material at a given radius. As said we consider the detector placed at a radius of $200M_\odot \approx 300\,\mathrm{km}$ as the fiducial detector through which to measure the amount and properties of the ejected material. To compute the total mass ejected, the flux of the rest-mass density through the detector's spherical surface is computed and then integrated over the whole sphere. This gives the total mass-flux which can be integrated over time to provide a measurement of the total dynamically ejected material $M_{\rm ej}$. In this calculation, only the flux associated to unbound fluid elements contributes to the integral. Explicitly, for a detector at a given radial distance, the total ejected mass is given by

$$M_{\rm ej}(t) := \int_0^t \int_\Omega \rho_* W(\alpha v^r - \beta^r)\sqrt{\gamma}_\Omega \mathrm{d}\Omega \mathrm{d}t' \,, \tag{6.10}$$

where $\sqrt{\gamma}_\Omega$ is the surface element on the detector (*i.e.* the square root of the determinant of the 2-metric induced on the detector by the spacetime 4-metric); the term $\rho_* W(\alpha v^r - \beta^r)$ is the flux of mass through the sphere, expressed in terms of the 3+1 quantities: the lapse function α, the shift vector β^i, and the

fluid 3-velocity v^i, the Lorentz factor $W := (1 - v^i v_i)^{-1/2}$ and the fraction of the rest-mass density that is unbound ρ_*, *i.e.* of fluid elements that do satisfy the geodesic criterion. The integral of the mass flux can then be integrated in time over the whole post merger period, *i.e.* from $t = 0$ to T_f. T_f is the time at the end of the simulation, which is far enough so that the mass flux becomes negligible and the integration can be stopped.

In figure 6.2 the amount of ejected material computed through equation (6.10) is plotted over time for the LS220 (blue), DD2 (green), and SFHO (red) EOSs and the different masses and mass ratios[1]. The results of figure 6.2 are also summarised in table 6.2, where $M_{\rm ej}$ refers to the mass ejected at $t = 10$ ms after merger.

The qualitative behaviour of all simulations is similar. There is a large ejection of material, due to tidal interactions and shock heating, that reaches the detector approximately 1 ms after merger and continues for about $4 - 5$ ms before the flux becomes zero. The details of the behaviour of the mass ejection over time, in particular the time at which the mass flux becomes negligible are partly due to the choice of the geodesic criterion. In section 6.5.5 we discuss how this picture changes when considering the Bernoulli criterion, which results in material being ejected also at later times.

Figure 6.2 shows that the amount of ejected material is in the range $0.5 - 1 \times 10^{-3} M_\odot$ in all cases, with two exceptions. The first is the binary `SFHO-M1.45`, which collapses immediately to a black hole and produces very little ejected material (almost an order of magnitude less than the others), as most matter is accreted back onto the black hole. Conversely, the binary model `SFHO-M1.35` ejects a significant amount of material when compared with the other models. This binary also collapses to a black hole around 9 ms after merger (see the star symbol in figure 6.2) and since the SHFO EOS is a rather soft one, the HMNS present before collapse is the most compact we have simulated. Under these conditions, it is natural that the larger compressions attained will lead to stronger shock heating and hence to a larger dynamical mass ejection.

An alternative method of measuring the amount of ejected mass with respect to equation (6.10) consists in evaluating a volume integral of the rest-mass density of the unbound material over the entire computational domain (Hotokezaka et al., 2013; Sekiguchi et al., 2015; Lehner et al., 2016; Dietrich et al., 2017b), *i.e.*

$$M_{\rm ej}(t) = \int \rho_* W \sqrt{\gamma} \mathrm{d}^3 x. \tag{6.11}$$

As a consistency cross-check we have employed this measurement for model `LS220-M1.35` and found that $M_{\rm ej}(t)$ in this case is obviously not a monotonically increasing function of time, but reaches a maximum of $M_{\rm ej} = 0.80 \times 10^{-3} M_\odot$. This measurement differs only by $4\,\%$ from that obtained via equation (6.10), showing the robustness of our mass ejection analysis procedure and that the 300 km measurement radius is the most robust choice. The reason why the use of of equation (6.11) results in a non-monotonically increasing curve, which is also an apparent downside of this method, is that because of the finite size of the domain, material that reaches the outer boundary is no longer

[1] Unless specified otherwise, from now on the same color scheme is employed to refer to the various EOSs: simulations with the LS220 EOS are shown in blue, DD2 in green, and SFHO in red. The different masses are instead denoted by different line styles: $1.25 M_\odot$ is dashed, $1.35 M_\odot$ is solid, $1.45 M_\odot$ is dotted, and $q = 0.9$ is dash-dotted.

include in the calculation and causes the total ejected mass to decrease. Considering this artefact, it is necessary to choose a time at which to evaluate the total ejected mass. We have evaluated equation (6.11) at ~ 3 ms after merger where it reaches a maximum. Note that this introduces some level of arbitrariness in the estimation of the total ejected mass. This specific arbitrariness does not arise with the flux-integral method (6.10), which is integrated over all time. However in that case a choice needs to be made for the extraction radius. In our calculations we have found that the difference between the detector at $300\,\mathrm{km}$ and a detector at $740\,\mathrm{km}$ of radius is about 30% in total ejected mass irrespective of EOS. Although detectors further away from the remnant have a slightly higher ejected mass, the properties of the fluid are very close to atmosphere at these radii, which should therefore be avoided.

It is interesting to note that our measured values of the ejected masses are systematically smaller than those reported in Sekiguchi et al. (2015) for the same masses and EOS. This is likely due to the simplistic neutrino treatment employed here and to the fact that more-sophisticated M1-scheme with heating, such as that used in Sekiguchi et al. (2015, 2016), can allow for material to be more energetic and hence to become more easily unbound (Foucart et al., 2016b). On the other hand our measurements agree well with those of Lehner et al. (2016), where a similar leakage approach was employed; at the same time, the preliminary use of an M0-scheme as that used in Radice et al. (2016) (which is a middle-ground alternative to leakage or M1-schemes in terms of sophistication and physical realism) is insufficient to explain this difference in the ejected mass. Since the amount of ejected material depends also on the specific properties of the computational infrastructure, such as the location of the extraction radius in equation (6.10), or the size of the computational domain in equation (6.11), only a direct comparison of the various neutrino-transport schemes within the same code can quantify the variance of the ejected matter on the neutrino treatment or the numerical specifications.

6.5.2 Electron fraction distribution

The electron fraction is a critical piece of information to determine the r-process nucleosynthesis yields since Y_e is effectively a measure of how many free neutrons are available. Typically low-Y_e environments (*i.e.* richer in neutrons) favour a robust r-process and yield a higher fraction of heavier elements while in high-Y_e regimes (*i.e.* with less free neutrons) the production of very heavy elements tends to be suppressed. Differences in Y_e also correspond to potential differences in the properties of the resulting kilonova signal, due to the efficient production (or lack thereof) of high-opacity elements such as lanthanides. In particular the so-called "blue" kilonovae (*i.e.* peaking at higher frequencies, in the optical band) are possible in environments with $Y_\mathrm{e} \gtrsim 0.25$ and "red" kilonovae (peaking in the infrared) in environments with $Y_\mathrm{e} \lesssim 0.25$ (Metzger and Zivancev, 2016; Metzger, 2017a) (we will discuss the angular distributions of the thermodynamical quantities and their impact on the kilonova in section 6.7 and 6.7.1).

In figure 6.3 histograms of the mass distribution of the ejected matter over the electron fraction are shown for all 12 simulations, as computed from the data relative to our fiducial detector at radius $300\,\mathrm{km}$; different panels refer to different EOSs, while the different lines refer to different masses and mass ra-

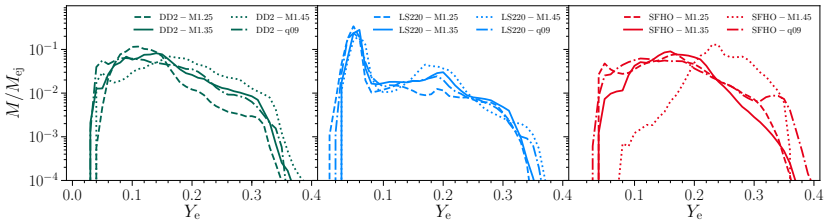

Figure 6.3: Distributions of the ejected mass fraction as function of the electron fraction $Y_{\rm e}$, as measured by a detector at radius $300\,\mathrm{km}$. The range of $Y_{\rm e}$ is divided into bins of width 0.01. The histograms are normalized over the total ejected mass $M_{\rm ej}$. The left panel refers to the DD2 EOS simulations, the middle one to the LS220 EOS and the right one to the SFHO EOS; different line types mark binaries with different masses and mass ratios. *Figure reproduced from Bovard et al. (2017).*

tios. To produce such histograms in each patch into which the detector sphere is subdivided the local electron fractino value is recorded and the local amount of ejected mass is estimated. These values are then integrated over time up to T_f to produce the mass ejected along with the corresponding $Y_{\rm e}$; the resulting $Y_{\rm e}$ range is divided into bins of width 0.01 and the unbound mass of each patch at each time is assigned to a bin according to its corresponding value of $Y_{\rm e}$, thereby generating the histograms shown in figure 6.3.

Irrespective of the EOS and mass configuration, common qualitative features can be spotted. For all EOSs the ejected mass is distributed in a range of $Y_{\rm e}$ varying from approximately 0.04 up to 0.4, peaking at $Y_{\rm e} \lesssim 0.2$. The only exception is the `SFHO-M1.45` model, in which little material is ejected due to black hole formation and whose distribution peaks at higher values of $Y_{\rm e}$. This spread of the electron fraction over a wide range is due to the inclusion of a neutrino treatment, which causes the number of electrons to change due to weak interactions. Failure to take such interaction into account would result in a very different distribution, sharply peaked at very low values of $Y_{\rm e}$, *i.e.* pure neutron matter (see *e.g.* Radice et al. (2016)).

The LS220 runs (left panel) exhibit very similar distributions for all mass configurations, peaking at approximately $Y_{\rm e} = 0.05$ with a secondary peak at $Y_{\rm e} \approx 0.2$ before sharply dropping off at electron fraction values of $Y_{\rm e} \gtrsim 0.3$. The distributions of the DD2 (middle panel) also all exhibit a similar behaviour, with a sharp increase at $Y_{\rm e} \sim 0.05$ before broadening out with a sharp drop around $Y_{\rm e} \sim 0.3$. Finally, the distributions of the SFHO runs (right panel) exhibit a somewhat different behaviour, although spanning a similarly broad range in $Y_{\rm e}$. The main differences in this case are the tail of the distribution at higher values of the electron fraction. In all cases most of the ejected matter is found at low values of the electron fraction, *i.e.* it is very neutron-rich, which suggests a robust r-process in all of the cases considered.

This conclusion is also supported by table 6.2, where the average values $\langle Y_{\rm e} \rangle$ of the electron fraction are reported for all 12 runs. The averages are computed over the mass/electron fraction histograms of figure 6.3. As can be seen in all simulations, the average value of the electron fraction in the ejecta is

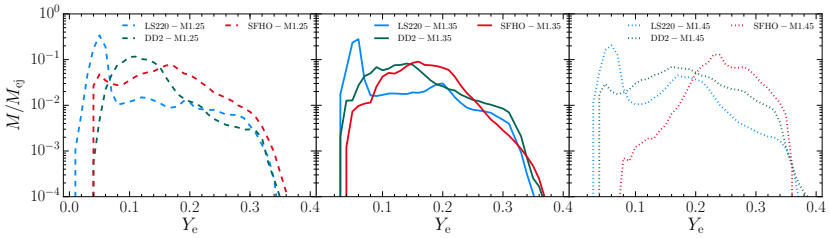

Figure 6.4: Distributions of the ejected mass fraction as function of the electron fraction $Y_{\rm e}$, as measured by a detector at radius $300\,{\rm km}$. This is the same as figure 6.3, except that the curves are here grouped by mass configuration rather than EOS so as to highlight the dependence on the latter. For clarity, unequal-mass binaries are not shown. *Figure reproduced from Bovard et al. (2017).*

approximately 0.15 or lower, indicating on average a very neutron-rich environment. The only exception is model `SFHO-M1.45` where $\langle Y_{\rm e}\rangle = 0.24$.

In figure 6.4, to help the comparison of the results across different EOSs, the distributions are arranged according to the total mass of the BNS (the unequal-mass cases are excluded) instead of EOS as in figure 6.3. In all panels there is a noticeable trend in the distributions of $Y_{\rm e}$, which is most evident in the $1.25M_{\odot}$-case (left panel). In this case $\langle Y_{\rm e}\rangle = 0.08$, 0.13, and 0.14 for LS220, DD2, and SFHO EOSs, respectively. This increase in $Y_{\rm e}$ is expected when considering that neutrino interactions depend strongly on the temperature. The average entropy (see section 6.5.3) of these simulations is 10.3, 13.9, and $15.6\ {\rm k_B/baryon}$ respectively. Entropy is related to temperature and the higher the entropy, the higher the average temperature, cf. figure 6.3, and hence more free neutrons are converted into neutrinos through positron capture, increasing $Y_{\rm e}$.

This effect is also related to the compactness of the object, albeit this relation should be treated carefully. SFHO is the softest EOS among the ones considered, which leads to the most compact objects. This results in higher temperatures during the merger, which causes an increase in the neutrino reactions, which decreases the number of neutrons and as expected has the higest average $Y_{\rm e}$. In contrast, from table 6.1 one would expect that because LS220 is more compact than DD2, LS220 should have a higher average $Y_{\rm e}$ and entropy when the opposite is this the case. This difference is due to compactness being a property calculated for cold beta-equilibrium where the effects of composition are minimal. As discussed in section 6.3, the LS220 EOS does not include light nuclei which can change the composition and the neutrino interactions, so this seemingly non-monotonic relation between compactness and average $Y_{\rm e}$ arises from different constructions of the EOS. When comparing DD2 and SFHO and excluding LS220, there is a clear monotonic relationship between $\mathcal{C}$ and $Y_{\rm e}$.

When comparing our results with those of simulations with similar initial data, there is a disagreement with computed values of the electron fraction. For example for the `DD2-M1.35` model with our measured value of $\langle Y_{\rm e}\rangle = 0.14$, the authors of Sekiguchi et al. (2015) report $\langle Y_{\rm e}\rangle = 0.29$ with an M1-scheme independent of resolution and $\langle Y_{\rm e}\rangle = 0.26$ with a leakage scheme with a resolution of 200 m. However a similar distribution in $Y_{\rm e}$ is observed in Palenzuela

et al. (2015); Lehner et al. (2016), which use a similar leakage scheme to the one used here.

6.5.3 Specific entropy distribution

The next thermodynamic quantity we consider is the distribution of the ejected material over the entropy per baryon s. The specific entropy is important in r-process nucleosynthesis as it is an indicator of the neutron-to-seed ratio, the "seeds" being the nuclei initially present in the matter and undergoing neutron capture. High initial neutron-to-seed ratios favour the production of heavy nuclei during the r-process nucleosynthesis, even at relatively high electron fractions. In radiative environments such as those found in the ejected matter the specific entropy will scale with the temperature as $s \propto T^3$, so that the shock-heated (and hotter) part of the dynamical ejecta will exhibit higher specific entropies. In turn at high temperatures the presence of high energy photons enhances the photodissociation of seed nuclei, do that a higher specific entropy will increase the neutron-to-seed ratio and thus r-process nucleosynthesis. In contrast the cold, tidal dynamic ejecta usually exhibit low entropy, but extremely neutron-rich material (Korobkin et al., 2012). The distribution of the specific entropy, computed with the same procedure as the electron fraction distribution in the previous section, is shown in figure 6.5, while the average values $\langle s \rangle$ are reported in table 6.2.

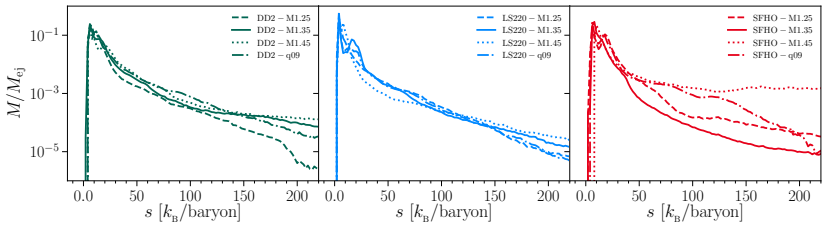

Figure 6.5: Distributions of the ejected mass fraction as function of the specific entropy s, measured by a detector at radius $300\,\mathrm{km}$ from the domain origin. The range of s is divided into bins of width $2\ \mathrm{k_B/baryon}$. The histograms are normalized over the total ejected mass $M_{\rm ej}$. The left panel refers to the LS220 EOS simulations, the middle one to the DD2 EOS and the right one to the SFHO EOS. *Figure reproduced from Bovard et al. (2017).*

Again many EOS-independent qualitative features can be observed. For all EOSs the mass distribution peaks at $s \approx 2\ \mathrm{k_B/baryon}$, rapidly decaying towards higher entropies. In the case of the binaries run with the DD2 EOS (middle panel), the qualitative behaviour of different mass configurations is similar up to approximately $s \simeq 100\ \mathrm{k_B/baryon}$. At larger entropies, the `DD2-M1.25` binary has a more rapid drop-off and there is very little material that reaches higher entropies. The remaining models exhibit similar behaviour with a flattening of the curve at higher entropies. The average entropy value is in all four cases $\langle s \rangle \approx 15\ \mathrm{k_B/baryon}$. All of binaries with the LS220 EOS (left panel) show a very similar qualitative behaviour among themselves and strong analogies with the DD2 binaries. In particular the distributions show a rapid increase at

around 2 $\mathrm{k_B/baryon}$ (for the $1.45M_\odot$ binary this peak is at around 8 $\mathrm{k_B/baryon}$ and is 4 times smaller), with an additional second peak at 20 $\mathrm{k_B/baryon}$ for the $1.35M_\odot$ case that is not present in the other masses. For all masses there is a rapid decrease in specific entropy, with average entropies that are slightly lower than the DD2 and SFHO binaries and with a smaller spread between the values, being approximately $s \sim 11$ $\mathrm{k_B/baryon}$.

The simulations with binaries employing the SFHO EOS (right panel) show a similar qualitative behaviour when compared with the other runs, at least at low entropies. The distributions peak at about 5 $\mathrm{k_B/baryon}$ and a rapid drop follows, although different binaries show different fall-offs rates at around 50 $\mathrm{k_B/baryon}$. In the `SFHO-M1.25` case the distribution begins to decrease less rapidly at higher entropies while the `SFHO-M1.35` model shows the fastest decrease. This is to be contrasted to the DD2 and LS220 simulations (where the specific entropies correlate with the initial masses of the stars) and is reflected in the average values of the specific entropy, with the `SFHO-M1.25` model having $\langle s \rangle = 15.6$ $\mathrm{k_B/baryon}$, while `SFHO-M1.35` a smaller value of $\langle s \rangle = 12.7$ $\mathrm{k_B/baryon}$. Lastly the average specific entropy of the `SFHO-M1.35` binary is almost twice as large, likely due to the fact that the small amount of ejected matter has been efficiently heated on account of its rarefaction. While somewhat puzzling, this non-monotonic behaviour of the specific entropy with the SFHO binaries is likely due to the comparative softness of this EOS, which enhances the nonlinearity associated with shock-heating effects.

Similarly to the behaviour of the electron-fraction distributions, the average entropy tends to increases with the softness of the EOS (taking however into consideration the cavets at the end of section 6.5.2), being highest for the softest EOS, *i.e.* SFHO. For example focusing on the $1.25M_\odot$ binaries, $\langle s \rangle = 10.3,\ 13.9,\ 15.6$ $\mathrm{k_B/baryon}$, for the LS220, DD2, SFHO EOSs, respectively. This dependence is not particularly surprising as softer EOSs produce a higher temperature and the temperature is directly related to the specific entropy. This relation holds for almost all cases, even when including the low-mass ejecta of `SFHO-M1.45`; the only exception is offered by the `SFHO-M1.35` binary, where this discrepancy is likely due to there being at least 5 times as much ejecta as the other binaries.

6.5.4 Ejection velocity distribution

Figure 6.6 shows the velocity distribution of the ejecta computed in analogy to those of the electron fraction or specific entropy distributions presented in the previous two sections. Note that unlike *e.g.* Radice et al. (2016), we here distinguish between the velocity of the ejected material $v_{\rm ej}$ as measured in the simulation and that of the ejecta at spatial infinity $v_{\rm inf}$. We compute $v_{\rm ej}$ directly from the local Lorentz factor W, *i.e.* $v_{\rm ej} = \left[(W^2-1)/W^2\right]^{1/2}$, where we assumed that the detectors are are sufficiently far away from the merger product so that the Minkowski metric holds. As discussed in Bovard and Rezzolla (2017), this is a rather good approximation since it was shown there that the ejected matter moves essentially radially and there is only a subdominant velocity component in the angular directions, hence $v^2 \approx v_r^2$, which enables us to compute $v_{\rm ej} \simeq v^r$ from W. An obvious consequence of distinguishing between $v_{\rm ej}$ and $v_{\rm inf}$ is that our values of the ejecta velocities are systematically higher

than in Radice et al. (2016).

Again, figure 6.6 reveals that every simulation exhibits similar qualitative behaviour. The ejecta velocity is never lower than $0.15\,c$; the bulk of the matter has velocities of $v_{\rm ej} \approx 0.25\,c$, and at higher velocities of $v_{\rm ej} \gtrsim 0.6\,c$ the mass distribution quickly drops to zero. Table 6.2 reports the average velocity $\langle v_{\rm ej} \rangle$ for all the runs. A trend clearly emerges from our data, with the higher-mass configurations systematically producing higher-ejecta velocities. More precisely the ejecta velocity appears to be tightly correlated with the compactness of the neutron stars involved in the merger (cf. table 6.1). Also in this case this trend is not particularly surprising since higher-mass configurations result in more compact starts, which in turn experience stronger torques and more efficient shock heating.

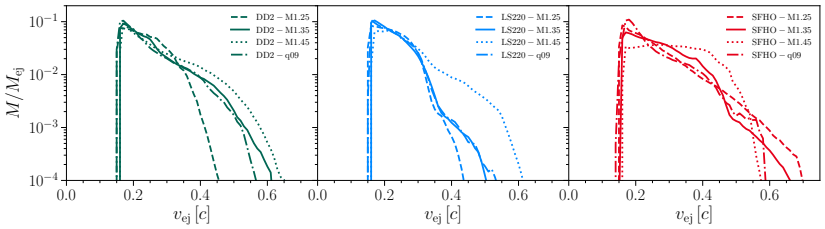

Figure 6.6: The same as in figure 6.3 but for the ejecta velocity $v_{\rm ej}$. The range of $v_{\rm ej}$ is divided into bins of width 0.05 and the histograms are normalized over the total ejected mass. *Figure reproduced from Bovard et al. (2017).*

In table 6.2 the column denoted by $\langle v_\infty \rangle$ shows estimates of the ejecta velocity at infinity, which is achieved in the homologous expansion phase. This velocity is used in our approximate model of kilonova emission (see section 6.7) and is computed assuming a ballistic radial motion from $r = 300$ km to infinity in the spherically symmetric gravitational field of an object with the same ADM mass of the BNS system under consideration, *i.e.*

$$\sqrt{1 - \frac{2M_{\rm ADM}}{r}}\,\frac{1}{\sqrt{1-\langle v_{\rm ej}\rangle^2}} = \frac{1}{\sqrt{1-\langle v_\infty\rangle^2}}\,. \tag{6.12}$$

In the Newtonian limit, $M_{\rm ADM} = M$ and expression (6.12) simply reduces to the familiar energy conservation equation: $\frac{1}{2}\langle v_{\rm ej}\rangle^2 - GM/R = \frac{1}{2}\langle v_\infty\rangle^2$.

6.5.5 Impact of the unbound material selection criterion

In section 6.2.3 we introduced the criteria by which we determine whether the material is bound or unbound, and considered only the geodesic criterion in pour analysis. This choice is justified by the simplicity of the criterion and by the fact that it provides a lower bound for the total ejected material (Kastaun and Galeazzi, 2015). An additional benefit is that it does not implicitly depend on the EOS selected, while the Bernoulli criterion h does, via the enthalpy dependence. This implies that a fluid element, with the same rest-mass density, temperature, and electron fraction, can be unbound or bound depending on the EOS when the Bernoulli criterion is employed. This is a relatively minor

trade-off since through the introduction of the enthalpy, the effects of pressure and temperature are taken into account. It is therefore interesting to study the dependence of the properties of the eject matter on the unboundedness criterion.

Since the specific enthalpy is always grater than one, $h \geq 1$, we have that

$$|hu_t| \geq |u_t| \,, \tag{6.13}$$

and thus the Bernoulli criterion will always result in more material being considered unbound. However a slight modification of this formula is required. In our simulations we have a so called atmosphere that acts as a lower bound for the hydrodynamical (and thermodynamical) quantities. As discussed in section 6.5.1 we have chosen to evaluate the ejecta at $300\,\mathrm{km}$ away from the merger remnant to avoid atmosphere-related effects at greater radii. But due to the introduction of the enthalpy in the Bernoulli criterion, we need to ensure that we are sufficiently above the atmosphere value to avoid unphysical entering our calculations. To achieve this instead of defining unbound elements as satisfying the relation $hu_t \leq -1$, we consider the following modified criterion

$$hu_t \leq (hu_t)|_{\mathrm{atmo}} \,, \tag{6.14}$$

where we evaluate hu_t at the values set by our atmosphere setup, which is EOS-dependent. For example, for the LS220 EOS this term assumes the value:

$$hu_t \leq -1.000163 \,, \tag{6.15}$$

instead of -1. Even though this difference is small, the modified constraint does exclude some material from being considered as unbound.

Having made this consideration, we compare the results of the geodesic criterion, the original Bernoulli criterion and the modified Bernoulli criterion in the fiducial case of the `LS220-M1.35` model. In figure 6.7 the differences between the three selection criteria are shown, using the mass ejection curve. Overall the behaviour we recover for the different criteria is similar, with an ejection phase beginning approximately $2\,\mathrm{ms}$ after merger followed by a decrease in the mass flux. While the material as selected by the geodesic criterion approaches a constant value of ejected mass at late times, both Bernoulli criteria show a slightly longer increasing phase before settling to a constant. In table 6.3 we show the comparison of the total amount of ejected material for the three criteria and find that by selecting one of the Bernoulli criteria, we obtain approximately 2.5 times as much ejected material when compared to the geodesic one. This increase in the amount of ejecta is similar across all simulations we have performed: the ejected mass is larger by a factor of 1.5 to 4 with the Bernoulli criterion as compared with the geodesic one.

In figure 6.8 we plot again the mass distribution in the ejecta of the various quantities relevant for the r-process nucleosyntehsis, for the representative `LS220-M1.35` model only. The average values are summarized in table 6.3. For the electron fraction and entropy, we do not see drastic changes and the overall structure of the distribution between different criteria. In both cases there is a slight increase in entropy and Y_{e} which is to be expected. With both Bernoulli criteria, taking the enthalpy into account includes some thermodynamic effects which will result in more material being ejected due to shock

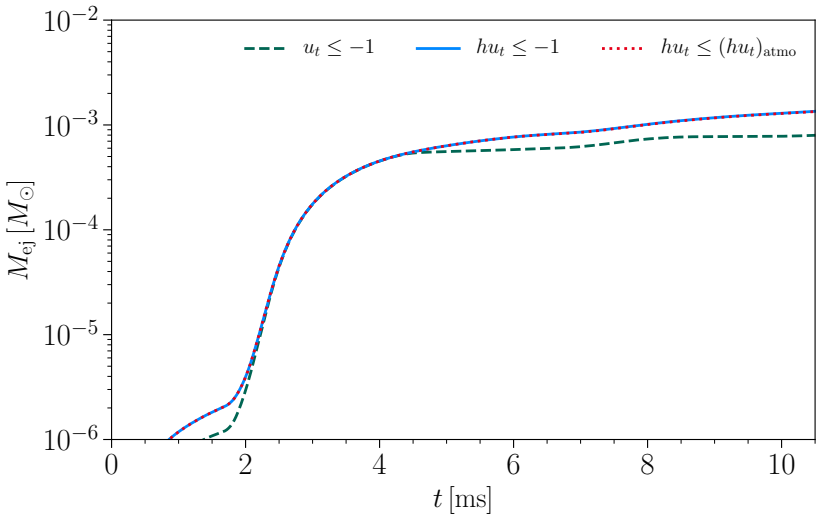

Figure 6.7: The mass ejection according to different unboundedness criteria for the `LS220-M1.35` model. In green is the geodesic criterion, blue is the original Bernoulli one, and red is the modified Bernoulli thresholded on the atmosphere value. All values have been measured through a detector at 300 km. *Figure reproduced from Bovard et al. (2017).*

Criterion	$M_{\rm ej}$ $[10^{-3}\,M_\odot]$	$\langle Y_{\rm e}\rangle$ -	$\langle s\rangle$ $[{\rm k_B}/{\rm baryon}]$	$\langle v_{\rm ej}\rangle$ $[10^{-1}{\rm c}]$
`geodesic`	0.82	0.10	12.3	0.22
`Bernoulli`	2.09	0.11	13.8	0.15
`modified Bernoulli`	2.07	0.11	13.1	0.15

Table 6.3: Average values of the ejected mass, electron fraction, specific entropy and ejecta velocity for different unboundedness criteria in the representative `LS220-M1.35` model. *Table reproduced from Bovard et al. (2017).*

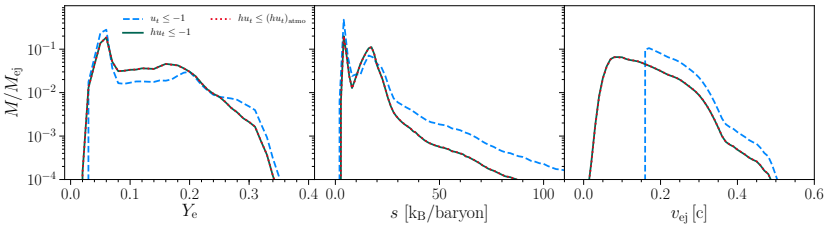

Figure 6.8: Comparison of the mass distribution of electron fraction, specific entropy and ejecta velocity in the ejected matter of the representative model `LS220-M1.35` for the three unboundedness criteria. *Figure reproduced from Bovard et al. (2017).*

heating. This implies a higher entropy and additionally, more material to undergo neutrino interactions. However the effects are minimal and the overall nucleosynthesis process will be essentially unaffected.

The most striking differences are to be found instead in the $v_{\rm ej}$ distribution. In the case of the geodesic criterion, interpreted in its Newtonian limit, a fluid element has to have non-zero velocity at infinity to be considered unbound. This implies a lower cutoff in the velocity distribution, as slowly moving elements, even though able to cross a given detector surface, would not be considered unbound. For both Bernoulli criteria this strict requirement is relaxed by the presence of the enthalpy, which acts as a multiplicative factor larger than one. This means that even slowly moving elements, provided they have sufficiently high enthalpy, would be counted as unbound, and so the velocity distribution acquires a lower end tail and its mean is shifted towards lower values.

6.6 r-process nucleosynthesis

This section is dedicated to the study of the r-process nucleosynthesis of the dynamically ejected matter and the resulting heavy element yields. We focus on the optimal selection of the tracers, on how the nucleosynthesis process varies with the specific entropy of the ejected matter and on those behaviours that are essentially independent of the EOS.

6.6.1 Comparison of tracer selection methods

In section 6.2.2 a method to associate a mass to the t passively advected tracers was mentioned. The method, developed in Bovard and Rezzolla (2017) essentially consists in locally integrating a mass flux through a sphere of given radius. In this section two additional tracer-selection criteria are introduced (keeping in mind that the unboundness criterion is always anyway enforced) and the corresponding procedures to associate a mass to the tracers; we then compare the impact that this different selection strategies have on the final nucleosynthesis yields.

The first criterion introduced in section 6.2.2 simply consists in considering from a given simulation all tracers that are unbound without further selection, associate to each of them a mass by locally integrating a mass flux through a sphere of given radius as in Bovard and Rezzolla (2017) (in the present case the sphere is the fiducial outflow detector at radius $200\,M_\odot$), then sum the nucleosynthesis yields from all tracers using the corresponding mass as weight to recover the final abundance pattern. Since the total number of unbound tracers in one of our simulations can reach several thousands ($40{,}000$ being a typical value), this approach involves the post-processing and book-keeping of many tracer trajectories, thus becoming computationally rather costly. For this reason, we develop the alternative selection criteria described below.

A first alternative consists in considering the distributions of the ejected mass as a function of the electron fraction presented in section 6.5.2 and drawing one representative, unbound tracer from each bin. Given the bin width of $\Delta Y_\mathrm{e} = 0.01$, this results in about 40 tracers for every simulation, a reduction of a factor of a thousand with respect to the first criterion. A mass is then associated to each tracer by assigning to it the mass of the bin it was drawn from. We refer to this procedure as to the "1D" criterion, since the tracers are drawn from a one-dimensional distribution.

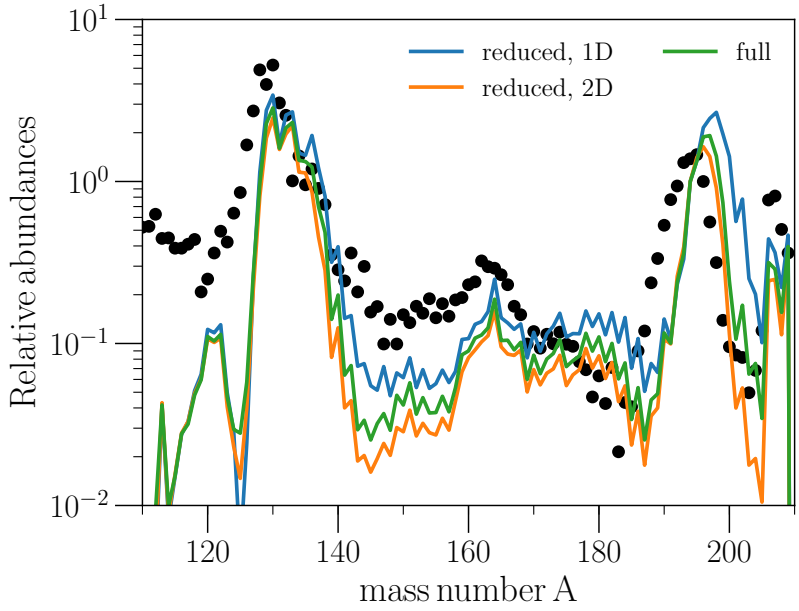

Figure 6.9: Comparison of the relative abundances Y_i of the r-process as function of the mass number A for the three tracer selection criteria. In blue, the abundances produced by the "1D" criterion; in orange the ones produced by the "2D" criterion; in green the abundances obtained considering all unbound tracers. The black filled circles indicate the solar abundances. *Figure reproduced from Bovard et al. (2017).*

A third selection criterion considered is essentially an improved version of

the 1D criterion. It consists in considering the ejected mass histogram over both the electron fraction and the specific entropy; we then draw one representative, unbound tracer from each bin, and associate to it the mass of the bin it was drawn from. We refer to this procedure as to the "2D" criterion, since the tracers are drawn from a two-dimensional distribution. For each simulation, this results in a total of roughly $1{,}000$ tracers to be considered (*i.e.* the number of Y_e/s bins used to produce the distribution).

We apply the nucleosynthesis computations to the tracers selected using the three criteria discussed above, computing the heavy element yields in the fiducial case of the binary model `LS220-M1.35`. The results are displayed in figure 6.9, where for comparison the abundance pattern of the solar system is also displayed (filled circles); the relative differences from our computations to the solar abundances are shown in the bottom panel. As can be seen, the original approach of considering all unbound tracers reproduces quite well the solar abundances over the whole range of mass numbers considered, as does the 2D criterion. The 1D criterion instead presents significant deviations, especially around the third peak (*i.e.* $A \simeq 195$) and around the rare-earth peak (*i.e.* $A \simeq 165$). The origin of these deviations is clear, a posteriori: it is due to the fact that the 1D criterion is systematically biased towards low-entropy tracers, which has a significant impact over the final abundances, as we discuss in the next section.

The so-called 2D criterion is computationally much less expensive than simply considering all unbound tracers; it allows for a simple and unambiguous definition of the tracer mass; yet it leads to an almost unbiased abundance calculation. Therefore we decided to adopt it as our preferred tracer-selection criterion and all following results are computed with this choice, unless otherwise stated.

6.6.2 Nucleosynthesis of heavy elements

Figure 6.10 illustrates the nucleosynthesis results for all $\sim$ $40{,}000$ unbound tracers of the representative simulation of the `LS220-M.1.35` binary. Individual tracers with $s < 70\ \mathrm{k_B/baryon}$ are plotted in gray while tracers with $s \geq 70\ \mathrm{k_B/baryon}$ are plotted in orange. The mass-integrated abundances are indicated by the blue line. As a consequence of the relatively low electron fractions in most of the ejected material (*i.e.* with $Y_\mathrm{e} \approx 0.1$; see figure 6.3 and table 6.2), for each tracer the strong r-process component (from the second to the third r-process peak) is well reproduced. We find however that the entropy distribution of the ejecta gives rise to specific features in the abundance pattern. The low-entropy component (*i.e.* $s < 70\ \mathrm{k_B/baryon}$) leads to the pattern that is observed in the neutron-rich ejecta of Newtonian simulations. On the contrary the high-entropy (*i.e.* $s \geq 70\ \mathrm{k_B/baryon}$) part of the ejecta, which carries only about $6\,\%$ of the total ejected mass, has a nucleosynthesis pattern with a shifted second and third peaks. Additionally it presents diminished abundances in the rare-earth region, and effectively fills the gap between third r-process peak and elements in the lead region. We note that the abundance pattern of these tracers is very similar to the "fast" ejecta found by Mendoza-Temis et al. (2015). While we do not find them to expand faster in the beginning, their unusual abundance distribution can be traced back to an extremely high initial neutron-to-seed ratio $Y_\mathrm{n}/Y_\mathrm{seed} \gtrsim 1{,}000$ and comparably

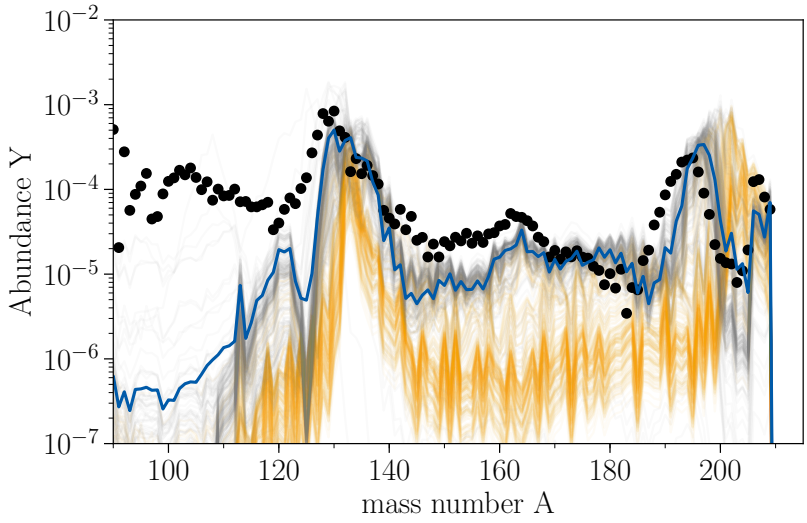

Figure 6.10: Final r-process abundances for all unbound tracers of the `LS220-M.1.35` binary. Gray lines are the yields for individual tracers with low entropies $s < 70\ \mathrm{k_B/baryon}$, and orange lines mark single tracers with high entropies $s \geq 70\ \mathrm{k_B/baryon}$. The mass-integrated nucleosynthesis yields are shown with a blue line, and the black filled circles show the solar abundances. *Figure reproduced from Bovard et al. (2017).*

low initial densities $\rho \lesssim 10^9\,\mathrm{g/cm^3}$. Due to the enormous amount of neutrons at low densities, the seed nuclei require substantially more time to incorporate the neutrons, delaying the freeze-out time (*i.e.* the time when $Y_\mathrm{n}/Y_\mathrm{seed} = 1$). In fact the time window for the r-process to occur in this minority part of the ejected material is $\gtrsim 100$s instead of $\lesssim 1$s. The r-process also runs along a path much closer to the valley of stability for these tracers, such that the magic neutron numbers are reached at higher mass numbers, and the abundances settle down for a pattern in between s-process and r-process.

Figure 6.11 reports the final heavy-elements relative abundances for all of the 12 BNS models outlined in table 6.1 as a function of the mass number A. As in previous figures, the different panels refer to the different EOSs considered and the various binaries are represented with lines of different types. In this plot the results are normalized to have a total mass fraction of 1 and again shown with filled circles are the scaled solar system r-process abundances. Clearly in all cases a successful r-process is obtained, leading to the production of the r-process pattern from the second (*i.e.* $A \sim 130$) to the third (*i.e.* $A \sim 195$) peak.

There are however different admixtures due to the different electron-fraction distributions of the ejected material as detailed in section 6.5.2. For the equal-mass binaries we observe a tendency towards slightly enhanced abundances below the second r-process peak with increasing mass of the neutron stars. This is because more massive BNS systems have a higher electron fraction on average. Furthermore, the contributions from tracers with high initial neutron-

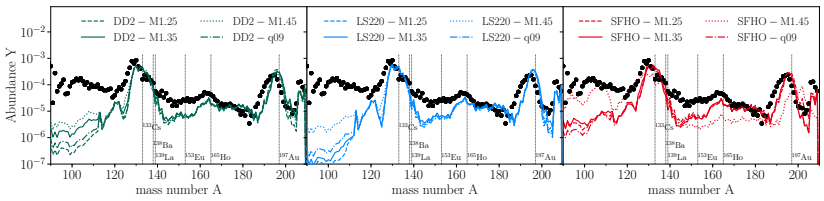

Figure 6.11: Final relative heavy-elements abundances for all the 12 BNS models as a function of mass number A. The abundances are normalized so that the total mass fraction is unity, while the different panels and lines refer to the various EOSs, masses and mass ratios, respectively (see legends). The black filled circles report instead the observed solar abundances, while the vertical lines mark a few representative r-process elements: ^{133}Cs, ^{138}Ba, ^{139}La, ^{153}Eu, ^{165}Ho, ^{197}Au. *Figure reproduced from Bovard et al. (2017).*

to-seed ratios enhance both the second r-process peak and the region with $A \approx 200$ in all cases. The most extreme example is the `SFHO-M1.45` binary, which immediately collapses to a black hole after merger, ejects very little mass and with a comparatively high electron fraction. As a result the part of ejected material with low specific entropy leads to nuclei that mainly have mass numbers with $A \lesssim 130$, while the material with high specific entropy – and thus high neutron-to-seed ratios – dominates the final abundances beyond the third r-process peak, leading to an enhanced abundance for $A \gtrsim 200$. The distinctive features observed in the final abundances in the case of the `SFHO-M1.45` binary suggests therefore the possibility of using the chemical yields either as a confirmation of the prompt production of a black hole after the merger, or as an indication of this process in the case in which the post-merger gravitational-wave signal is not available.

All things considered however, the most striking result shown in figure 6.11 is the very good and robust agreement of the various abundance patterns, where by robust we mean a behaviour that is only very weakly dependent on the EOS or the initial neutron-star masses, at least for the sample considered here. For example when considering the second peak at $A \sim 130$, all four different types of initial data predict a similar abundance of ^{133}Cs. Although the lanthanides show a slight disagreement with the solar abundances around the mass number $A \sim 145$ (which may be explained by other forms of ejecta, for example from accretion disks (Siegel and Metzger, 2017)), from ^{153}Eu up ^{197}Au in the third r-process peak, there is no disagreement in the final abundances for different initial data and EOSs.

While this agreement might be partly aided by our simplified neutrino treatment, this result not only confirms the robustness of the r-process yields from BNS mergers already noted in the literature, but it also shows how the uncertainties associated in modelling the microphysics and initial data of BNS mergers have a very limited impact on the nucleosynthesis produced from the merger. As discussed later in section 6.7, although the final abundance curves are essentially independent of the initial data and EOS, the kilonova light curves produced from the decaying elements depend strongly on these parameters and thus allow for a way to distinguish between the different sce-

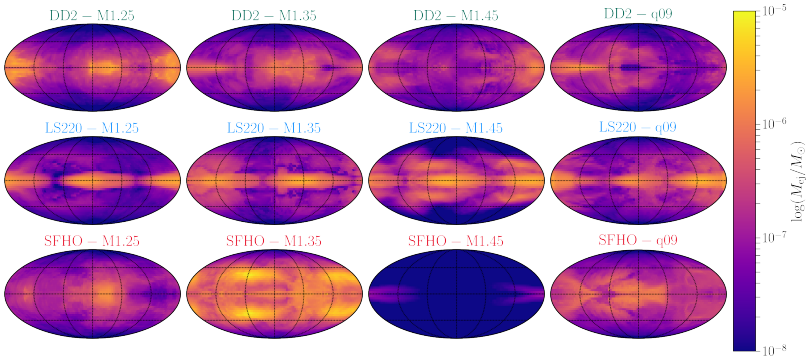

Figure 6.12: Angular distribution of the ejected mass at the final time for all simulations. *Figure reproduced from Bovard et al. (2017).*

narios.

Note that in fact the spread in our r-process patterns due to different choices of EOSs or initial masses is much less than the one associated to uncertainties in the nuclear-physics modelling of nuclei involved in the r-process, *e.g.* the choice of the fission fragment distribution (Eichler et al., 2015) or the nuclear-mass model (see *e.g.* Mumpower et al. (2015); Martin et al. (2016)) where variations can change the abundance of a given element by an order of magnitude.

6.7 Ejecta morphology and kilonova light curves

6.7.1 Angular distributions of the ejected matter

Outflow detectors allows to study not only the global properties of the ejected material, but also the angular distribution of the ejected material on the detector surface and hence virtually at spatial infinity. Besides having an interest in their own right, anisotropies in the distribution of the ejected matter could have important consequences on the kilonova signal of a given binary configuration, and impact its detectability, especially when considering the effect that the viewing angle could have on the effective observed kilonova signal in presence of such anisotropies. To the best of our knowledge this is the first time that an analysis of this type has been carried out.

We consider the angular distribution of ejected mass as defined by equation (6.10), where in this case however the integration over the angular directions does not span the whole 2-sphere, but only a single patch of the outflow detector. We also study the mass-averaged distribution of the electron fraction, the specific entropy and the ejecta velocity. Similarly to equation (6.10), these are defined as

$$\langle \chi \rangle := \int_0^{T_f} \int_{\Delta\Omega} \chi \, \rho_* W (\alpha v^r - \beta^r) S \, d\Omega \, dt \; / \\ \int_0^{T_f} \int_{\Delta\Omega} \rho_* W (\alpha v^r - \beta^r) S \, d\Omega \, dt \, , \tag{6.16}$$

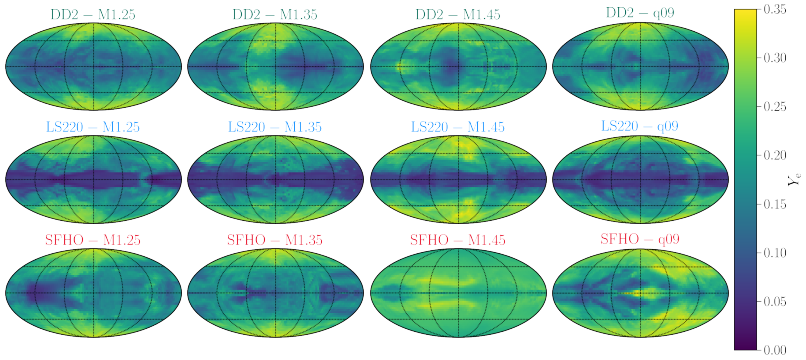

Figure 6.13: The same as in figure 6.12 but for the electron fraction. *Figure reproduced from Bovard et al. (2017).*

where χ is any one of Y_e, s or v_{ej}, and the same consideration as above applies to the integration over the angles.

In figure 6.12 we collect Mollweide projections of the fiducial outflow detector relative to the time-integrated rest mass for all models. Several properties of the angular distribution of the ejected matter are apparent. Firstly the binary `SFHO-M1.45`, which immediately collapses to a black hole after the merger, is immediately identifiable as there is close to no ejected matter in this case. Secondly it is clear that in each binary most of the mass is ejected on the orbital plane, which is consistent with expectations that the material ejected here is mostly of dynamical origin and the ejection mechanism is due to the torques in the system at merger (other types of ejecta, such as neutrino/magnetically driven winds or ejecta from viscous heating would display a more isotropic structure). Third, while concentrated at low latitudes, the ejected mass is not uniformly distributed but shows considerable anisotropies; this is simply due to the disruption of the flow produced by the tidal torques and this concentrates the emission of matter into rather small regions on the detector surface. The only binary that appears to evade this trend is `SFHO-M1.35`, which has ejected matter also at latitudes as high as $\sim 45°$ and seems to peak around $\sim 30°$.

In a similar fashion, the distribution of the electron fraction Y_e is shown in figure 6.13. It is apparent how the electron fraction tends to anticorrelate with the amount of ejected mass: regions in which the ejected mass fraction is higher (such as the orbital plane) tend to have very low Y_e and vice-versa. This consistent with the results of section 6.5.2, where most of the ejected mass is shown to be very neutron-rich. On the other hand it can be seen that in other regions, such as the poles, the material is very neutron-poor, but has correspondingly low values of ejected mass. The evidence provided in figure 6.13 that matter ejected around the poles is less neutron-rich (*i.e.* with $Y_e \gtrsim 0.25$) suggests the possibility that material there might undergo a less robust r-process, leading to a suppressed production of lanthanides and thus to a lower opacity. This bimodal anisotropy in the distribution of the electron fraction could then lead to either a "blue" kilonova, *i.e.* to a kilonova signal with a comparatively strong optical component, if the line of sight is mostly along

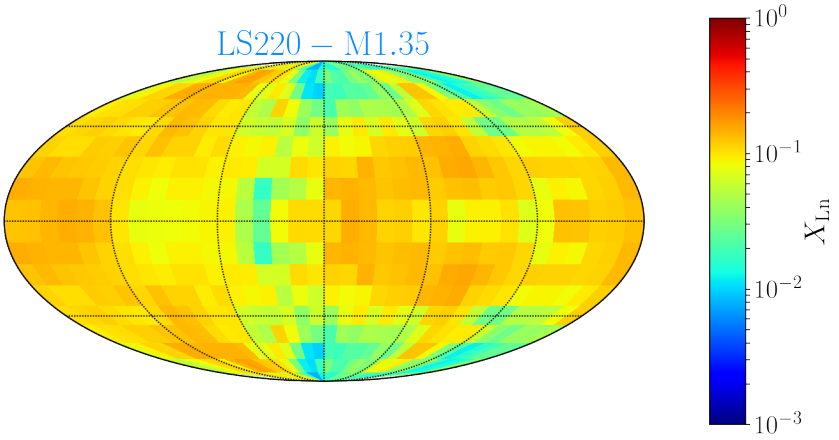

Figure 6.14: Angular distribution of the mass fraction of lanthanides in the representative case of the binary `LS220-M1.35`; the data refers to the final simulation time.. *Figure reproduced from Bovard et al. (2017).*

the polar regions, or to a "red" kilonova, *i.e.* to a kilonova signal peaking in the infrared, if the line of sight is mostly along the equatorial regions Metzger (2017a); Tanaka (2016).

To check the plausibility of such a scenario we have explicitly computed the angular distribution of the lanthanides mass fraction in the representative `LS220-M1.35` model, *i.e.* by computing the lanthanides mass fraction of every unbound tracer in the simulation and by plotting their location on the 2-sphere, as shown in figure 6.14; to produce this plot the lanthanides mass fraction values have been averaged over patches of angular size $10^\circ \times 10^\circ$. As can be seen, even near the poles the lanthanides mass fraction is rather high, *i.e.* $X_{\rm La} \approx 10^{-2}$. This is far larger than the generally accepted limit on this value that leads to a sufficient suppression of the medium opacity for a blue kilonova to be observed, *i.e.* $X_{\rm La} \sim 10^{-5}$. Very similar values have been obtained in all other BNS models. Therefore this result seems to indicate that a blue-kilonova scenario is probably unlikely to originate from the dynamical ejecta in view of GW170817 (Metzger, 2017b), according to our calculations. Note however that despite the three orders of magnitude difference between the expected value of the lanthanides mass fraction and the one computed here, our conclusions may be biased by an oversimplified neutrino treatment. A proper neutrino-transfer treatment of the propagation of neutrinos in the ejected matter could in fact modify, in part at least, our results. Indeed more sophisticated neutrino treatments, such as the one employed in Foucart et al. (2016c), have been shown to produce higher values of the electron fraction around the polar regions. All things considered, our results suggest that while a blue kilonova component cannot be ruled out conclusively, it also seems to require an electron-fraction distribution that is considerably different from the one computed here.

Similar observations as for the $Y_{\rm e}$ morphology hold true for the distribution of the specific entropy, as shown in figure 6.15: the entropy anticorrelates with the ejected matter, as regions close to the orbital plane tend to have small entropies, while around the poles values of the entropy can be very high. These

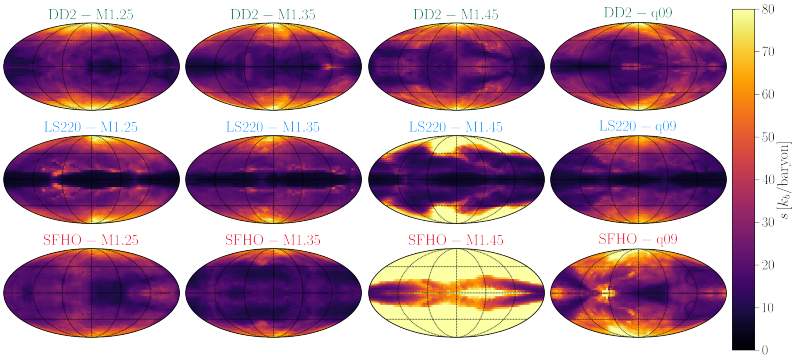

Figure 6.15: The same as in figure 6.12 but for the specific entropy.

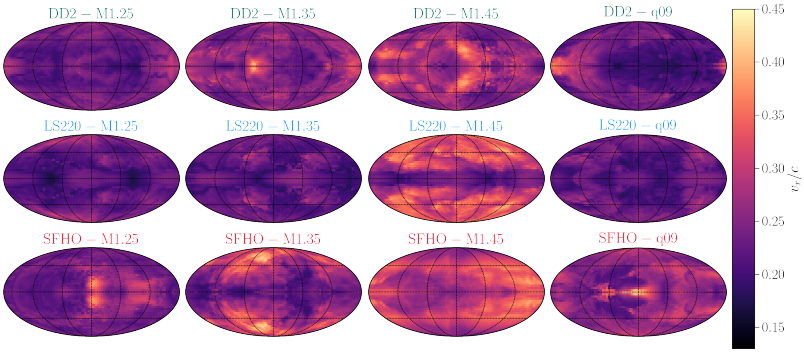

Figure 6.16: The same as in figure 6.12 but for the ejecta velocity.

corresponds to the tails shown in figure 6.5, extending to specific entropies of 200 k_B/baryon and above. The case of the `SFHO-M1.45` model is particularly striking, with most of the ejected material at extremely high entropy. As observed in the previous discussion, however, this model also ejects an almost negligible amount of mass, which enhances the shock-heating efficiency.

The velocity distribution, shown in figure 6.16, is instead rather peculiar. For many models, especially the lower mass ones, including the unequal-mass models in the rightmost column of the figure, the material appears to be expanding at the same velocity in most directions, save for a few "hot" or "'cold" spots of limited angular size. In the three higher mass models, shown in the third column of figure 6.16, some large-scale structure could be present, but there is no evidence of the correlation observed for the electron fraction or entropy.

6.7.2 Kilonova light curves and observability

We use the simple gray opacity model of kilonovae developed in Grossman et al. (2014) to assess the observability of the infrared transients associated to the decay of r-process elements. The comparatively small ejected masses resulting from our simulations preclude the use of more sophisticated radiative

transfer treatments (left for future work) when these ejecta could be a significant source of opacity (the "lanthanide curtain") for potential secondary outflows, such as magnetically Siegel et al. (2014) and viscously driven wind from an accretion disk, or neutrino-driven wind from the hypermassive neutron star Perego et al. (2014).

In the model of Grossman et al. (2014) the background dynamical ejecta are approximated by a homologously expanding spherically symmetric shell of density $\rho(r,t) = \rho_0(t_0/t)^3(1 - v^2/v_{\rm max}^2)^3$ (also described in detail in Wollaeger et al. (2017)), and $v_{\rm max} = 2\langle v_\infty \rangle$, taken from table 6.2. The luminosity output is computed by integrating the nuclear heating rate from the nuclear network over the layer of matter from which photons can diffuse out. A similar model is used in (Perego et al., 2014; Martin et al., 2015b; Rosswog et al., 2017). We employ an effective gray opacity $\kappa = 10\ {\rm cm}^2\ {\rm g}^{-1}$, which was recently demonstrated to reproduce the infrared luminosity of lanthanide- and actinide-contaminated ejecta reasonably well (Wollaeger et al., 2017). Note that the same study shows the flux in the optical bands to be strongly suppressed when detailed opacities of lanthanides are used; for this reason, we consider here only the infrared magnitudes J, H and K-bands in the Two Micron All Sky Survey (2MASS) Skrutskie et al. (2006).

The nuclear heating which powers the kilonova for each model is calculated with the nuclear network code `WinNet` (Winteler et al., 2012; Korobkin et al., 2012) (cf. section 6.2.4) using the average electron fraction $\langle Y_{\rm e} \rangle$, specific entropy $\langle s \rangle$ and expansion velocity $\langle v_\infty \rangle$ as given in table 6.2. We compute the nucleosynthesis yields with reaction rates based on the finite-range droplet model (FRDM) (Möller et al., 2012) only. This is motivated by the fact that nuclear mass models show little discrepancy in the heating rates at epochs around $t \simeq 1$ day (Rosswog et al., 2017), where the peak magnitudes for our models are expected.

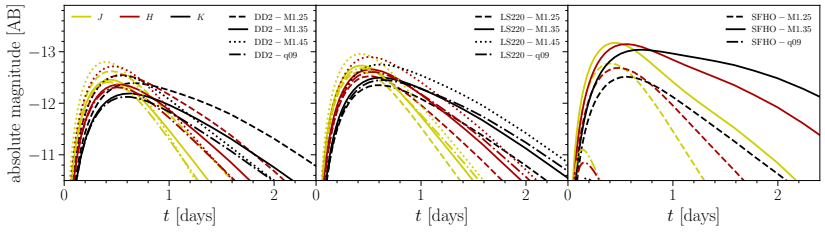

Figure 6.17: Synthetic light curves in the infrared 2MASS J, H and K-bands for all of the binaries considered. *Figure reproduced from Bovard et al. (2017).*

The resulting peak bolometric luminosities, peak magnitudes in the infrared bands, and the peak epochs in the H-band are presented in table 6.2, while the light curves in the three infrared bands (indicated by different line colors) are shown in figure 6.17, with different line types referring to the different binaries.

Clearly all of our models show a very similar behaviour, peaking around half a day in the H-band and rapidly decreasing in luminosity after one day, reaching a maximum magnitude of -13. We note that these luminosities are smaller than those normally expected (see *e.g.* (Tanaka, 2016) for a recent re-

view), which peak around magnitude of ~ -15; this difference is not surprising and is mostly due to the amounts of ejected mass, which is normally assumed to be $\sim 10^{-2}\,M_\odot$ and hence at least one order of magnitude larger than what measured here. With 3-minute J-band exposure on the VISTA telescope (Emerson et al., 2004), these magnitudes result in a detection horizon of ~ 100 Mpc, which, in combination with a very short time around the peak, makes these light curves extremely difficult to detect in a follow-up survey. As observed in the follow-ups to GW170817, light curves were observed that originate from a kilonova (The LIGO Scientific Collaboration and The Virgo Collaboration, 2017; Cowperthwaite et al., 2017; Metzger, 2017b) which suggests that a significant amount of material, on the order of $10^{-2}M_\odot$, became unbound. As this amount of ejecta is above the amount we have seen in dynamical merger simulations, this suggests that the source of the radioactive decay powering the kilonova is not in the dynamical ejecta, but in other sources such as neutrino drive winds or viscous ejecta (Metzger, 2017b).

6.8 Constraints on BNS merger rates

In section 6.6 the robustness of the r-process nucleosynthesis from BNS mergers has been shown; it is necessary to establish whether the amount of ejected material in such a BNS merger is sufficient to explain the observed amounts of r-process material in the Milky Way. To this end (following Rosswog et al. (2017)) we show in figure 6.18 the constraints on the rate of BNS mergers and the required amount of ejected material needed per merger. More specifically, assuming the total amount of r-process material in the Galaxy is $M_{\rm r,gal} \approx 19{,}000\,M_\odot$ and given a certain merger rate – either per year and galaxy equivalent ($\rm yr^{-1}\ gal^{-1}$, bottom horizontal axis) or per year and cubic Gigaparsec ($\rm yr^{-1}\ Gpc^{-1}$, top horizontal axis) – the black line shows the amount of ejected material per merger required to explain the observed abundances. Similarly the red line has the same meaning, but only takes into account elements with $A \gtrsim 130$, with a total galactic mass of $M_{\rm r,gal} \approx 2{,}530 M_\odot$ (McMillan, 2011; Rosswog et al., 2017). The blue-shaded horizontal region indicates the range of dynamically ejected material from BNS mergers in quasi-circular (QC) orbits covered by our simulations as reported in table 6.2 (note that the `SFHO-M1.45` model has been omitted because it is not representative); the other two shaded horizontal regions report instead the typical abundances coming from the secular ejecta (pink-shaded region) or from the dynamic ejecta relative to mergers of BNSs in eccentric orbits (green-shaded region).

These constraints should be compared with actual measurements of the merger rates as deduced from different experiments and indicated as vertical lines. We show as the dot-dashed black line the predicted merger rate from the GW170817 observation (The LIGO Scientific Collaboration and The Virgo Collaboration, 2017). In addition we show the observed upper bound on BNS mergers observed in the first LIGO operating run O1, and the predicted upper bounds for the planned future runs O2 and O3 (Abbott et al., 2016b). Different population-synthesis models are also displayed corresponding to galactic chemical evolution (GCE) (Côté et al., 2017), supernova (SN) (Chruslinska et al., 2017), and SGRBS (Petrillo et al., 2013).

The red line, the horizontal-blue shaded region, and the GW170817-relate

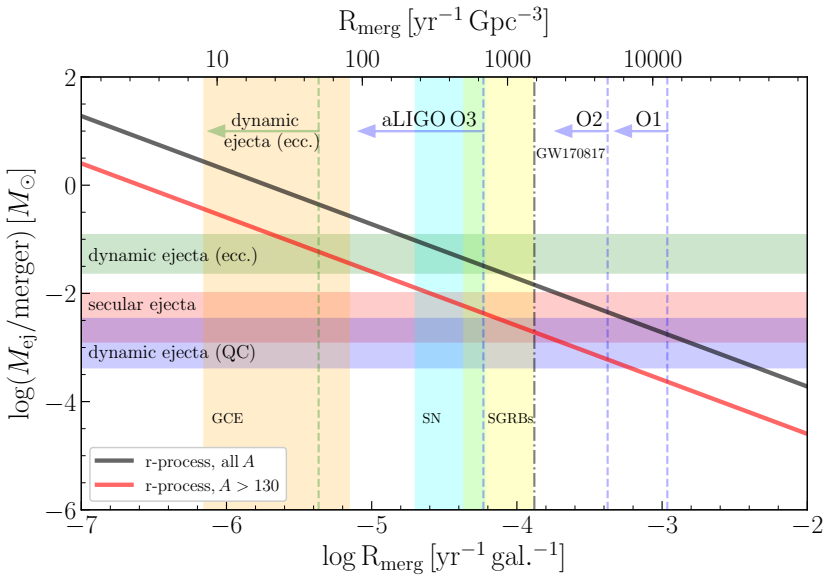

Figure 6.18: Ejected material per merger for a given BNS merger rate required to reproduce the observed mass of all (black) and $A > 130$ (red) r-process elements in the Milky Way. The dark blue-shaded regions correspond to the range of values of ejected mass reported in Table 6.2. The red-shaded region corresponds to ejected masses from other sources of ejecta. The dashed vertical gray lines report the observed, O1, and predicted, O2 and O3, upper bounds on BNS mergers from LIGO. The dot-dashed black line is predicted merger rate from GW170817. The orange, light blue, and yellow shaded regions correspond to observational constraints from galactic chemical evolution (GCE), supernova (SN), and short gamma-ray bursts (SGRBs) population synthesis models as defined in the text. *Figure reproduced from Bovard et al. (2017).*

curve overlap in figure 6.18 which indicates that the measured amount of dynamical ejecta of $\sim 10^{-3} M_\odot$ from the presented simulations is sufficient to reproduce the observed r-process mass abundances with $A > 130$ in the Milky Way. Associated with GW170817 was a SGRB (The LIGO Scientific Collaboration et al., 2017a; LIGO Scientific Collaboration et al., 2017) and this confirms that BNS mergers are the central engine of SGRBS and thus the rate constraint predicted by SGRBS (Petrillo et al., 2013) is likely indicative of BNS merger rates. This implies that although we find that there is lower amounts of dynamical ejecta then reported in Newtonian simulations (cf. section 6.5) the frequency of BNSs merger is likely to be sufficiently high to compensate. Furthermore, the geodesic criterion that we employ is a conservative one and only provides a lower bound on the amount of material ejected; by adopting a different criterion, *e.g.* the Bernoulli one (see discussion in section 6.5.5), the amount of ejected material can increase up to a factor of 4 for the same simulation.

A different, more exotic scenario of the source r-process is dynamical ejecta from eccentric BNSs megers. Ejecta masses from these configurations are in fact much larger (Radice et al., 2016; **?**), and would be sufficient to explain the

observed mass values; however these events are likely very rare and current rate constraints are not well understood (Lee et al., 2010).

It is important to note that our simulations only focus on the dynamical ejecta. There are multiple other channels through which material can be ejected from a merger as mentioned in the introduction to this chapter and they will contribute to the total amount of r-process elements created. For example simulations of neutrino-driven winds have found similar amounts of ejected material as dynamical ejecta (Fujibayashi et al., 2017). Likewise, matter ejected from a BH-torus system could be as high as $0.1\,M_\odot$, as estimated semi-analytically in Giacomazzo et al. (2013). This suggests that even if the mass ejected from a single channel is alone insufficient to explain the observed r-process masses, the combination of all ejected material from a BNS merger is likely to. In this sense the blue-shaded horizontal region only represents a lower bound on the total ejected material.

6.9 Conclusions

Observations, especially the recent simultaneous detection of an electromagnetic counterpart and a gravitational wave signal from a binary neutron star merger, now support the conclusion that material is dynamically ejected from the merger of neutron stars binaries and that such material is neutron-rich and its nucleosynthesis can provide the astrophysical site for the production of heavy elements in the Universe. Furthermore, this simultaneous detection provides confirmation of the long-standing conjecture that the merger of neutron stars is behind the origin of SGRBs.

With the use of fully general-relativistic simulations of the inspiral and merger of binary systems of neutron stars, we have investigated in this work the impact that the variation in initial masses, mass ratio, and most importantly the EOS have on the r-process nucleosynthesis taking place in the dynamical ejecta from BNS mergers, on its heavy-element yield and on the resulting kilonova signal.

We have shown that the r-process nucleosynthesis from BNS mergers is very robust in that it depends only very weakly on the properties of the binary system, particularly the EOS, bearing in mind however that a parameter space exploration depending on the EOS is still rather limited (also partly due to the lack of publicly available fully temperature dependent EOS tables). In the future we intend to explore it more fully with a larger set of EOSs. While similar conclusions have been reported before, the confirmation coming from our study strengthens the evidence that BNS mergers are the site of production of the r-process elements in the galaxy.

With the two different approaches we have employed to measure the amount of matter ejected dynamically, we found that it is $\lesssim 10^{-3}\,M_\odot$, which is smaller than usually assumed. There are a however number of factors that need to be taken into account in considering this estimation, such as: the EOS considered; the neutrino treatment; the criterion for matter unboundness; the resolution; and finally the numerical methods used. Although these systematic factors can lead to differences as large as one order of magnitude even for the same initial data, we find it unlikely that the mass ejected dynamically can ever reach the values sometimes assumed in the literature of $10^{-2} - 10^{-1}\,M_\odot$. Clearly a more

detailed and comparative study is necessary to better constrain the uncertainties behind the amount of mass lost by these systems.

Using a simplified and gray-opacity model we have assessed the observability of the infrared transients associated to the decay of r-process elements, *i.e.* of the kilonova emission. We have found that all our binaries present a very similar behaviour, with light curves peaking around $\sim 1/2$ day in the H-band and rapidly decreasing in luminosity after one day, reaching a maximum magnitude of -13. These rather low luminosities are most probably the direct consequence of the small amounts of ejected matter, thus making the prospects for detecting kilonovae rather limited. Observations of the kilonova associated with GW170817 suggest in fact higher total ejecta masses (Abbott et al., 2017) but this total also includes other ejection mechanisms apart from dynamical tides, such as neutrino driven winds, disk or viscous ejecta. Thus a detailed comparison with the new observations will require more sophisticated calculations with improved neutrino treatments to disentagle all sources of ejecta.

As a final remark we note that even though the r-process abundance pattern does not give us simple clues to the original BNS parameters, *e.g.* it does not allow to disentangle various EOS and mass configurations, there are distinguishing features in the ensuing kilonova signal relatable through the difference in ejecta properties obtained in our simulations. We have found that softer EOSs tend to result in a higher average electron fraction, which implies differences in the type of kilonova produced (blue vs red kilonova). We have also found that this difference in electron fraction is highly angular dependent with higher electron fractions around the polar regions and lower along the orbital plane. Even though there is significantly less material ejected along the poles versus the plane, our simulations show that the simplified kilonova modelling, such as that of a homogeneously expanding group of material, need to be adjusted to account for this anisotropic emission. We reserve the investigation of this issue to future studies, where an improved neutrino treatment will be also implemented.

Part V

Conclusions

Chapter 7

Conclusions

The study of binary systems of compact objects is a fascinating field of research, richly connected to a variety of issues and open questions of mathematical, numerical and physical nature. In fact, it can be argued that no single area of specialization covers the full spectrum of expertise needed to describe these complex systems; only the interplay between different fields can lead to a satisfactory understanding of them. Furthermore, such an understanding would have important repercussions and would be able to shed light on many unresolved questions in various areas of physics, which naturally pushes binaries of compact objects at the forefront of research. Among the most pressing of such open questions it is worth citing the nature of the gravitational interaction, *i.e.* the search for a theory of gravitation alternative to general relativity; the details of the equation of state governing matter at the highest densities, beyond nuclear saturation density, and the repercussions this would have of our understanding of nuclear forces; and the precise mechanism and characteristics of the electromagnetic transient signals that are thought to be associated with these systems, in particular short gamma ray bursts and kilonovae.

In the last decade numerical relativity has become one of the most important and powerful tools to investigate these systems. A numerical approach has the advantages of being able to treat very general, non-idealized systems; to include, in principle at least, as much physical details as needed; and to test the prediction of theories for which no experimental test is available. On the other hand, numerical relativity raises a number of intrinsic issues which have to be addressed as well to ensure its usefulness as a research tool. In this work I have considered various mathematical, numerical and physical issues that arise in, or can be treated with, the field of numerical relativity.

First I have tackled the problem of the stability of the formulation of Einstein equations is employed in numerical simulations, by contributing to the development of the FO-CCZ4 formulation. This formulation has been proved hyperbolic, and therefore able to sustain stable simulations in a variety of conditions. While FO-CCZ4 is not the first formulation for which a proof of hyperbolicity exists, historically progresses in the stability of formulations have been achieved heuristically, with a mathematical understanding being developed only later. Therefore this is an important addition to the state of the filed. Furthermore, the FO-CCZ4 is first order in both space and time, which makes it suitable to be discretized with the highly efficient, accurate and scalable DG

methods. DG methods are currently a hot topic in computational research and the field of numerical relativity in particular, since their superior scalability properties makes them ideal to harness the power of next generation supercomputers. Indeed, we verified that a state of the art ADER-DG implementation of the FO-CCZ4 formulation produces results of remarkable accuracy and stability for all relevant test cases. It is in fact hoped that this formulation and its ADER-DG discretization scheme will make one of the basic algorithms in the upcoming software framework `ExaHyPE` (Charrier et al., 2018), which is being developed by a consortium of various institutions to address precisely these needs.

The need for better numerical methods is clearly not limited to the context of Einstein equations, but for all other systems of equations the solution of which is needed to obtain a complete description of the system under consideration; including, for baryon matter system such as binary neutron stars, the relativistic Euler equations. In this case however an additional difficulty arises in that the Euler equations can generate shocks in a finite time, which means the numerical method used to solve them has to be not only accurate and efficient, but able to deal with discontinuous solutions. To this end I have developed the ELH scheme, alternative to the HRSC methods commonly employed in numerical relativity. Being a flux-limiter method, based on a simple hybridisation procedure of the numerical flux, the scheme is much simpler than most HRSC schemes and amenable to efficient implementation. In fact, even in the non-optimized implementation developed so far it has showed a marked performance improvement over the HRSC-type MP5 scheme. Furthermore the hybridisation of the flux in this scheme is based on a self-consistent thermodynamical property of perfect fluids, *i.e.* the local production of entropy, known to denote the onset of a shock. The ELH scheme has been shown to reach comparable or sometimes better accuracy than MP5 in a number of tests at a fraction of the computational cost. In the future, a modification of the scheme to adapt it to the DG framework would make for a more than competitive alternative to current hydrodynamics evolution schemes. At the same time the scheme can be extended and improved, applying it to the solution of the magnetohydrodynamics equations and possibly even to the equations of neutrino transport.

The final topic addressed in this work is more of physical nature than the previous two, which are mathematical/numerical issues arising the use of numerical methods, and therefore could also be seen from a certain point of view as technical points in the development of a research tool, rather than a research subject in their own right. It concerns the final outcome of binary neutron star mergers in general, and in particular the details of two physical process of great importance that are thought to take place in the ejecta from neutron star mergers, namely the r-process nucleosynthesis and the kilonova emission. One of the points in understanding these processes, not closely investigated up until now, is their dependence, if any, of the neutron star equation of state, which is itself still not conclusively constrained. To this end I have participated in a project involving running detailed, large scale simulations of binary neutron star mergers varying systematically the equation of state of dense matter and the initial masses of the neutron stars involved. By extracting the abundances of heavy elements produced in each model system with the help of a nuclear network, we were able show that the physics of the r-process is rather

insensitive to these changes, producing in each case an abundance pattern in agreement with the one measured in the Solar system or in our Galaxy. Furthermore the distribution of the thermo- and hydrodynamical properties of the ejected matter with respect to the viewing angle of the system revealed a complex structure which might be of great importance to properly predict the properties of the kilonova signal and that will be the focus of future investigations.

In summary, the work presented in this thesis presents a series of steps forward in the understanding of binaries of compact objects. It has been partially published in Dumbser, Guercilena, Koeppel, Rezzolla, and Zanotti (2017); Guercilena, Radice, and Rezzolla (2017) and Bovard, Martin, Guercilena, Arcones, Rezzolla, and Korobkin (2017), and embodies my genuine contribution. I hope that it will provide a useful advancement on the final goal of numerical relativity, *i.e.* to produce a physically complete, mathematically self-consistent, accurate description of relativistic astrophysical systems, from which details of their behaviour can be reliably extracted.

Zusammenfassung

Kompakte Objekte - Schwarze Löcher und Neutronensterne - sind nicht nur für Astrophysiker faszinierende Objekte, sondern auch für eine breite Schicht anderer Wissenschaftler, etwa Astronomen, theoretische Physiker, Kern- und Teilchenphysiker, Festkörperphysiker und wohl auch für interessierte Laien.

Zuerst vorhergesagt in der ersten Hälfte des 20. Jahrhunderts (Schwarzschild, 1916; Baade and Zwicky, 1934), wurden diese Objekte lange Zeit als exotische Ideen und mathematische Kuriositäten abgetan. Dies änderte sich erst mit der Entdeckung von Pulsaren in den späten 1960-Jahren (Hewish et al., 1968), die bald als rotierende und Energie abstrahlende Neutronensterne identifiziert wurden, sowie 1972 durch die Beobachtung von Cygnus X-1, dem ersten Kandidaten für ein Schwarzes Loch (Shipman, 1975).

Die Gründe für das Interesse an schwarzen Löchern kann man leicht verstehen, wenn man bedenkt, dass kompakte Objekte viele verschiedene Bereiche der Physik berühren und somit ideale Laboratorien sind um das Wechselspiel dieser Bereiche zu untersuchen.

Schwarze Löcher, die rein gravitative Objekte sind, eignen sich perfekt um das Wesen der Gravitation, seine Manifestierung in Effekten wie Gravitationswellen und die Unterschiede zwischen den verschiedensten Gravitationstheorien in dem Bereich zu studieren in dem sie am wesentlichsten sind, nämlich im Regime mit besonders starken Feldern. Genauso wie alle anderen massiven astrophysikalischen Objekte sind Schwarze Löcher von besonderer Bedeutung für Akkretionsprozesse, welche als die Energiequelle von einigen sehr hellen astrophysikalischen Emittern elektromagnetischer Signale, wie z.B. von aktiven Galaxiekernen oder Röntgendoppelsternen, vermutet werden.

Zudem gibt es Schwarze Löcher auf einer Vielzahl von Massenskalen, angefangen bei stellaren Massen bis hin zu supermassereichen Schwarze Löchern, welche millionen- bis milliardenfach schwerer als ihre stellaren Konterparts sind. Supermassereiche schwarze Löcher spielen eine wichtige, wenn auch noch nicht ganz verstandene Rolle in der Entstehung und Entwicklung von ganzen Galaxien und darüber hinaus der Struktur des beobachtbaren Universums, wodurch sie auch für die Kosmologie relevant sind. Neutronensterne teilen sich mit Schwarzen Löchern die Eigenschaft, durch Gravitation dominiert zu sein, jedoch zeigen Neutronensterne durch ihren Aufbau aus baryonischer Materie ein reicheres dynamisches Verhalten. Bereits früh wurde realisiert, dass Materie in Neutronensternkernen extreme Dichten erreicht, welche die von Atomkernen noch übersteigt. Daraus folgt, dass Neutronensterne wichtige Informationen über Materie unter solch extremen Bedingungen (welche nicht im Labor erreicht werden können) liefern können, unter anderem Details der nu-

klearen Wechselwirkungen, der Eigenschaften von Hyperonen oder des Quark-Gluon-Plasmas.

Es wird außerdem vermutet, dass Neutronensterne Vorläufer von einigen der energiereichsten kurzlebigen astrophyskalischen Signale sind, beispielweise kurzen Gammastrahlenausbrüchen, welche als Nachwirkungen von Verschmelzungen von Doppelneutronensternsystemen angenommen werden (Baiotti and Rezzolla, 2017).

Doppelneutronensterne werden auch zunehmend als die höchstwahrscheinlich einzige Produktionstelle schwerer Elemente identifiziert, durch die r-Prozess Kernsynthese, die in der von ihrer Verschmelzung hinausgeworfen Materie stattfindet; außerdem wird erwartet, dass dieser Kernsyntheseprozess (oder besser gesagt der radioaktive Zerfall der Erzeugnisse) ein weiteres sehr interessantes Übergangssignal generiert, die sogenannte Kilonova (in der Literatur auch Macronova genannt) (Metzger, 2017a; Rosswog, 2013a).

Obwohl noch viele Fragen offen sind, ist in den vergangenen Jahrzehnten seit ihrer Entdeckung ein signifikanter Fortschritt in deren Verständnis erzielt worden. Dies wurde durch ein Wechselspiel and theoretischen Weiterentwicklungen und neuen Beobachtungen erreicht, darunter sind z.B. die Entdeckung eines ultrarelativistischen Doppelpulsars sowie die Bestimmung seiner Orbitparameter mit beeindruckender Präzission durch Radiobeobachtungen (Kramer and Wex, 2009), das Verfolgen der Umlaufbahnen von Sternen nahe unserem galaktischen Zentrums, wodurch direkte Rückschlüsse auf die Masse des supermassiven Schwarzen Lochs im Zentrum der Milchstraße möglich sind (Gillessen et al., 2009), sowie den immer genauer werdenden Beobachtungen astrophysikalischer Jetstrukturen mittels Langbasisinterferometrie (VLBI: very long baseline interferometry). Die beeindruckendste und jüngste Entwicklung ist jedoch die kürzlich erfolgte Detektion von Gravitationswellen zweier verschmelzender Schwarzer Löcher mit dem LIGO Observatorium (Laser Interferometer Gravitational-Wave Observatory), welche eine neue Ära der Gravitationswellenastronomie eingeleitet hat (The LIGO Scientific Collaboration and the Virgo Collaboration, 2016).

Auf der anderen Seite haben theoretische Studien und Modelle unser Verständnis kompakter Objekte wesentlich vorangebracht. Beim Verständnis der mathematischen Struktur der allgemeinen Relativitätstheorie sowie der Entwicklung relativistischer Theorien der Hydrodynamik, Viskosität, Elektrodynamik und Neutrinowechselwirkungen, Approximationen der Einsteingleichungen wie die Post-Newtonsche (PN) Entwicklung (Blanchet, 2006), Gravitation-Self-Force-Formalismus (GSF) (Barack and Ori, 2003) oder der effektiven Einkörperapproximation (EOB) (Buonanno and Damour, 1999) wurden große Fortschritte erzielt. Dies erlaubt etwa die Bestimmung der Gravitationswellen die von einem Doppelsystem (BNS: Binary Neutron Star oder BBH: Binary Black Hole-System) emittiert werden. Fortschritte wurden auch bei effektiven Modellen für die starke Wechselwirkung erzielt, welche stets verbesserte Zustandsgleichungen (EOS: equation of State) ergeben, die sich dazu eignen Materie in Neutronensternen zu beschreiben. Ein weiteres Beispiel sind Theorien zur Bestimmung der Opazität von BNS-Massenauswürfen, die ein wesentlicher Baustein in der Berechnung von Kilonova-Lichtkurven sind (Barnes et al., 2016). An dieser Stelle wäre es natürlich möglich noch unzählige weitere Beispiele aufzulisten.

Im vergangenen Jahrzehnt hat sich allerdings eine grundlegend neue Me-

thode etabliert, ein gravitativ gebundenes System von kompakten Objekten zu beschreiben. Diese Methode wird Numerische Relativitätstheorie genannt und besteht daraus, auf vergleichsweise großen Längen- und Massenskalen die Relativitätstheorie auf dem Computer numerisch zu lösen und dabei interessante Observablen zu extrahieren. Diese wissenschaftliche Disziplin ist relativ jung – die erste erfolgreiche Simulation von zwei umeinander kreisenden und verschmelzende Schwarzen Löchern bei der auch das Gravitationswellensignal berechnet werden konnte, wurde von Pretorius (2005) durchgeführt – wurde aber schnell zur vollen Reife entwickelt und hat sich mittlerweile als mächtiges Forschungswerkzeug fest etabliert, da es traditionelle Methoden gut ergänzen kann. In diesem Kontext wurde die vorliegende Arbeit entwickelt und durchgeführt.

Die größte Stärke der numerischen Relativitätstheorie ist, dass sie Lösungen für nicht-idealisierte und damit nichttriviale gravitative Systeme liefern kann, welche einer analytischen Betrachtung nicht zugänglich sind. Die damit erzeugten Daten können auf die gleiche Weise analysiert werden wie experimentelle Messungen oder Beobachtungen und erlauben Forschern damit wichtige Rückschlüsse auf die Eigenschaften dieser Systeme zu ziehen. Dadurch konnten numerische Untersuchungen wichtige Beiträge liefern, etwa zum Gravitationswellensignal eines gerade verschmolzenen Doppelsternsystems ("Post-Merger") (Takami et al., 2015), den thermo- und hydrodynamischen Eigenschaften von Materie, die bei solchen Ereignissen das System verlässt oder zur Topologie und Intensität von magnetischen Feldern (Baiotti and Rezzolla, 2017).

Die Durchführung von numerischen Simulationen ist an und für sich ein nichttriviales Unterfangen und erfordert eine besondere Aufmerksamkeit, um erfolgreich zu sein. Die Gleichungen, die die relevanten physikalischen Theorien beschreiben müssen in eine geeignete Form gebracht werden, um eine numerisch stabile Evolution zu gestatten. Effiziente, stabile und akkurate Methoden müssen entwickelt werden, um sowohl die Anfangswerte als auch deren Zeitentwicklung auf dem Computer zu berechnen. Die Umsetzung des Algorithmus in einer geeigneten Programmiersprache erfordert Konzentration und Aufmerksamkeit, ferner müssen Analysemethoden erdacht und entwickelt werden, um den berechneten Daten einen Sinn zu entnehmen. Letztlich sind die rechnerischen Kosten einer relevanten numerische Simulation nicht zu vernachlässigen, sie erfordern den Einsatz von Supercomputern.

Eines der ersten Probleme, denen man im Bereich der numerischen Relativitätstheorie begegnet, ist die Umformulierung der allgemeinen Relativitätstheorie zu einem numerisch integrierbaren Anfangswertproblem. Ich habe dazu beigetragen, eine neue Formulierung erster Ordnung namens FO-CCZ4 zu entwickeln, die in Dumbser, Guercilena, Koeppel, Rezzolla, and Zanotti (2017) veröffentlicht ist. Um numerisch stabil integriert werden zu können, müssen solche Gleichungssysteme zuerst in hyperbolische Form gebracht werden. Diese mathematische Voraussetzung bedeutet physikalisch, dass Information sich nur mit endlicher Geschwindigkeit ausbreiten kann, was eine natürliche Eigenschaft moderner relativistischer Theorien ist (Sarbach and Tiglio, 2012). Es lässt sich weiter zeigen, dass aus Hyperbolizität die Wohldefiniertheit eines Differentialgleichungssystems folgt. Die Einsteingleichungen in ihrer typischen vierdimensionalen und kovarianten Formulierungen sind nicht unmittelbar als hyperbolisch erkennbar und müssen daher in geeigneter Weise umgeformt

werden, um ihre hyperbolische und wohldefinierte Natur preiszugeben.

Man konnte zeigen, dass die FO-CCZ4-Formulierung, die in dieser Arbeit beschrieben wird, stark hyperbolisch ist und sich somit für stabile Langzeitentwicklungen eignet. Ebenso wie die CCZ4-Formulierung (Alic et al., 2012, 2013), auf welcher die FO-CCZ4-Formulierung basiert, beinhaltet sie einen Dämpfungsmechanismus um die Verletzungen der Zwangsbedingungen zu reduzieren und damit die lokale Genauigkeit zu erhöhen. Außerdem ist das Gleichungssystem in all seinen charakteristischen Feldern manifest linear degeneriert, sodass keine Stoßwellen (Schocks) erzeugt werden können und damit das Problem von Diskontinuitäten in der numerischen Lösung nicht auftritt. Dies ist zwar auf Grund von physikalischen Argumenten keine überraschende Eigenschaft, aber sehr wohl leiden einige Formulierungen unter diesem Problem. Zuguterletzt ist das FO-CCZ4-System eine partielle Differentialgleichung erster Ordnung in Zeit und Raum. Dadurch ist es geeignet, mit sehr akkuraten, effizienten und skalierbaren diskontinuierlichen Galerkin-Verfahren (DG) gelöst zu werden (Hesthaven and Warburton, 2007). Wir entwickelten dementsprechend eine Umsetzung dieser Formulierung in Form eines Computerprogramms, welche auf einem modernen ADER-DG-Verfahren mit WENO-Subcell-Limiter basiert. Wir haben demonstriert, dass der Code mühelos alle Standardtests mit erstaunlicher Genauigkeit besteht und haben ihn erfolgreich auf die Zeitentwicklung eines statischen (isolierten) sowie zweier kollidierenden schwarzen Löcher angewendet. Es sei angemerkt, dass dies die ersten dreidimensionalen Simulationen von Schwarzen Löchern mit DG-Verfahren sind. Um auch nicht materiefreie Raumzeiten wie z.B. BNS oder Akkretionsscheiben behandeln zu können, müssen die Einsteingleichungen mit den Bewegungsgleichungen der Materiefelder gekoppelt werden. In den meisten Fällen wird zur Beschreibung von Materie eine ideale Flüssigkeit verwendet (Font, 2008), welche den relativistischen Eulergleichungen unterliegt, die dann zusammen mit den Einsteingleichungen gelöst werden müssen. Die Eulergleichungen sind allerdings inherent nichtlinear (Leveque, 1992), d.h. sie können bereits aus den Anfangswerten Stoßwellen entwickeln. Die besondere Herausforderung zum Lösen dieser Gleichungen ist daher die Entwicklung von numerischen Methoden die nicht nur akkurat sind, sondern die auch Diskontinuitäten scharf auflösen können ohne dabei künstliche Oszillationen o.ä. zu entwickeln. Die Standardwahl in der numerischen Relativitätstheorie fällt daher auf hochauflösende schockeinfangende Techniken (HRSC: High-resolution shock-capturing) (Rezzolla and Zanotti, 2013). Ich habe alternativ zu den HRSC-Methoden eine neue numerische Methode entwickelt, die sich "Entropie-beschränkte Hydrodynamik" (ELH: Entropy limited hydrodynamics) nennt (Guercilena, Radice, and Rezzolla, 2017). Die ELH-Methode ist numerisch einfacher als HRSC-Methoden und erlaubt damit schnellere Rechnungen ohne Verlust von Genauigkeit. Das ELH-Schema begrenzt den erhaltenen Strom und verbindet eine akkurate Flussformel höherer Ordnung mit einer numerisch stabileren niedriger Ordnung in einem lösungsabhängigen Verhältnis. Dieses Verhältnis, mit welchem die beiden Formeln miteinander gemischt werden, wird durch eine "Viskositätsfunktion" bestimmt, welche proportional zur lokalen Produktion von Entropie im Fluid ist. Da Entropie in perfekten Fluiden nur durch Stoßwellen erzeugt werden kann, wird das korrekte aber mit niedriger Ordnung rechnende Verfahren nur in Gegenwart von Stoßwellen angewandt, während das Verfahren höherer Ordnung automatisch im glatten Bereich der Lösung

angewandt wird. Ich habe das ELH-Schema in einem Finite-Differenzen-Code (FD) implementiert und erfolgreich an einer Anzahl von speziell-relativistischen Testfällen sowie allgemein relativistisch berechneten isolierten Neutronensternen getestet. In speziell relativistischen eindimensionalen Tests wie den Stoßrohrtests kann der Code Diskontinuitäten scharf auflösen und dabei gleichzeitig die theoretische Konvergenzordnung im Bereich der homogenen Lösung aufrechterhalten. In dreidimensionalen allgemeinrelativistischen Zeitentwicklungen von Neutronensternen habe ich die Methode mit einem MP5-Verfahren (einer typischen HRSC-Methode) verglichen und sie als stabil und akkurat verifizieren können. Sie zeigte sich außerdem in der Lage, stark relativistische Ereignisse wie den Gravitationskollaps eines Neutronensterns zu einem schwarzen Loch korrekt zu beschreiben. Darüberhinaus ist das Verfahren in einigen Fällen rechnerisch um bis zu 50% schneller als vergleichbare HRSC-Methoden, obwohl bei der Implementierung auf Performanz kein besonderes Augenmerk gelegt wurde. Nachdem all diesen Themen wie Korrektheit, Stabilität und rechnerischer Effizient Zeit und Raum gegeben wurde, können numerische Simulationen ihre Fähigkeit als Werkzeuge zur Untersuchung der Physik kompakter Objekte unter Beweis stellen. Ein spezielles Rätsel welches numerische Simulationen vor kurzem erfolgreich angegangen sind ist die Untersuchung zum Ursprung von schweren Elementen in unserem Universum. Es ist bekannt , dass chemische Elemente die schwerer als Eisen sind zuvorderst durch Neutroneneinfang von leichteren Saat-Nuklei entstanden sind. Im Gegenzug sind Elemente mit Massenzahl $A \gtrsim 120$ in erster Linie durch den schnellen Neutroneneinfach (r-Prozess) entstanden. Dieser Prozess kann in Umgebungen stattfinden, in denen das Verhältnis von Neutronen zu Saat-Nuklei so hoch ist, dass die Zeitskalen für Betazerfälle viel länger werden als die für Neutroneneinfang. Während man noch vor einiger Zeit davon ausging, dass die durch Kernkollaps-Supernovae (CCSN: Core-collapse supernovae) emittierte Materie der Hauptort zum Abspielen von r-Prozessen ist, ist mittlerweile der Ausstoß von Doppelneutronensternsystemen – auch durch spektroskopische Untersuchungen bestätigt (Ji et al., 2016) – ein vielversprechenderer Kandidat geworden. Die Isotopenhäufigkeit von schweren Elementen die durch Simulationen von Neutronensternverschmelzungen berechnet wurden zeigen sich als kompatibel mit denen, welche in unserer Galaxie und unserem Sonnensystem gemessen wurden (Radice et al., 2016).

Zu diesem Themenbereich habe ich beigetragen, den Zusammenhang zwischen der Isotopenhäufigkeit und Zustandsgleichungen von Neutronensternen zu untersuchen (Bovard, Martin, Guercilena, Arcones, Rezzolla, and Korobkin, 2017). Durch akkurate Parameterstudien an Langzeitsimulationen von Verschmelzungen von Doppelsternsystemen in welchen die Massen der beiden untersuchten Sterne systematisch verändert wurden sowie durch den Einsatz von verschiedenen Hochtemperaturzustandsgleichungen die einen großen Bereich an Steifheit abdecken waren wir in der Lage, die totale Menge von emittierter Masse (eine weitere sehr relevante, aber bislang kaum bestimmte Variable, (Dietrich and Ujevic, 2017; Dietrich et al., 2017b)) sowie die hydro- und thermodynamischen Eigenschaften dieser Materie (inklusive ihrer Morphologie und Winkelabhängigkeit) zu bestimmen. Mit den Messdaten fütterten wir anschließend ein Nukleares Reaktionsnetzwerk (Winteler, 2012) und berechneten die Isotopenhäufigkeiten von schweren Elementen für jedes BNS-Modell. Wir fanden heraus, dass trotz einer gewissen Korrelation zwischen

Ejekta und Steifheit der EOS, die r-Prozess Ausbeute erstaunlich robust gegenüber Variationen der astrophysikalischen Bedingungen ist und konsistent die Isotopenhäufigkeiten im Sonnensystem mit ihren derzeitigen Ungenauigkeiten in Bezug auf die Eigenschaften neutronenreichen Nukeli abbildet. Wir waren ebenfalls in der Lage, die Lichtkurve des elektromagnetischen Signals, welches durch den radioaktiven Zerfall der Elemente erzeugt wird, zu verfolgen – die sogenannte Kilonovae (auch Macronovae genannt) – sowie eine der derzeit aufwändigsten Untersuchungen bezüglich der Winkelverteilung des Ejektas durchzuführen. Diese hatte zum Ergebnis, dass die Abhängigkeit der Eigenschaften der ausgeworfenen Materie wie der Elektronendichte Y_e auf den Betrachtungswinkel einen großen Einfluss auf die Lichtkurven, Spektren und Detektierbarkeit der Kilonovae haben kann. Immer leistungsfähigere Computer erlauben zunehmend realistischere Simulationen und treiben um so mehr die Forschung an geeigneteren Formulierungen der Gleichungen sowie der numerischen Methoden, mit denen sie gelöst werden, vorran. Insbesondere müssen sich die Methoden den architektonischen Gegebenheiten der Computergenerationen anpassen. Es würde sich daher lohnen, eine optimierte, vektorisierte Version der ELH-Methode zu entwickeln und mit einem hochskalierenden DG- oder kompakten FD-Schema (Lele, 1992) zu koppeln. Solche Fortschritte lassen an eine Simulation hoffen, die ein komplettes und konsistentes Bild des Eindrehens und Verschmelzens von Neutronensternsystemen inklusive relativistischen Effekten, Neutrinointeraktionen, Viskosität, Wärmetransport, magnetischen Feldern und möglicherweise Multifluiden (Andersson et al., 2017). Solche Simulationen können viele offene Forschungsfragen klären, etwa den präzisen Zusammenhang von der Menge der ausgeworfenen Masse zu den Anfangswerten und ihrer Mikrophysik, der Kilonova-Signatur und ihrer Detektierbarkeit oder dem dynamischen Feedback der r-Prozess Nukleosynthese auf die Morphologie der Ejekta.

Publications and contributions

- Damour T., **Guercilena F.**, Hinder I., Hopper S., Nagar A. and Rezzolla L.
  Strong-field scattering of two black holes: Numerics versus analytics
  Phys. Rev. D, 89, 081503(R) (2014)

  Contributions to this work:

  - discuss and suggest issues and techniques in the comparison between numerical and analytic data;
  - perform the numerical simulations;
  - discuss and suggest data analysis techniques;
  - analyze and visualize the simulations' data;
  - write and summarize the content of the research carried out in the form of an article, including the production of plots, graph and figures;
  - revise, correct and improve the article during the peer reviewing process.

- **Guercilena F.**, Radice D. and Rezzolla L.
  Entropy-limited hydrodynamics: a novel approach to relativistic hydrodynamics
  Computational Astrophysics and Cosmology, 4:3 (2017)

  Contributions to this work:

  - analyze, adapt and reformulate the original "entropy viscosity" method of Guermond et al. (2011) to the general-relativistic case;
  - devise the form of the entropy residual equation;
  - numerically implement the method in the `WhiskyTHC` code, resulting in the development of the `WhiskyTHCEL` code;
  - discuss and suggest testing scenarios for both the method and the code;
  - perform the numerical tests;
  - interpret the resulting data;

  - write and summarize the content of the research carried out in the form of an article, including the production of plots, graph and figures;
  - revise, correct and improve the article during the peer reviewing process.

- Bovard L., Martin D., Korobkin O., **Guercilena F.**, Rezzolla L. and Arcones A.
  On r-process nucleosynthesis from matter ejected in binary neutron star mergers
  Phys. Rev. D, 96, 124005 (2017)

  Contributions to this work:

  - provide help in performing the binary neutron stars numerical simulations;
  - analyze, visualize and interpret the generated data;
  - independently cross-check the data analysis results;
  - assess the significance of said results;
  - lead the development of the work presented in section 6.7.1
  - write and summarize the content of our research in the form of an article, including the production of plots, graph and figures;
  - revise, correct and improve the article during the peer reviewing process.

- Dumbser M., **Guercilena F.**, Köppel S., Rezzolla L. and Zanotti O.
  A strongly hyperbolic first-order CCZ4 formulation of the Einstein equations and its solution with discontinuous Galerkin schemes
  Submitted for publication to Physical Review D (2017)

  Contributions to this work:

  - discuss, suggest and develop the form of the FO-CCZ4 equations;
  - cross-check analytical derivations of the equations;
  - discuss and suggest numerical tests of the equations;
  - perform such numerical tests with the CCZ4 and BSSN formulations and different numerical methods in order to validate the results obtained with the FO-CCZ4 formulation;
  - interpret the test results;
  - write and summarize the content of the research carried on in the form of an article;
  - revise and improve the article during the peer reviewing process.

Bibliography

B. P. Abbott, R. Abbott, T. D. Abbott, M. R. Abernathy, F. Acernese, K. Ackley, C. Adams, T. Adams, P. Addesso, R. X. Adhikari, and et al. GW151226: Observation of Gravitational Waves from a 22-Solar-Mass Binary Black Hole Coalescence. *Phys. Rev. Lett.*, 116(24):241103, June 2016a. doi: 10.1103/PhysRevLett.116.241103.

B. P. Abbott, R. Abbott, T. D. Abbott, M. R. Abernathy, F. Acernese, K. Ackley, C. Adams, T. Adams, P. Addesso, R. X. Adhikari, and et al. Upper Limits on the Rates of Binary Neutron Star and Neutron Star-Black Hole Mergers from Advanced LIGOs First Observing Run. *Astrophys. J. Lett.*, 832:L21, December 2016b. doi: 10.3847/2041-8205/832/2/L21.

B. P. Abbott, R. Abbott, T. D. Abbott, F. Acernese, K. Ackley, C. Adams, T. Adams, P. Addesso, R. X. Adhikari, V. B. Adya, and et al. Estimating the Contribution of Dynamical Ejecta in the Kilonova Associated with GW170817. *Astrophys. J. Lett.*, 850:L39, December 2017. doi: 10.3847/2041-8213/aa9478.

Miguel Alcubierre. *Introduction to* $3+1$ *Numerical Relativity*. Oxford University Press, Oxford, UK, 2008. doi: 10.1093/acprof:oso/9780199205677.001.0001.

Miguel Alcubierre, Gabrielle Allen, Thomas W. Baumgarte, Carles Bona, David Fiske, Tom Goodale, Francisco Siddhartha Guzmán, Ian Hawke, Scott Hawley, Sascha Husa, Michael Koppitz, Christiane Lechner, Lee Lindblom, Denis Pollney, David Rideout, Marcelo Salgado, Erik Schnetter, Edward Seidel, Hisa aki Shinkai, Deirdre Shoemaker, Béla Szilágyi, Ryoji Takahashi, and Jeffrey Winicour. Towards standard testbeds for numerical relativity. *Class. Quantum Grav.*, 21(2):589–613, 2004a.

Miguel Alcubierre, Gabrielle Allen, Carles Bona, David Fiske, Tom Goodale, F. Siddharta Guzmán, Ian Hawke, Scott H. Hawley, Sascha Husa, Michael Koppitz, Christiane Lechner, Denis Pollney, David Rideout, Marcelo Salgado, Erik Schnetter, Edward Seidel, Hisa aki Shinkai, Belá Szilágyi, Deirdre Shoemaker, Ryoji Takahashi, and Jeffrey Winicour. Toward standard testbeds for numerical relativity. *Class. Quantum Grav.*, 21:589, 2004b.

D. Alic, C. Bona, and C. Bona-Casas. Towards a gauge-polyvalent numerical relativity code. *Phys. Rev. D*, 79(4):044026, February 2009. doi: 10.1103/PhysRevD.79.044026.

D. Alic, C. Bona-Casas, C. Bona, L. Rezzolla, and C. Palenzuela. Conformal and covariant formulation of the Z4 system with constraint-violation damping. *Phys. Rev. D*, 85(6):064040, March 2012. doi: 10.1103/PhysRevD.85.064040.

D. Alic, W. Kastaun, and L. Rezzolla. Constraint damping of the conformal and covariant formulation of the Z4 system in simulations of binary neutron stars. *Phys. Rev. D*, 88(6):064049, September 2013. doi: 10.1103/PhysRevD.88.064049.

N Andersson, K Dionysopoulou, I Hawke, and G L Comer. Beyond ideal magnetohydrodynamics: resistive, reactive and relativistic plasmas. *Classical and Quantum Gravity*, 34(12):125002, 2017. URL http://stacks.iop.org/0264-9381/34/i=12/a=125002.

Nils Andersson and Gregory L. Comer. Relativistic fluid dynamics: Physics for many different scales. *Living Rev. Relativ.*, 10(1):1–83, 2007. URL http://www.livingreviews.org/lrr-2007-1.

A. M. Anile. *Relativistic Fluids and Magneto-fluids*. Cambridge University Press, Cambridge, UK, February 1990.

Marcus Ansorg, Bernd Brügmann, and Wolfgang Tichy. A single-domain spectral method for black hole puncture data. *Phys. Rev. D*, 70:064011, 2004.

Richard Arnowitt, Stanley Deser, and Charles W. Misner. The dynamics of general relativity. In L. Witten, editor, *Gravitation: An introduction to current research*, pages 227–265. John Wiley, New York, 1962.

Abhay Ashtekar and Badri Krishnan. Dynamical horizons and their properties. *Phys. Rev. D*, 68:104030, 2003.

W. Baade and F. Zwicky. Remarks on Super-Novae and Cosmic Rays. *Phys. Rev.*, 46:76–77, 1934.

L. Baiotti, I. Hawke, P. J. Montero, F. Löffler, L. Rezzolla, N. Stergioulas, J. A. Font, and E. Seidel. Three-dimensional relativistic simulations of rotating neutron-star collapse to a Kerr black hole. *Phys. Rev. D*, 71(2):024035, January 2005. doi: 10.1103/PhysRevD.71.024035.

Luca Baiotti and Luciano Rezzolla. Challenging the paradigm of singularity excision in gravitational collapse. *Phys. Rev. Lett.*, 97:141101, 2006.

Luca Baiotti and Luciano Rezzolla. Binary neutron-star mergers: a review of Einstein's richest laboratory. *Rept. Prog. Phys.*, 80(9):096901, 2017. doi: 10.1088/1361-6633/aa67bb.

Luca Baiotti, Ian Hawke, Pedro Montero, and Luciano Rezzolla. A new three-dimensional general-relativistic hydrodynamics code. In R. Capuzzo-Dolcetta, editor, *Computational Astrophysics in Italy: Methods and Tools*, volume 1, page 210, Trieste, 2003. MSAIt.

Luca Baiotti, Ian Hawke, Luciano Rezzolla, and Erik Schnetter. Gravitational-wave emission from rotating gravitational collapse in three dimensions. *Phys. Rev. Lett.*, 94:131101, 2005.

Luca Baiotti, Ian Hawke, and Luciano Rezzolla. On the gravitational radiation from the collapse of neutron stars to rotating black holes. *Class. Quantum Grav.*, 24:S187–S206, 2007.

Luca Baiotti, Thibault Damour, Bruno Giacomazzo, Alessandro Nagar, and Luciano Rezzolla. Analytic modelling of tidal effects in the relativistic inspiral of binary neutron stars. *Phys. Rev. Lett.*, 105:261101, 2010. doi: 10.1103/PhysRevLett.105.261101.

F. Banyuls, J. A. Font, J. M. Ibáñez, J. M. Martí, and J. A. Miralles. Numerical 3+1 general-relativistic hydrodynamics: A local characteristic approach. *Astrophys. J.*, 476:221, 1997. doi: 10.1086/303604.

Leor Barack and Amos Ori. Gravitational self-force on a particle orbiting a kerr black hole. *Phys. Rev. Lett.*, 90:111101, 2003.

J. Barnes, D. Kasen, M.-R. Wu, and G. Martínez-Pinedo. Radioactivity and Thermalization in the Ejecta of Compact Object Mergers and Their Impact on Kilonova Light Curves. *Astrophys. J.*, 829:110, October 2016. doi: 10.3847/0004-637X/829/2/110.

T. W. Baumgarte and S. L. Shapiro. Numerical integration of Einstein's field equations. *Phys. Rev. D*, 59(2):024007, January 1999. doi: 10.1103/PhysRevD.59.024007.

T. W. Baumgarte and S. L. Shapiro. *Numerical Relativity: Solving Einstein's Equations on the Computer*. Cambridge University Press, Cambridge, UK, 2010. doi: 10.1017/cbo9781139193344.

A. Bauswein, S. Goriely, and H.-T. Janka. Systematics of Dynamical Mass Ejection, Nucleosynthesis, and Radioactively Powered Electromagnetic Signals from Neutron-star Mergers. *Astrophys. J.*, 773:78, August 2013. doi: 10.1088/0004-637X/773/1/78.

A. M. Beloborodov. Hyper-accreting black holes. In M. Axelsson, editor, *American Institute of Physics Conference Series*, volume 1054 of *American Institute of Physics Conference Series*, pages 51–70, September 2008. doi: 10.1063/1.3002509.

M. Ben-Artzi and P. G. LeFloch. Well-posedness theory for geometry compatible hyperbolic conservation laws on manifolds. *ArXiv Mathematics e-prints*, dec 2006.

E. Berger. Short-Duration Gamma-Ray Bursts. *Annual Review of Astron. and Astrophys.*, 52:43–105, August 2014. doi: 10.1146/annurev-astro-081913-035926.

E. Berger, W. Fong, and R. Chornock. An r-process Kilonova Associated with the Short-hard GRB 130603B. *Astrophys. J.*, 774:L23, September 2013. doi: 10.1088/2041-8205/774/2/L23.

Marsha J. Berger and P. Colella. Local adaptive mesh refinement for shock hydrodynamics. *J. Comput. Phys.*, 82:64–84, 1989. doi: 10.1016/0021-9991(89)90035-1.

S. Bernuzzi and T. Dietrich. Gravitational waveforms from binary neutron star mergers with high-order weighted-essentially-nonoscillatory schemes in numerical relativity. *Phys. Rev. D*, 94(6):064062, September 2016. doi: 10.1103/PhysRevD.94.064062.

Sebastiano Bernuzzi and David Hilditch. Constraint violation in free evolution schemes: comparing BSSNOK with a conformal decomposition of Z4. *Phys. Rev. D*, 81:084003, 2010. doi: 10.1103/PhysRevD.81.084003.

Horst Beyer and Olivier Sarbach. On the well posedness of the Baumgarte-Shapiro- Shibata-Nakamura formulation of Einstein's field equations. *Phys. Rev. D*, 70:104004, 2004.

M. Bezares, C. Palenzuela, and C. Bona. Final fate of compact boson star mergers. *Phys. Rev. D*, 95(12):124005, June 2017. doi: 10.1103/PhysRevD.95.124005.

N. T. Bishop and L. Rezzolla. Extraction of gravitational waves in numerical relativity. *Living Reviews in Relativity*, 19:2, October 2016. doi: 10.1007/s41114-016-0001-9.

Luc Blanchet. Gravitational radiation from post-newtonian sources and inspiralling compact binaries. *Living Rev. Relativ.*, 9(4), 2006. URL http://www.livingreviews.org/lrr-2006-4.

C. Bona, J. Massó, E. Seidel, and J. Stela. New Formalism for Numerical Relativity. *Phys. Rev. Lett.*, 75:600–603, July 1995.

C. Bona, Joan Massó, E. Seidel, and J. Stela. First order hyperbolic formalism for numerical relativity. *Phys. Rev. D*, 56:3405–3415, 1997.

C. Bona, T. Ledvinka, C. Palenzuela, and M. Zácek. General-covariant evolution formalism for numerical relativity. *Phys. Rev. D*, 67(10):104005, May 2003. doi: 10.1103/PhysRevD.67.104005.

C. Bona, T. Ledvinka, C. Palenzuela, and M. Zácek. Symmetry-breaking mechanism for the Z4 general-covariant evolution system. *Phys. Rev. D*, 69(6):064036, March 2004. doi: 10.1103/PhysRevD.69.064036.

C. Bona, C. Palenzuela-Luque, and C. Bona-Casas. *Elements of Numerical Relativity and Relativistic Hydrodynamics: From Einstein's Equations to Astrophysical Simulations*. Lecture Notes in Physics. Springer, Berlin Heidelberg, 2009. ISBN 9783642011634. URL http://books.google.co.uk/books?id=KgPGHaCUaAYC.

C. Bona, C. Bona-Casas, and C. Palenzuela. Action principle for Numerical Relativity evolution systems. *Phys. Rev. D*, 82:124010, 2010. doi: 10.1103/PhysRevD.82.124010.

R Borges, M Carmona, B Costa, and W Don. An improved weighted essentially non-oscillatory scheme for hyperbolic conservation laws. *Journal of Computational Physics*, 227(6):3191–3211, March 2008. ISSN 00219991. doi: 10.1016/j.jcp.2007.11.038. URL http://linkinghub.elsevier.com/retrieve/pii/S0021999107005232.

W. Boscheri and M. Dumbser. Arbitrary-Lagrangian-Eulerian Discontinuous Galerkin schemes with a posteriori subcell finite volume limiting on moving unstructured meshes. *Journal of Computational Physics*, 346:449–479, October 2017. doi: 10.1016/j.jcp.2017.06.022.

L. Bovard and L. Rezzolla. On the use of tracer particles in simulations of binary neutron stars. *Classical and Quantum Gravity*, 34(21):215005, 2017. URL http://stacks.iop.org/0264-9381/34/i=21/a=215005.

L. Bovard, D. Martin, F. Guercilena, A. Arcones, L. Rezzolla, and O. Korobkin. On r-process nucleosynthesis from matter ejected in binary neutron star mergers. *Phys. Rev. D*, 96:124005, December 2017.

S. Brandt and B. Brügmann. A simple construction of initial data for multiple black holes. *Phys. Rev. Lett.*, 78(19):3606–3609, 1997.

C. Breu and L. Rezzolla. Maximum mass, moment of inertia and compactness of relativistic stars. *Mon. Not. R. Astron. Soc.*, 459:646–656, June 2016. doi: 10.1093/mnras/stw575.

David Brown, Peter Diener, Olivier Sarbach, Erik Schnetter, and Manuel Tiglio. Turduckening black holes: an analytical and computational study. *Phys. Rev. D*, 79:044023, 2009a. doi: 10.1103/PhysRevD.79.044023. URL http://arxiv.org/abs/0809.3533.

David Brown, Peter Diener, Olivier Sarbach, Erik Schnetter, and Manuel Tiglio. Turduckening black holes: An analytical and computational study. *Phys. Rev. D*, 79(4):044023, Feb 2009b. URL http://dx.doi.org/10.1103/PhysRevD.79.044023.

David J. Brown. Covariant formulations of Baumgarte, Shapiro, Shibata, and Nakamura and the standard gauge. *Phys. Rev. D*, 79(10):104029, May 2009. doi: 10.1103/PhysRevD.79.104029.

J. D. Brown, P. Diener, S. E. Field, J. S. Hesthaven, F. Herrmann, A. H. Mroué, O. Sarbach, E. Schnetter, M. Tiglio, and M. Wagman. Numerical simulations with a first-order BSSN formulation of Einstein's field equations. *Phys. Rev. D*, 85(8):084004, April 2012. doi: 10.1103/PhysRevD.85.084004.

A. Buonanno and T. Damour. Effective one-body approach to general relativistic two-body dynamics. *Phys. Rev. D*, 59(8):084006, April 1999. doi: 10.1103/PhysRevD.59.084006.

E. M. Burbidge, G. R. Burbidge, W. A. Fowler, and F. Hoyle. Synthesis of the Elements in Stars. *Rev. Mod. Phys.*, 29:547–650, 1957. doi: 10.1103/RevModPhys.29.547.

M.J. Castro, J.M. Gallardo, and C. Parés. High-order finite volume schemes based on reconstruction of states for solving hyperbolic systems with nonconservative products. applications to shallow-water systems. *Mathematics of Computation*, 75:1103–1134, 2006.

M.J. Castro, A. Pardo, C. Parés, and E.F. Toro. On some fast well-balanced first order solvers for nonconservative systems. *Mathematics of Computation*, 79: 1427–1472, 2010.

J. Centrella, J. G. Baker, B. J. Kelly, and J. R. van Meter. Black-hole binaries, gravitational waves, and numerical relativity. *Reviews of Modern Physics*, 82: 3069–3119, October 2010. doi: 10.1103/RevModPhys.82.3069.

D. E. Charrier, M. Dumbser, K. Duru, F. Fambri, A. Gabriel, J. M. Gallard, S. Köppel, A. Osorio, L. Rannabauer, L. Rezzolla, M. Tavelli, and T. Weinzierl. ExaHyPE: An Exascale Hyperbolic pde Engine, 2018. http://exahype.eu/.

GQ Chen. Euler equations and related hyperbolic conservation laws. *...of Differential Equations: Evolutionary Equations*, 2, 2006. doi: 10.1016/S1874-5717(06)80004-6. URL http://www.sciencedirect.com/science/article/pii/S1874571706800046.

Gui-Qiang Chen and Hermano Frid. Extended divergence-measure fields and the euler equations for gas dynamics. *Communications in Mathematical Physics*, 236(2):251, 2003. doi: 10.1007/s00220-003-0823-7.

Gui-Qiang Chen, William P. Ziemer, and Monica Torres. Gauss-green theorem for weakly differentiable vector fields, sets of finite perimeter, and balance laws. *Communications on Pure and Applied Mathematics*, 62(2):242, 2009. doi: 10.1002/cpa.20262.

M. Chruslinska, K. Belczynski, T. Bulik, and W. Gladysz. Constraints on the Formation of Double Neutron Stars from the Observed Eccentricities and Current Limits on Merger Rates. *Acta Astronomica*, 67:37–50, March 2017.

R. Ciolfi and D. M. Siegel. Short Gamma-Ray Bursts in the "Time-reversal" Scenario. *Astrophys. J.*, 798:L36, January 2015. doi: 10.1088/2041-8205/798/2/L36.

B. Cockburn. Discontinuous Galerkin methods. *Zamm*, 83(11):731–754, November 2003. ISSN 0044-2267. doi: 10.1002/zamm.200310088. URL http://doi.wiley.com/10.1002/zamm.200310088.

P. Colella and M. D. Sekora. A limiter for PPM that preserves accuracy at smooth extrema. *Journal of Computational Physics*, 227:7069–7076, July 2008. doi: 10.1016/j.jcp.2008.03.034.

Phillip Colella and Paul R. Woodward. The piecewise parabolic method (ppm) for gas-dynamical simulations. *Journal of Computational Physics*, 54(1):174–201, 1984. ISSN 0021-9991. doi: DOI:10.1016/0021-9991(84)90143-8. URL http://www.sciencedirect.com/science/article/B6WHY-4DD1PHM-SJ/2/13d69a59afba3d6a5d6bbf1144d860aa.

I. Cordero-Carrión, P. Cerdá-Durán, H. Dimmelmeier, J. L. Jaramillo, J. Novak, and E. Gourgoulhon. Improved constrained scheme for the Einstein equations: An approach to the uniqueness issue. *Phys. Rev. D*, 79(2):024017, January 2009. doi: 10.1103/PhysRevD.79.024017.

B. Côté, K. Belczynski, C. L. Fryer, C. Ritter, A. Paul, B. Wehmeyer, and B. W. O'Shea. Advanced LIGO Constraints on Neutron Star Mergers and r-process Sites. *Astrophys. J.*, 836:230, February 2017. doi: 10.3847/1538-4357/aa5c8d.

R. Courant, K. Friedrichs, and H. Lewy. Über die partiellen Differenzengleichungen der mathematischen Physik. *Mathematische Annalen*, 100:32–74, 1928. doi: 10.1007/BF01448839.

P. S. Cowperthwaite, E. Berger, V. A. Villar, B. D. Metzger, M. Nicholl, R. Chornock, P. K. Blanchard, W. Fong, R. Margutti, M. Soares-Santos, K. D. Alexander, S. Allam, J. Annis, D. Brout, D. A. Brown, R. E. Butler, H.-Y. Chen, H. T. Diehl, Z. Doctor, M. R. Drout, T. Eftekhari, B. Farr, D. A. Finley, R. J. Foley, J. A. Frieman, C. L. Fryer, J. García-Bellido, M. S. S. Gill, J. Guillochon, K. Herner, D. E. Holz, D. Kasen, R. Kessler, J. Marriner, T. Matheson, E. H. Neilsen, Jr., E. Quataert, A. Palmese, A. Rest, M. Sako, D. M. Scolnic, N. Smith, D. L. Tucker, P. K. G. Williams, E. Balbinot, J. L. Carlin, E. R. Cook, F. Durret, T. S. Li, P. A. A. Lopes, A. C. C. Lourenço, J. L. Marshall, G. E. Medina, J. Muir, R. R. Muñoz, M. Sauseda, D. J. Schlegel, L. F. Secco, A. K. Vivas, W. Wester, A. Zenteno, Y. Zhang, T. M. C. Abbott, M. Banerji, K. Bechtol, A. Benoit-Lévy, E. Bertin, E. Buckley-Geer, D. L. Burke, D. Capozzi, A. Carnero Rosell, M. Carrasco Kind, F. J. Castander, M. Crocce, C. E. Cunha, C. B. D'Andrea, L. N. da Costa, C. Davis, D. L. DePoy, S. Desai, J. P. Dietrich, A. Drlica-Wagner, T. F. Eifler, A. E. Evrard, E. Fernandez, B. Flaugher, P. Fosalba, E. Gaztanaga, D. W. Gerdes, T. Giannantonio, D. A. Goldstein, D. Gruen, R. A. Gruendl, G. Gutierrez, K. Honscheid, B. Jain, D. J. James, T. Jeltema, M. W. G. Johnson, M. D. Johnson, S. Kent, E. Krause, R. Kron, K. Kuehn, N. Nuropatkin, O. Lahav, M. Lima, H. Lin, M. A. G. Maia, M. March, P. Martini, R. G. McMahon, F. Menanteau, C. J. Miller, R. Miquel, J. J. Mohr, E. Neilsen, R. C. Nichol, R. L. C. Ogando, A. A. Plazas, N. Roe, A. K. Romer, A. Roodman, E. S. Rykoff, E. Sanchez, V. Scarpine, R. Schindler, M. Schubnell, I. Sevilla-Noarbe, M. Smith, R. C. Smith, F. Sobreira, E. Suchyta, M. E. C. Swanson, G. Tarle, D. Thomas, R. C. Thomas, M. A. Troxel, V. Vikram, A. R. Walker, R. H. Wechsler, J. Weller, B. Yanny, and J. Zuntz. The Electromagnetic Counterpart of the Binary Neutron Star Merger LIGO/Virgo GW170817. II. UV, Optical, and Near-infrared Light Curves and Comparison to Kilonova Models. *Astrophys. J. Lett.*, 848: L17, October 2017. doi: 10.3847/2041-8213/aa8fc7.

Michael G. Crandall and Andrew Majda. Monotone Difference Approximations for Scalar Conservation Laws. *Mathematics of Computation*, 34(149): 1, January 1980. ISSN 00255718. doi: 10.2307/2006218. URL http://www.jstor.org/stable/2006218?origin=crossref.

Michael G. Crandall and Luc Tartar. Some relations between nonexpansive and order preserving mappings. *Proceedings of the American Mathematical Society*, 78(3):385–385, March 1980. ISSN 0002-9939. doi: 10.1090/S0002-9939-1980-0553381-X. URL http://www.ams.org/jourcgi/jour-getitem?pii=S0002-9939-1980-0553381-X.

J. DeBuhr, B. Zhang, M. Anderson, D. Neilsen, and E. W. Hirschmann. Relativistic Hydrodynamics with Wavelets. *ArXiv e-prints*, December 2015.

A. Dedner, F. Kemm, D. Kröner, C. D. Munz, T. Schnitzer, and M. Wesenberg. Hyperbolic Divergence Cleaning for the MHD Equations. *Journal of Computational Physics*, 175:645–673, January 2002. doi: 10.1006/jcph.2001.6961.

L. Dessart, C. D. Ott, A. Burrows, S. Rosswog, and E. Livne. Neutrino Signatures and the Neutrino-Driven Wind in Binary Neutron Star Mergers. *Astrophys. J.*, 690:1681–1705, January 2009. doi: 10.1088/0004-637X/690/2/1681.

T. Dietrich and M. Ujevic. Modeling dynamical ejecta from binary neutron star mergers and implications for electromagnetic counterparts. *Classical and Quantum Gravity*, 34(10):105014, May 2017. doi: 10.1088/1361-6382/aa6bb0.

T. Dietrich, S. Bernuzzi, M. Ujevic, and B. Brügmann. Numerical relativity simulations of neutron star merger remnants using conservative mesh refinement. *Phys. Rev. D*, 91(12):124041, June 2015. doi: 10.1103/PhysRevD.91.124041.

T. Dietrich, S. Bernuzzi, and W. Tichy. Closed-form tidal approximants for binary neutron star gravitational waveforms constructed from high-resolution numerical relativity simulations. *ArXiv e-prints*, June 2017a.

T. Dietrich, M. Ujevic, W. Tichy, S. Bernuzzi, and B. Brügmann. Gravitational waves and mass ejecta from binary neutron star mergers: Effect of the mass ratio. *Phys. Rev. D*, 95(2):024029, January 2017b. doi: 10.1103/PhysRevD.95.024029.

Ronald J. DiPerna. Measure-valued solutions to conservation laws. *Archive for Rational Mechanics and Analysis*, 88(3):223–270, 1985. ISSN 0003-9527. doi: 10.1007/BF00752112. URL http://www.springerlink.com/index/10.1007/BF00752112.

R. Donat and A. Marquina. Capturing Shock Reflections: An Improved Flux Formula. *Journal of Computational Physics*, 125:42–58, April 1996. doi: 10.1006/jcph.1996.0078.

M. Dumbser and D.S. Balsara. A new, efficient formulation of the HLLEM Riemann solver for general conservative and non-conservative hyperbolic systems. *Journal of Computational Physics*, 304:275–319, 2016.

M. Dumbser and M. Kaeser. Arbitrary high order non-oscillatory finite volume schemes on unstructured meshes for linear hyperbolic systems. *Journal of Computational Physics*, 221:693–723, February 2007. doi: 10.1016/j.jcp.2006.06.043.

M. Dumbser and E. F. Toro. A simple extension of the Osher Riemann solver to non-conservative hyperbolic systems. *Journal of Scientific Computing*, 48:70–88, 2011.

M. Dumbser and O. Zanotti. Very high order PNPM schemes on unstructured meshes for the resistive relativistic MHD equations. *Journal of Computational Physics*, 228:6991–7006, October 2009. doi: 10.1016/j.jcp.2009.06.009.

M. Dumbser, M. Kaeser, V. A. Titarev, and E. F. Toro. Quadrature-free non-oscillatory finite volume schemes on unstructured meshes for nonlinear hyperbolic systems. *Journal of Computational Physics*, 226:204–243, September 2007. doi: 10.1016/j.jcp.2007.04.004.

M. Dumbser, C. Enaux, and E.F. Toro. Finite volume schemes of very high order of accuracy for stiff hyperbolic balance laws. *Journal of Computational Physics*, 227:3971–4001, 2008.

M. Dumbser, M. Castro, C. Parés, and E.F. Toro. ADER schemes on unstructured meshes for non-conservative hyperbolic systems: Applications to geophysical flows. *Computers and Fluids*, 38:1731–1748, 2009.

M. Dumbser, A. Hidalgo, M. Castro, C. Parés, and E.F. Toro. FORCE schemes on unstructured meshes II: Non–conservative hyperbolic systems. *Computer Methods in Applied Mechanics and Engineering*, 199:625–647, 2010.

M. Dumbser, O. Zanotti, A. Hidalgo, and D. S. Balsara. ADER-WENO finite volume schemes with space-time adaptive mesh refinement. *Journal of Computational Physics*, 248:257–286, September 2013. doi: 10.1016/j.jcp.2013.04.017.

M. Dumbser, A. Hidalgo, and O. Zanotti. High Order Space-Time Adaptive ADER-WENO Finite Volume Schemes for Non-Conservative Hyperbolic Systems. *Computer Methods in Applied Mechanics and Engineering*, 268:359–387, 2014.

M. Dumbser, F. Guercilena, S. Koeppel, L. Rezzolla, and O. Zanotti. A strongly hyperbolic first-order CCZ4 formulation of the Einstein equations and its solution with discontinuous Galerkin schemes. *arXiv:1707.09910*, July 2017.

D. Eichler, M. Livio, T. Piran, and D. N. Schramm. Nucleosynthesis, neutrino bursts and gamma-rays from coalescing neutron stars. *Nature*, 340:126–128, July 1989. doi: 10.1038/340126a0.

M. Eichler, A. Arcones, A. Kelic, O. Korobkin, K. Langanke, T. Marketin, G. Martinez-Pinedo, I. Panov, T. Rauscher, S. Rosswog, C. Winteler, N. T. Zinner, and F.-K. Thielemann. The Role of Fission in Neutron Star Mergers and Its Impact on the r-Process Peaks. *Astrophys. J.*, 808:30, July 2015. doi: 10.1088/0004-637X/808/1/30.

B. Einfeldt. On Godunov-type methods for gas dynamics. *SIAM J. Numer. Anal.*, 25:294–318, 1988.

B. Einfeldt, P. L. Roe, C. D. Munz, and B. Sjogreen. On Godunov-type methods near low densities. *Journal of Computational Physics*, 92:273–295, February 1991. doi: 10.1016/0021-9991(91)90211-3.

Einstein Toolkit Website. Einstein Toolkit: Open Software for Relativistic Astrophysics. `http://einsteintoolkit.org`.

J. P. Emerson, W. J. Sutherland, A. M. McPherson, S. C. Craig, G. B. Dalton, and A. K. Ward. The Visible & Infrared Survey Telescope for Astronomy. *The Messenger*, 117:27–32, September 2004.

R. Fernández and B. D. Metzger. Delayed outflows from black hole accretion tori following neutron star binary coalescence. *Mon. Not. R. Astron. Soc.*, 435:502–517, October 2013. doi: 10.1093/mnras/stt1312.

S. E. Field, J. S. Hesthaven, S. R. Lau, and A. H. Mroue. Discontinuous Galerkin method for the spherically reduced Baumgarte-Shapiro-Shibata-Nakamura system with second-order operators. *Phys. Rev. D*, 82(10):104051, November 2010. doi: 10.1103/PhysRevD.82.104051.

T. Fischer, S. C. Whitehouse, A. Mezzacappa, F.-K. Thielemann, and M. Liebendörfer. Protoneutron star evolution and the neutrino-driven wind in general relativistic neutrino radiation hydrodynamics simulations. *Astron. Astrophys.*, 517:A80, July 2010. doi: 10.1051/0004-6361/200913106.

J. A. Font. Numerical hydrodynamics and magnetohydrodynamics in general relativity. *Living Rev. Relativ.*, 6:4; http://www.livingreviews.org/lrr–2008–7, 2008. URL http://www.livingreviews.org/lrr-2008-7.

J. A. Font, T. Goodale, S. Iyer, M. Miller, L. Rezzolla, E. Seidel, N. Stergioulas, W.-M. Suen, and M. Tobias. Three-dimensional numerical general relativistic hydrodynamics. II. Long-term dynamics of single relativistic stars. *Phys. Rev. D*, 65(8):084024, April 2002. doi: 10.1103/PhysRevD.65.084024.

Bengt Fornberg. Generation of finite difference formulas on arbitrarily spaced grids. *Mathematics of Computation*, 51(184):699–706, October 1988. doi: doi: 10.2307/2008770.

F. Foucart, M. B. Deaton, M. D. Duez, E. O'Connor, C. D. Ott, R. Haas, L. E. Kidder, H. P. Pfeiffer, M. A. Scheel, and B. Szilagyi. Neutron star-black hole mergers with a nuclear equation of state and neutrino cooling: Dependence in the binary parameters. *Phys. Rev. D*, 90(2):024026, July 2014. doi: 10.1103/PhysRevD.90.024026.

F. Foucart, M. Chandra, C. F. Gammie, and E. Quataert. Evolution of accretion discs around a kerr black hole using extended magnetohydrodynamics. *Mon. Not. R. Astron. Soc.*, 456:1332–1345, February 2016a. doi: 10.1093/mnras/stv2687.

F. Foucart, R. Haas, M. D. Duez, E. O'Connor, C. D. Ott, L. Roberts, L. E. Kidder, J. Lippuner, H. P. Pfeiffer, and M. A. Scheel. Low mass binary neutron star mergers: Gravitational waves and neutrino emission. *Phys. Rev. D*, 93(4):044019, February 2016b. doi: 10.1103/PhysRevD.93.044019.

F. Foucart, E. O'Connor, L. Roberts, L. E. Kidder, H. P. Pfeiffer, and M. A. Scheel. Impact of an improved neutrino energy estimate on outflows in neutron star merger simulations. *Phys. Rev. D*, 94(12):123016, December 2016c. doi: 10.1103/PhysRevD.94.123016.

C. Freiburghaus, S. Rosswog, and F.-K. Thielemann. R-Process in Neutron Star Mergers. *Astrophys. J. Lett.*, 525:L121–L124, November 1999. doi: 10.1086/312343.

Helmut Friedrich. Conformal Einstein evolution. *Lect. Notes Phys.*, 604:1–50, 2002.

K O Friedrichs. Symmetric hyperbolic linear differential equations. *Communications on Pure and Applied Mathematics*, 7(2):345–392, 1954. ISSN 1097-0312. doi: 10.1002/cpa.3160070206. URL http://dx.doi.org/10.1002/cpa.3160070206.

C. Fröhlich, G. Martínez-Pinedo, M. Liebendörfer, F.-K. Thielemann, E. Bravo, W. R. Hix, K. Langanke, and N. T. Zinner. Neutrino-Induced Nucleosynthesis of A>64 Nuclei: The νp Process. *Phys. Rev. Lett.*, 96(14):142502–+, April 2006. doi: 10.1103/PhysRevLett.96.142502.

S. Fujibayashi, Y. Sekiguchi, K. Kiuchi, and M. Shibata. Properties of Neutrino-driven Ejecta from the Remnant of Binary Neutron Star Merger : Purely Radiation Hydrodynamics Case. *ArXiv e-prints*, March 2017.

S.-i. Fujimoto, N. Nishimura, and M.-a. Hashimoto. Nucleosynthesis in Magnetically Driven Jets from Collapsars. *Astrophys. J.*, 680:1350-1358, June 2008. doi: 10.1086/529416.

F. Galeazzi, W. Kastaun, L. Rezzolla, and J. A. Font. Implementation of a simplified approach to radiative transfer in general relativity. *Phys. Rev. D*, 88 (6):064009, September 2013. doi: 10.1103/PhysRevD.88.064009.

G.a. Gerolymos, D. Sénéchal, and I. Vallet. Very-high-order weno schemes. *Journal of Computational Physics*, 228(23):8481–8524, December 2009. ISSN 00219991. doi: 10.1016/j.jcp.2009.07.039. URL http://linkinghub.elsevier.com/retrieve/pii/S0021999109003908.

B. Giacomazzo, R. Perna, L. Rezzolla, E. Troja, and D. Lazzati. Compact Binary Progenitors of Short Gamma-Ray Bursts. *Astrophys. J.*, 762:L18, January 2013. doi: 10.1088/2041-8205/762/2/L18.

S. Gillessen, F. Eisenhauer, S. Trippe, T. Alexander, R. Genzel, F. Martins, and T. Ott. Monitoring Stellar Orbits Around the Massive Black Hole in the Galactic Center. *Astrophys. J.*, 692:1075–1109, February 2009. doi: 10.1088/0004-637X/692/2/1075.

S. K. Godunov. A difference method for numerical calculations of discontinuous solutions of the equations of hydrpdynamics. *Mat. Sb.*, 47:271, 1959. in Russian.

J.B. Goodman and R.J. LeVeque. On the accuracy of stable schemes for 2D scalar conservation laws. *Mathematics of Computation*, 45(171): 15–21, 1985. URL http://www.ams.org/mcom/1985-45-171/S0025-5718-1985-0790641-4/S0025-5718-1985-0790641-4.pdf.

S. Goriely, A. Bauswein, and H.-T. Janka. r-process Nucleosynthesis in Dynamically Ejected Matter of Neutron Star Mergers. *Astrophys. J.*, 738:L32, September 2011. doi: 10.1088/2041-8205/738/2/L32.

S. Gottlieb, C.-W. Shu, and E. Tadmor. Strong Stability-Preserving High-Order Time Discretization Methods. *SIAM Review*, 43:89–112, January 2001. doi: 10.1137/S003614450036757X.

Sigal Gottlieb, David Ketcheson, and Chi-Wang Shu. High order strong stability preserving time discretizations. *Journal of Scientific Computing*, 38: 251–289, 2009. ISSN 0885-7474. URL http://dx.doi.org/10.1007/s10915-008-9239-z. 10.1007/s10915-008-9239-z.

E. Gourgoulhon, P. Grandclément, K. Taniguchi, J. A. Marck, and S. Bonazzola. Quasiequilibrium sequences of synchronized and irrotational binary neutron stars in general relativity: Method and tests. *Phys. Rev. D*, 63:064029, 2001.

Eric Gourgoulhon. *3+1 Formalism in General Relativity*, volume 846 of *Lecture Notes in Physics, Berlin Springer Verlag*. 2012. doi: 10.1007/978-3-642-24525-1.

D. Grossman, O. Korobkin, S. Rosswog, and T. Piran. The long-term evolution of neutron star merger remnants - II. Radioactively powered transients. *Mon. Not. R. Astron. Soc.*, 439:757–770, March 2014. doi: 10.1093/mnras/stt2503.

Federico Guercilena, David Radice, and Luciano Rezzolla. Entropy-limited hydrodynamics: a novel approach to relativistic hydrodynamics. *Computational Astrophysics and Cosmology*, 4(1):3, Jul 2017. ISSN 2197-7909. doi: 10.1186/s40668-017-0022-0. URL http://dx.doi.org/10.1186/s40668-017-0022-0.

J. L. Guermond and R. Pasquetti. Entropy-based nonlinear viscosity for Fourier approximations of conservation laws. *C. R. Acad. Sci. Paris*, 346(346):801–806, 208. ISSN 1631073X. doi: 10.1016/j.crma.2008.05.013.

J. L. Guermond, R. Pasquetti, and B. Popov. Entropy viscosity method for nonlinear conservation laws. *J. Comput. Phys.*, 230(11):4248–4267, 2011. ISSN 00219991. doi: 10.1016/j.jcp.2010.11.043. URL http://linkinghub.elsevier.com/retrieve/pii/S0021999110006583.

Carsten Gundlach and Jose M. Martin-Garcia. Hyperbolicity of second-order in space systems of evolution equations. *Class. Quantum Grav.*, 23:S387–S404, 2006.

Carsten Gundlach, Jose M. Martin-Garcia, G. Calabrese, and I. Hinder. Constraint damping in the Z4 formulation and harmonic gauge. *Class. Quantum Grav.*, 22:3767–3774, 2005. doi: 10.1088/0264-9381/22/17/025.

E. Hairer and G. Wanner. *Solving Ordinary Differential Equations II - Stiff and Differential-Algebraic Problems*. Springer, 2nd edition, 1996.

E. Hairer, S. P. Norsett, and G. Wanner. *Solving Ordinary Differential Equations I - Nonstiff Problems*. Springer, 2nd edition, 1993.

M. Hanauske, K. Takami, L. Bovard, L. Rezzolla, J. A. Font, F. Galeazzi, and H. Stöcker. Rotational properties of hypermassive neutron stars from binary mergers. *Phys. Rev. D*, 96(4):043004, August 2017. doi: 10.1103/PhysRevD.96.043004.

A. Harten, J. M. Hyman, P. D. Lax, and B. Keyfitz. On finite-difference approximations and entropy conditions for shocks. *Communications on Pure and Applied Mathematics*, 29(3):297–322, May 1976. ISSN 00103640. doi: 10.1002/cpa.3160290305. URL http://doi.wiley.com/10.1002/cpa.3160290305.

A. Harten, P. D. Lax, and B. van Leer. On upstream differencing and godunov-type schemes for hyperbolic conservation laws. *SIAM Rev.*, 25:35, 1983. doi: 10.1137/1025002.

A. Harten, B. Engquist, S. Osher, and S. R. Chakravarthy. Uniformly High Order Accurate Essentially Non-oscillatory Schemes III. *Journal of Computational Physics*, 71:231–303, August 1987. doi: 10.1016/0021-9991(87)90031-3.

Andrew K. Henrick, Tariq D. Aslam, and Joseph M. Powers. Mapped weighted essentially non-oscillatory schemes: Achieving optimal order near critical points. *Journal of Computational Physics*, 207(2):542–567, August 2005. ISSN 00219991. doi: 10.1016/j.jcp.2005.01.023. URL http://linkinghub.elsevier.com/retrieve/pii/S0021999105000409.

J.S. Hesthaven and T. Warburton. *Nodal Discontinuous Galerkin Methods: Algorithms, Analysis, and Applications*. Texts in Applied Mathematics. Springer, 2007. ISBN 9780387720654. URL http://books.google.it/books?id=APQkDOmwyksC.

A. Hewish, S. J. Bell, J. D. H. Pilkington, P. F. Scott, and R. A. Collins. Observation of a Rapidly Pulsating Radio Source. *Nature*, 217:709–713, February 1968. doi: 10.1038/217709a0.

D. Hilditch, S. Bernuzzi, M. Thierfelder, Z. Cao, W. Tichy, and B. Brügmann. Compact binary evolutions with the Z4c formulation. *Phys. Rev. D*, 88(8): 084057, October 2013. doi: 10.1103/PhysRevD.88.084057.

David Hilditch and Ronny Richter. Hyperbolicity of high-order systems of evolution equations. *Journal of Hyperbolic Differential Equations*, 12(01):1–35, 2015. doi: 10.1142/S0219891615500010. URL http://www.worldscientific.com/doi/abs/10.1142/S0219891615500010.

W. R. Hix and F. K. Thielemann. Computational methods for nucleosynthesis and nuclear energy generation. *Journal of Computational and Applied Mathematics*, 109:321–351, February 1999.

K. Hotokezaka, K. Kiuchi, K. Kyutoku, H. Okawa, Y.-i. Sekiguchi, M. Shibata, and K. Taniguchi. Mass ejection from the merger of binary neutron stars. *Phys. Rev. D*, 87(2):024001, January 2013. doi: 10.1103/PhysRevD.87.024001.

X. Y. Hu, N. A. Adams, and C.-W. Shu. Positivity-preserving method for high-order conservative schemes solving compressible Euler equations. *Journal of Computational Physics*, 242:169–180, June 2013. doi: 10.1016/j.jcp.2013.01.024.

L. Hüdepohl, B. Müller, H.-T. Janka, A. Marek, and G. G. Raffelt. Neutrino signal of electron-capture supernovae from core collapse to cooling. *Phys. Rev. Lett.*, 104:251101, Jun 2010a. doi: 10.1103/PhysRevLett.104.251101. URL https://link.aps.org/doi/10.1103/PhysRevLett.104.251101.

L. Hüdepohl, B. Müller, H.-T. Janka, A. Marek, and G. G. Raffelt. Erratum: Neutrino signal of electron-capture supernovae from core collapse to cooling [phys. rev. lett. 104, 251101 (2010)]. *Phys. Rev. Lett.*, 105:249901, Dec 2010b. doi: 10.1103/PhysRevLett.105.249901. URL https://link.aps.org/doi/10.1103/PhysRevLett.105.249901.

Sascha Husa. In L. Fernández and L. Manuel González, editors, *Current trends in relativistic astrophysics*, volume 617 of *Lecture Notes in Physics*. Springer, 2002.

A. P. Ji, A. Frebel, A. Chiti, and J. D. Simon. R-process enrichment from a single event in an ancient dwarf galaxy. *Nature*, 531:610–613, March 2016. doi: 10.1038/nature17425.

Guang-Shan Jiang and Chi-Wang Shu. Efficient implementation of weighted eno schemes. *J. Comput. Phys*, 126:202–228, 1996.

Z.-P. Jin, X. Li, Z. Cano, S. Covino, Y.-Z. Fan, and D.-M. Wei. The Light Curve of the Macronova Associated with the Long-Short Burst GRB 060614. *Astrophys. J. Lett.*, 811:L22, October 2015. doi: 10.1088/2041-8205/811/2/L22.

Z.-P. Jin, K. Hotokezaka, X. Li, M. Tanaka, P. D'Avanzo, Y.-Z. Fan, S. Covino, D.-M. Wei, and T. Piran. The Macronova in GRB 050709 and the GRB-macronova connection. *Nature Communications*, 7:12898, September 2016. doi: 10.1038/ncomms12898.

O. Just, A. Bauswein, R. A. Pulpillo, S. Goriely, and H.-T. Janka. Comprehensive nucleosynthesis analysis for ejecta of compact binary mergers. *Mon. Not. R. Astron. Soc.*, 448:541–567, March 2015. doi: 10.1093/mnras/stv009.

O. Just, M. Obergaulinger, H.-T. Janka, A. Bauswein, and N. Schwarz. Neutron-star Merger Ejecta as Obstacles to Neutrino-powered Jets of Gamma-Ray Bursts. *Astrophys. J. Lett.*, 816:L30, January 2016. doi: 10.3847/2041-8205/816/2/L30.

W. Kastaun and F. Galeazzi. Properties of hypermassive neutron stars formed in mergers of spinning binaries. *Phys. Rev. D*, 91(6):064027, March 2015. doi: 10.1103/PhysRevD.91.064027.

W. Kastaun, F. Galeazzi, D. Alic, L. Rezzolla, and J. A. Font. Black hole from merging binary neutron stars: How fast can it spin? *Phys. Rev. D*, 88(2): 021501, July 2013. doi: 10.1103/PhysRevD.88.021501.

W. Kastaun, R. Ciolfi, and B. Giacomazzo. Structure of stable binary neutron star merger remnants: A case study. *Phys. Rev. D*, 94(4):044060, August 2016. doi: 10.1103/PhysRevD.94.044060.

A.M Khokhlov. Fully threaded tree algorithms for adaptive refinement fluid dynamics simulations. *Journal of Computational Physics*, 143(2):519 – 543, 1998.

L. E. Kidder, Mark A. Scheel, and Saul A. Teukolsky. Extending the lifetime of 3D black hole computations with a new hyperbolic system of evolution equations. *Phys. Rev. D*, 64:064017, 2001.

Jae Wook Kim and Richard D. Sandberg. Efficient parallel computing with a compact finite difference scheme. *Computers & Fluids*, 58:70–87, 2012. ISSN 00457930. doi: 10.1016/j.compfluid.2012.01.004. URL http://dx.doi.org/10.1016/j.compfluid.2012.01.004.

K. Kiuchi, K. Kyutoku, and M. Shibata. Three-dimensional evolution of differentially rotating magnetized neutron stars. *Phys. Rev. D*, 86(6):064008, September 2012. doi: 10.1103/PhysRevD.86.064008.

O. Korobkin, S. Rosswog, A. Arcones, and C. Winteler. On the astrophysical robustness of the neutron star merger r-process. *Mon. Not. R. Astron. Soc.*, 426:1940–1949, November 2012. doi: 10.1111/j.1365-2966.2012.21859.x.

M Kramer and N Wex. TOPICAL REVIEW: The double pulsar system: a unique laboratory for gravity. *Class. Quantum Grav.*, 26(7):073001, April 2009. doi: 10.1088/0264-9381/26/7/073001.

Heinz Otto Kreiss and J. Lorenz. *Initial-boundary value problems and the Navier-Stokes equations*. Academic Press, New York, 1989.

Heinz Otto Kreiss and Joseph Oliger. *Methods for the approximate solution of time dependent problems*. GARP publication series No. 10, Geneva, 1973.

S N Kružkov. FIRST ORDER QUASILINEAR EQUATIONS IN SEVERAL INDEPENDENT VARIABLES. *Mathematics of the USSR-Sbornik*, 10(2):217–243, February 1970. ISSN 0025-5734. doi: 10.1070/SM1970v010n02ABEH002156. URL http://stacks.iop.org/0025-5734/10/i=2/a=A06?key=crossref.4eecd9c5a212905d35fc0614fd12cc90.

K. Kyutoku, K. Ioka, and M. Shibata. Ultrarelativistic electromagnetic counterpart to binary neutron star mergers. *Mon. Not. R. Astron.Soc.*, 437:L6–L10, January 2014. doi: 10.1093/mnrasl/slt128.

James M. Lattimer and F. Douglas Swesty. A generalized equation of state for hot, dense matter. *Nucl. Phys. A*, 535:331–376, 1991.

P. D. Lax and R. D. Richtmyer. Survey of the stability of linear finite difference equations. *Communications on Pure and Applied Mathematics*, 9(2): 267–293, May 1956. ISSN 00103640. doi: 10.1002/cpa.3160090206. URL http://doi.wiley.com/10.1002/cpa.3160090206.

P. D. Lax and B. Wendroff. Systems of conservation laws. *Commun. Pure Appl. Math.*, 13:217–237, 1960.

W. H. Lee, E. Ramirez-Ruiz, and G. van de Ven. Short Gamma-ray Bursts from Dynamically Assembled Compact Binaries in Globular Clusters: Pathways, Rates, Hydrodynamics, and Cosmological Setting. *Astrophys. J.*, 720:953–975, September 2010. doi: 10.1088/0004-637X/720/1/953.

L. Lehner, S. L. Liebling, C. Palenzuela, O. L. Caballero, E. O'Connor, M. Anderson, and D. Neilsen. Unequal mass binary neutron star mergers and multimessenger signals. *Classical and Quantum Gravity*, 33(18):184002, September 2016. doi: 10.1088/0264-9381/33/18/184002.

Sanjiva K. Lele. Compact Finite Difference Schemes with Spectral-like Resolution. *J. Comput. Phys.*, 103:16–42, 1992.

R. J. Leveque. *Numerical Methods for Conservation Laws*. Birkhauser Verlag, Basel, 1992.

R. J. Leveque. *Finite Volume Methods for Hyperbolic Problems*. Cambridge University Press, New York, 2002.

L.-X. Li and B. Paczyński. Transient Events from Neutron Star Mergers. *Astrophys. J.*, 507:L59–L62, November 1998. doi: 10.1086/311680.

LIGO Scientific Collaboration, Virgo Collaboration, F. Gamma-Ray Burst Monitor, and INTEGRAL. Gravitational waves and gamma-rays from a binary neutron star merger: Gw170817 and grb 170817a. *Astrophys. J. Lett.*, 848 (2):L13, 2017. URL http://stacks.iop.org/2041-8205/848/i=2/a=L13.

L. Lindblom, M. A. Scheel, L. E. Kidder, R. Owen, and O. Rinne. A new generalized harmonic evolution system. *Class. Quantum Grav.*, 23:447, August 2006. doi: 10.1088/0264-9381/23/16/S09.

J. Lippuner and L. F. Roberts. SkyNet: A MODULAR NUCLEAR REACTION NETWORK LIBRARY. 2017.

X.-D. Liu, S. Osher, and T. Chan. Weighted Essentially Non-oscillatory Schemes. *Journal of Computational Physics*, 115:200–212, November 1994. doi: 10.1006/jcph.1994.1187.

F. Löffler, J. Faber, E. Bentivegna, T. Bode, P. Diener, R. Haas, I. Hinder, B. C. Mundim, C. D. Ott, E. Schnetter, G. Allen, M. Campanelli, and P. Laguna. The Einstein Toolkit: a community computational infrastructure for relativistic astrophysics. *Class. Quantum Grav.*, 29(11):115001, June 2012. doi: 10.1088/0264-9381/29/11/115001.

M. Maggiore. *Gravitational Waves: Volume 1: Theory and Experiments*. Gravitational Waves. Oxford University Press, USA, 2007. ISBN 9780198570745. URL http://books.google.de/books?id=AqVpQgAACAAJ.

Antonio Marquina. Local piecewise hyperbolic reconstruction of numerical fluxes for nonlinear scalar conservation laws. *SIAM Journal on Scientific Computing*, 15(4):892–915, 1994. doi: 10.1137/0915054. URL https://doi.org/10.1137/0915054.

J. M. Martí and E. Müller. Numerical hydrodynamics in special relativity. *Living Rev. Relativ.*, 6:7; http://www.livingreviews.org/lrr–2003–7, 2003. URL http://www.livingreviews.org/lrr-2003-7.

J. M. Martí and E. Müller. Grid-based Methods in Relativistic Hydrodynamics and Magnetohydrodynamics. *Living Reviews in Computational Astrophysics*, 1, December 2015. doi: 10.1007/lrca-2015-3.

D. Martin, A. Perego, A. Arcones, O. Korobkin, and F.-K. Thielemann. Nucleosynthesis in the Ejecta of Neutron Star Mergers. *ArXiv e-prints*, September 2015a.

D. Martin, A. Perego, A. Arcones, F.-K. Thielemann, O. Korobkin, and S. Rosswog. Neutrino-driven Winds in the Aftermath of a Neutron Star Merger: Nucleosynthesis and Electromagnetic Transients. *Astrophys. J.*, 813: 2, November 2015b. doi: 10.1088/0004-637X/813/1/2.

D. Martin, A. Arcones, W. Nazarewicz, and E. Olsen. Impact of Nuclear Mass Uncertainties on the r Process. *Phys. Rev. Lett.*, 116(12):121101, March 2016. doi: 10.1103/PhysRevLett.116.121101.

P. J. McMillan. Mass models of the Milky Way. *Mon. Not. R. Astron. Soc.*, 414: 2446–2457, July 2011. doi: 10.1111/j.1365-2966.2011.18564.x.

D. L. Meier. Multidimensional astrophysical structural and dynamical analysis. i. development of a nonlinear finite element approach. *Astrophys. J.*, 518(2): 788, 1999. doi: 10.1086/307292.

J. d. J. Mendoza-Temis, M.-R. Wu, K. Langanke, G. Martínez-Pinedo, A. Bauswein, and H.-T. Janka. Nuclear robustness of the r process in neutron-star mergers. *Physical Review C*, 92(5):055805, November 2015. doi: 10.1103/PhysRevC.92.055805.

R. Menikoff and B. J. Plohr. The Riemann problem for fluid flow of real materials. *Reviews of Modern Physics*, 61:75–130, January 1989. doi: 10.1103/RevModPhys.61.75.

B. D. Metzger. Kilonovae. *Living Reviews in Relativity*, 20:3, May 2017a. doi: 10.1007/s41114-017-0006-z.

B. D. Metzger. Welcome to the Multi-Messenger Era! Lessons from a Neutron Star Merger and the Landscape Ahead. *ArXiv e-prints*, October 2017b.

B. D. Metzger and C. Zivancev. Pair fireball precursors of neutron star mergers. *Mon. Not. R. Astron. Soc.*, 461:4435–4440, October 2016. doi: 10.1093/mnras/stw1800.

B. D. Metzger, A. L. Piro, and E. Quataert. Time-dependent models of accretion discs formed from compact object mergers. *Mon. Not. R. Astron. Soc.*, 390: 781–797, October 2008. doi: 10.1111/j.1365-2966.2008.13789.x.

B. D. Metzger, G. Martínez-Pinedo, S. Darbha, E. Quataert, A. Arcones, D. Kasen, R. Thomas, P. Nugent, I. V. Panov, and N. T. Zinner. Electromagnetic counterparts of compact object mergers powered by the radioactive decay of r-process nuclei. *Mon. Not. R. Astron. Soc.*, 406:2650–2662, August 2010. doi: 10.1111/j.1365-2966.2010.16864.x.

V. Mewes, F. Galeazzi, J. A. Font, P. J. Montero, and N. Stergioulas. On the dynamics of tilted black hole-torus systems. *Mon. Not. R. Astron. Soc.*, 461: 2480–2489, September 2016. doi: 10.1093/mnras/stw1490.

A. Mignone, P. Tzeferacos, and G. Bodo. High-order conservative finite difference glm-mhd schemes for cell-centered mhd. *Journal of Computational Physics*, 229:5896–5920, aug 2010. doi: 10.1016/j.jcp.2010.04.013.

J.M. Miller and E. Schnetter. An operator-based local discontinuous galerkin method compatible with the bssn formulation of the einstein equations. *Classical and Quantum Gravity*, 34(1):015003, March 2017. doi: 10.1088/1361-6382/34/1/015003. URL http://stacks.iop.org/0264-9381/34/i=1/a=015003.

Charles W. Misner, Kip S. Thorne, and John A. Wheeler. *Gravitation*. W. H. Freeman, San Francisco, 1973.

P. Möller, J. R. Nix, W. D. Myers, and W. J. Swiatecki. Nuclear Ground-State Masses and Deformations. *Atomic Data and Nuclear Data Tables*, 59(2):185 – 381, 1995. ISSN 0092-640X. doi: http://dx.doi.org/10.1006/adnd.1995.1002. URL http://www.sciencedirect.com/science/article/pii/S0092640X85710029.

P. Möller, B. Pfeiffer, and K.-L. Kratz. New calculations of gross β-decay properties for astrophysical applications: Speeding-up the classical r process. *Physical Review C*, 67(5):055802, May 2003. doi: 10.1103/PhysRevC.67.055802.

P. Möller, W. D. Myers, H. Sagawa, and S. Yoshida. New Finite-Range Droplet Mass Model and Equation-of-State Parameters. *Phys. Rev. Lett.*, 108(5):052501, February 2012. doi: 10.1103/PhysRevLett.108.052501.

V. Moncrief. Gravitational perturbations of spherically symmetric systems. I. the exterior problem. *Annals of Physics*, 88:323–342, 1974.

P. Mösta, S. Richers, C. D. Ott, R. Haas, A. L. Piro, K. Boydstun, E. Abdikamalov, C. Reisswig, and E. Schnetter. Magnetorotational Core-collapse Supernovae in Three Dimensions. *Astrophys. J. Lett.*, 785:L29, April 2014. doi: 10.1088/2041-8205/785/2/L29.

M. R. Mumpower, R. Surman, D.-L. Fang, M. Beard, P. Möller, T. Kawano, and A. Aprahamian. Impact of individual nuclear masses on r -process abundances. *Physical Review C*, 92(3):035807, September 2015. doi: 10.1103/PhysRevC.92.035807.

A. Murguia-Berthier, G. Montes, E. Ramirez-Ruiz, F. De Colle, and W. H. Lee. Necessary Conditions for Short Gamma-Ray Burst Production in Binary Neutron Star Mergers. *Astrophys. J.*, 788:L8, June 2014. doi: 10.1088/2041-8205/788/1/L8.

Alessandro Nagar and Luciano Rezzolla. Gauge-invariant non-spherical metric perturbations of Schwarzschild black-hole spacetimes. *Class. Quantum Grav.*, 22(16):R167–R192, 2005. erratum-ibid. **23**, 4297, (2006).

T. Nakamura, K. Oohara, and Y. Kojima. General Relativistic Collapse to Black Holes and Gravitational Waves from Black Holes. *Progress of Theoretical Physics Supplement*, 90:1–218, 1987. doi: 10.1143/PTPS.90.1.

R. Narayan, B. Paczynski, and T. Piran. Gamma-ray bursts as the death throes of massive binary stars. *Astrophys. J. Lett.*, 395:L83–L86, August 1992. doi: 10.1086/186493.

Ezra T. Newman and Roger Penrose. An approach to gravitational radiation by a method of spin coefficients. *J. Math. Phys.*, 3(3):566–578, 1962. doi: 10.1063/1.1724257. erratum in J. Math. Phys. 4, 998 (1963).

N. Nishimura, H. Sawai, T. Takiwaki, S. Yamada, and F.-K. Thielemann. The Intermediate r-process in Core-collapse Supernovae Driven by the Magnetorotational Instability. *Astrophys. J. Lett.*, 836:L21, February 2017. doi: 10.3847/2041-8213/aa5dee.

Martin Obergaulinger. *Astrophysical magnetohydrodynamics and radiative transfer: numerical methods and applications*. PhD thesis, Technische Universität München, 2008. URL https://mediatum.ub.tum.de/doc/632729/632729.pdf.

C. Palenzuela, S. L. Liebling, D. Neilsen, L. Lehner, O. L. Caballero, E. O'Connor, and M. Anderson. Effects of the microphysical equation of state in the mergers of magnetized neutron stars with neutrino cooling. *Phys. Rev. D*, 92(4):044045, August 2015. doi: 10.1103/PhysRevD.92.044045.

I. V. Panov, E. Kolbe, B. Pfeiffer, T. Rauscher, K.-L. Kratz, and F.-K. Thielemann. Calculations of fission rates for r-process nucleosynthesis. *Nuclear Physics A*, 747:633–654, January 2005. doi: 10.1016/j.nuclphysa.2004.09.115.

I. V. Panov, I. Y. Korneev, T. Rauscher, G. Martínez-Pinedo, A. Kelić-Heil, N. T. Zinner, and F.-K. Thielemann. Neutron-induced astrophysical reaction rates for translead nuclei. *Astron. Astrophys.*, 513:A61, April 2010. doi: 10.1051/0004-6361/200911967.

Carlos Pares. Numerical methods for nonconservative hyperbolic systems: a theoretical framework. *SIAM J. Numer. Anal.*, 44(1):300–321, 2006.

V. Paschalidis. General relativistic simulations of compact binary mergers as engines for short gamma-ray bursts. *Classical and Quantum Gravity*, 34(8):084002, April 2017. doi: 10.1088/1361-6382/aa61ce.

A. Perego, S. Rosswog, R. M. Cabezón, O. Korobkin, R. Käppeli, A. Arcones, and M. Liebendörfer. Neutrino-driven winds from neutron star merger remnants. *Mon. Not. R. Astron. Soc.*, 443:3134–3156, October 2014. doi: 10.1093/mnras/stu1352.

C. E. Petrillo, A. Dietz, and M. Cavaglià. Compact Object Coalescence Rate Estimation from Short Gamma-Ray Burst Observations. *Astrophys. J.*, 767:140, April 2013. doi: 10.1088/0004-637X/767/2/140.

T. Piran, E. Nakar, and S. Rosswog. The electromagnetic signals of compact binary mergers. *Mon. Not. R. Astron. Soc.*, 430:2121–2136, April 2013. doi: 10.1093/mnras/stt037.

D. Pollney, C. Reisswig, E. Schnetter, N. Dorband, and P. Diener. High accuracy binary black hole simulations with an extended wave zone. *Phys. Rev. D*, 83(4):044045, February 2011. doi: 10.1103/PhysRevD.83.044045.

Frans Pretorius. Evolution of binary black hole spacetimes. *Phys. Rev. Lett.*, 95:121101, 2005.

D. Radice and L. Rezzolla. Discontinuous Galerkin methods for general-relativistic hydrodynamics: Formulation and application to spherically symmetric spacetimes. *Phys. Rev. D*, 84(2):024010, July 2011. doi: 10.1103/PhysRevD.84.024010.

D. Radice and L. Rezzolla. THC: a new high-order finite-difference high-resolution shock-capturing code for special-relativistic hydrodynamics. *Astron. Astrophys.*, 547:A26, June 2012. doi: 10.1051/0004-6361/201219735.

D. Radice, L. Rezzolla, and T. Kellerman. Critical phenomena in neutron stars: I. Linearly unstable nonrotating models. *Class. Quantum Grav.*, 27(23):235015, December 2010. doi: 10.1088/0264-9381/27/23/235015.

D. Radice, L. Rezzolla, and F. Galeazzi. Beyond second-order convergence in simulations of binary neutron stars in full general-relativity. *Mon. Not. R. Astron. Soc. L.*, 437:L46–L50, June 2014a. doi: 10.1093/mnrasl/slt137.

D. Radice, L. Rezzolla, and F. Galeazzi. High-order fully general-relativistic hydrodynamics: new approaches and tests. *Class. Quantum Grav.*, 31(7):075012, April 2014b. doi: 10.1088/0264-9381/31/7/075012.

D. Radice, L. Rezzolla, and F. Galeazzi. High-Order Numerical-Relativity Simulations of Binary Neutron Stars. 498:121, October 2015.

D. Radice, F. Galeazzi, J. Lippuner, L. F. Roberts, C. D. Ott, and L. Rezzolla. Dynamical Mass Ejection from Binary Neutron Star Mergers. *Mon. Not. R. Astron. Soc.*, 460:3255–3271, August 2016. doi: 10.1093/mnras/stw1227.

T. Rauscher and F.-K. Thielemann. Astrophysical Reaction Rates From Statistical Model Calculations. *Atomic Data and Nuclear Data Tables*, 75:1–351, May 2000. doi: 10.1006/adnd.2000.0834.

C. Reisswig and D. Pollney. Notes on the integration of numerical relativity waveforms. *Class. Quantum Grav.*, 28:195015, 2011.

L. Rezzolla and P. Kumar. A Novel Paradigm for Short Gamma-Ray Bursts With Extended X-Ray Emission. *Astrophys. J.*, 802:95, April 2015. doi: 10.1088/0004-637X/802/2/95.

L. Rezzolla and O. Zanotti. *Relativistic Hydrodynamics*. Oxford University Press, Oxford, UK, 2013. ISBN 9780198528906. doi: 10.1093/acprof:oso/9780198528906.001.0001.

L. Rezzolla, L. Baiotti, B. Giacomazzo, D. Link, and J. A. Font. Accurate evolutions of unequal-mass neutron-star binaries: properties of the torus and short GRB engines. *Class. Quantum Grav.*, 27(11):114105, June 2010. doi: 10.1088/0264-9381/27/11/114105.

L. Rezzolla, B. Giacomazzo, L. Baiotti, J. Granot, C. Kouveliotou, and M. A. Aloy. The Missing Link: Merging Neutron Stars Naturally Produce Jet-like Structures and Can Power Short Gamma-ray Bursts. *Astrophys. J. Letters*, 732:L6, May 2011. doi: 10.1088/2041-8205/732/1/L6.

S. Rhebergen, O. Bokhove, and J.J.W. van der Vegt. Discontinuous Galerkin finite element methods for hyperbolic nonconservative partial differential equations. *Journal of Computational Physics*, 227:1887–1922, 2008.

Robert D. Richtmyer and K.W. Morton. *Difference Methods for Initial Value Problems*. Kreiger, Malabar, USA, 2nd edition, 1994. ISBN 0-89464-763-6.

L. F. Roberts, D. Kasen, W. H. Lee, and E. Ramirez-Ruiz. Electromagnetic Transients Powered by Nuclear Decay in the Tidal Tails of Coalescing Compact Binaries. *Astrophys. J. Lett.*, 736:L21, July 2011. doi: 10.1088/2041-8205/736/1/L21.

P. L. Roe. Approximate riemann solvers, parameter vectors and difference schemes. *J. Comput. Phys.*, 43:357, 1981.

S. Rosswog. Astrophysics: Radioactive glow as a smoking gun. *Nature*, 500: 535–536, August 2013a. doi: 10.1038/500535a.

S. Rosswog. The dynamic ejecta of compact object mergers and eccentric collisions. *Royal Society of London Philosophical Transactions Series A*, 371:20272, April 2013b. doi: 10.1098/rsta.2012.0272.

S. Rosswog and M. Liebendörfer. High-resolution calculations of merging neutron stars - II. Neutrino emission. *Mon. Not. R. Astron. Soc.*, 342:673–689, July 2003. doi: 10.1046/j.1365-8711.2003.06579.x.

S. Rosswog, M. Liebendörfer, F.-K. Thielemann, M. B. Davies, W. Benz, and T. Piran. Mass ejection in neutron star mergers. *Astron. Astrophys.*, 341:499–526, January 1999.

S. Rosswog, T. Piran, and E. Nakar. The multimessenger picture of compact object encounters: binary mergers versus dynamical collisions. *Mon. Not. R. Astron. Soc.*, 430:2585–2604, April 2013. doi: 10.1093/mnras/sts708.

S. Rosswog, U. Feindt, O. Korobkin, M.-R. Wu, J. Sollerman, A. Goobar, and G. Martinez-Pinedo. Detectability of compact binary merger macronovae. *Classical and Quantum Gravity*, 34(10):104001, May 2017. doi: 10.1088/1361-6382/aa68a9.

M. Ruffert, H.-T. Janka, and G. Schaefer. Coalescing neutron stars - a step towards physical models. I. Hydrodynamic evolution and gravitational-wave emission. *Astron. Astrophys.*, 311:532–566, July 1996.

Milton Ruiz, David Hilditch, and Sebastiano Bernuzzi. Constraint preserving boundary conditions for the Z4c formulation of general relativity. *Phys. Rev. D*, 83:024025, 2011. doi: 10.1103/PhysRevD.83.024025.

P. Sagaut and R. Grohens. Discrete filters for large eddy simulation. *Int. J. Numer. Meth. Fluids*, 31:1195–1220, 1999. doi: 10.1103/PhysRevD.79.104029.

N. Sanchis-Gual, P. J. Montero, J. A. Font, E. Müller, and T. W. Baumgarte. Fully covariant and conformal formulation of the Z4 system in a reference-metric approach: Comparison with the BSSN formulation in spherical symmetry. *Phys. Rev. D*, 89(10):104033, May 2014. doi: 10.1103/PhysRevD.89.104033.

Olivier Sarbach and Manuel Tiglio. Continuum and discrete initial-boundary value problems and einstein's field equations. *Living Rev. Relativity*, 15(9), 2012. URL http://www.livingreviews.org/lrr-2012-9.

E. Schnetter, S. H. Hawley, and I. Hawke. Evolutions in 3D numerical relativity using fixed mesh refinement. *Class. Quantum Grav.*, 21:1465–1488, March 2004. doi: 10.1088/0264-9381/21/6/014.

Karl Schwarzschild. Über das Gravitationsfeld eines Massenpunktes nach der Einsteinchen Theorie. *Sitzungsber. Dtsch. Akad. Wiss. Berlin, Kl. Math. Phys. Tech.*, 1:189–196, 1916.

Y. Sekiguchi, K. Kiuchi, K. Kyutoku, and M. Shibata. Dynamical mass ejection from binary neutron star mergers: Radiation-hydrodynamics study in general relativity. *Phys. Rev. D*, 91(6):064059, March 2015. doi: 10.1103/PhysRevD.91.064059.

Y. Sekiguchi, K. Kiuchi, K. Kyutoku, M. Shibata, and K. Taniguchi. Dynamical mass ejection from the merger of asymmetric binary neutron stars: Radiation-hydrodynamics study in general relativity. *Phys. Rev. D*, 93(12):124046, June 2016. doi: 10.1103/PhysRevD.93.124046.

M. Shibata. *Numerical Relativity*. World Scientific, Singapore, 2016. ISBN 978-981-4699-71-6. doi: 10.1142/9692.

M. Shibata and T. Nakamura. Evolution of three-dimensional gravitational waves: Harmonic slicing case. *Phys. Rev. D*, 52:5428–5444, November 1995. doi: 10.1103/PhysRevD.52.5428.

M. Shibata, Y. Suwa, K. Kiuchi, and K. Ioka. Afterglow of a Binary Neutron Star Merger. *Astrophys. J.l*, 734:L36, June 2011. doi: 10.1088/2041-8205/734/2/L36.

Masaru Shibata and Keisuke Taniguchi. Coalescence of black hole-neutron star binaries. *Living Rev. Relativity*, 14(6), 2011. URL http://www.livingreviews.org/lrr-2011-6.

H. L. Shipman. The implausible history of triple star models for Cygnus X-1 Evidence for a black hole. *Astrophysical Letters*, 16:9–12, February 1975.

C. W. Shu. Essentially non-oscillatory and weighted essentially non-oscillatory schemes for hyperbolic conservation laws. Lecture notes ICASE Report 97-65; NASA CR-97-206253, NASA Langley Research Center, 1997. URL http://ntrs.nasa.gov/archive/nasa/casi.ntrs.nasa.gov/19980007543_1998045663.pdf.

C.-W. Shu and S. Osher. Efficient Implementation of Essentially Non-oscillatory Shock-Capturing Schemes, II. *Journal of Computational Physics*, 83:32, July 1989. doi: 10.1016/0021-9991(89)90222-2.

C. W. Shu and S. J. Osher. Efficient implementation of essentially non-oscillatory shock-capturing schemes. *J. Comput. Phys.*, 77:439, 1988.

Chi-Wang Shu. Total-variation-diminishing time discretizations. *SIAM Journal on Scientific and Statistical Computing*, 9(6):1073–1084, 1988. doi: 10.1137/0909073. URL https://doi.org/10.1137/0909073.

D. M. Siegel and B. D. Metzger. Three-dimensional GRMHD simulations of the remnant accretion disks from neutron star mergers: outflows and r-process nucleosynthesis. *ArXiv e-prints*, May 2017.

D. M. Siegel, R. Ciolfi, and L. Rezzolla. Magnetically Driven Winds from Differentially Rotating Neutron Stars and X-Ray Afterglows of Short Gamma-Ray Bursts. *Astrophys. J.*, 785:L6, April 2014. doi: 10.1088/2041-8205/785/1/L6.

M. F. Skrutskie, R. M. Cutri, R. Stiening, M. D. Weinberg, S. Schneider, J. M. Carpenter, C. Beichman, R. Capps, T. Chester, J. Elias, J. Huchra, J. Liebert, C. Lonsdale, D. G. Monet, S. Price, P. Seitzer, T. Jarrett, J. D. Kirkpatrick, J. E. Gizis, E. Howard, T. Evans, J. Fowler, L. Fullmer, R. Hurt, R. Light, E. L. Kopan, K. A. Marsh, H. L. McCallon, R. Tam, S. Van Dyk, and S. Wheelock. The Two Micron All Sky Survey (2MASS). *Astronomical Journal*, 131:1163–1183, February 2006. doi: 10.1086/498708.

J. Smoller and B. Temple. Global solutions of the relativistic Euler equations. *Communications in Mathematical Physics*, 156:67–99, September 1993. doi: 10.1007/BF02096733.

G. A. Sod. A survey of several finite difference methods for systems of nonlinear hyperbolic conservation laws. *Journal of Computational Physics*, 27:1–31, April 1978. doi: 10.1016/0021-9991(78)90023-2.

A. W. Steiner, M. Hempel, and T. Fischer. Core-collapse Supernova Equations of State Based on Neutron Star Observations. *Astrophys. J.*, 774:17, September 2013. doi: 10.1088/0004-637X/774/1/17.

Stellarcollapse Website. Stellarcollapse. `https://stellarcollapse.org/`.

N. Stergioulas and J. L. Friedman. Comparing models of rapidly rotating relativistic stars constructed by two numerical methods. *Astrophys. J.*, 444:306–311, May 1995. doi: 10.1086/175605.

N. Straumann. *General relativity and relativistic astrophysics*. Springer-Verlag, Berlin and New York, 1984.

A. Suresh and H. T. Huynh. Accurate monotonicity-preserving schemes with runge-kutta time stepping. *Journal of Computational Physics*, 136(1):83–99, 1997. ISSN 0021-9991. doi: DOI:10.1006/jcph.1997.5745. URL `http://www.sciencedirect.com/science/article/B6WHY-45V7FSX-6/2/d88d3b5c02364ae5aa69b21d0e0787e7`.

K. Takami, L. Rezzolla, and S. Yoshida. A quasi-radial stability criterion for rotating relativistic stars. *Mon. Not. R. Astron. Soc.*, 416:L1–L5, September 2011. doi: 10.1111/j.1745-3933.2011.01085.x.

K. Takami, L. Rezzolla, and L. Baiotti. Spectral properties of the post-merger gravitational-wave signal from binary neutron stars. *Phys. Rev. D*, 91(6):064001, March 2015. doi: 10.1103/PhysRevD.91.064001.

M. Tanaka. Kilonova/Macronova Emission from Compact Binary Mergers. *Advances in Astronomy*, 2016:634197, 2016. doi: 10.1155/2016/6341974.

N. R. Tanvir, A. J. Levan, A. S. Fruchter, J. Hjorth, R. A. Hounsell, K. Wiersema, and R. L. Tunnicliffe. A 'kilonova' associated with the short-duration γ-ray burst GRB130603B. *Nature*, 500:547–549, August 2013. doi: 10.1038/nature12505.

I. Tews, J. M. Lattimer, A. Ohnishi, and E. E. Kolomeitsev. Symmetry Parameter Constraints From A Lower Bound On The Neutron-Matter Energy. *ArXiv e-prints*, November 2016.

The LIGO Scientific Collaboration and the Virgo Collaboration. Observation of Gravitational Waves from a Binary Black Hole Merger. *Phys. Rev. Lett.*, 116 (6):061102, February 2016. doi: 10.1103/PhysRevLett.116.061102.

The LIGO Scientific Collaboration and The Virgo Collaboration. Gw170817: Observation of gravitational waves from a binary neutron star inspiral. *Phys. Rev. Lett.*, 119:161101, Oct 2017. doi: 10.1103/PhysRevLett.119.161101. URL https://link.aps.org/doi/10.1103/PhysRevLett.119.161101.

The LIGO Scientific Collaboration, the Virgo Collaboration, B. P. Abbott, R. Abbott, T. D. Abbott, F. Acernese, K. Ackley, C. aAdams, T. Adams, P. Addesso, and et al. Multi-messenger observations of a binary neutron star merger. *Astrophys. J. Lett.*, 848(2):L12, 2017a. URL http://stacks.iop.org/2041-8205/848/i=2/a=L12.

The LIGO Scientific Collaboration, the Virgo Collaboration, B. P. Abbott, R. Abbott, T. D. Abbott, F. Acernese, K. Ackley, C. Adams, T. Adams, P. Addesso, and et al. GW170104: Observation of a 50-Solar-Mass Binary Black Hole Coalescence at Redshift 0.2. *ArXiv e-prints*, June 2017b.

M. Thierfelder, S. Bernuzzi, D. Hilditch, B. Bruegmann, and L. Rezzolla. The trumpet solution from spherical gravitational collapse with puncture gauges. *Phys. Rev. D*, 83:064022, December 2010.

M. Thierfelder, S. Bernuzzi, and B. Brügmann. Numerical relativity simulations of binary neutron stars. *Phys. Rev. D*, 84(4):044012, August 2011. doi: 10.1103/PhysRevD.84.044012.

F. X. Timmes and Dave Arnett. The accuracy, consistency, and speed of five equations of state for stellar hydrodynamics. *Astrophysical Journal, Supplement Series*, 125(1):277–294, 11 1999. ISSN 0067-0049. doi: 10.1086/313271.

F. X. Timmes and F. D. Swesty. The Accuracy, Consistency, and Speed of an Electron-Positron Equation of State Based on Table Interpolation of the Helmholtz Free Energy. *Astrophys. J., Supp.*, 126:501–516, February 2000. doi: 10.1086/313304.

V. A. Titarev and E. F. Toro. ADER: Arbitrary High Order Godunov Approach. *Journal of Scientific Computing*, 17:609, December 2002.

V. A. Titarev and E. F. Toro. ADER schemes for three-dimensional non-linear hyperbolic systems. *Journal of Computational Physics*, 204:715–736, April 2005. doi: 10.1016/j.jcp.2004.10.028.

E. F. Toro. *Riemann Solvers and Numerical Methods for Fluid Dynamics*. Springer-Verlag, third edition, 2009.

E. F. Toro and V. A. Titarev. Derivative Riemann solvers for systems of conservation laws and ADER methods. *Journal of Computational Physics*, 212(1): 150–165, 2006.

E. F. Toro, A. Hidalgo, and M. Dumbser. FORCE schemes on unstructured meshes I: Conservative hyperbolic systems. *Journal of Computational Physics*, 228:3368–3389, May 2009. doi: 10.1016/j.jcp.2009.01.025.

Petr Tsatsin and Pedro Marronetti. Initial data for neutron star binaries with arbitrary spins. *Phys. Rev. D*, 88:064060, Sep 2013. doi: 10.1103/PhysRevD.88.064060. URL http://link.aps.org/doi/10.1103/PhysRevD.88.064060.

S. Typel, G. Röpke, T. Klähn, D. Blaschke, and H. H. Wolter. Composition and thermodynamics of nuclear matter with light clusters. *Phys. Rev. C*, 81(1): 015803, January 2010. doi: 10.1103/PhysRevC.81.015803.

K. A. van Riper and J. M. Lattimer. Stellar core collapse. I - Infall epoch. *Astrophys. J.*, 249:270–289, October 1981. doi: 10.1086/159285.

R. Vichnevetsky and J. B. Bowles. *Fourier Analysis of Numerical Approximations of Hyperbolic Equations*. SIAM, Philadelphia, USA, 1982.

Robert M. Wald. *General relativity*. The University of Chicago Press, Chicago, 1984. ISBN 0-226-87032-4 (hardcover), 0-226-87033-2 (paperback).

S. Wanajo, Y. Sekiguchi, N. Nishimura, K. Kiuchi, K. Kyutoku, and M. Shibata. Production of All the r-process Nuclides in the Dynamical Ejecta of Neutron Star Mergers. *Astrophys. J.*, 789:L39, July 2014. doi: 10.1088/2041-8205/789/2/L39.

Shinya Wanajo. The r-process in proto-neutron-star wind revisited. *Astrophys. J. Lett.*, 770(2):L22, 2013. URL http://stacks.iop.org/2041-8205/770/i=2/a=L22.

Andreas Weyhausen, Sebastiano Bernuzzi, and David Hilditch. Constraint damping for the Z4c formulation of general relativity. *Phys. Rev. D*, D85: 024038, 2012. doi: 10.1103/PhysRevD.85.024038.

J. Winicour. Characteristic Evolution and Matching. *Living Rev. Relativity*, 8:10, December 2005.

C. Winteler, R. Käppeli, A. Perego, A. Arcones, N. Vasset, N. Nishimura, M. Liebendörfer, and F.-K. Thielemann. Magnetorotationally Driven Supernovae as the Origin of Early Galaxy r-process Elements? *Astrophys. J. Lett.*, 750:L22, May 2012. doi: 10.1088/2041-8205/750/1/L22.

Christian Winteler. *Light element production in the big bang and the synthesis of heavy elements in 3D MHD jets from core-collapse supernovae*. dissertation, University of Basel, 2012.

R. T. Wollaeger, O. Korobkin, C. J. Fontes, S. K. Rosswog, W. P. Even, C. L. Fryer, J. Sollerman, A. L. Hungerford, D. R. van Rossum, and A. B. Wollaber. Impact of ejecta morphology and composition on the electromagnetic signatures of neutron star mergers. *ArXiv e-prints*, May 2017.

Kailiang Wu. Design of provably physical-constraint-preserving methods for general relativistic hydrodynamics. *Phys. Rev. D*, 95:103001, May 2017. doi: 10.1103/PhysRevD.95.103001. URL https://link.aps.org/doi/10.1103/PhysRevD.95.103001.

B. Yang, Z.-P. Jin, X. Li, S. Covino, X.-Z. Zheng, K. Hotokezaka, Y.-Z. Fan, T. Piran, and D.-M. Wei. A possible macronova in the late afterglow of the long-short burst GRB 060614. *Nature Communications*, 6:7323, June 2015. doi: 10.1038/ncomms8323.

S. Yoshida and Y. Eriguchi. Quasi-radial modes of rotating stars in general relativity. *Mon. Not. R. Astron. Soc.*, 322:389, 2001.

O. Zanotti and M. Dumbser. A high order special relativistic hydrodynamic and magnetohydrodynamic code with space-time adaptive mesh refinement. *Computer Physics Communications*, 188:110–127, March 2015. doi: 10.1016/j.cpc.2014.11.015.

O. Zanotti, F. Fambri, and M. Dumbser. Solving the relativistic magnetohydrodynamics equations with ADER discontinuous Galerkin methods, a posteriori subcell limiting and adaptive mesh refinement. *Mon. Not. R. Astron. Soc.*, 452:3010–3029, September 2015a. doi: 10.1093/mnras/stv1510.

O. Zanotti, F. Fambri, M. Dumbser, and A. Hidalgo. Space-time adaptive ader discontinuous galerkin finite element schemes with a posteriori sub-cell finite volume limiting. *Computers and Fluids*, 118(0):204 – 224, 2015b.

Weiqun Zhang and A.I. MacFadyen. RAM: A relativistic adaptive mesh refinement hydrodynamics code. *The Astrophysical Journal Supplement Series*, 164:255, 2006. URL http://iopscience.iop.org/0067-0049/164/1/255.

M. Zilhão and F. Löffler. An Introduction to the Einstein Toolkit. *International Journal of Modern Physics A*, 28:1340014, September 2013. doi: 10.1142/S0217751X13400149.

Valentin Zingan, Jean Luc Guermond, Jim Morel, and Bojan Popov. Implementation of the entropy viscosity method with the discontinuous Galerkin method. *Computer Methods in Applied Mechanics and Engineering*, 253:479–490, 2013. ISSN 00457825. doi: 10.1016/j.cma.2012.08.018.